ERGODIC THEORY OF CLIMATE: VARIABILITY, STABILITY AND RESPONSE

Alexis Jean Jacques Tantet

Alexis Jean Jacques Tantet
Institute for Marine and Atmospheric research Utrecht (IMAU)
Ocean and climate

Present address:
Institute for Marine and Atmospheric research Utrecht (IMAU)
Utrecht University
P.O. Box 80005, 3508 TA Utrecht, The Netherlands
a.j.j.tantet@uu.nl

Cover designed by Clémentine Tantet

ISBN: 978-90-393-6505-2
Printing: GVO drukkers & vormgevers B.V.

ERGODIC THEORY OF CLIMATE: VARIABILITY, STABILITY AND RESPONSE

Ergodentheorie van het klimaat: variabiliteit, stabiliteit en respons

(met een samenvatting in het Nederlands)

Proefschrift

ter verkrijging van de graad van doctor aan de Universiteit Utrecht op gezag van de rector magnificus, prof.dr. G.J. van der Zwaan, ingevolge het besluit van het college voor promoties in het openbaar te verdedigen op

maandag 25 april 2016 des middags te 12.45 uur

door

ALEXIS JEAN JACQUES TANTET

geboren op 19 juli 1989
te Paris, Frankrijk

PROMOTOR: Prof. dr. ir. H. A. Dijkstra

This thesis was accomplished as part of the LINC project (no. 289447) funded by EC's Marie-Curie ITN program (FP7-PEOPLE-2011-ITN).

À mes parents, pour leur amour sans réserve, leur soutient et leur patience

We believe in the value of the interplay between mathematics and physics, although either discipline offers only incomplete results. A mathematical theorem can prevent us from making "intuitive" assumptions that are already proved to be invalid. On the other hand, the relation between the two disciplines can help us to formulate mathematical conjectures which are made plausible on the basis of our experience as physicists. We are fortunate that the theory of dynamical systems has reached a stage where this kind of attitude seems especially fruitful.

Eckmann and Ruelle (1985)

CONTENTS

LIST OF FIGURES

LIST OF TABLES

FREQUENTLY USED ACRONYMS

DDE Delay Differential Equation

EBM Energy Balance Model

ENSO El Niño-Southern Oscillation

GCM General Circulation Model

MLE Maximum Likelihood Estimator

ODE Ordinary Differential Equation

PDE Partial Differential Equation

RDS Random Dynamical System

SDDE Stochastic Delay Differential Equation

SDE Stochastic Differential Equation

SST Sea Surface Temperature

OU Ornstein-Uhlenbeck process

SUMMARY

Climate studies deal with changes in the statistics rather than in the exact state of the Earth system. Ergodic theory is the art of relating the dynamics of a system to its statistical properties and is thus particularly suitable to a unifying theory of climate.

This work introduces concepts of ergodic theory to the study of climate variability, stability and response to forcing. The focus is on the spectrum of transfer operators, governing the evolution of statistics by the dynamics. It is shown that crucial information about a system's stability can be extracted from approximations of the transfer operators and their ergodicity spectrum. These results are first applied to stochastic systems relevant to climate and in particular to El Niño-Southern Oscillation (ENSO), the dominant pattern of climate variability on interannual time-scales. Novel analytical formulas are found for the ergodicity spectrum of these systems. A key result is the direct relation between the shrinkage of this spectrum and the slowing down of a system undergoing a crisis, i.e. a dramatic change in its statistics. In addition, it is shown that the ergodicity eigenvectors are very sensitive to nonlinear effects and could allow to unravel the nature of dominant patterns of variability such as ENSO.

It is a matter of great debate whether the Earth system can undergo such dramatic events and if state-of-the-art climate models are able to resolve them and to give early-warnings. The transition from a warm to a snow-covered Earth due to the ice-albedo feedback found in the Planet Simulator, a General Circulation Model (GCM) of intermediate complexity, is an example of such crisis. We explain for the first time how slowing down occurring at the crisis is due to the shrinkage of the ergodicity spectrum. The study of the ergodicity spectrum thus allows to discuss the validity of concepts such as climate sensitivity or linear response as well as the applicability of early-warning indicators of crises to high-dimensional systems such as climate.

Lastly, we show that transfer operators can be applied to the study of midlatitude blocking events. These atmospheric regimes of increased persistence have a large impact on the climate of western Europe and North America. In a hemispheric barotropic model of the troposphere with realistic forcing, it is found that these regimes are associated with the ergodicity spectrum responsible for a slow decay of correlations. This allows to extract them as almost-invariant sets connected by preferred transition paths. These paths constitute a source of predictability allowing to design an early-warning indicator of transition from the zonal to the blocked regime.

As a general conclusion, this work supports ergodic and dynamical systems theory as a unifying mathematical framework to climate dynamics and the study of its natural variability, stability and response to forcing.

SAMENVATTING

In de klimaatwetenschap probeert men de statistische veranderingen in weerpatronen te beschrijven in plaats van de exacte toestand van het weer. Ergodische theorie relateert de dynamiek van een system aan de statistische eigenschappen ervan en is daarom een bijzonder geschikt fundament om een universele theorie van het klimaat op te ontwikkelen. In dit proefschrift worden concepten uit de ergodische theorie geïntroduceerd in de studie van klimaatvariabiliteit en stabiliteit en de reactie van het klimaatsysteem op bepaalde veranderingen in de forcering. Cruciale informatie over de stabiliteit van het systeem kan bijvoorbeeld worden afgeleid uit benaderingen van de transfer operatoren en de bijbehorende spectra.

De resultaten zijn toegepast op stochastische systemen die relevant zijn voor het klimaat zoals de ENSO, het meest dominante patroon van klimaatvariabiliteit op tijdschalen van meerdere jaren. Voor de ergodische spectra van dit systeem zijn nieuwe analytische vergelijkingen geformuleerd. Een van de belangrijkste resultaten is dat er een relatie is tussen het krimpen van het betreffende spectrum en het vertragen van het systeem tijdens een crisis, d.w.z. een drastische verandering in de statistische eigenschappen van het systeem. Bovendien blijken de ergodische eigenvectoren zeer gevoelig te zijn voor niet-lineaire effecten. Ze kunnen daarom mogelijk helpen de geheimen te ontrafelen van patronen zoals ENSO.

Er is groot debat gaande over het feit of het klimaatsysteem dramatische transities kan ondergaan en bovendien of klimaatmodellen deze op een realistische manier kunnen oplossen en daarmee tijdig alarm kunnen slaan. Een voorbeeld van zoń crisis is de transitie van de aarde van een warme toestand naar een toestand volledig bedekt met sneeuw door de ijs-albedo feedback. Deze crisis was gevonden in de Planet Simulator, een algemeen circulatie model van gemiddelde complexiteit. In dit proefschrift leggen we voor het eerst de vertraging uit die optreedt tijdens de crisis aan de hand van het krimpen van het ergodische spectrum. Het bestuderen van dit spectrum geeft daarmee een handvat om niet alleen de validiteit van concepten zoals klimaatgevoeligheid of lineaire reacties te testen, maar ook de toepasbaarheid van alarm-indicatoren voor crises in hoog-dimensionele systemen zoals het klimaat.

Tot slot laten we zien dat transfer operatoren gebruikt kunnen worden om situaties te bestuderen waarin zich een blokkade in de atmosfeer vormt. Deze typische patronen in de circulatie van de atmosfeer in de gematigde zones hebben een grote impact op het weer in West-Europa en Noord-Amerika. In een hemisferisch, barotroop model van de troposfeer met realistische forcering laten we zien dat deze regimes geassocieerd zijn met het ergodische spectrum dat verantwoordelijk is voor het langzaam afnemen van correlaties. Hierdoor is het mogelijk om bijna-invariante paren af te lei-

den die verbonden zijn door de meest waarschijnlijke paden van de transitie. Deze meest waarschijnlijke paden hebben een bepaald voorspellend vermogen en op basis daarvan kan een alarmindicator gedefinieerd worden voor de transitie van een zonaal naar een geblokkeerd regime.

Dit proefschrift geeft met de theorie van ergodiciteit en dynamische systemen een algemene, mathematische basis voor klimaatdynamica en de natuurlijke variabiliteit, stabiliteit en de reactie op forcering van het klimaatsysteem.

1

INTRODUCTION

This dissertation is concerned in the broad sense with problems such as characterizing low-frequency climate, climate stability and its response to a forcing. Let us first motivate the unifying approach of ergodic theory and dynamical systems analysis to study such problems.

1.1 WHAT IS CLIMATE?

Historically, "climate" would refer to the expected value of meteorological quantities, such as surface temperature or precipitation, in different regions of the Earth. These expectations would be calculated from long-time averages, possibly for a given month, to take into account the seasonal cycle due to the rotation of the Earth around the Sun (Hartmann, 1994).

While such a statistical picture of the climates of the globe is already valuable for example for urban development, agricultural planning or marine trade, it became clear at the end of the 19th century and especially during the 20th century, that such a picture is far from being complete and that the climate of the Earth (as well as of other planets such as Jupiter) is much richer and dynamic than previously thought (Peixoto and Oort, 1992). In particular, with the advent of long instrumental and proxy records, the satellite era and the study of deterministic chaos, it was understood that climate exhibits natural and forced variability on a broad range of time scales, from days to thousands of years and that such variability could have a major impact on life and societies. This can be seen from the artistic view of the composite power spectrum of climatic time series represented in figure 1.1 (giving

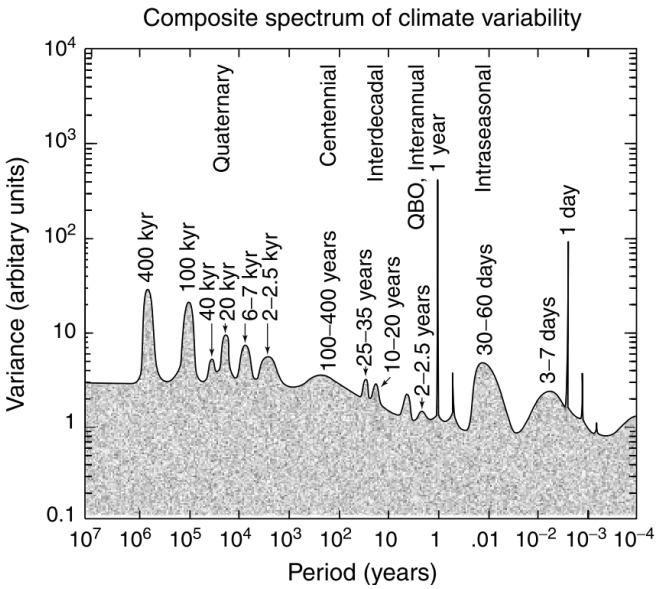

Figure 1.1: An "artist's rendering" of the composite power spectrum of climate variability showing the amount of variance in each frequency range. From Ghil (2002).

the density of explained variance per frequency). In addition to the daily and yearly cycles, associated with the orbital parameters of the solar system, broad peaks superimposed on a continuous background are visible on intraseasonal, interannual to longer time scales. To analyze such climate variability, the statistical measures had to be extended to include higher-order moments such as the variance and covariance as well the autocorrelation function in time or its counterpart in the frequency domain, the power spectrum (von Storch and Zwiers, 1999). These measures can be applied to observations to analyze the shorter term variability. However, the study of long time scales requires the use of numerical models due to the limited length and extent of the observational record and to limitations inherent to laboratory experiments.

Over the years, it has become a major challenge to characterize the origin of this variability and to understand the physical mechanisms behind it (Ghil, 2001). There are several reasons for this. First, to understand to what kind of climatic conditions life on earth should be able to resist to (e.g how high should a Dutch dyke be to prevent one in a 10000 years flooding event?). Second, to distinguish changes which are natural (i.e from internal dynamics or from natural changes in the forcing, such as the Milankovitch cycle) from changes caused by humans (the anthropogenic forcing). Indeed, in addition to the fact that climate variability can impact the life of a

human being, an entire society or the ecological system, it was discovered that humans themselves could have an influence on climate, e.g. through the emission of greenhouse gas, deforestation or urbanization (Stocker et al., 2013). Distinguishing natural changes from changes due to mankind would allow (and partially has) to clarify the role of Man in the observed global warming of the twentieth century and to design incentives so as to prevent and mitigate such a change. It thus turns out to be essential to understand how sensitive climate is to changes in forcing, whether natural (such as the solar forcing or volcanic eruptions) or anthropogenic. That is, whether the response of climate to forcing is predominantly linear or whether nonlinear or even abrupt changes can occur due to instabilities is crucial for a cautious society willing to preserve the delicate climatic conditions favorable for life as we know it (Lucarini et al., 2013).

Thirdly, characterizing climate variability is key to understand the degree of predictability of climate on long time scales (can we predict El Niño events a year ahead even though weather forecasts more than one week ahead are pour?) and improve forecast skills of weather and climate models (Held, 2005; Williams et al., 2013). This last point raises the question of the distinction between weather an climate. Indeed, both terms refer to a particular state of the Earth system, so that the physics associated to them intersect. This is manifested by the fact that General Circulation Models (GCMs) used in weather forecasting or climate projections are in many ways similar and are often sharing the same dynamical cores (Warner, 2010). However, it is clear that the exercise of forecasting the temperature and amount of precipitation at a precise hour and location with a lead time of a few days should be classified as weather forecasting. Following the pioneering work of Lorenz (1963), it is usually accepted that beyond a "predictability range" of a few weeks, such exercise is hopeless, due to the sensitive dependence of the earth system to initial conditions. However, it is apparent that anticipating, for instance, what time averages of temperatures around the globe would be in a 100 years if we continue to increase our greenhouse gas emissions constitutes a different exercise one can refer to as climate projection. Yet, in which category the prediction of atmospheric blocking events (Barriopedro et al., 2006) or of interannual events such as El Niño should fall into? Along these lines, what is the relationship between variability, predictability and stability and what are the mathematical structures behind these concepts? We will see that ergodic theory and dynamical systems provide crucial elements of answer to these questions.

1.2 HISTORICAL DEVELOPMENTS IN ERGODIC THEORY, DYNAMICAL SYSTEMS AND CHAOS

Ergodic theory and *dynamical systems analysis* (including stochastic processes) constitute the mathematical physics foundation of the present dissertation. Interestingly,

even though both theories emerged rather independently, with one focusing on the statistical properties of a system and the other on its topology, both approaches quickly converged and raised the interest of both mathematicians and physicists. A nonexhaustive summary of the past developments in ergodic theory, bifurcation theory and chaos will help understand the relevance of such approaches to the study of climate.

The advent of dynamical systems analysis started with the early discovery of chaos and pioneering work of Poincaré (1881) who studied the qualitative behavior of solutions of differential equations which are not integrable (due to the presence of homoclinic orbits, Poincaré, 1892) and the following works by Lyapunov (1892) and Perron (1929) on the stability of these solutions (one should also mention the important contribution of Bendixson, 1899, to the demonstrations of results from Pointcaré). Meanwhile, inspired by the work of Maxwell (1860), who derived a probability distribution of molecular velocities on heuristic grounds, the young Boltzmann (1909) revolutionized modern physics with his mechanical interpretation of the second law of thermodynamics and the association of an equilibrium state with a probability distribution μ (or, in modern terms, measure) invariant under the dynamics. Such a description proved very well suited to understand the macroscopic properties of systems with many degrees of freedom, such as an ideal gas, and led the foundations of equilibrium thermodynamics. Boltzmann's work was subsequently extended by Gibbs (1902), in his developments of statistical physics. The existence of such a distribution relies on an "ergodic hypothesis" and guaranties that the (macroscopic) average $\bar{g}$ of an observable g, such as the energy, exists independently of an initial (microscopic) state x, such that

$$\bar{g} = \lim_{T\to\infty} \frac{1}{T} \int_0^T g(\phi(t)x)dt = \int g(x)\mu(dx), \tag{1.1}$$

where the flow $\phi(t), t \geq 0$ yields the state at time t of a solution of the system with initial state x . The last identity is true when μ is unique (i.e when μ is ergodic) and was proved by Birkhoff (1931) who further developed the link made by Boltzmann and Gibbs between ergodic theory and dynamical systems analysis (Birkhoff, 1927), while Doob (1934) made the bridge with stochastic processes. The ergodic theorem was also proved in a different functional context by von Neumann (1932) following the ideas of Stone (1930), who considered groups of unitary operators in Hilbert space, and Koopman (1931), in application to the evolution of observables induced by the flow (see Chap. 2). Note that while Poincaré's recurrence theorem (Poincaré, 1890) guaranties than an initial state in a set of positive measure returns infinitely often to this set, Birkhoff's ergodic theorem gives information on the rates at which they do so, according to Kac's lemma (Kac, 1947).

In the footsteps of Poincaré and Bendixson, the "Moscow school" of Andronov and his wife Leontovich started in the late 30s to develop bifurcation theory in the plane (Andronov et al., 1971), after Andronov and Pontryagin (1937) had introduced the

important concept of structural stability of a vector field. Bifurcation theory is a particular branch of dynamical systems theory introduced by Poincaré (1885) and concerned with the study of qualitative changes in solutions of dynamical systems with a parameter. However, the study of chaos took off later, in particular with the seminal work of Kolmogorov (1954) (followed by Moser, 1962; Arnold, 1963) who showed that the integrability of Hamiltonian systems was robust to small perturbations but that irregular behavior could occur for larger perturbations, and with the early work of Chirikov (1960) on Hamiltonian chaos. Both works precede the advent of scientific computing and were followed by major contributions among which those of Henon and Heiles (1964), Zaslavsky and Chirikov (1964) and Arnold and Avez (1967). At this time, Kolmogorov (1958) and Sinai (1959) had the great intuition that the concepts from thermodynamics could be extended to chaotic systems with the study of the evolution of distributions in phase space rather than that of unpredictable and apparently stochastic trajectories. This led to the definition of the Kolmogorov-Sinai entropy as a measure of the degree of chaoticity or predictability of a system. As it became clear that the positive entropy of dynamical systems is related to the exponential divergence of orbits originating at nearby points, Oseledets (1968), a student of Sinai, extended the definition of Lyapunov exponents to nonlinear systems and proved their existence. It was then Pesin (1977) who proved the relation between the entropy and the sum of the positive Lyapunov exponents (i.e. the total expansion rate of the system) and developed the ergodic theory for nonuniformly hyperbolic systems with notable extensions by Katok (1980) and Ledrappier and Young (1985). The interested reader is redirected to the review by Livi et al. (2003) for more details on the role of Kolmogorov in the study of chaos.

On the other hand, the appreciation of the importance of chaos to forced-dissipative systems, such as climate, really started with the work of Lorenz (1963). He not only showed, thanks to extensive numerical integrations, that such systems could have aperiodic, yet bounded, solutions exhibiting sensitive dependance to initial conditions, but also that these solutions are attracted to some complicated set, a strange attractor, which is neither a fixed point nor a periodic orbit or a torus. His study had profound consequences regarding the inherent limitations of numerical weather predictions (a first example of which is the numerical weather prediction by Charney, FJortoft, and von Neumann (1950) on the ENIAC computer) and the clarity of his exposure and quality of his intuition inspired many subsequent work on chaos.

Soon followed several breakthroughs in the field. Bifurcation theory was further developed in higher dimensions by the "Gorky school" (former Nizhny Novgorod), led by Shilnikov who showed that homoclinic orbits play a key role in the route to chaos (as already suspected by Poincaré). In particular, the discovery of spiral chaos near a saddle-node loop (Shilnikov, 1965) was a genuinely paradigmatic shift for bifurcation theory (Afraimovich et al., 2014). Indeed, it provides one of the simplest route to chaos for dissipative systems and it was found in many real-world systems (Shilnikov, 1984) such as the in the Lorenz model (Shilnikov et al., 1995). Another

major contribution is due to Smale (1967) who characterized unstable orbits of dissipative systems by dynamics of stretching and the due to the boundedness of the attractor and worked on the problem of structural stability of a vector field (Smale, 1966). The topological approach of Stephen Smale greatly inspired that of Anosov (1962). Indeed, Anosov showed that even though orbits of chaotic systems are sensitive to perturbations, their statistical properties can be robust, as long as the system is sufficiently chaotic (i.e hyperbolic). This topological approach also raised the interest of Ruelle and Takens (1971) who demonstrated that strange attractors, such as the famous "butterfly" of Lorenz, are bound to emerge in forced-dissipative system far from equilibrium and who suggested that such an attractor could be at the origin of turbulence.

Anosov and Smale having shed light on the relevance of hyperbolic systems to the study of dissipative chaos, the link between the dynamics of such systems and their statistical properties was formalized by Sinai (1972) and Bowen and Ruelle (1975). They showed, that even though nonconservative forces continually push a dissipative system out of equilibrium (so that classical statistical mechanics does not apply), a unique invariant probability measure with physical relevance exists (the Sinai-Ruelle-Bowen or SRB measure), taking the role of the Gibbs measure found in equilibrium thermodynamics. As a consequence, the SRB measure was naturally coined the term of Non-Equilibrium Steady State (NESS) by Gallavotti and Ruelle (1997) and coworkers. The strong connections between the topological and statistical approaches was summarized in the inspiring review by Eckmann and Ruelle (1985).

While the invariant measure μ allows to calculate averaged quantities, the correlation function between two observables f and g, defined as

$$C_{f,g}(t) = \int f\, g \circ \phi(t) d\mu - \int f\, d\mu \int g d\mu$$

gives a measure, in time domain, of the variability of a system (where the $\phi(t), t \geq 0$ is the flow). A striking result regarding the statistical properties of chaotic systems is that the correlation function of many such systems, called *mixing*, decays rapidly to zero, as in the stochastic case. While the metric entropy introduced by Kolmogorov and Sinai gives a measure of predictability due to the divergence of nearby trajectories, the rate at which the correlation function decays with time is another particularly important quantity, which, roughly speaking, indicates of how fast a mixing system converges to the invariant measure. Pollicott (1985) and Ruelle (1986b) related this rate of decay with the spectral properties of the nonequilibrium counterparts of the operators introduced by Koopman and von Neumann half a century before. Ruelle (1997) could then relate this spectrum to the response of hyperbolic systems to forcing (i.e. to the differentiability of the SRB measure). Such results and others gave a strong revival to the development of nonequilibrium statistical mechanics (which had been much slower than for the equilibrium case). In particular, Ruelle (1997) gave a generalization to systems far from equilibrium of the linear response formula by

Kubo (1966). Furthermore, the relevance of hyperbolic systems for the study of more general chaotic systems with a large number of degrees of freedom found in physics was argued by Gallavotti and Cohen (1995), who, inspired by the work of Ruelle (1980) on the statistical properties of turbulence and the role of thermal fluctuations (Ruelle, 1979), proposed an extension of the "ergodic hypothesis" to nonequilibrium systems, namely, the "chaotic hypothesis". These successful developments led Ruelle (1999) and Gallavotti (2014) to propose smooth dynamical systems and SRB measures as the appropriate framework for the rigorous study of nonequilbirum statistical mechanics. Along these lines and as a final remark, the late twentieth century was thus marked by a formidable convergence between mathematicians and physicists in the domain of dynamical systems and statistical mechanics, as witnessed by Sinai (Bolibruch et al., 2005, page 399).

1.3 APPLICABILITY TO CLIMATE

As a chaotic system with many degrees of freedom, climate constitutes an eligible system for the application of methods from ergodic theory and dynamical systems analysis (Dymnikov and Gritsoun, 2001). For example, the range of predictability of the system due to sensitive dependence to initial conditions limits the potential of weather forecasts to a few weeks (Lorenz, 1969; Leith, 1978; Simmons and Hollingsworth, 2002). Such a forecast corresponds to a numerical integration of a model from an initial state x_0 over a period T, resulting in a trajectory $\{\phi(t)x_0\}_{0\leq t\leq T}$, in the phase space $X = \mathbb{R}^d$, where d is the dimension of the system, or, in other words, the number of prognostic variables. Here, the evolution equation for the system is assumed well-posed (in Hadamard's sense, see Engel and Nagel, 2001) so that the flow $\phi(t), t \geq 0$ yields the unique solution $\phi(t)x_0$ at time t with initial condition x_0. The initial state is determined from (incomplete) measurements usually complemented by data assimilation (Charney et al., 1969; Leith, 1975a). The spatial sparsity of these measurements is a major source of error which is amplified during numerical integrations due to instabilities associated with positive Lyapunov exponents. Moreover, small-scale errors are transferred to the large scales by the nonlinearities (Leith and Kraichnan, 1972) and there is a dependance of the error growth rate on the scale (e.g. the range of predictability of synoptic weather systems is much longer that that of thunderstorms, see also Hoskins, 2013). In theory, the degree of predictability can be measured by the Kolmogorov-Sinai entropy (Kolmogorov, 1958; Sinai, 1959), mentioned in the previous section 1.2, as the sum of the positive Lyapunov exponents (Pesin, 1977). In practice, several methods have been proposed to evaluate the rate of error growth with time of atmospheric flows based on numerical models, analogs or statistical theory of turbulence (Lorenz, 1969; Leith, 1975a).

Since the seminal work of Epstein (1969) and Leith (1974), a common exercise to improve weather forecasts and quantify their uncertainty is to simulate trajectories

of an ensemble of members with initial states perturbed around a reference (Leutbecher and Palmer, 2008). An observable of interest, such as the temperature at a location, can then be averaged over the ensemble to give an arguably more accurate prediction than for a single trajectory and the variance of the observable over the ensemble can give an indication of the reliability of the prediction. Such a practice conforms with the study of the evolution of statistics advocated by Kolmogorov, Sinai and others rather than that of a single chaotic trajectory. Indeed, this mathematically corresponds to studying the evolution of the initial distribution $\rho_0(x) = \frac{1}{m}\sum_{i=1}^{m}\delta(x-x_0^{(i)})$ induced by the dynamics, where each $x_0^{(i)}$ corresponds to a perturbed initial state and δ is the Dirac distribution. The transferred distribution $\rho(x,t)$ after a time t is such that, for any smooth observable $g : X \to \mathbb{R}$,

$$\int_X \rho(x,t)g(x)dx = \int_X \rho_0(x)g(\phi(t)x)dx = \frac{1}{m}\sum_{i=1}^{m} g(\phi(t)x_0^{(i)}). \tag{1.2}$$

The term $\int_X \rho_0(x)g(\phi(t)x)$ is the average of the observable g after a time t with respect to the initial distribution ρ_0. From the definition of ρ_0, this term coincides with the ensembles average $\frac{1}{m}\sum_{i=1}^{m} g(\phi(t)x_0^{(i)})$ calculated by taking the sample mean of the observable g evaluated at the final states of each member after a time t. The first equality is valid for any distribution in appropriate functional spaces and the so-defined distribution $\rho(t)$ is unique (Lasota and Mackey, 1994, Chap. 3). Thus, there exists a linear operator $\mathscr{P}_t$, the *transfer operator*, such that $\rho(t) = \mathscr{P}_t\rho_0$, yielding the evolution of distributions after a finite time t. It follows that performing an ensemble simulation is nothing but numerically calculating the evolution by $\mathscr{P}_t$ of a distribution constituted of a countable number of Dirac distributions. This is illustrated figure 1.2, where the first integral in (1.2) corresponds to the situation represented in panel (a), for which the average of the observable g is taken with respect to the transferred density $\rho(t) = \mathscr{P}_t\rho_0$. The second integral in (1.2) corresponds to the situation represented in panel (b), for which the average of the transferred observable $g \circ \phi(t)$ is taken with respect to the initial density ρ_0.

A key concept in ergodic theory is that of invariant measure, which leads to the mathematical definition of a mean climatic state (Dymnikov et al., 2006). In order to determine the mean state of the climate system, a long time series $\{\phi(t)x\}_{0\leq t\leq T}$ is usually taken (from observations or from a simulation) and it is assumed that, for an observable g, the time average

$$\bar{g} = \lim_{T\to\infty}\frac{1}{T}\int_0^T g(\phi(t)x)dt, \tag{1.3}$$

is well-defined (exists uniquely) and is given by the phase space average

$$\bar{g} = \int_X g(x)\mu(dx), \tag{1.4}$$

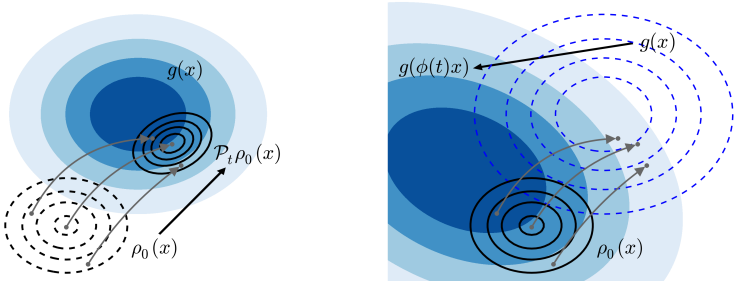

(a) (b)

Figure 1.2: Two equivalent calculations of the average of the observable g at time t for an initial ensemble ρ_0. (a) The integral of g (contours filled in blue) is taken with respect to the initial density ρ_0 (dashed black line contours) transferred forward to $\mathscr{P}_t\rho_0$ (thick black line contours), as for the first term of (1.2). (b) The integral of g (dashed blue line contours) transferred backward to $g \circ \phi(t)$ (contours filled in blue) is taken with respect to the initial density ρ_0 (thick black line contours), as for the second term of (1.2) The thin gray arrows give an example of three states evolved for a time t as individual trajectories by the flow $\phi(t)$ and as an ensemble by $\mathscr{P}_t$, according to (1.2)

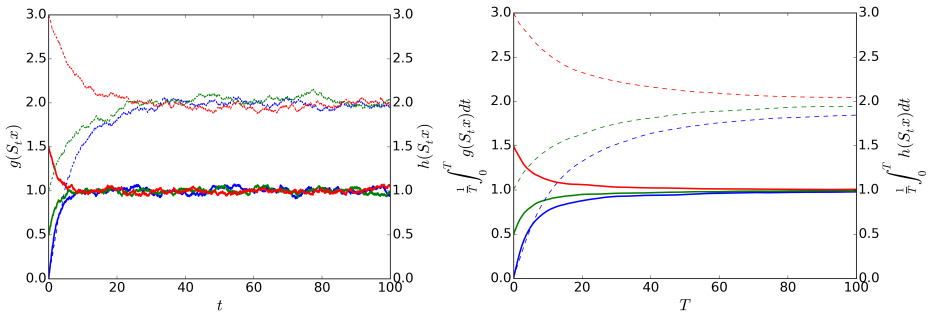

(a) (b)

Figure 1.3: (a) Time series of observables g (thick lines) and h (dashed lines) for three arbitrary simulations starting from three different initial states. (b) Finite time average of g (thick lines) and h (dashed lines).

with respect to a unique invariant measure μ. A measure μ is invariant under the flow $\phi(t), t \geq 0$ if for any Borel set A, $\mu(\phi(t)^{-1}(A)) = \mu(A)$. As such, these measures are the only appropriate ones to calculate averages which do not depend on the time at which the initial states are taken (recalling that $\phi(t)x \in A$ is equivalent to $x \in \phi(t)^{-1}A$). In fact, for any integrable observable g and μ-almost every initial state x (i.e. for any x in a set of positive measure μ), the existence (and uniqueness) of the time average (1.3) is guarantied by Birkhoff's pointwise ergodic theorem (Birkhoff, 1931) when an invariant measure μ exists (and is unique, i.e *ergodic*). Unfortunately, the ergodic theorem holds for initial states x taken in sets of positive measure μ, while a strange attractor typically carries uncountably many distinct invariant measures which are singular with respect to the Lebesgue measure (Eckmann and Ruelle, 1985). Thus, the ergodic theorem does not apply to initial states in sets outside the attractor for such measures. Yet, as noted by Kolmogorov, most physical systems or computer simulations appear to produce well-defined time averages for any randomly chosen initial state (i.e. for any x in a set of positive Lebesgue measure as opposed to a set of positive measure μ). Such selection process thus defines a particular measure of physical relevance, therefore called *physical measure*, for which the equality (1.4) between time averages and ensemble averages holds for any initial states in sets of positive Lebesgue measure. This is illustrated in figure 1.3 where artificial examples of climatic time series of two observables g and h for three randomly chosen initial conditions are represented. One can see that, as the averaging window width T is increased, the time average of each observable converges to a unique value independent of the initial state. The averages however converge at different rates, depending on the observable, as will be explained below.

Determining the mean climate thus boils down to finding the physically relevant invariant measure(s) μ, accordingly referred to as statistical steady state(s) (Ruelle, 1999; Gallavotti, 2014). It follows that changes in the mean climate in response to forcing are associated with changes in the invariant measure μ. This sheds lights to the interpretation of climatic projections such as those of the Coupled Model Intercomparison Project - Phase 5 (CMIP5, Hurrel et al., 2011). Indeed, since the range of predictability of the climate system is known to be limited to a few weeks, it would be absurd to attempt to predict the particular state of the climate system during a particular day of, say, year 2100. Yet, in both numerical weather predictions and climate projections, one performs the numerical integration of a single trajectory starting from an initial state (or of a relatively small ensemble). The fundamental difference in both exercises is that in the first, one is interested in the final state of the integration, while in the second, the final state has absolutely no relevance and it is rather the long time averages of observables such as in (1.3) (say over the last decade) that one is interested in. For transient projections, such as those for the 21st century, the period over which the average is taken should be long enough to give a good approximation of $\int_X g(x)\mu(dx)$ in (1.4) but also short enough so as to neglect transient effects. The reasons why ensembles are often used for climate projections are at least two fold. First it allows to get a better estimate of (1.4) by not only averaging in time but also among the members. Second, it can allow to test the eventual existence of multiple statistical steady states, in which case the system would not be ergodic.

In climate studies, one is not only interested in the mean climate but also in its natural variability (i.e without any changes in the forcing). It is thus customary to study climate variability from the correlation function $t \to C_{f,g}(t)$ between two observables f and g, defined as

$$C_{f,g}(t) = \int_X f(x)g(\phi(t)x)\mu(dx) - \int_X f(x)\mu(dx)\int_X g(x)\mu(dx). \qquad (1.5)$$

In particular, taking $g = f$, the Fourier transform of the *autocorrelation function* $C_{g,g}(t)$ yields the *power spectrum* $S_{g,g}(\omega)$ of g (von Storch and Zwiers, 1999). When the measure μ is ergodic, the correlation function coincides with the sample mean $\hat{C}_{f,g}(t) = \lim_{T\to\infty} \frac{1}{T}\int_0^T (f(x)-\bar{f})(g(\phi(t)x)-\bar{g})dt$, which is commonly used in practice. The behavior of the correlation function for chaotic systems can be understood by the following. Due to the chaotic divergence of trajectories (or to stochasticity, e.g. when fast-scale processes are modeled by random fluctuations), an ensemble $\rho(t)$ is expected to spread on the attractor. Thus the variance of an observable with respect to the ensemble increases, as can be seen from typical examples of ensemble weather prediction. Eventually, if the initial ensemble is so large as to be considered

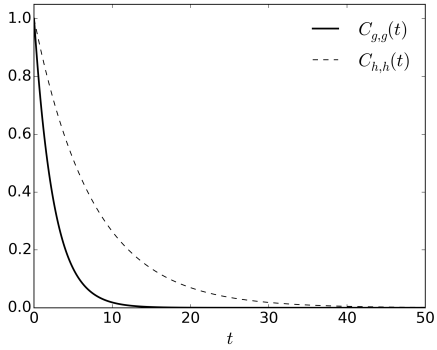

Figure 1.4: Autocorrelation function of the observables g (thick line) and h (thin dashed line) corresponding to the time series of figure 1.3.

as a (smooth) density ρ_0, the average of the observable with respect to the ensemble should converge in time, that is

$$\lim_{t\to\infty} \int_X \mathscr{P}_t \rho_0(x) g(x) dx = \int_X g(x)\mu(dx),$$

assuming the existence of a unique invariant measure μ. Such a system is called *mixing* because a density evolving under the dynamics eventually converges (weakly) to the invariant measure, quite as a blob of dye diffuses in a glass of water. More precisely, a system is mixing if for any two sets A and B,

$$\lim_{t\to\infty} \mu(A \cap \phi(t)^{-1} B) = \mu(A)\mu(B), \tag{1.6}$$

which means that, after a long-enough time, the probability of a state initially in A to end-up in B depends only on the size of the sets and not on the initial state, so that all information about the initial state has been lost. This property is stronger than ergodicity and implies that the correlation function (1.5) decays to zero with time. This is usually the case for climate time series, as illustrated in figure 1.4 where the correlation functions of the observables g and h corresponding to the system of figure 1.3 are represented by a thick line and a thin dashed line, respectively. One can see that the autocorrelation functions of both observables converge to zero as the lag t is increased, indicative of the loss of information with time about the initial state of the system by the chaotic (or stochastic) dynamics. However, both functions have different characteristic decay times, the one for g being of about 3 time units and the one for h of about 8 time units. A slow rate of decay of the correlation function and the presence of eventual weakly-damped oscillations will result in peaks in the power spectrum at a position given by the frequency of the oscillations. We will see that the

latter are determined by the spectrum of the transfer operators $\mathscr{P}_t$, referred to here as the *ergodicity spectrum*, so that these operators not only govern the evolution of statistics but also the variability in the system (in its statistical sense given by the correlation function). By extension, invoking a version of the fluctuation-dissipation theorem (Leith, 1975b; Dymnikov et al., 2006; Ruelle, 2009; Hairer and Majda, 2010; Ragone et al., 2015), the important role of this spectrum in the statistical response of dissipative systems to perturbations will also be discussed.

In both the case of the prediction of the state of the atmosphere in a few days and of the study of the mean state and variability of climate, the distinction between weather and climate is pretty clear. However, what about the study and prediction of modes of low-frequency variability such as El Niño-Southern Oscillation (ENSO) (Neelin et al., 1998)? Analysing this mode of variability from averages, correlations and spectra of some observables such as the Sea Surface Temperature (SST) obviously relies on the invariant measure μ and the transfer operators $\mathscr{P}_t, t \geq 0$ through (1.4) and (1.5), respectively. However, in an attempt to predict the evolution of ENSO, one or an ensemble of trajectories in phase space are integrated forward in time from a particular initial state with a dynamical model. Such exercise is akin to weather prediction, in the sense that one is interested in the evolution of the state of the system during a period of time as long as possible before all the information about the initial state is "forgotten" (i.e before the members of the ensemble are spread over the attractor, sampling the invariant measure). Doing so, one implicitly assumes that, even though the state of the atmosphere is not predictable after a few weeks, there are directions in phase space (e.g corresponding to coupled ocean-atmosphere dynamics in the case of ENSO) corresponding to slow dynamics predictable over months or years (i.e associated with Lyapunov exponents close to 0). Thus, in this case, one is not interested in the complete state of the system but rather on the projection of some observables on the space on which the slow variables live. In mathematical terms, this corresponds to averaging the observable g of the predicted state $x = y + z$ over the fast variables $z \in Z$ by taking the expectation

$$g(y) = \int_Z g(y,z)\mu_y(dz), \tag{1.7}$$

of the observable g conditioned on the slow variables $y \in Y$. From the disintegration theorem (Kallenberg, 2002, Chap. 6), the conditional measures $\mu_y, y \in Y$ are well-defined and fully determined by the invariant measure μ and the projection $\mathscr{R} : x \mapsto y$ on the slow variables.

Thus, one can see that the theory of ergodic dynamical systems is directly applicable to the study of climate dynamics and allow to rigorously define and extend commonly used concepts in the field. Furthermore, we will see in chapter 2 that a more detailed understanding of the spectral properties of the transfer operators allow to characterize the stability of a system as well as its response to perturbations

in terms of statistics. Having motivated the applicability of ergodic theory to climate science, the main physical problems considered in this thesis will be exposed.

1.4 MAIN QUESTIONS AND APPROACH

The present work is an attempt to apply the ideas presented and the previous sections to particular problems in the study of climate variability and stability. These includes the dynamics of ENSO - the dominant pattern of variability on interannual time scales (Neelin et al., 1998), a chaotic attractor crisis associated with a transition from warm to snowball Earth due to the ice-albedo feedback (Lucarini et al., 2010) and the prediction of atmospheric regime transitions (Crommelin, 2003).

All three cases rely on the ideas from ergodic theory presented in the previous section 1.3. The theory and in particular that of semigroup of transfer operators and their spectrum will be described in greater details in chapter 2. These theoretical considerations will be accompanied by a presentation of an approximation method for transfer operators and their spectrum based on a projection on a lower-dimensional space, recently introduced to the climate community by Chekroun et al. (2014). Interestingly, it will be shown that the correlation function of observables acting on the reduced space can be calculated exactly from these reduced operators and that the latter gives bounds to the one of the transfer operators. The chapter will end-up with a simple yet very insightful example of a multi-dimensional Ornstein-Uhlenbeck process (OU) (Gardiner, 2009), a particular case of which has been used by Hasselmann (1976) to motivate stochastic modeling of climate. It will be shown that our numerical approximation of the ergodicity spectrum compares well with the analytical formula of (Metafune et al., 2002) and their relation to the correlation function and the power spectrum will be illustrated.

As a first case study, chapter 3 will be concerned with the dynamics of ENSO, the dominant pattern of variability on interannual time scales. Since the seminal paper of Zebiak and Cane (1987), it is generally accepted that coupled ocean-atmosphere dynamics are key to the evolution of ENSO, through the so-called Bjerknes' feedbacks in which the trade winds respond to SST anomalies and in turn cause an adjustment of the ocean masses and of the thermocline. Much more controversial is the nature of the dynamics of ENSO, whether self-sustained or stochastically forced (Roulston and Neelin, 2000), linear nonnormal (**?**) or nonlinear (Dijkstra, 2005, , Chap. 7). One candidate is the presence of a Hopf bifurcation (Strogatz, 1994) in the coupled ocean-atmosphere dynamics associated with travelling Rossby and Kelvin waves and with the adjustment of the ocean heat content (Jin and Neelin, 1993). Such a bifurcation is found in the Zebiak-Cane model as well as in the delayed oscillator, a Delay Differential Equation (DDE) suggested by Suarez and Schopf (1988) and Battisti and Hirst (1989) as a conceptual model of ENSO. These two models will be used in chapter 3 as test-beds to show that the ergodicity spectrum gives a particularly interesting

characterization of the variability of a dynamical system and that it allows to give a description of the evolution of statistics during a bifurcation. First, the results on the OU presented in chapter 2 will allow us to give analytical formulas for the leading part of the ergodicity spectrum of general linear DDEs, such as the linear delayed oscillator of Battisti and Hirst (1989), and of Stochastic Delay Differential Equations (SDDEs). The nonlinear case with noise will then be treated. New results on the ergodicity spectrum of a simple form of stochastic Hopf bifurcation as well as approximations for the nonlinear delayed oscillator of Suarez and Schopf (1988) with noise will be given. In particular, it will be shown that the ergodicity spectrum approaches the imaginary axis at the bifurcation, resulting in critical slowing down. This will shed light on early-warning indicators of tipping points (Lenton, 2011) in high dimension as well as on the relationship between the structural stability of a system and the evolution of statistics. Finally, these results will be compared to that found for the Zebiak-Cane model and the important role played by the eigenvectors of the transfer operators will be discussed. In particular, the eigenvectors reveal patterns in phase space responsible for the slow dynamics and bear the signature of the nonlinearities, allowing to discriminate the subcritical from the supercritical situation as well as the linear from the nonlinear case. These results thus offer promising perspectives regarding the understanding of the nature of real-world ENSO.

The study of chapter 3 confirms that much can be learned about the variability and stability of dynamical systems from the spectral properties of transfer operators. Yet, even though the Zebiak-Cane model has thousands of degrees of freedom, the dynamics of the Hopf bifurcation is two dimensional and nonchaotic. Of major importance is to understand whether high-dimensional and chaotic systems such as climate can undergo rough changes in their statistical properties with changes in the forcing, just as their low-dimensional counterpart do. Ergodic theory is particularly well suited to study high-dimensional chaotic systems. To demonstrate this, a chaotic attractor crisis relevant to climate is studied in chapter 4. It is known that in the one-dimensional Energy Balance Models (EBMs) studied by Budyko (1969) and Sellers (1968), a bifurcation occurs when the solar constant is decreased further than a critical value, during which the steady state of the system switches from a warm climate, comparable to present-day conditions, to a cold climate, in which the Earth is covered with ice (Ghil, 1976). Such a transition is also found in the Planet Simulator (PlaSim, Fraedrich et al., 2005a; Lucarini et al., 2010), a GCM of intermediate complexity with tens of thousands of degrees of freedom and chaotic dynamics (Schalge et al., 2013). It will be shown in chapter 4 that a slowing down of the decay of correlations of physically relevant observables occurs at the approach of the crisis. Furthermore, this slow decay of correlations will prove to result from the approach of the ergodicity spectrum to the imaginary axis. These results suggest that the spectral properties of transfer operators constitute a good framework for the study of chaotic attractor crises. Moreover, they show that even though early-warning indicators such as the lag-1 autocorrelation (Held and Kleinen, 2004) are affected by the crisis (due

to critical slowing down), their signal may be limited by the expected smoothness of the changes of the ergodicity spectrum with the parameters of the system or the forcing (Gouëzel and Liverani, 2006).

Chapter 5 will deal with the midlatitude low-frequency atmospheric variability, namely, blocking events over Europe and North America (Barriopedro et al., 2006). Such events occur when a persistent anticyclonic system deviates the predominant westerlies meridionally and are believed to result in an increase of predictability on time scales of weeks to months, in a region otherwise dominated by baroclinically unstable synoptic weather systems. Using a barotropic model of the midlatitude troposphere with realistic forcing (Selten, 1995), it will be shown that the reduced operators presented in chapter 2 allow to detect meta-stable regimes as almost-invariant sets (Dellnitz and Junge, 1999). Such sets are associated with the leading eigenvectors of the transfer operators and an algorithm based on Markov chain reduction is designed to detect them. Furthermore, it is shown that the preferred transition paths connecting the different regimes are responsible for an increase of predictability and of a weakening of memory effects due to the projection of the dynamics on the reduced space (Chorin et al., 2002). This allows to use the reduced operators to give an early-warning indicator of transition from one regime to the other. Such an indicator is statistical in nature and thus well suited for long-term predictions of chaotic systems.

To conclude, chapter 6 will provide a summary of the results of our application of ergodic theory to the study of the climate system and give some perspectives on the applicability of the framework to a broader range of climate-related problems.

2

ERGODICITY SPECTRUM: THEORY AND METHODOLOGY

A brief summary of concepts from ergodic theory useful to climate dynamics has been presented in the previous chapter 1. Here, we describe in more details the theoretical foundations and the methodology used in this work, with a focus on the semigroup of transfer operators and its spectrum, referred to as the *ergodicity spectrum*. The latter characterizes the evolution of statistics by the dynamics and it is shown that the spectral gap separating the leading ergodicity eigenvalues is directly related to the rate of decay of correlations.

These theoretical considerations motivate the analysis of the ergodicity spectrum to study the variability of climate, its stability and its response to a forcing. Unfortunately, this spectrum is hardly accessible, since the transfer operators act on (infinite dimensional) spaces of functions acting on a high-dimensional phase space. For this reason, a numerical method to extract information relative to the ergodicity spectrum is presented based on reduced transition matrices describing the coarse-grained evolution of densities and observables acting on a reduced space (of lower dimension than the phase space) defined by an observation operator. The value of this method is supported by a theorem by Chekroun et al. (2014) relating transition probabilities between sets in the reduced space to transition probabilities between sets in phase space. An important corollary is further proved which attests that the gap between the leading eigenvalues of the reduced transition matrices gives an upper bound to the gap between the true ergodicity eigenvalues. It is also shown that the correlation functions between observables in the reduced space can be calculated from the reduced transition matrices or their spectral decomposition.

Finally, the numerical method is applied to the simple yet very instructive example of a multi-dimensional Ornstein-Uhlenbeck process. Such a process has been shown to be of the utmost relevance for climate by Hasselmann (1976) as it is the simplest model of slow-fast system allowing to explain the red-noise spectrum typical of climate time series and analytical formula for their spectrum by Metafune et al. (2002) will be used in chapter 3 to study the ergodicity spectrum of linear SDDEs. Here, it is found that the numerical approximation of the ergodicity spectrum agrees well with the analytical results and that it fully describes the correlation functions, giving confidence regarding the application of the method to larger problems.

2.1 TRANSITION SEMIGROUPS, SPECTRUM AND DECAY OF CORRELATIONS

First, we give a brief overview of the theory of the semigroup of transfer operators and explain how their spectrum characterizes the relaxation of distributions (or ensemble) to a statistical steady state and the decay of correlations. While the appellation and definition of the these semigroups vary with the context, we will refer to their spectrum with the general term of *ergodicity spectrum* (also called Ruelle-Policott resonances, correlation spectrum or Liouvillian spectrum).

2.1.1 *Stochastic evolution*

Unless specified, the mathematical setting of this study will be that of Stochastic Differential Equations (SDEs). There are several reasons for this choice. First of all, the study of the ergodic properties of SDEs, is an important topic on its own (Da Prato and Zabczyk, 1996), noise being ubiquitous to systems found in physics, engineering, social sciences and finance (Gardiner, 2009). Nevertheless, only few results exist regarding the ergodicity spectrum of stochastic (as well as deterministic) systems, apart for some systems which are linear (Metafune et al., 2002) or low dimensional (Dekker and van Kampen, 1979; Gaspard et al., 1995; Gaspard and Tasaki, 2001), because the calculation of the ergodicity spectrum usually involves solving nonlinear Ordinary Differential Equations (ODEs) / SDEs or Partial Differential Equations (PDEs) with varying coefficients (see e.g. Gaspard et al., 1995). There is thus a need for methods of numerical approximation of the transition semigroups and their spectrum. Moreover, even though trajectories of stochastic systems are highly irregular, spectral properties of stochastic systems can usually be studied in spaces of smooth functions (Da Prato and Zabczyk, 1996), contrary to forced-dissipative deterministic systems for which the interesting part of the spectrum belongs to spaces of distributions (Gouëzel and Liverani, 2006; Baladi and Tsujii, 2007), due to the positive contraction rate of volumes in phase space (Gallavotti, 2014). Finally, the study of stochastic dynamical systems can provide very useful insight regarding dissipative deterministic systems and delayed stochastic systems, as, on one hand, the ergodicity spectrum of some smooth hyperbolic systems is robust to stochastic perturbations (Gouëzel and Liverani, 2006) and, on the other hand, Stochastic Delay Differential Equations (SDDEs) can be represented by infinite-dimensional SDEs (Chojnowska-Michalik, 1978).

We start with a nonlinear SDE (Da Prato and Zabczyk, 1992) on a probability space $(\Omega, \mathscr{F}, \mathbb{P})$ with values in H

$$\begin{aligned} dX = &\quad (AX + F(X))dt + \Sigma(X)dW, \\ X(0) = &\qquad\qquad\qquad x, \end{aligned}$$

where $X(t,x)$ is a stochastic process with values in a separable Hilbert space H, $W(t)$ is a Wiener process, A is a linear operator on H and F and Σ are mappings from H

into H. Furthermore, we assume that the A, F and Σ satisfy sufficient Lipschitz or dissipative conditions for a unique mild solution $X(t,x)$ of (2.1) depending regularly on the initial condition x to exist (i.e. the problem is well-posed, Da Prato and Zabczyk, 1996). We also assume that a unique invariant measure μ exists. Finally, the SDE (2.1) generates the Random Dynamical System (RDS)

$$\phi : \quad \mathbb{R}\times\Omega\times H \quad \to H \tag{2.1}$$

$$\text{such that} \qquad t \qquad \mapsto \phi(t,\cdot)x = X(t,x) \tag{2.2}$$

is the solution of the SDE (2.1) (Arnold, 2003, Chap. 2).

Remark 1 (SDEs in infinite dimension)**.** *In this study, the infinite-dimensional setting has been chosen for the study of SDEs (Da Prato and Zabczyk, 1992), because it allows to represent SDDEs by SDEs (Chojnowska-Michalik, 1978), as we will see in chapter 3. For a thorough presentation of SDEs in the more accessible finite-dimensional setting, see Gardiner (2009).*

2.1.2 *Transition semigroups for SDEs*

We now introduce a Borel σ-algebra $\mathscr{B}(H)$ in order to define the measure space $(H,\mathscr{B}(H),\mu)$. Under the conditions of section 2.1.1, for any initial state $x \in H$, the process $X(t,x)$ satisfying (2.1) is a Markov process (Da Prato and Zabczyk, 1992, Theorem 9.8), which is stationary, as implied by the invariance of μ. As a consequence, the *Koopman operators* $\mathscr{U}_t$, $t \geq 0$, or *backward transition operators*, giving the expected backward evolution of any bounded and continuous observable g by the RDS ϕ, can be defined as

$$\mathscr{U}_t g(x) = \mathbb{E}[g(\phi(t,\cdot)x)], \quad t \geq 0, \quad x \in H,, \tag{2.3}$$

where the expectation $\mathbb{E}[g(\cdot)] = \int_\Omega g(\omega)\mathbb{P}(\omega)$ yields the average of g over the sample paths on Ω.

Remark 2. *For a deterministic system with flow $\phi(t), t \geq 0$, one would simply have $\mathscr{U}_t g(x) = g(\phi(t)x)$, as in equation (1.2) and figure 1.2 of the previous chapter 1.*

Remark 3. *In this work, it is more natural to define the Koopman operators by (2.3). This should not bring confusion with the other possible definition as the group of linear transformations induced by the canonical dynamical system associated with the transition semigroup of the Markov process (c.f. Da Prato and Zabczyk, 1996, Chap. 2.2).*

It follows from their definition (2.3) and the evolution equation (2.1) that the *Koopman operators* $\mathscr{U}_t$, $t \geq 0$ constitute a one-parameter semigroup of bounded operators. A family of operators $\mathscr{U}_t$, $t \geq 0$ is a one-parameter semigroup if

$$\begin{aligned} \mathscr{U}_{s+t} &= \mathscr{U}_s\mathscr{U}_t = \mathscr{U}_t\mathscr{U}_s, \quad s,t \geq 0 \\ \mathscr{U}_0 &= I, \end{aligned}$$

where I is the identity. As first noted by Hadamard, the semigroup property is very important and strongly related to evolution equations and the exponential function (Engel and Nagel, 2001, Chap. VII). Moreover, the existence of an invariant measure μ allows to extend the semigroup of Koopman operators $\mathscr{U}_t, t \geq 0$ (or backward transition semigroup) to a strongly continuous semigroup of contractions on $L^2_\mu(H)$ (Yosida, 1980, Theorem 1, page 381). Let us recall that $L^2_\mu(H)$ is the space of twice integrable functions w.r.t. the invariant measure μ (i.e. $f \in L^2_\mu(H)$ if $\int_H |f|^{1,2}\mu(dx) < +\infty$, assuring the existence of the mean and variance of f). This contraction property, also referred to as the stability property, is very important because it means that the distance between two functions transferred by $\mathscr{U}_t$ can decrease but never increase with time (Lasota and Mackey, 1994, Chap. 3).

On the other hand, the semigroup of *transfer operators* $\mathscr{L}_t$, $t \geq 0$ on $L^2_\mu(H)$, or *forward transition semigroup*, can be defined as the adjoints of the bounded Koopman operators with respect to the invariant measure μ. That is

$$\langle \mathscr{L}_t f, g\rangle_\mu = \langle f, \mathscr{U}_t g\rangle_\mu, \tag{2.4}$$

where

$$\langle f, g\rangle_\mu = \int_H f(x)g^*(x)\mu(dx),$$

is the scalar product associated with the invariant measure μ, with g^* denoting the complex conjugate of g ($g^* = g$ if the observable has values in $\mathbb{R}$). The semigroup of transfer operators $\mathscr{L}_t$, $t \geq 0$ yields the finite-time forward-evolution of any density ρ (more generally, of any μ-integrable function) by the stochastic dynamics, as illustrated in figure 1.2(a). It is related to the transition probabilities of the Markov process with evolution equation (2.1) by

$$\mathbb{P}_\mu(X(t,x) \in D | x \in C) = \frac{\langle \mathscr{L}_t \chi_C, \chi_D\rangle_\mu}{\mu(C)}, \tag{2.5}$$

where $\mu(C) = \int_C \mu(dx) = \int_H \chi_C(x)\mu(dx)$ is the measure of the Borel set C by μ.

Remark 4. *In the deterministic case, assuming that the flow ϕ is invertible and that μ is invariant by ϕ, one has that $\mathscr{L}_t = \mathscr{U}_{-t}, t \in \mathbb{R}$, so that the transition operators constitute a group of unitary transformations on the Hilbert space $L^2_\mu(H)$ (Koopman, 1931; Lasota and Mackey, 1994, Chap. 7.10). For a RDS, this is generally not the case, even if $\mathbb{P}$ is invariant for the noise system, because of the averaging over the noise realizations in the definition of the transition semigroups.*

Remark 5 (μ- and Lebesgue-transfer operators)**.** *It is essential to understand that the semigroup of (μ-)transfer operators has been defined in (2.4) for the invariant measure μ in order to study the evolution of densities with respect to μ, in accordance to the*

methodology presented in the following section 2.2. In application, the invariant measure μ is generally not known, so that it should be determined. Instead, one could study the semigroup of (Lebesgue-)transfer operators $\mathscr{P}_t, t \geq 0$, adjoints of the Koopman operators with respect to the Lebesgue measure dx. In this case, if μ has a density $p(x)$ w.r.t. the Lebesgue measure (i.e. if μ is absolutely continuous with respect to dx so that $\mu(dx) = p(x)dx$), the density $p(x)$ is given by the eigenvector associated with the leading eigenvalue of the semigroup of Lebesgue-transfer operators (see Froyland, 2001, and below). In addition, we have that

$$\mathscr{L}_t f = \begin{cases} \frac{1}{p}\mathscr{P}_t(pf) & \text{where } p > 0 \\ 0 & \text{where } p = 0, \end{cases} \tag{2.6}$$

for any μ-integrable function f (Collet and Eckmann, 2006, Chap. 5.6). As a consequence, the semigroup of μ-transfer operators $\mathscr{L}_t, t \geq 0$, yields information about the dynamics, such as the transition probabilities (2.5), only on the support of the invariant measure μ (i.e on sets of positive measure μ). Such a restriction has profound consequences in the case of dissipative deterministic systems for which the support of the physical invariant measure is contained in the nonwandering set (the set of recurrent points on the attractor) and not in the full phase space (Foias et al., 2001, remark 1.4, p 197).

Closing this parenthesis, the infinitesimal forward-evolution of a Lebesgue-density $\rho(t)$ is described by a conservation equation known as the *Fokker-Planck* or *forward Kolmogorov equation* (Lasota and Mackey, 1994; Gardiner, 2009). For the purpose of this study, it is sufficient to consider its formulation for a finite dimensional space $H = \mathbb{R}^d$

$$\begin{aligned} \frac{\partial}{\partial t}\rho(t,x) = \quad & -\sum_{i=1}^{d} \tfrac{\partial}{\partial x_i}\left[(A+F)_i(x)\rho(t,x)\right] \\ & +\tfrac{1}{2}\sum_{i=1}^{d}\sum_{j=1}^{d} \tfrac{\partial^2}{\partial x_i \partial x_j}\left[(\Sigma\Sigma^*)_{ij}(x)\rho(t,x)\right] \end{aligned} \tag{2.7}$$

where Σ is the covariance matrix and Σ^* its conjugate transpose. The right-hand side of (2.7) defines an infinitesimal operator $\mathscr{G}$ which, having assumed the system defined by the SDE (2.1) to be well-posed, generates the strongly continuous semigroup of Lebesgue-transfer operators $\mathscr{P}_t$, $t \geq 0$ (Engel and Nagel, 2001, Chap. II.6). This means that, formally, $\mathscr{P}_t = e^{t\mathscr{G}}, t \geq 0$, as in the finite-dimensional case (although care should be taken in defining the domain $D(\mathscr{G})$ of the generator as well as the exponential function).

Remark 6 (Liouville equation)**.** *In the deterministic case when $\Sigma = 0$, one recovers the* Liouville equation

$$\frac{\partial}{\partial t}\rho(t,x) = \quad -\sum_{i=1}^{d} \tfrac{\partial}{\partial x_i}\left[(A+F)_i(x)\rho(t,x)\right] = -\nabla\cdot\left((A+F)(x)\rho(t,x)\right) \tag{2.8}$$

The Liouville equation is a statement of conservation of probabilities in phase space (Lasota and Mackey, 1994, Chap. 7.8) and is thus the counterpart of the continuity equation stating conservation of mass in compressible hydrodynamics (e.g. Vallis, 2006).

Remark 7. *Let us insist on the fact that, even though the evolution equation (2.1) for trajectories can be nonlinear, the evolution of densities given by (2.7) or (2.8) is linear, to the price of dealing with an (infinite dimensional) functional equation.*

The Fokker-Planck equation (2.7), $\mathscr{G}$ and $\mathscr{P}_t, t \geq 0$ apply to densities with the Lebesgue measure. However, because the semigroup of μ-transfer operators $\mathscr{L}_t, t \geq 0$ extends to a strongly continuous semigroup of contraction on $L^2_\mu(H)$, it is generated by a unique closed linear operator $\mathscr{G}_\mu$ densely defined on $L^2_\mu(H)$ (Engel and Nagel, 2001, Chap. 2.1, theorem 1.4), so that the spectrum of $\mathscr{G}_\mu$ can be defined and related to that of $\mathscr{L}_t, t \geq 0$, as will be used in the following subsection 2.1.3.

2.1.3 *Ergodicity spectrum of transition semigroups*

As mentioned in chapter 1, the spectrum of the transition semigroups is at the core of ergodic theory. Indeed, not only it allows to characterize whether a system is ergodic or mixing, but it also defines the backbone of the evolution of statistics, of the decay of correlations and of the correlation spectrum. The study of the ergodicity spectrum can be made difficult by the fact that, the transition operators acting on infinite dimensional spaces, their spectrum can have a continuous part and depends on the functional spaces considered. Most often, however, one is interested in the discrete part of the spectrum so that, for the convenience of the exposition and for reasons which will become apparent below, we will assume that the spectrum of the transition semigroups considered is purely discrete. Moreover, the study of the spectral properties of stochastic systems is facilitated by the fact that eigenvectors in the spaces $L^2_\mu(H)$ of twice integrable functions with respect to the invariant measure μ are of interest (i.e functions for which the mean and variance is defined), while for deterministic dissipative systems, spaces of distributions should be considered (Gouëzel and Liverani, 2006; Baladi and Tsujii, 2007).

A vector ψ^f_k is a (forward) eigenvector of $\mathscr{L}_t$, for a given $t > 0$, associated with the eigenvalue $\zeta_k(t)$ if

$$\mathscr{L}_t \psi^f_k = \zeta_k(t)\psi^f_k, \quad \zeta_k(t) \in \mathbb{C}.$$

Furthermore, to the complex conjugate $\zeta_k(t)^*$ of $\zeta_k(t)$ is associated a (backward) eigenvector ψ^b_k of $\mathscr{U}_t$, so that the family $\psi^f_k, \psi^b_k, k \geq 1$ forms a bi-orthonormal set for the inner product in $L^2_\mu(H)$. Because $\mathscr{L}_t$ and $\mathscr{U}_t$, $t \geq 0$, are semigroups, the eigenvectors ψ^f_k and ψ^b_k are independent of time, contrary to the eigenvalue $\zeta_k(t)$. Moreover from the Spectral Mapping Theorem (SMT, Engel and Nagel, 2001, Chap.

4.3, theorem 3.7) for strongly continuous semigroups, the eigenvalues $\zeta_k(t), t \geq 0$ of the semigroup of transfer operators $\mathscr{L}_t, t \geq 0$ are related to the eigenvalues λ_k of the generator $\mathscr{G}_\mu$ by

$$\zeta_k(t) = e^{\lambda_k t}, \quad t \geq 0. \tag{2.9}$$

For the dissipative systems considered here, $|\zeta_k(t)| \leq 1$, so that the eigenvalues of the transfer operators belong to the unit disc of the complex plane. Equivalently, $\Re(\lambda_k) \leq 0$, so that the eigenvalues of the generator are to the left of the imaginary axis. This is illustrated in figure 2.1 where an example of spectrum represented as eigenvalues $\zeta_k(t)$ of the transfer operators and as eigenvalues λ_k of the generator are plotted panel (a) and (b), respectively. At this point, the origin of these spectra is not important, the example being given for a purely didactic purpose. Both representations convey exactly the same information. However, the spectrum $\sigma(\mathscr{G}_\mu) = \{\lambda_k\}_{k\geq 1}$ of the generator (assumed purely discrete) is more convenient, since it is independent of time, making its physical interpretation more straightforward. Thus, in the following, we will refer to $\{\lambda_k\}_{k\geq 1}$, $\{\psi_k^f\}_{k\geq 1}$ and $\{\psi_k^b\}_{k\geq 1}$ as the *ergodicity eigenvalues*, the *forward eigenvectors* and the *backward eigenvectors*, respectively. These families will be ordered by increasing distance of the λ_k from the imaginary axis (i.e by decreasing real part).

Remark 8 (Eigenvectors of the μ- and the Lebesgue-transfer operators)**.** *When the invariant measure μ has a density $p(x)$ w.r.t. the Lebesgue measure, one can see from (2.6) that multiplying the eigenvectors of the μ-transfer operator $\mathscr{L}_t$ by the density $p(x)$ yields eigenvectors of the Lebesgue-transfer operator $\mathscr{P}_t$, where $p(x) > 0$, associated with the same eigenvalue. However, in the dissipative deterministic case, the spectrum of the Lebesgue-transfer operators corresponding to contraction towards the attractor does not belong to the spectrum of the μ-transfer operators, since, as explained in remark 5, the invariant measure μ is supported by the nonwandering set on the attractor.*

For the systems considered in this study, an invariant probability measure μ exists. As a consequence the leading ergodicity eigenvalue λ_1 is 0 (corresponding to $\zeta_1(t) = 1$) and is associated with the eigenvector $\psi_1^f = 1$ (Da Prato and Zabczyk, 1996, Chap. 2.1). That is,

$$\mathscr{L}_t 1 = 1, \quad t \geq 0.$$

It follows from remark 8 that, the stationary density $p(x)$ associated with the invariant measure μ is a fixed point for the semigroup of Lebesgue-transfer operators $\mathscr{P}_t, t \geq 0$, i.e. $\mathscr{P}_t p = p$. The corresponding ergodicity eigenvalue $\lambda_1 = 0$ is represented in red in figure 2.1 and in the following figures. If the first eigenvalue is simple, the invariant measure is unique and it follows that the system is ergodic (Da Prato and Zabczyk, 1996, Theorem 3.2.6).

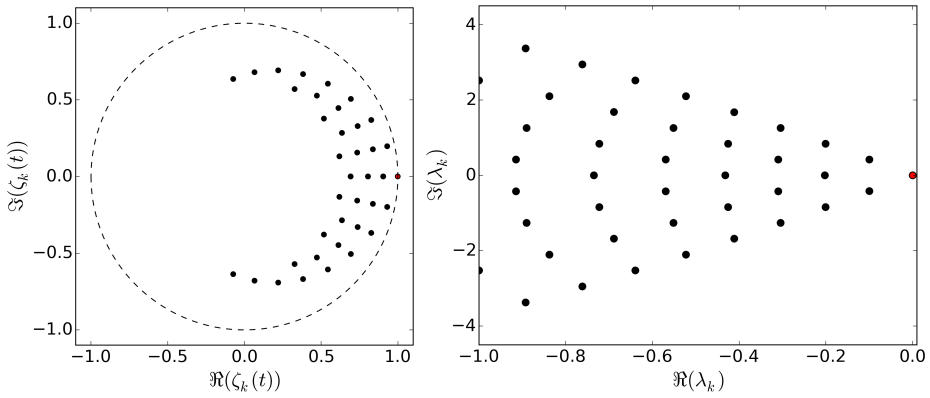

(a) (b)

Figure 2.1: Example of leading eigenvalues of (a) the transfer operator $\mathscr{L}_t$, for $t = 1/2$ and (b) the generator $\mathscr{G}_\mu$, in the complex plane.

Let us now assume that there exists an eigenvalue λ_k with vanishing real part but non-vanishing imaginary part ω_k, associated with the eigenvector ψ_k^f. Then, one has that

$$\mathscr{L}_t \psi_k^f = e^{i\omega_k t}\psi_k, \quad t \geq 0.$$

The forward eigenvector ψ_k^f is thus transferred periodically with period $2\pi/\omega_k$ by the transfer operators with its norm conserved, preventing the (weak) convergence of transferred densities $\mathscr{L}_t\rho_0$ to the stationary density $p(x)$. In this case, as can be seen from the definition (1.6) in chapter 1, the system cannot be mixing. On the other hand, if no ergodicity eigenvalue lies on the imaginary axis but the leading one λ_1 (accordingly, if no $\zeta_k(t)$ lies on the unit circle but ζ_1), as is the case for the example represented figure 2.1, one can write $\lambda_k = r_k + i\omega_k$ with $r_k < 0$ for $k > 1$, such that

$$\begin{aligned} \lim_{t\to\infty} \left|\left\langle \mathscr{L}_t \psi_k^f, g\right\rangle_\mu\right| &= \lim_{t\to\infty} e^{r_k t} \left|\left\langle \psi_k^f, g\right\rangle_\mu\right| \\ &= 0. \end{aligned}$$

Thus, the contributions of the eigenvectors associated with other ergodicity eigenvalues than 0 decay exponentially with time at a rate given by the real part of the eigenvalues and the system is mixing (Da Prato and Zabczyk, 1996, Theorem 3.4.1).

We can see that the ergodicity spectrum sheds light on the statistical properties of a dynamical system. In particular, it provides a full description of the correlation function $C_{f,g}(t)$ for two observables f and g in $L^2_\mu(H)$, defined as

$$\begin{aligned} C_{f,g}(t) = &\quad \int_H f(x)\mathscr{U}_t g(x)\mu(dx) - \mu(f)\mu(g) \\ = &\quad \int_H \mathscr{L}_t f(x) g(x)\mu(dx) - \mu(f)\mu(g), \end{aligned} \tag{2.10}$$

where $\mu(f) = \langle f, 1\rangle_\mu = \int_H f\mu(dx)$ is the average of f for μ. Indeed, the spectral decomposition in the Hilbert space $L^2_\mu(H)$ (Kato, 1995, Chap. 5.2) of the transition semigroups on the ergodicity spectrum (assumed simple, for convenience) yields for the correlation function

$$C_{f,g}(t) = \quad \sum_{k=1}^{\infty} e^{\lambda_k t} \left\langle f, \psi_k^b \right\rangle_\mu \left\langle \psi_k^f, g \right\rangle_\mu - \langle f, 1\rangle_\mu \langle 1, g\rangle_\mu \tag{2.11}$$

Thus, in agreement with the preceding developments, one can see that if $\lambda_1 = 0$ is the only eigenvalue on the imaginary axis (and if the spectrum is purely discrete), the correlation function converges to zero for any pair of observables, a consequence of the mixing property (Lasota and Mackey, 1994, Chap. 5.5). Moreover, the decay rate of the correlation function is determined by the ergodicity eigenvalues λ_k closest to the imaginary axis, weighted by the components of the observable f and g on the eigenvectors ψ_k^b and ψ_k^f of the backward and forward transition semigroups, respectively.

Remark 9 (Continuous spectrum)**.** *In this study, the ergodicity spectrum will be assumed purely discrete, as is the case for finite-dimensional or compact operators (Kato, 1995). In some cases, however, the ergodicity spectrum can be continuous, in which case the sum in the decomposition of the correlation function (2.11) must be replaced by an integral, resulting in an algebraic decay of correlations (i.e. as a power law). One interesting such case is for deterministic systems undergoing a bifurcation (Gaspard et al., 1995; Gaspard and Tasaki, 2001). Indeed, while away from the bifurcation point, the ergodicity spectrum of such systems is discrete, it accumulates at the imaginary axis at the bifurcation point, resulting in the* critical slowing down *of the system.*

Finally, the correlation spectrum $S_{f,g}(\omega)$ is given by the Fourier transform of the correlation function $C_{f,g}(t)$. When the latter is decomposed following (2.11), the correlation spectrum between two observables f and g takes the particular form

$$S_{f,g}(\omega) = \sum_{k=2}^{\infty} \left\langle f, \psi_k^b \right\rangle_\mu \left\langle \psi_k^f, g \right\rangle_\mu \frac{\Re(\lambda_k)}{(\omega - \Re(\lambda_k))^2 + \Im(\lambda_k)^2}. \tag{2.12}$$

Thus, this spectrum is a linear combination of *Lorentzian profiles* centered on the angular frequencies $\Im(\lambda_k)$ with half-widths $\Re(\lambda_k)$. Thus, peaks in the correlation spectrum are associated with ergodicity eigenvalues close to the imaginary axis, as

will be illustrated in figure 2.3 of the coming section 2.3. The closer a particular ergodicity eigenvalue to the imaginary axis, the sharper the spectral peak associated to it. The position of the peak is given by the imaginary part of the ergodicity eigenvalue and its intensity by the product of the components of the observables f and g on the backward and forward eigenvectors, respectively. In fact, the ergodicity eigenvalues are poles of the resolvent operator $R(\lambda, \mathscr{G}_\mu) = (\lambda - \mathscr{G}_\mu)^{-1}, \lambda \in \mathbb{C} \setminus \sigma(\mathscr{G}_\mu)$, which, where well defined, is the Laplace transform of the semigroup of transfer operators giving their frequency response (see Arendt et al., 2011, for more details). Note also that this type of spectrum is ubiquitous to nature and is found in particular in quantum mechanics for which the *natural broadening* of an emission line of an atom is due to the uncertainty principle and for which $\Re(\lambda_k)$ would be the spontaneous emission rate of the atom (Hollas, 2004). Another example is the famous climatic red-noise spectrum studied by Hasselmann (1976) arising for one-dimensional Ornstein-Uhlenbeck process (OU), which is easily recovered from (2.12) and will be extended in section 2.3.

2.2 APPROXIMATION BY REDUCED TRANSITION MATRICES

From the previous sections, it should be clear that the spectrum of the transition semigroups can provide precious information on the characteristic evolution of statistics. Yet, their analytical study is limited to a few simple cases (Dekker and van Kampen, 1979; Gaspard et al., 1995; Gaspard and Tasaki, 2001), due to the infinite dimensionality of the operators and, possibly, to the high dimensionality of the phase space. Thus, there is a strong need for good approximation methods. A Galerkin approximation of the transition semigroups (defined in (2.3) and (2.4)) on a finite-dimensional set of disjoint characteristic functions, known as *Ulam's method* (Ulam, 1964; Dellnitz and Junge, 1999), is supported, in the deterministic case, by the fact that the discrete spectrum of the transition semigroups of smooth uniformly hyperbolic systems acting on appropriate Banach spaces is stable to perturbations (Gouëzel and Liverani, 2006; Butterley and Liverani, 2007; Froyland, 2007) and, in the stochastic case, by the fact that such method introduces numerical diffusion having a similar effect as the additive noise in (2.1) (Froyland et al., 2013). This method and others (Mezić, 2013) led to many interesting applications in dynamical systems theory (Dellnitz and Junge, 1997; Froyland and Padberg, 2009; Koltai, 2010), stochastic modelling (Froyland et al., 2014a), physical oceanography (Froyland et al., 2007; Dellnitz et al., 2009; van Sebille et al., 2012; Froyland et al., 2014b), hydrodynamics (Rowley et al., 2009; Mezić, 2013) and molecular dynamics (Deuflhard et al., 1999; Schütte et al., 1999; Bittracher et al., 2015). Yet, for high-dimensional systems, Ulam's method becomes intractable, as the size of the grid, for an equivalent refinement, grows exponentially with the dimension. Only recently has a rigorous method already used by Schütte et al. (1999) in molecular dynamics been

extended and introduced to the climate community by (Chekroun et al., 2014) in order to deal with high-dimensional systems. This method relies on the projection of the dynamics on a reduced space and will now be presented before to apply it in the next chapters.

2.2.1 *Reduced Markov operators*

Instead of attempting to approximate the full transfer operator $\mathscr{L}_t$ on the phase space H, only a reduced transfer operator $\mathfrak{L}_t^{\mathscr{R}}$ given by a particular orthogonal projection of the transfer operator on a space of measurable functions acting on a lower-dimensional space $Y = \mathbb{R}^p$, ($p < \dim H$) than the phase space H is approximated (Chekroun et al., 2014). The reduced space Y is defined by an appropriately chosen continuous observation operator $\mathscr{R} : H \to Y$ and induces a reduced measure $\mathfrak{m}$ such that $\mathfrak{m}(B) = \mu(\mathscr{R}^{-1}(B))$ for any Borel set B in the σ-algebra $\mathscr{B}(Y)$ associated with the reduced space Y (i.e. $\mathfrak{m}$ is the push-forward of μ with respect to $\mathscr{R}$). Technically, the reduced transfer operator $\mathfrak{L}_t^{\mathscr{R}}$ is constructed from the conditional expectation $E[\cdot|\mathscr{B}(Y)]$ as described by the following diagram.

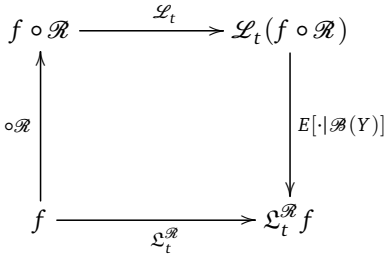

First, the observable f acting on the reduced space Y is lifted to the space of measurable functions on the phase space H by the composition with the observation operator $\mathscr{R}$. The resulting observable $f \circ \mathscr{R}$ corresponds to a crude representation of f on H (i.e. $f \circ \mathscr{R}$ is constant on the space $H \backslash Y$ orthogonal to Y in H). As a second step, the true transfer operator $\mathscr{L}_t$ is applied to the lifted observable $f \circ \mathscr{R}$. Last, the transferred observable is descended back to the space of measurable functions on Y by taking its conditional expectation with respect to $\mathscr{B}(Y)$. The conditional expectation is well-defined, as assured by the disintegration theorem applied to the measure μ (Kallenberg, 2002, Chap. 6) and corresponds to a Hilbert space orthogonal projection from $L^2_\mu(H)$ to $L^2_{\mathfrak{m}}(Y)$. Therefore, the reduced operator $\mathfrak{L}_t^{\mathscr{R}}$ inherits from the Markov property of $\mathscr{L}_t$ (Chekroun et al., 2014). Moreover, it follows from the invariance of μ and the definition of reduced operator that the characteristic function supported by Y is an eigenvector of $\mathfrak{L}_t^{\mathscr{R}}$ associated with the leading eigenvalue 1.

As a consequence, transition probabilities between sets any two sets E and F in the reduced space Y coincide with transition probabilities between their pre-images

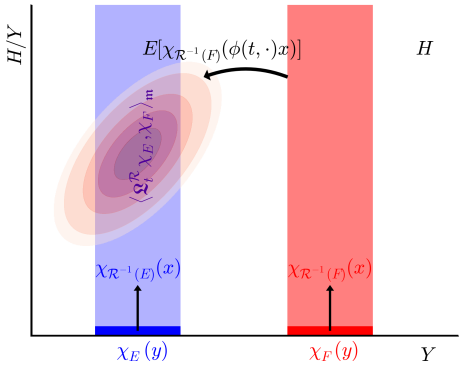

Figure 2.2: Schematic of the calculation of transition probabilities between two sets E and F in the reduced space from their pre-image in the phase space.

$\mathscr{R}^{-1}(E)$ and $\mathscr{R}^{-1}(F)$ in the phase space H and are given by the reduced transfer operator $\mathfrak{L}_t^{\mathscr{R}}$ according to

$$\frac{\left\langle \mathfrak{L}_t^{\mathscr{R}} \chi_E, \chi_F \right\rangle_{\mathfrak{m}}}{\mathfrak{m}(E)} = \mathbb{P}_\mu(X(t,x) \in \mathscr{R}^{-1}(F) | x \in \mathscr{R}^{-1}(E)), \quad E, F \in \mathscr{B}(Y) \tag{2.13}$$

as follows from the fact that

$$\frac{\left\langle \mathfrak{L}_t^{\mathscr{R}} \chi_E, \chi_F \right\rangle_{\mathfrak{m}}}{\mathfrak{m}(E)} = \frac{\left\langle \mathscr{L}_t \chi_{\mathscr{R}^{-1}(E)}, \chi_{\mathscr{R}^{-1}(F)} \right\rangle_\mu}{\mu(\mathscr{R}^{-1}(E))} = \frac{\left\langle \chi_{\mathscr{R}^{-1}(E)}, \mathscr{U}_t \chi_{\mathscr{R}^{-1}(F)} \right\rangle_\mu}{\mu(\mathscr{R}^{-1}(E))}. \tag{2.14}$$

This is the content of Theorem A by Chekroun et al. (2014), which can be extended to the stochastic case, as illustrated in figure 2.2. On this figure, the two sets E and F, respectively represented in blue and red, belong to the reduced space Y represented by the horizontal black line. These two sets are first lifted to the phase space H, represented by the plane, by taking their pre-images $\mathscr{R}^{-1}(E)$ and $\mathscr{R}^{-1}(F)$ w.r.t. the observation operator $\mathscr{R}$, represented in light blue and light red, respectively. The expectation with respect to the noise of the pre-image of $\mathscr{R}^{-1}(F)$ by the RDS ϕ is then taken. In fact, this does not make sense in the nondeterministic case because this operation does not result in a set. Rather, it is the backward transfer $\mathscr{U}_t \chi_{\mathscr{R}^{-1}(F)}$ of the characteristic function supported by the pre-image of F by $\mathscr{R}$ which is taken, as represented by the red contours. The transition probability from E to F are then given by the scalar product of $\chi_{\mathscr{R}^{-1}(E)}$ and $\mathscr{U}_t \chi_{\mathscr{R}^{-1}(F)}$ normalized by the measure of F, as in (2.14). It follows also immediately from the identities (2.14), that the

correlation function of any observables $f, g \in L^2_{\mathrm{m}}(Y)$ can be calculated exactly from the reduced operators $\mathfrak{L}^{\mathscr{R}}_t, t \geq 0$ by

$$\begin{aligned} C_{f,g}(t) = C_{f\circ\mathscr{R},g\circ\mathscr{R}}(t) &= \left\langle \mathscr{L}_t(f\circ\mathscr{R}), g\circ\mathscr{R}\right\rangle_\mu \\ &= \left\langle \mathfrak{L}^{\mathscr{R}}_t f, g\right\rangle_{\mathrm{m}}. \end{aligned} \tag{2.15}$$

This of course not the case for the correlation function of any observables in $L^2_\mu(H)$.

However, contrary to $\mathscr{L}_t, t \geq 0$, the family $\mathfrak{L}^{\mathscr{R}}_t, t \geq 0$ does not constitute a semigroup because information is lost each time the conditional expectation is taken. This is illustrated in the following diagram,

$$\begin{array}{ccc} f\circ\mathscr{R} & \xrightarrow{\mathscr{L}_s} & \mathscr{L}_s(f\circ\mathscr{R}) \\ {\scriptstyle\circ\mathscr{R}}\uparrow & & \downarrow{\scriptstyle E[\cdot|\mathscr{B}(Y)]} \\ f & \xrightarrow{\mathfrak{L}^{\mathscr{R}}_s} & \mathfrak{L}^{\mathscr{R}}_s f \end{array} \qquad \begin{array}{ccc} (\mathfrak{L}^{\mathscr{R}}_s f)\circ\mathscr{R} & \xrightarrow{\mathscr{L}_t} & \mathscr{L}_t[(\mathfrak{L}^{\mathscr{R}}_s f)\circ\mathscr{R}] \\ {\scriptstyle\circ\mathscr{R}}\uparrow & & \downarrow{\scriptstyle E[\cdot|\mathscr{B}(Y)]} \\ \mathfrak{L}^{\mathscr{R}}_s f & \xrightarrow{\mathfrak{L}^{\mathscr{R}}_t} & \mathfrak{L}^{\mathscr{R}}_t\mathfrak{L}^{\mathscr{R}}_s f \end{array}$$

where the observable f is transferred to time step $s+t$ in two steps of length s and t. In between, the lift of f transferred by $\mathscr{L}_t$ is projected on the space of measurable functions on the reduced space Y and lifted back to the space of measurable functions on the phase space H. This operation results in a loss of information because $f \mapsto \circ\mathscr{R}$ is not a left-inverse of $g \mapsto E[g|\cdot]$. This differs from the situation,

$$\begin{array}{ccc} f & & \mathfrak{L}^{\mathscr{R}}_{s+t} f \\ & \xrightarrow{\mathfrak{L}^{\mathscr{R}}_{s+t}} & \\ {\scriptstyle\circ\mathscr{R}}\downarrow & & \uparrow{\scriptstyle E[\cdot|\mathscr{B}(Y)]} \\ f\circ\mathscr{R} & \xrightarrow{\mathscr{L}_{s+t}} & \mathscr{L}_{s+t}(f\circ\mathscr{R}) \end{array}$$

in which the observable f is directly transferred to time step $s+t$, without projecting to Y in between, so that $\mathfrak{L}^{\mathscr{R}}_{s+t}$ differs from $\mathfrak{L}^{\mathscr{R}}_t\mathfrak{L}^{\mathscr{R}}_s$. This loss of the semigroup property, and a fortiori of the Markov property, can be understood in terms of Mori-Zwanzig formalism (Zwanzig, 2001; Chorin and Hald, 2009), which teaches us that projecting an evolution equation on a reduced space introduces memory effects since past realizations of the projected process are needed to predict its future state.

2.2.2 *Calculating the reduced transition matrix*

In practice, the reduced transfer operator $\mathfrak{L}^{\mathscr{R}}_t$ needs to be discretized. Therefore, the Galerkin approximation of $\mathfrak{L}^{\mathscr{R}}_t$ is taken by projecting it on the set of characteristic functions $\{\chi_{B_i}\}_{1\leq i\leq n}$ supported by n disjoint grid boxes $\{B_i\}_{1\leq i\leq n}$ covering a compact

subset G of the reduced space Y. This results in a reduced transition matrix $\mathbf{P}_t^{\mathscr{R}}$ with elements the transition probabilities

$$(\mathbf{P}_t^{\mathscr{R}})_{ij} = \frac{\left\langle \mathfrak{L}_t^{\mathscr{R}} \chi_{B_i}, \chi_{B_j} \right\rangle_{\mathfrak{m}}}{\mathfrak{m}(B_i)} = \mathbb{P}_\mu(X(t,x) \in \mathscr{R}^{-1}(B_j) | x \in \mathscr{R}^{-1}(B_i)),$$

of an observation given by $\mathscr{R}$ initially in box B_i to be in box B_j after a time t. These transition probabilities can be estimated from a long time series $\{x_s\}_{1 \le s \le T}$ of the system by the Maximum Likelihood Estimator (MLE) (e.g. Billingsley, 1961) as such

$$(\hat{\mathbf{P}}_t^{\mathscr{R}})_{ij} = \frac{\#\{(y_s \in B_i) \wedge (y_{s+t} \in B_j)\}}{\#\{y_s \in B_i\}}, \tag{2.16}$$

where $y_s = \mathscr{R}(x_s)$ is the observation of the sth realization of the time series and $\#\{y_s \in B_i\}$ counts the number of observations falling in B_i over the period of the time series. In fact, the vector $\hat{\mathbf{m}}$ with elements $\hat{m}_i = \#\{y_s \in B_i\}/\#\{y_s \in G\}$ is the normalized histogram on the grid (or probability density function) giving a discrete estimate of the Lebesgue-density of the reduced measure $\mathfrak{m}$ from the long time series of the observable.

Remark 10 (Restriction to the support of the invariant measure)**.** *Because of the high dimensionality of the phase space H, it is not possible to estimate the transition probabilities from many short simulations starting from different initial conditions seeding the phase space, as is usually done for Ulam's method (Dellnitz and Junge, 1999). Instead, taking advantage of the ergodicity of the invariant measure, only one long simulation with spin-up removed is used (if the system was not ergodic, the present method would select one of its ergodic components, depending on the initial condition). This is why we have focused on the transfer operators defined w.r.t. to the invariant measure rather than the Lebesgue measure. For deterministic dissipative systems, such method does not allow to resolve motions of contraction towards the attractor (see chapter 4), because only transition probabilities between sets on the attractor are resolved (see remarks 5 and 8). In the presence of noise, however, the system is perturbed away from the attractor, so that motions corresponding to contraction towards the attractor can be resolved (see also Cessac and Sepulchre, 2007; Colangeli and Lucarini, 2014) as long as the time series is long enough to sample the whole phase space (of course, due to the finite length of the time series, only a compact region of the phase space can be sampled in practice). Other important issues of spin-up, round-off errors and convergence regarding the use of a long time series have been stressed by Froyland (2001).*

The transition matrix $\mathbf{P}_t^{\mathscr{R}}$ constitutes a finite-dimensional approximation of (when acting on the left) the (forward) reduced operator $\mathfrak{L}_t^{\mathscr{R}}$ and of (when acting on the right) its adjoint, the (backward) reduced operator $\mathfrak{U}_t^{\mathscr{R}}$, defined by replacing the transfer operator $\mathscr{L}_t$ by the Koopman operator $\mathscr{U}_t$ in the diagram defining $\mathfrak{L}_t^{\mathscr{R}}$. To see this, let us define the space $\tilde{L}^2_{\mathfrak{m}}(Y)$, the discrete counterpart of $L^2_{\mathfrak{m}}(Y)$, such that

for any $f \in \tilde{L}^2_{\mathfrak{m}}(Y)$, $f(x) = \sum_{i=1}^n f_i \chi_{B_i}(x), f_i \in \mathbb{C}$. For $f, g \in \tilde{L}^2_{\mathfrak{m}}(Y)$, the inner product $\langle f, g \rangle_{\mathfrak{m}}$ is given by

$$\langle f, g \rangle_{\mathfrak{m}} = \sum_{i=1}^n f_i m_i g_i^* = \mathbf{f}\mathbf{D}(\mathbf{m})\mathbf{g}^*,$$

where $\mathbf{f}$ is the row vector $(f_1, ..., f_n)$, $\mathbf{f}^*$ its conjugate transpose and $\mathbf{D}(\mathbf{m})$ the diagonal matrix with diagonal elements $m_i, 1 \leq i \leq n$, giving the discrete approximation of the density of $\mathfrak{m}$ with respect to the Lebesgue measure. Thus, the action of the reduced Markov operators on the discretized space $\tilde{L}^2_{\mathfrak{m}}(Y)$ is such that

$$\left\langle \mathfrak{L}_t^{\mathscr{R}} f, \chi_{B_j} \right\rangle_{\mathfrak{m}} = \left(\mathbf{f}\mathbf{D}(\mathbf{m})\mathbf{P}_t^{\mathscr{R}}\right)_j, \qquad 1 \leq j \leq n \tag{2.17}$$

$$\left\langle \chi_{B_i}, \mathfrak{U}_t^{\mathscr{R}} f \right\rangle_{\mathfrak{m}} = \left(\mathbf{P}_t^{\mathscr{R}} \mathbf{f}^*\right)_i, \qquad 1 \leq i \leq n. \tag{2.18}$$

The first identity means that the Galerkin approximation of the transfer of a density $f \in \tilde{L}^2_{\mathfrak{m}}(Y)$ by the reduced transfer operator $\mathfrak{L}_t^{\mathscr{R}}$ is obtained by applying the matrix $\mathbf{D}(\mathbf{m})\mathbf{P}_t^{\mathscr{R}}$ to the right of the vector representation $\mathbf{f}$ of f. Correspondingly, the second identity means that the Galerkin approximation of the transfer of an observable $g \in \tilde{L}^2_{\mathfrak{m}}(Y)$ by the reduced Koopman operator $\mathfrak{U}_t^{\mathscr{R}}$ is obtained by applying the matrix $\mathbf{P}_t^{\mathscr{R}}$ to the left of the vector representation $\mathbf{g}$ of g.

Interestingly, the MLE estimate $\hat{\mathbf{P}}_t^{\mathscr{R}}$ of the reduced transition matrix can be used to recover other sample-based estimators. First, we have seen that the normalized histogram $\hat{\mathbf{m}}$ with elements $\hat{m}_i = \#\{y_s \in B_i\}/\#\{y_s \in G\}$ gives an estimate of the discretization of the density $m(x)$ of the reduced measure $\mathfrak{m}$. It is in fact the first left-eigenvector of $\hat{\mathbf{P}}_t^{\mathscr{R}}$ associated with the eigenvalue 1, since

$$\begin{aligned}
(\hat{\mathbf{m}}\hat{\mathbf{P}}_t^{\mathscr{R}})_j &= \sum_{k=1}^n \hat{m}_k (\hat{\mathbf{P}}_t^{\mathscr{R}})_{kj} \\
&= \sum_{k=1}^n \frac{\#\{y_s \in B_k\}}{\#\{y_s \in G\}} \times \frac{\#\{(y_s \in B_k) \wedge (y_{s+t} \in B_j)\}}{\#\{y_s \in B_k\}} \\
&= \sum_{k=1}^n \frac{\#\{(y_s \in B_k) \wedge (y_{s+t} \in B_j)\}}{\#\{y_s \in G\}} \\
&= \frac{\#\{y_{s+t} \in B_j\}}{\#\{y_s \in G\}} \\
&= m_j,
\end{aligned}$$

so that $\hat{\mathbf{m}}$ is a fixed point for $\hat{\mathbf{P}}_t^{\mathscr{R}}$ (which is unique by construction from a single time series). More interestingly, the sample correlation function $\hat{C}_{f,g}(t)$ for two observables $f, g \in \tilde{L}^2_{\mathfrak{m}}(Y)$, defined as

$$\hat{C}_{f,g}(t) = \frac{1}{T} \sum_{s=0}^T (f(x_s) - \bar{f})(g(x_{s+t}) - \bar{g})^*, \tag{2.19}$$

where $\bar{f} = \frac{1}{T} \sum_{s=0}^T f(x_s) = \mathbf{f}\hat{\mathbf{m}}$ is the sample mean of f, coincides with the transition matrix estimate $\tilde{C}_{f,g}(t)$ of the correlation function, defined as

$$\tilde{C}_{f,g}(t) = \mathbf{f}\mathbf{D}(\hat{\mathbf{m}})\hat{\mathbf{P}}_t^{\mathscr{R}}\mathbf{g}^* - (\mathbf{f}\hat{\mathbf{m}})(\hat{\mathbf{m}}\mathbf{g}^*), \tag{2.20}$$

as expected from the identity (2.15). Indeed, from (2.16) and for $f, g \in \tilde{L}^2_{\mathfrak{m}}(Y)$,

$$\tilde{C}_{f,g}(t) = \frac{1}{T}\sum_i \sum_j f_i \#\{y_s \in B_i, y_{s+t} \in B_j\} g_j^* - \bar{f}\,\bar{g}^*.$$

On the other hand,

$$\begin{aligned}
\hat{C}_{f,g}(t) = & \quad \tfrac{1}{T}\textstyle\sum_{s=0}^{T} f(y_s) g(y_{s+t})^* - \bar{f}\,\bar{g}^* \\
= & \quad \tfrac{1}{T}\textstyle\sum_i \sum_j \sum_{y_s \in B_i, y_{s+t} \in B_j} f(x_s) g(x_{s+t})^* - \bar{f}\,\bar{g}^* \\
= & \quad \tfrac{1}{T}\textstyle\sum_i \sum_j \sum_{y_s \in B_i, y_{s+t} \in B_j} f_i g_j^* - \bar{f}\,\bar{g}^* \\
= & \quad \tfrac{1}{T}\textstyle\sum_i \sum_j f_i \#\{y_s \in B_i, y_{s+t} \in B_j\} g_j^* - \bar{f}\,\bar{g}^*.
\end{aligned}$$

Thus, for any $f, g \in \tilde{L}^2_{\mathfrak{m}}(Y)$, the sample and transition correlation functions $\hat{C}_{f,g}(t)$ and $\tilde{C}_{f,g}(t)$ coincide and give an estimate of the true correlation function $C_{f,g}(t)$ defined in (2.10) and satisfying (2.15).

2.2.3 *Spectrum of the reduced transition matrix and correlations*

Once the transition matrix $\mathbf{P}_t^{\mathscr{R}}$ has been estimated for a continuous observation operator $\mathscr{R}$ and a lag t, its eigenvalues $\hat{\zeta}_k^{\mathscr{R}}(t), 1 \leq k \leq n$ can be calculated, together with its left eigenvectors $\hat{\mathbf{e}}_k^{\mathscr{R}}(t)$ and right eigenvectors $\hat{\mathbf{f}}_k^{\mathscr{R}}(t)$. From the identities (2.17) and (2.18), one can see that the forward reduced ergodicity eigenvectors $\psi_k^{\mathscr{R},f}(t)$ of the reduced transfer operator $\mathfrak{L}_t^{\mathscr{R}}$ are approximated by the left eigenvectors $\hat{\mathbf{e}}_k^{\mathscr{R}}(t)$ of $\hat{\mathbf{P}}_t^{\mathscr{R}}$ divided by $\hat{\mathbf{m}}$ and that the backward ergodicity eigenvectors $\psi_k^{\mathscr{R},b}(t)$ of the reduced Koopman operator $\mathfrak{U}_t^{\mathscr{R}}$ are approximated by the right eigenvectors $\hat{\mathbf{f}}_k^{\mathscr{R}}(t)$ of $\hat{\mathbf{P}}_t^{\mathscr{R}}$. To get an approximation of the ergodicity eigenvalues λ_k, the complex logarithm of the eigenvalues of the reduced transition matrix $\hat{\mathbf{P}}_t^{\mathscr{R}}$ divided by t is taken as such

$$\begin{aligned}
\Re\left(\hat{\lambda}_k^{\mathscr{R}}(t)\right) = & \quad \log\left(\left|\hat{\zeta}_k^{\mathscr{R}}(t)\right|\right)/t \\
\Im\left(\hat{\lambda}_k^{\mathscr{R}}(t)\right) = & \quad \arg\left(\hat{\zeta}_k^{\mathscr{R}}(t)\right)/t.
\end{aligned} \tag{2.21}$$

From the SMT (2.9), if $\hat{\mathbf{P}}_t^{\mathscr{R}}$ was the true transfer operator $\mathscr{L}_t$, the $\hat{\lambda}_k^{\mathscr{R}}(t)$ would yield the leading eigenvalues of the generator $\mathscr{G}_\mu$. The eigenvalues $\hat{\lambda}_k^{\mathscr{R}}(t)$, together with the eigenvectors $\hat{\psi}_k^{\mathscr{R},f}(t)$ and $\hat{\psi}_k^{\mathscr{R},b}(t)$, would then be independent of the lag t, but because the semigroup property is lost due to the projection on the space of functions of the reduced space Y, transition matrices estimated for different lags can yield different $\hat{\lambda}_k^{\mathscr{R}}(t), \hat{\psi}_k^{\mathscr{R},f}(t), \hat{\psi}_k^{\mathscr{R},b}(t)$, as stressed by the addition of the argument t. The importance of the choice of the lag t is discussed in more details in chapter 5. As a rule of thumb, shorter lags allow to access shorter time scales but longer lags allow to treat the fast unresolved variables as decorrelated noise and to resolve longer time scales better.

Remark 11 (Choosing the observation operator)**.** *While the quality of the approximation of the spectrum of the semigroup of transfer operators by the spectrum of transition matrices depends on the choice of the observation operator $\mathscr{R}$ together with the grid and sampling of the time series, it is expected from the results presented in the previous subsection 2.2.1 and in Chekroun et al. (2014) that the reduced transfer operator $\mathscr{L}_t^{\mathscr{R}}$ contains partial information on the transfer operator $\mathscr{L}_t$. In order to maximize this information, the observation operator $\mathscr{R}$ should be chosen in order for the leading ergodicity eigenvectors to project significantly on the space of functions on Y so as for the leading ergodicity eigenvalues to be captured. Moreover, it is shown in the following subsection 2.2.4 that an estimate of the spectral gap separating the ergodicity eigenvalues of the transfer operators can be given from the one between the eigenvalues of the reduced Markov operators.*

Last but not least, knowing the eigenvalues $\hat{\zeta}_k^{\mathscr{R}}(t)$ and the eigenvectors $\hat{\mathbf{e}}_k^{\mathscr{R}}(t)$ and $\hat{\mathbf{f}}_k^{\mathscr{R}}(t)$, the transition matrix $\hat{\mathbf{P}}_t^{\mathscr{R}}$ can be diagonalized as such

$$\hat{\mathbf{P}}_t^{\mathscr{R}} = \hat{\mathbf{F}}_t^{\mathscr{R}} \hat{\mathbf{Z}}_t^{\mathscr{R}} \hat{\mathbf{E}}_t^{\mathscr{R}}, \tag{2.22}$$

where $\hat{\mathbf{Z}}_t^{\mathscr{R}}$ is the diagonal matrix with elements the eigenvalues $\hat{\zeta}_k^{\mathscr{R}}(t), 1 \leq i \leq n$, $\hat{\mathbf{E}}_t^{\mathscr{R}}$ is the matrix of the left eigenvectors of $\hat{\mathbf{P}}_t^{\mathscr{R}}$ with its kth row giving the eigenvector $\hat{\mathbf{e}}_k^{\mathscr{R}}(t)$ and $\hat{\mathbf{F}}_t^{\mathscr{R}}$ is the matrix of the right eigenvectors of $\hat{\mathbf{P}}_t^{\mathscr{R}}$, with its kth column giving the eigenvector $\hat{\mathbf{f}}_k^{\mathscr{R}}(t)$. The spectral decomposition (2.22) of the transition matrix $\hat{\mathbf{P}}_t^{\mathscr{R}}$ can be used to calculate the transition matrix correlation function $\tilde{C}_{f,g}(t)$, defined in (2.20) directly from the spectrum of $\hat{\mathbf{P}}_t^{\mathscr{R}}$, as such

$$\begin{aligned} \tilde{C}_{f,g}(t) = & \quad \mathbf{f}\mathbf{D}(\hat{\mathbf{m}})\hat{\mathbf{P}}_t^{\mathscr{R}}\mathbf{g}^* - (\mathbf{f}\hat{\mathbf{m}})(\hat{\mathbf{m}}\mathbf{g}^*) \\ = & \quad (\mathbf{f}\mathbf{D}(\hat{\mathbf{m}})\hat{\mathbf{F}}_t^{\mathscr{R}})\hat{\mathbf{Z}}_t^{\mathscr{R}}(\hat{\mathbf{E}}_t^{\mathscr{R}}\mathbf{g}^*) - (\mathbf{f}\hat{\mathbf{m}})(\hat{\mathbf{m}}\mathbf{g}^*), \end{aligned} \tag{2.23}$$

where the last identity corresponds to the spectral decomposition (2.11) for $f, g \in \tilde{L}^2_{\mathrm{m}}(Y)$. In the decomposition (2.23), we have used the eigenvalues and eigenvectors of reduced transition matrices $\hat{\mathbf{P}}_t^{\mathscr{R}}$ for $t \geq 0$, which, apart from sampling errors and imprecisions in the resolution of the eigenvalue problem, should give exactly the correlation function $C_{f,g}(t)$ for observables f and g in the discrete space $\tilde{L}^2_{\mathrm{m}}(Y)$. Estimating the transition matrices $\hat{\mathbf{P}}_t^{\mathscr{R}}$ for many lags t and calculating their spectrum is computationally expensive. Instead, one can calculate the spectrum of a single transition matrix $\hat{\mathbf{P}}_\tau^{\mathscr{R}}$ for a carefully chosen lag τ and replace the matrix $\hat{\mathbf{Z}}_t^{\mathscr{R}}$ in (2.23) by the matrix $e^{t\hat{\Lambda}_\tau^{\mathscr{R}}}$ with diagonal elements $e^{t\hat{\lambda}_k^{\mathscr{R}}(\tau)}, 1 \leq k \leq n$, keeping the eigenvectors fixed at lag τ, as such

$$\tilde{C}_{f,g}(t) \approx (\mathbf{f}\mathbf{D}(\hat{\mathbf{m}})\hat{\mathbf{F}}_\tau^{\mathscr{R}})e^{t\hat{\Lambda}_\tau^{\mathscr{R}}})(\hat{\mathbf{E}}_\tau^{\mathscr{R}}\mathbf{g}^*) - (\mathbf{f}\hat{\mathbf{m}})(\hat{\mathbf{m}}\mathbf{g}^*), \tag{2.24}$$

Because the semigroup property is lost due to the projection, one cannot expect the decomposition (2.24) to be exact, even for observables in the discrete space $\tilde{L}^2_{\mathrm{m}}(Y)$.

However, if the observation operator $\mathscr{R}$ is chosen so as to capture the slowest motions, the leading eigenvalues of the transition matrix are expected to be robust to the choice of the lag τ (see chapter 5 for a detailed discussion). On the other hand, the contribution associated with the secondary eigenvalues far from the imaginary axis will decay quickly with time. Thus, the constance of the reduced ergodicity eigenvalues with the lag as well as the quality of the reconstruction (2.24) of the correlation function constitute a good test of the quality of the approximation of the ergodicity spectrum by the spectrum of reduced transition matrices.

As a final remark, most of this work focuses on the ergodicity eigenvalues in order to study the time scales of the mixing properties of the system and the next subsection 2.2.4 gives a theorem relating the spectrum of the reduced transfer operator to the ergodicity spectrum of the semigroup of transfer operators. However, we will also see in chapter 3, that much can be learned from the ergodicity eigenvectors as well, in particular about the heterogenous character and the nature of the dynamics in phase space.

2.2.4 *Reduced spectral gap theorem*

We have seen in subsection 2.2.1 that, due to the projection $E[\cdot|\mathscr{B}(Y)] : L^2_\mu(H) \to L^2_{\mathfrak{m}}(H)$, iterations of the reduced transfer operator $\mathfrak{L}^{\mathscr{R}}_t$ cause a loss of information about the dynamics which in turn results in a breakdown of the semigroup property that the family of transfer operators enjoys. As a consequence, one cannot expect the reduced ergodicity eigenvalues $\lambda^{\mathscr{R}}_k(t)$ of $\mathfrak{L}^{\mathscr{R}}_t$ to coincide with the ergodicity eigenvalues λ_k of the semigroup of transfer operators. Instead, one can only hope to capture the leading ergodicity eigenvalues responsible for the slowest decay of correlations when the observation operator $\mathscr{R}$ is chosen so as for the slowest motions to project on the reduced space Y (i.e. for the eigenvectors associated with these leading eigenvalues to project significantly on the space of measurable functions on Y). In particular, for the applications of the following chapters, the most important information is provided by the spectral gap between the real parts of the first eigenvalue $\lambda_1 = 0$ and the second eigenvalue λ_2 of the generator $\mathscr{G}_\mu$, or, correspondingly, by the spectral gap $\delta_{\mathscr{L}_t}$ between the modulus of the first eigenvalue $\zeta_1(t) = 1$ and the modulus of the second eigenvalue $\zeta_2(t)$ of the transfer operator $\mathscr{L}_t$. Indeed, this spectral gap gives a measure of the rate of decay of correlations (or rate of mixing), as can be seen from the spectral decomposition (2.11) of the correlation function.

The question thus boils down to whether the reduced spectral gap $\delta_{\mathfrak{L}^{\mathscr{R}}_t} = 1 - |\zeta^{\mathscr{R}}_2(t)|$ of the reduced transfer operator $\mathfrak{L}^{\mathscr{R}}_t$ can give a good estimate of the true spectral gap $\delta_{\mathscr{L}_t} = 1 - |\zeta_2(t)|$. Intuitively, one expects this reduced spectral gap to give an upper bound to the true spectral. Indeed, the projection of the dynamics on the reduced space Y induces an apparent increase of the mixing, manifested by the crossing of the observed trajectory $\mathscr{R}(X(t,x))$ on Y, as well as by the extra diffusion,

or coarse-graining, associated with each iteration of the reduced transfer operator $\mathfrak{L}_t^{\mathscr{R}}$, as illustrated by the diagrams of subsection 2.2.1. This idea is confirmed by the following theorem, subsequently proved for the special case of compact operators.

Theorem 1 (Reduced spectral gap). *We assume that the SDE (2.1) on the Hilbert space H is well-posed and that an invariant measure μ exists. Let $\mathscr{L}_t, t \geq 0$ be the semigroup of transfer operator with respect to μ of the SDE, which can be extended to a semigroup of contraction on $L^2_\mu(H)$. Let $\mathscr{R}$ be a continuous mapping from the phase space H to the reduced space $Y = \mathbb{R}^p, p < \dim H$, inducing a pull-back measure $\mathfrak{m} = \mathscr{R} * \mu$ on the Borel σ-algebra $\mathscr{B}(Y)$. Let $\mathfrak{L}_t^{\mathscr{R}}$ on $L^2_{\mathfrak{m}}(Y)$ be the reduced transfer operator associated with the observation operator $\mathscr{R}$ (see subsection 2.2.1 and Chekroun et al., 2014). We further assume that the transfer operators are compact.*
Then, the spectral gap $\delta_{\mathfrak{L}_t^{\mathscr{R}}} = 1 - |\zeta_2^{\mathscr{R}}(t)|$ of $\mathfrak{L}_t^{\mathscr{R}}$ is such that

$$\delta_{\mathfrak{L}_t^{\mathscr{R}}} \geq \delta_{\mathscr{L}_t} \quad t \geq 0$$

where $\delta_{\mathscr{L}_t} = 1 - |\zeta_2(t)|$ is the spectral gap of the transition operator $\mathscr{L}_t$.

The important assumption of the theorem is the compactness of the transfer operator $\mathscr{L}_t$. This should not come as a surprise as compact operators in infinite dimension share many properties of finite dimensional operators, in particular the discreteness of the spectrum, as assumed for the spectral decomposition of the correlation function (2.11). The proof relies on the extension of the *min-max variational principle* to compact nonselfadjoint adjoint operators on Hilbert space by Ramm (1981) (see also Ramm, 1983, for a generalization to Banach spaces). Mainly, the eigenvalue problem for $\mathfrak{L}_t^{\mathscr{R}}$ on the reduced space is lifted to an eigenvalue problem for $\mathscr{L}_t$ on the full space, for which the eigenvectors of the reduced operator can only be sub-optimal. Let us first define the space

$$V^{\mathscr{R}} = \left\{ (\psi^{\mathscr{R},f}, \psi^{\mathscr{R},b}) \in L^2_{\mathfrak{m}}(Y) \times L^2_{\mathfrak{m}}(Y) : \begin{array}{rcl} \left\langle \psi^{\mathscr{R},f}, 1 \right\rangle_{\mathfrak{m}} & = & 0 \\ \left\langle 1, \psi^{\mathscr{R},b} \right\rangle_{\mathfrak{m}} & = & 0 \\ \left\langle \psi^{\mathscr{R},f}, \psi^{\mathscr{R},b} \right\rangle_{\mathfrak{m}} & = & 1 \end{array} \right\},$$

of couples of $L^2_{\mathfrak{m}}(Y)$ which are bi-orthonormal with the first eigenvectors $\psi_1^{\mathscr{R},f} = 1$ and $\psi_1^{\mathscr{R},b} = 1$ of $\mathfrak{L}_t^{\mathscr{R}}$ and its adjoint. Thus, the second eigenvectors $(\psi_2^{\mathscr{R},f}, \psi_2^{\mathscr{R},b})$ associated with the eigenvalue $\zeta_2^{\mathscr{R}}(t)$ of $\mathfrak{L}_t^{\mathscr{R}}$ and its adjoint are in $V^{\mathscr{R}}$. From the disintegration of the measure μ (Kallenberg, 2002, Chap. 6), we have that

$$\begin{array}{rcl} \psi^{\mathscr{R}} \in L^2_{\mathfrak{m}}(Y) & \Leftrightarrow & \psi^{\mathscr{R}} \circ \mathscr{R} \in L^2_\mu(H) \\ \left\langle \psi^{\mathscr{R},f}, 1 \right\rangle_{\mathfrak{m}} = 0 & \Leftrightarrow & \left\langle \psi^{\mathscr{R},f} \circ \mathscr{R}, 1 \right\rangle_\mu = 0, \\ \left\langle 1, \psi^{\mathscr{R},b} \right\rangle_{\mathfrak{m}} = 0 & \Leftrightarrow & \left\langle 1, \psi^{\mathscr{R},b} \circ \mathscr{R} \right\rangle_\mu = 0, \\ \left\langle \psi^{\mathscr{R},f}, \psi^{\mathscr{R},b} \right\rangle_{\mathfrak{m}} = 1 & \Leftrightarrow & \left\langle \psi^{\mathscr{R},f} \circ \mathscr{R}, \psi^{\mathscr{R},b} \circ \mathscr{R} \right\rangle_\mu = 1. \end{array}$$

Thus, $\psi^{\mathscr{R}} \mapsto \psi^{\mathscr{R}} \circ \mathscr{R}$ is an isometry from $V^{\mathscr{R}}$ to

$$V = \left\{ (\psi^f, \psi^b) \in L^2_\mu(H) \times L^2_\mu(H) : \begin{array}{c} \exists \psi^{\mathscr{R},f}, \psi^{\mathscr{R},b} \in L^2_{\mathfrak{m}}(Y) \text{ s.t.} \\ \psi^f = \psi^{\mathscr{R},f} \circ \mathscr{R}, \quad \psi^b = \psi^{\mathscr{R},b} \circ \mathscr{R} \\ \left\langle \psi^f, 1 \right\rangle_\mu = 0, \quad \left\langle 1, \psi^b \right\rangle_\mu = 0, \quad \left\langle \psi^f, \psi^b \right\rangle_\mu = 1 \end{array} \right\},$$

the set of couples of $L^2_\mu(H)$ which are bi-orthonormal to the first eigenvectors $\psi^f_1 = 1$ and $\psi^b_1 = 1$ of $\mathscr{L}_t$ and its adjoint. From its definition, V is included in the space

$$W = \left\{ (\psi^f, \psi^b) \in L^2_\mu(H) \times L^2_\mu(H) : \begin{array}{rcl} < \psi^f, 1 >_\mu & = & 0 \\ < 1, \psi^b >_\mu & = & 0 \\ < \psi^f, \psi^b >_\mu & = & 1 \end{array} \right\},$$

to which the second eigenvectors (ψ^f_2, ψ^b_2) of $\mathscr{L}_t$ and its adjoint belong, since $\psi^f_1 = 1$ and $\psi^b_1 = 1$ are the first eigenvectors of $\mathscr{L}_t$ and its adjoint, respectively. The second eigenvalue $\zeta^{\mathscr{R}}_2(t)$, eigenvector $\psi^{\mathscr{R},f}_2$ and adjoint eigenvector $\psi^{\mathscr{R},b}_2$ of $\mathfrak{L}^{\mathscr{R}}_t$ are such that

$$|\zeta^{\mathscr{R}}_2(t)| = \left| \frac{< \mathfrak{L}^{\mathscr{R}}_t \psi^{\mathscr{R},f}_2, \psi^{\mathscr{R},b}_2 >_{\mathfrak{m}}}{< \psi^{\mathscr{R},f}_2, \psi^{\mathscr{R},b}_2 >_{\mathfrak{m}}} \right|,$$

so that, from the disintegration of the measure μ, the unique couple (ν^f, ν^b) in V such that $\nu^f = \psi^{\mathscr{R},f}_2 \circ \mathscr{R}$ and $\nu^b = \psi^{\mathscr{R},b}_2 \circ \mathscr{R}$ satisfies

$$|\zeta^{\mathscr{R}}_2(t)| = \left| \frac{< \mathscr{L}_t \nu^f, \nu^b >_\mu}{< \nu^f, \nu^b >_\mu} \right| = \left| < \mathscr{L}_t \nu^f, \nu^b >_\mu \right| \tag{2.25}$$

Moreover, from the variational principle of Ramm (1981) applied to the operator $\mathscr{L}_t$, assumed compact on the Hilbert space $L^2_\mu(H)$, the second eigenvalue of $\mathscr{L}_t$ is such that

$$\begin{array}{rccc} |\zeta_2| = & \max & \min & | < \mathscr{L}_t \psi^f, \psi^b >_\mu | \\ & \psi^f \in L^2_\mu(H) & \psi^b \in L^2_\mu(H) & \\ & < \psi^f, 1 >_\mu = 0 & < 1, \psi^b >_\mu = 0 & \\ & & < \psi^f, \psi^b >_\mu = 1 & \end{array} \tag{2.26}$$

Thus, $(\nu^f, \nu^b) = (\psi^{\mathscr{R},f}_2 \circ \mathscr{R}, \psi^{\mathscr{R},b}_2 \circ \mathscr{R}) \in V$ can only be a sub-optimum of the variational problem (2.26), since $V \subseteq W$ and it follows, from the identity (2.25), that $|\zeta^{\mathscr{R}}_2(t)| \leq |\zeta_2|$, hence the statement of the *reduced spectral gap theorem*.

Remark 12 (Applicability of the theorem)**.** *The compactness of the transition semigroups is a very strong property. It has been proven to be satisfied by some stochastic systems in $L^2_\mu(H)$ (the space of twice integrable functions with respect to the invariant measure μ on the Hilbert space H) such as finite-dimensional OUs (Chojnowska-Michalik and Goldys, 1995; Metafune et al., 2002) and some dissipative SDEs (Da Prato et al., 2002). For dissipative deterministic systems, however, one cannot expect the transition semigroups to be compact, let alone on the Hilbert space $L^2_\mu(H)$, because of the presence of an essential spectrum to the left of the discrete eigenvalues. Instead, these operators may be quasi-compact, as was shown for expanding maps (Rychlik, 1983; Ruelle, 1989c) and hyperbolic systems (Blank et al., 2002; Gouëzel and Liverani, 2006; Baladi and Tsujii, 2007; Butterley and Liverani, 2007; Baladi and Liverani, 2012). This essential spectrum may result in a decay of correlations which is not exponential (see e.g. Butterley, 2015). It is thus expected that our theorem can extend to the quasi-compact case only for short lags t, depending on the degree of hyperbolicity of the system.*

2.3 APPLICATION TO AN ORNSTEIN-UHLENBECK PROCESS

As a first application of the theory exposed in section 2.1 and as a first test for the methodology presented in the previous section 2.2, we study the spectrum of a d-dimensional OU, $1 \leq d < \infty$. Such an OU is obtained by setting the nonlinear part F of the general SDE (2.1) to zero and identifying the linear operator A and the noise operator Σ with the matrices A_0 and Q, respectively. That is

$$dX = A_0 X\,dt + Q\,dW, \tag{2.27}$$

The matrix A_0 is the linear and deterministic part of the process, while the real, symmetric and nonnegative matrix Q gives the crosscorrelations between the d components of the noise. In the following, we assume that the spectrum $\sigma(A_0)$ of A_0 has strictly negative real part, so that the OU process is stable and has a unique invariant measure μ (Da Prato and Zabczyk, 1996; Metafune et al., 2002).

It has been shown in Metafune et al. (2002) (see also Chojnowska-Michalik and Goldys, 1996; Metafune, 2001), that the ergodicity spectrum $\sigma(\mathscr{G})$ in $L^p_\mu(\mathbb{R}^d)$, $1 < p < \infty$, of a d-dimensional OU is discrete and given by linear combinations (with coefficients in the natural numbers) of the eigenvalues of A_0

$$\sigma(\mathscr{G}_\mu) = \left\{ \sum_{l=1}^{m} n_l \gamma_l \quad \text{such that} \quad \gamma_l \in \sigma(A_0), n_l \in \mathbb{N}, m \geq 1 \right\}. \tag{2.28}$$

Interestingly, the eigenvalues λ_k, $k \geq 0$, depend on Q only through the dependence of the invariant measure μ defining $L^p_\mu(\mathbb{R}^d)$ on Q. We will see in chapter 3, that this is generally not the case for nonlinear systems. Moreover, the forward and backward eigenvectors (which, in the one dimensional case, are given by Hermite polynomials,

respectively) are affected by the noise level in such way that their width increases as the noise level is increased (Gaspard et al., 1995; Metafune et al., 2002).

To demonstrate the potential of the numerical method presented section 2.2 and in view of the forthcoming applications, we take as an example a two-dimensional OU with

$$A_0 = \begin{pmatrix} 0.196 & 0.513 \\ -0.513 & -0.396 \end{pmatrix}, \quad Q = \begin{pmatrix} 1 & 0 \\ 0 & 1 \end{pmatrix}. \tag{2.29}$$

The matrix A_0 has been designed in order to have a pair of complex conjugate eigenvalues $\gamma_{1,2} = -0.1 \pm 2\pi/15$ so that the corresponding linear system has a stable focus point at 0 to which solutions converge with a characteristic time-scale of 10 time-units, spiralling with a period of 15 time-units. The ergodicity spectrum is approximated following the method described in section 2.2, from a simulation of the OU process $X(t,x)$ using the Euler-Maruyama scheme with a time-step δt of 0.01 for a duration D of 10^6 time-units (i.e 10^8 time-steps). For the initial condition x not to be in a weakly sampled region of the phase space, a spin-up period of 10^5 time-units is removed. The dimension of the two-dimensional phase space being small, no reduction is necessary for an estimation of the transition matrix $\mathbf{P}_t^{\mathscr{R}}$, so that the observation operator $\mathscr{R}$ is simply taken as the identity on H. The transition matrix $\mathbf{P}_t^{\mathscr{R}}$ for a lag t of 0.5 time-unit was estimated on a grid of 200-by-200 boxes spanning -4 to +4 standard deviations in both directions. The leading eigenvalues of the resulting transition matrix $\hat{\mathbf{P}}_t^{\mathscr{R}}$, converted to generator-like eigenvalues by applying the formula (2.21), are represented in figure 2.3(a) as red and black solid dots, together with the analytical eigenvalues given by the analytical formula (2.28) as blue crosses. The left eigenvector of $\hat{\mathbf{P}}_t^{\mathscr{R}}$ associated with the ergodicity eigenvalue $\hat{\lambda}_1^{\mathscr{R}} = 0$ and approximating of the density of the invariant measure μ is also represented in figure 2.3(b).

As expected (see e.g. Da Prato and Zabczyk, 1996), the approximated invariant density represented in figure 2.3(b) is bivariate-normal, with a correlation matrix determined by A_0 and Q. By comparing the position of the solid dots and the crosses in figure 2.3, one can see that the leading eigenvalues of the ergodic semigroup corresponding to (2.27) are well captured by the approximation. Indeed, the first 10 eigenvalues have a relative error of less than 1%. The real parts of eigenvalues far from the imaginary axis tend to be overestimated (in absolute value), while the imaginary parts of eigenvalues far from the real axis are underestimated. Note that the eigenvalues which are the farthest from the imaginary axis correspond to very fast time scales so that they become more and more sensitive to the finite time-step δt of 0.01 used in the integration scheme. The numerical method used here is thus promising, since, in most applications of ergodic theory, one is interested in the slowest time scales, i.e those responsible for the slow decay of correlations.

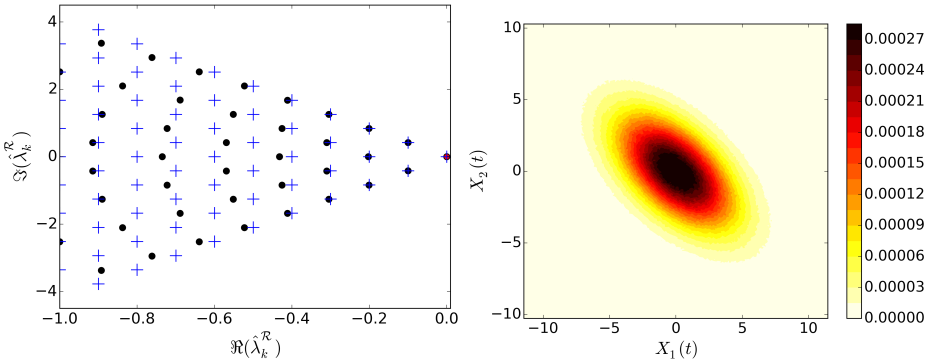

(a) (b)

Figure 2.3: (a) Approximated ergodicity eigenvalues of the two-dimensional OU defined in (2.29). The red and black solid dots represent its approximation from the transition matrix $\hat{\mathbf{P}}_t^{\mathcal{R}}$ estimated for a lag t of 1 time-unit on a grid of 200-by-200 boxes spanning -4 to +4 standard deviations in both directions. The blue crosses represent the analytical spectrum as given by (2.28). (b) Approximation of the density of the invariant measure as the left eigenvector of $\hat{\mathbf{P}}_t^{\mathcal{R}}$ associated with the ergodicity eigenvalue zero.

The pyramidal array of ergodicity eigenvalues represented in figure 2.3 is characteristic of linear systems with a stable focus point, i.e. for which the leading eigenvalues of the linear operator constitute a complex pair of eigenvalues. As a consequence the leading pair of secondary ergodicity eigenvalues, which, by formula (2.28), is identical to that of the linear operator, is responsible for correlation functions to oscillate at an angular frequency given by their imaginary part of the complex pair and decaying at a rate given by their real part. This can be seen in figure 2.4(a), where the sample autocorrelation function (2.19) for the observables $f(x) = g(x) = x$ is represented by a thick blue line. The slowly decaying oscillations in the correlation functions represented in figure 2.4(a) associated with the leading complex pair of ergodicity eigenvalues are responsible for a peak in the power spectrum (2.12), as can be seen from the periodogram $\hat{S}_{x,x}(\omega)$ of figure 2.4(b), calculated as the Fourier transform of the sample correlation function $\hat{C}_{f,g}(t)$ (von Storch and Zwiers, 1999) applying a hamming window to reduce spectral leakage. As discussed at the end of subsection 2.1.3, the position of the peak is determined by the imaginary part of the ergodicity eigenvalues and its width by its real part (ergodicity eigenvalues close to the imaginary axis being responsible sharp peaks). The transition matrix correlation function (2.20) reconstructed from the leading 200 eigenvalues and eigenvectors of the single transition matrix $\hat{\mathbf{P}}_t^{\mathcal{R}}$ by applying (2.24) is also represented in figure 2.4(a) by a dashed red line. We can see that both correlation functions coincide almost identically (which would also be the case if only the first complex pair of eigenvalues

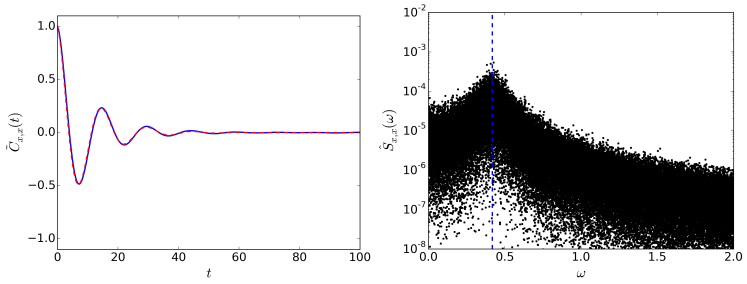

(a) (b)

Figure 2.4: (a) Sample correlation function $\hat{C}_{x,x}(t)$ (thick blue line) and spectral reconstruction of the correlation function $\tilde{C}_{x,x}(t)$ (green dashed line). (b) Periodogram $\hat{S}_{x,x}(\omega)$ calculated as the Fourier transform of the sample correlation function $\hat{C}_{x,x}(t)$. The vertical dashed blue line marks the imaginary part of the leading complex pair of ergodicity eigenvalues.

and eigenvectors would be used) because, not only the leading ergodicity eigenvalues represented figure 2.3 are well approximated, but also the eigenvectors associated to them, and that, since no reduction is performed, the semigroup property is only vulnerable to the discretization and the finite sampling, in this case. Indeed, only the discretization and the approximation of the spectrum from a long but finite time series is tested here. However, armed with the theorem of Chekroun et al. (2014) and the reduced spectral gap theorem of section 2.2.4, we will see in the coming chapters that much can be learned even if the transition matrix is estimated on a much lower-dimensional space than the phase space itself.

3

ERGODICITY SPECTRUM OF STOCHASTIC EVOLUTION EQUATION: THEORY AND APPLICATION TO EL NIÑO

The relationship between the ergodicity spectrum and the stability of a dynamical system is revealed in the context of bifurcation theory. As a system becomes unstable, it takes more and more time to recover from perturbations, a phenomenon known as critical slowing down. Thus, densities are expected to converge less quickly to the invariant measure so that the ergodicity eigenvalues should approach the imaginary axis. These ideas are applied to simple dynamical models of El Niño-Southern Oscillation (ENSO) undergoing a Hopf bifurcation. The first model, the stochastic delayed oscillator, is an SDDE, while the second, the Zebiak-Cane model, is a Galerkin truncation of a PDE.

As a first step, novel formulas are given for the leading part of the ergodicity eigenvalues of general linear SDDEs. These formulas are derived from the ergodicity spectrum of OUs and are supported by Galerkin approximations of the SDDEs. These results are applied to the linear version of the stochastic delayed oscillator and it is found that the numerical approximations of the ergodicity eigenvalues agree well with the conjectured formulas, even though a reduction from an infinite-dimensional space to a two-dimensional one is performed. It follows that the numerical method presented in chapter 2 can prove very fruitful in studying stochastic bifurcations.

The nonlinear case is subsequently treated. First, novel results are found regarding the ergodicity spectrum of a simple form of stochastic Hopf bifurcation, which sheds light on the characteristic evolution of statistics of such systems in terms of diffusive periodic orbit. In particular, the ergodicity eigenvalues are found to approach the imaginary as the system gets closer to the bifurcation and noise-induced oscillations are possible even before the Hopf bifurcation. This analytical study allows to interpret the numerical results obtained for the nonlinear version of the stochastic delayed oscillator as well as for the Zebiak-Cane model. In particular, the ergodicity eigenvectors bear the signature of the nonlinearities active along the bifurcation. As a consequence, they allow to discriminate a linear system from a nonlinear one as well as the subcritical case from the supercritical case. The applicability of this promising method to observations or more realistic models to unravel the nature of ENSO is finally discussed.

3.1 INTRODUCTION

The evolution of correlations between observables is crucial for interpretation of special phenomena, such as transitions or emergence, in dynamical systems. In the climate system, a particular phenomenon of interest is the El Niño-Southern Oscillation (ENSO) (Neelin et al., 1998), an interannual variation in the Pacific Ocean Sea Surface Temperature (SST). The first model which was able to simulate realistic ENSO events was the Zebiak-Cane model (Zebiak and Cane, 1987). Much of the theory developed for ENSO is based on the analysis of simulation results of this model.

The oscillatory nature of ENSO derives from an instability of the coupled ocean-atmosphere system, where SST anomalies cause surface wind anomalies that in turn cause changes in surface ocean velocities. Through the associated heat fluxes, SST is affected; in this way positive feedbacks exist of which the strength is measured by a coupling strength μ. When μ exceeds a critical value μ_c, SST anomalies are amplified and the background climate state of the Pacific is unstable. The interannual time scale of ENSO is caused by an adjustment of the ocean circulation due to equatorial wave processes, which induce a negative feedback on the SST. A conceptual model of the ENSO cycle was proposed in Suarez and Schopf (1988) and Battisti and Hirst (1989) as a delayed oscillator governed by a delay equation where the delay is given by the travel time of specific ocean waves.

A general linear scalar Stochastic Delay Differential Equations (SDDEs) with one delay has the form

$$dy(t) = (a_0 y(t) + a_1 y(t-d_1))\,dt + q dW(t)., \tag{3.1}$$

Solutions of these SDDEs can be unstable, depending on the coefficients and the delays. In particular, the special case of the one-dimensional linear Delay Differential Equation (DDE) with one lag (3.1), with $a_0 = 2.2$ yr^{-1} and $a_1 = -3.9$ yr^{-1} considered by Battisti and Hirst (1989), is unstable for a delay d_1 larger than $d_c \approx 110$ days. For this reason, Suarez and Schopf (1988) have added an ad hoc cubic term to (3.1) acting as a nonlinear damping able to stabilize the system. Hence, as the delay is increased, a Hopf bifurcation occurs, in which a fixed point looses its stability while a stable periodic orbit emerges (Strogatz, 1994).

Hence, a stochastic version of this *nonlinear delayed oscillator*, in which the noise could represent fast atmospheric processes such as westerly wind-bursts, is given by

$$dy(t) = \left(a_0 y(t) + c_0 y(t)^3 + a_1 y(t-d_1)\right)dt + q dW(t). \tag{3.2}$$

A bifurcation analysis of the deterministic part of (3.2) has been pursued by Suarez and Schopf (1988). Interestingly, it has been shown by Jin (1997b), that the linear deterministic part of the delayed oscillator can be derived from Ordinary Differential Equation (ODE)-type models of ENSO in which a shallow-water model of the ocean is coupled to a linear atmosphere. The first model of the kind was developed by Zebiak

and Cane (1987) and it is known that a Hopf bifurcation also occurs in this model as well as in its fully-coupled version by van der Vaart et al. (2000). Furthermore, it has been shown by Roulston and Neelin (2000) that noise-induced oscillations could occur, before the bifurcation, when various kind of noise products are added to the wind stress.

Bifurcation theory, the study of rough changes in the dynamics when a parameter is smoothly changed, is fairly complete for deterministic system (Guckenheimer and Holmes, 1983; Arnold, 1986; Ruelle, 1989b; Strogatz, 1994; Kuznetsov, 1998). Stochastic bifurcation theory, however, is much less mature (Arnold, 2003, Chap. 9). One possible explanation for this is that the changes in bifurcation diagrams due to stochasticity are various, the position of the bifurcation may change, bifurcation intervals may arise, branches may disappear. Another is that different types of bifurcations may occur such as Dynamical Bifurcations (D-Bifurcations) or Phenomenological Bifurcations (P-Bifurcations), making the development of a systematic approach to stochastic bifurcation theory difficult. Moreover, the derivation of normal forms, i.e finding an equivalent representation of a system “as simple as possible", can be very tedious in the stochastic case and the results may not be as simple as hoped for (Arnold, 2003, Chap. 8), compared to their deterministic counterpart. For this reason, approximation methods are being developed and recent developments in this direction by Chekroun et al. (2015b) and Chekroun et al. (2015c) are promising. Finally, while the direct forward integration of evolution equations may be sufficient to study deterministic bifurcations, such method may hide the richness behind Random Dynamical Systems (RDSs) which only pull-back approaches (Arnold, 2003) can reveal (Chekroun et al., 2011).

In this chapter, the results on the Ornstein-Uhlenbeck process (OU) presented in chapter 2 are first applied to give novel analytical formulas for the leading part of the ergodicity spectrum of general linear SDDEs, such as the stochastic linear delayed oscillator. We then focus on the ergodicity eigenvalues and eigenvectors of the stochastic nonlinear delayed oscillator (3.2) and of the stochastic Zebiak-Cane model near criticality. Supported by novel analytical results for a simple form of stochastic Hopf bifurcation it will be shown that, while the reduced ergodicity eigenvalues of both models are qualitatively similar, the ergodicity eigenvectors differ due to nonlinear effects. Such results contribute to the challenge which is to understand whether ENSO variability is the result (i) of the excitation of linear modes (**?**), (ii) of a nonlinear sustained oscillation (Zebiak and Cane, 1987; Suarez and Schopf, 1988), or (iii) of a nonlinear noise-induced oscillation (Roulston and Neelin, 2000; Dijkstra, 2013). While other indicators have been developed to answer this question, such as the Bjerknes' index (Jin et al., 2006), we present here another approach based on the analysis of the ergodicity eigenvectors.

In section 3.2, we start with new analytical formulas regarding the ergodicity eigenvalues of linear SDDE. The nonlinear case is then considered, starting with new analytical results on the ergodicity spectrum of a simple form of the stochastic Hopf

bifurcation in section 3.3. The derived system is not a normal form of the stochastic Hopf bifurcation per se, yet it will prove very powerful to interpret the changes in the ergodicity spectrum of the SDDE considered in section 3.4. These results will be used to understand the changes in the ergodicity spectrum of the stochastic Zebiak-Cane model, as presented in section 3.5. A summary and discussion of the main results in section 3.6 concludes the chapter.

3.2 APPLICATION TO LINEAR STOCHASTIC DELAY DIFFERENTIAL EQUATIONS

To our knowledge, the ergodicity spectrum of SDDEs has not been studied yet. However, such systems arise in many applications such as population dynamics (Fargue, 1973; Wörz-Busekros, 1978), control theory (Dugard and Verriest, 1998), stochastic modelling (Kondrashov et al., 2015) and climate dynamics (Bhattacharya et al., 1982; Roques et al., 2014; Suarez and Schopf, 1988; Battisti and Hirst, 1989; Tziperman et al., 1994; Jin, 1997a,b) and could benefit from an ergodic approach, as will be demonstrated in this study.

3.2.1 *A brief introduction to the stability theory of linear SDDEs*

Before to present novel results on the ergodicity spectrum of linear and nonlinear SDDEs, let us recall some important facts regarding the stability of linear SDDEs. In this section, the focus is on linear SDDEs with discrete delays of the form

$$\begin{aligned} dy(t) = &\quad \left(A_0 y(t) + \textstyle\sum_{l=1}^{r} A_l y(t-d_l)\right) dt + Q dW(t) \\ y(0) = &\quad y_0 \in \mathbb{R}^d \\ y(\theta) = &\quad y_1(\theta), \quad \theta \in [-d_l, 0], \end{aligned} \tag{3.3}$$

where $0 < d_1 < ... < d_r$, are discrete delays, $A_0, A_l, l \in \{1, ..., r\}$ and Q are finite d-by-d matrices and $W(\cdot)$ is a d dimensional Wiener process. It is known that y in (3.3) can be extended to a process X function of the history interval $[-d_r, 0]$. One possible extension, which plays an important role in DDE theory, is on space of continuous functions of the interval $[-d_r, 0]$ (Hale and Verduyn Lunel, 1993; Diekmann et al., 1995). In accordance to the functional setting of chapter 2, we prefer the extension on the Hilbert space $H = \mathbb{R}^d \times L^2([-d_r, 0), \mathbb{R}^d)$, classically used in control or approximation theory of DDEs (see Curtain and Zwart, 1995, , Sect. 2.4) The Hilbert space H is endowed with the inner product defined for any $(\beta_1, f_1), (\beta_2, f_2) \in H$ as:

$$\left\langle (\beta_1, f_1), (\beta_2, f_2) \right\rangle_H = \langle \beta_1, \beta_2 \rangle + \frac{1}{d_r} \int_{-d_r}^{0} \left\langle f_1(\theta), f_2(\theta) \right\rangle d\theta,$$

where $\langle \cdot, \cdot \rangle$ denotes the Euclidean inner product of $\mathbb{R}^d$. The stochastic case has been considered by (Chojnowska-Michalik, 1978) (see also Da Prato and Zabczyk, 1996, , Chap. 10), such that the process X is defined as

$$X(t) = \begin{pmatrix} y(t) \\ y_t(\cdot) \end{pmatrix}, \quad t \geq 0, \tag{3.4}$$

where

$$y_t(\theta) = y(t+\theta), \quad t \geq 0, \quad \theta \in [-d_r, 0].$$

The process $X(t)$ is a mild solution of the infinite-dimensional OU

$$dX = \mathscr{A} X dt + \mathscr{B} dW, \tag{3.5}$$

where the operators $\mathscr{A}$ and $\mathscr{B}$ on are defined as follows

$$\mathscr{A} \begin{pmatrix} \phi(0) \\ \phi \end{pmatrix} = \begin{pmatrix} A_0\phi(0) + \sum_{l=1}^{r} A_l \phi(-d_l) \\ \frac{d\phi}{d\theta} \end{pmatrix} \tag{3.6}$$

$$\text{with domain} \quad D(\mathscr{A}) = \left\{ \begin{pmatrix} \phi(0) \\ \phi \end{pmatrix} : \phi \in H^1([-d_r, 0), \mathbb{R}^d) \right\},$$

$$\mathscr{B} u = \begin{pmatrix} bu \\ 0 \end{pmatrix}, \quad u \in \mathbb{R}^d.$$

$H^1([-d_r, 0), \mathbb{R}^d)$ denotes the standard Sobolev subspace of $L_2([-d_r, 0); \mathbb{R}^d)$ of square integrable functions with square integrable first order weak derivative. The operator $\mathscr{A}$ on $D(\mathscr{A})$ generates a linear strongly continuous semigroup on H (Curtain and Zwart, 1995), so that the Cauchy problem associated with the linear equation $\dot{\phi} = \mathscr{A}\phi$ is well-posed in Hadamard's sense. Moreover, the spectrum $\sigma(\mathscr{A})$ of $\mathscr{A}$ is identical to its point spectrum $P\sigma(\mathscr{A})$ and is of the form

$$\sigma(\mathscr{A}) = \left\{ \gamma \in \mathbb{C} : \det \left[\gamma I - A_0 - \sum_{l=1}^{r} e^{-\gamma d_l} A_l \right] = 0 \right\} \tag{3.7}$$

and the semigroup $S_t, t \geq 0$ generated by $\mathscr{A}$ is exponentially stable if and only if (Hale and Verduyn Lunel, 1993)

$$\sup \left\{ \Re(\gamma) : \gamma \in \sigma(\mathscr{A}) \right\} < 0. \tag{3.8}$$

In other words, the semigroup $S_t, t \geq 0$ is exponentially stable if and only if the spectrum $\sigma(\mathscr{A})$ of its generator, is located to the left of the imaginary axis, strictly. Depending on the matrices $A_l, 0 \leq l \leq r$, whether the stability condition (3.8) holds may depend on the delays or not. The particular one-dimensional case with one lag will be studied in section 3.2.3, see Dugard and Verriest (1998) for more details.

Remark 13. *The characteristic equation in (3.7) for (3.5) is a transcendental equation which can be solved numerically (cf. section 3.2.3, for an example), contrary to characteristic equations of finite systems of* ODEs*, which are polynomial.*

3.2.2 *The ergodicity eigenvalues of linear* SDDEs

It is shown in chapter 10.2 by Da Prato and Zabczyk (1996) that if the stability condition (3.8) is satisfied, then there exists exactly one (ergodic) invariant measure for (3.3). However, little is known regarding the ergodicity spectrum of (3.3). Yet, that the linear SDDE (3.3) can be extended to an infinite-dimensional OU (3.5), shows that the ergodicity spectrum of a linear SDDE is that of the OU (3.5) on the Hilbert space $H = \mathbb{R}^d \times L^2([-d_r, 0), \mathbb{R}^d)$.

Unfortunately, even when the stability condition (3.8) is satisfied, so that a unique invariant measure μ exists for (3.5), the results on the ergodicity spectrum of a finite-dimensional OU by Metafune et al. (2002), summarized in section 2.3, cannot be directly extended to an infinite-dimensional setting. However, a recent work by Chekroun et al. (2015a) shows that a large class of nonlinear DDEs satisfying sufficient Lipschitz conditions can be approximated by a convergent Galerkin scheme on Koornwinder polynomials (that can be built from Legendre polynomials), rescaled so as to form an orthogonal basis of the Hilbert space $H = \mathbb{R}^d \times L^2([-d_r, 0), \mathbb{R}^d)$ considered here. In addition to analytical formulas for the scalar case (Sect. 4), Chekroun et al. (2015a) give examples in section 6 of approximations of chaotic DDEs similar to those considered here which reproduce very well the statistics of the original system.

We have seen in the previous subsection 3.2.1 that a linear SDDE can be extended to an abstract OU. From the results of Chekroun et al. (2015a), this infinite-dimensional OU can be approximated by its projection on a truncated set of polynomials, resulting in a finite-dimensional OU. As a consequence, it is expected that at least the predominant statistical properties of a linear SDDE are that of a finite-dimensional OU. In particular, it can be conjectured that the ergodicity eigenvalues of a linear SDDE close to the imaginary axis are given by linear combinations of the spectrum $\sigma(\mathscr{A})$ (which, according to (3.7), is discrete) of its linear operator $\mathscr{A}$.

Conjecture 1. *Let the linear* SDDE *(3.3), extended to the Hilbert space* $H = \mathbb{R}^d \times L^2([-d_r, 0), \mathbb{R}^d)$*, satisfy the stability condition (3.8) for its linear operator* $\mathscr{A}$*, defined in (3.6).*
Then, the ergodicity eigenvalues $\sigma(\mathscr{G}_\mu)$ *of the generator of the semigroup of transfer operators* $\mathscr{L}_t, t \geq 0$ *(see chapter 2) are such that*

$$\sigma(\mathscr{G}_\mu) = \left\{ \sum_{l=1}^{m} n_l \gamma_l \quad \textit{such that} \quad \gamma_l \in P\sigma(\mathscr{A}), n_l \in \mathbb{N}, m \geq 1 \right\}, \tag{3.9}$$

where the the spectrum $\sigma(\mathscr{A})$ of the linear operator is such that

$$\sigma(\mathscr{A}) = \left\{ \gamma \in \mathbb{C} : \det\left[\gamma I - A_0 - \sum_{l=1}^{r} e^{-\gamma d_l} A_l \right] = 0 \right\}.$$

We will see, in the following subsection (3.2.3), that this conjecture is supported by the fact that (i) the leading eigenvalues of a Galerkin approximation of the linear SDDE (3.1) are indistinguishable from those obtained by solving the characteristic equation (3.7) and that (ii) the reduced ergodicity eigenvalues calculated following the method of chapter 2 are very close to the leading ergodicity eigenvalues calculated from the formula (3.9).

3.2.3 *Application to the stochastic linear delayed oscillator*

We now take a simple SDDE relevant for climate science and show that, in this simple case, (i) the ergodicity eigenvalues satisfy (3.9) and (ii) the leading part of the ergodicity spectrum can be approximated from a transition matrix on a two-dimensional reduced space (see section 2.2). The SDDE considered is a one-dimensional linear DDE with one delay proposed by Battisti and Hirst (1989) as a model of ENSO with the addition of noise

$$dy(t) = (a_0 y(t) + a_1 y(t-d_1))\, dt + q dW(t), \tag{3.10}$$

where y represents the SST anomalies in the Eastern part of the Pacific ocean.

3.2.3.1 *Stability analysis*

The characteristic equation, defined in (3.7), for the deterministic part of (3.10) takes the simple form

$$\gamma - a_0 - a_1 e^{-\gamma d_1} = 0. \tag{3.11}$$

Applying the stability condition (3.8), the stability of (3.10) can be studied in the plane Oa_0a_1 (Dugard and Verriest, 1998, Chap. I). One finds that (3.10) is stable independently of the delay d_1 for every couple (a_0, a_1) such that $a_0 + a_1 < 0$ and $a_0 \leq -|a_1|$ and stable for some delay d_1 smaller than a critical delay d_c for every couple (a_0, a_1) such that $a_1 > |a_0|$. This critical delay d_c is given by the *neutral curves* found by solving (3.11) for $\Re(\gamma) = 0$. In the case of (3.10), these curves are given by

$$\Im(\gamma^c) = \pm\sqrt{a_1^2 - a_0^2} \tag{3.12}$$

$$d_c = \frac{1}{|\Im(\gamma^c)|} \arccos\left(-\frac{a_0}{a_1}\right), \tag{3.13}$$

where γ_c is the critical value of γ for which $\Re(\gamma) = 0$, such that, if $\Re(\gamma) > \Re(\gamma_c)$, the system is unstable and d_c is the critical value of the delay d_1 at which this happens.

As an example of numerical application, we set $a_0 = 2.2\ \mathrm{yr}^{-1}$ and $a_1 = -3.9\ \mathrm{yr}^{-1}$. These values are taken from section 2.c by Battisti and Hirst (1989) and correspond to realistic estimates of the local processes responsible for the growth of SSTs and of the damping due to reflected Kelvin waves from the western part of the Pacific ocean, respectively. For these values of a_0 and a_1, the linear delayed oscillator (3.10) is not stable for a delay d_1 larger than $d_c \approx 110$ days (according to 3.13) and the instability has a characteristic period $P_{\gamma_c} = 2\pi/\Im(\gamma_c) \approx 2.0$ yr (according to 3.12).

Moreover, the spectrum $\sigma(\mathscr{A})$ of the linear operator corresponding to the deterministic part of the linear SDDE (3.10) can be calculated by solving the characteristic equation (3.11) numerically. For instance, one can use the Levenberg-Marquardt algorithm (Levenberg, 1944), a hybrid method between the Gauss-Newton algorithm and the gradient descent which is implemented in the MINPACK-1 Fortran package (More et al., 1980). The so-calculated eigenvalues are represented in the complex plane as solid blue dots in figure 3.1(a) and (b) for a delay d_1 of 90 days and of 180 days, respectively. On top of these solutions are also plotted as black pluses the eigenvalues of the matrix A_{60} corresponding to the Galerkin projection of the linear operator $\mathscr{A}$ of the linear SDDE on 60 Koornwinder polynomials (Chekroun et al., 2015a, Sect. 5). Classically, these eigenvalues are solutions of the characteristic polynomial of the matrix A_{60}. The delay of 180 days is taken from Battisti and Hirst (1989) and corresponds to an oceanic wave speed of 2.9 m s^{-1}. In this case, $d_1 > d_c$ so that the deterministic part of (3.10) is unstable, as confirmed by the fact that the leading pair of eigenvalues $(\gamma_1, \gamma_2 = \gamma_1^*)$ has positive real part (cf. figure 3.1(b)), corresponding to a characteristic time $d_{\gamma_1} = |\Re(\gamma_1)^{-1}|$ of around 1.1 yr. Its imaginary part corresponds to a period $P_{\gamma_1} = 2\pi/|\Im(\gamma_1)|$ of around 3.0 yr (approximatively 6 times as much as the delay d_1). One can see that the eigenvalues calculated as solutions of the transcendental characteristic equation (3.11) corresponding to the linear SDDE (3.10) and those calculated as zeros of the characteristic polynomial of the Galerkin approximation A_{60} are practically indistinguishable. Only the eigenvalues of the Galerkin projection very far left of the imaginary axis start to diverge, but they correspond to fast time scales of the order of a month and better results could be obtained by increasing the number of polynomials used for the Galerkin approximation. This indicates that the Galerkin approximation proposed by Chekroun et al. (2015a) is able to capture the spectral properties of the original linear SDDE.

For a delay of 90 days, the deterministic part of the linear delayed oscillator (3.10) is stable, as confirmed by the fact that all the eigenvalues of $\mathscr{A}$ are to the left of the imaginary axis (cf. figure 3.1(a)). In this case, the leading complex pair of eigenvalues corresponds to a characteristic time τ_{γ_1} of around 1.4 yr and to a period P_{γ_1} of around 1.7 yr. Again, both calculations of the eigenvalues are indistinguishable. Note that the time scale corresponding to the real part of the first complex pair of eigenvalues is more than a factor ten larger than that of the second pair, indicative of a strong time-

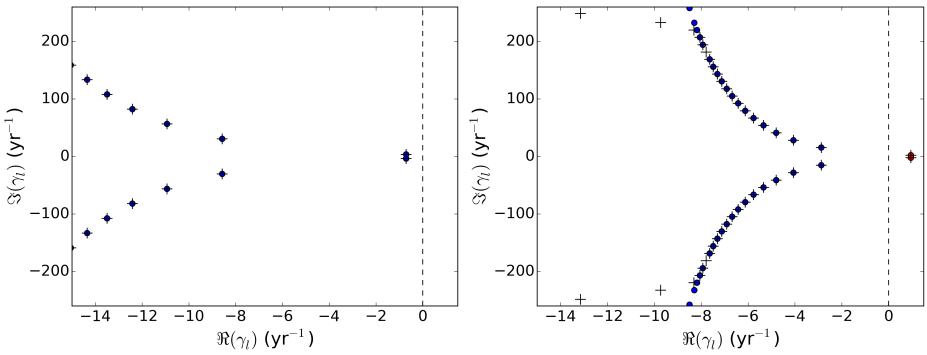

Figure 3.1: Spectrum $\sigma(\mathscr{A})$ of the linear operator for the delayed oscillator (3.10) with $a_0 = 2.2\ \mathrm{yr}^{-1}$, $a_1 = -3.9\ \mathrm{yr}^{-1}$ and (a) $d_1 = 90$ days (stable) or (b) $d_1 = 180$ days (unstable). The solid blue dots represent the eigenvalues calculated as roots of the transcendental characteristic equation (3.11), with the eigenvalues with negative (positive) real part colored in blue (red). The black pluses represent the eigenvalues calculated as roots of the characteristic polynomial of the matrix A_{60} of the Galerkin approximation of the SDDE on 60 Koornwinder polynomials (Chekroun et al., 2015a).

scale separation between the linear modes. This is indicative that conjecture 1 holds in this case and that, according to (3.9), the leading part of the ergodicity eigenvalues should be given by combinations of the leading pair of eigenvalues γ_1 and $\gamma_2 = \gamma_1^*$ of $\mathscr{A}$.

3.2.3.2 *Ergodicity eigenvalues*

Having estimated the spectrum $\sigma(\mathscr{A})$ of the linear operator of the delayed oscillator (3.10), we can now apply the method presented in 2 to approximate the ergodicity eigenvalues from transition matrices on a reduced space and test their agreement with the one given by the conjectured formula (3.9). Here, the noise level q is set to 0.1. The stochastic process was simulated using the Euler-Maruyama scheme with a time step of 0.001 yr for 10^5 yr.

Because of the periodicity in the process $y(t)$ governed by the linear SDDE (3.10), as seen from the non-vanishing imaginary parts of the eigenvalues of the linear operator $\mathscr{A}$ represented in figure 3.1, a reduced space Y of at least two dimensions is used. A classical strategy to extend the one-dimensional valued process $y(t)$ to larger dimensions, which has been developed to define embeddings of attractors (Takens, 1981), is to concatenate several delayed versions of the process as

$(y(t), y(t-\delta_1), y(t-\delta_2), ...)$. Rigorous results in the case of SDDEs regarding the approximation of attractors using such embedding have recently been given by Dellnitz et al. (2015). In our case, we will see that, even though the linear SDDE (3.10) corresponds to an infinite-dimensional Stochastic Differential Equation (SDE) (cf. section 3.2.1), adding only one delayed time series is sufficient to get a good approximation of the ergodicity spectrum, resulting in a two-dimensional reduced space Y. Here, an embedding delay δ_1 equal to the delay d_1 in (3.10) seems appropriate. Another choice could be to define δ_1 as the characteristic time τ_{γ_1} or as the characteristic period P_{γ_1} associated with the leading complex pair of eigenvalues of the linear operator $\mathscr{A}$. The following results are, however, relatively robust to the choice of δ_1.

Proceeding a such, we have defined an observation operator $\mathscr{R}$ from $H = \mathbb{R}^d \times L^2([-d_r, 0), \mathbb{R}^d)$ onto $Y = \mathbb{R}^2$ mapping $X(t)$, defined in (3.4), to $(y(t), y(t-d_1))$. Then, following the methodology of chapter 2, the transition matrix $\mathbf{P}_\tau^{\mathscr{R}}$ is estimated for a lag τ of 0.1 yr on a grid 200-by-200 grid boxes spanning a square of ±4 standard deviations in both directions. The eigenvalues and eigenvectors of this matrix are subsequently calculated to give an approximation of the ergodicity spectrum. According to (2.21), these eigenvalues $\hat{\zeta}_k^{\mathscr{R}}(t)$ are converted to generator-eigenvalues $\hat{\lambda}_k^{\mathscr{R}}(t)$. The resulting reduced ergodicity eigenvalues are represented as solid dots in figure 3.2(a) to (c) for a delay d_1 of 90 days, of 100 days and of 105 days, respectively (i.e for a less and less stable process). In addition, linear combinations of the leading complex pair of eigenvalues of the linear operator $\mathscr{A}$ (fig. 3.1) are represented as blue pluses, in order to compare the reduced ergodicity eigenvalues to the one given by the conjectured formula (3.9).

We can see that the leading part of the reduced ergodicity eigenvalues represented in figure 3.2 agrees well with the conjectured analytical one given by (3.9). This pyramidal structure of eigenvalues arises from linear combinations of the leading complex pair of eigenvalues of the linear operator $\mathscr{A}$ (fig. 3.1). This pyramidal structure is characteristic of a stable focus (a fixed point to which solutions converge spiraling with a characteristic period, see Gaspard et al., 1995). The gap between the imaginary parts of the ergodicity eigenvalues is a multiple of the fundamental angular frequency $|\Im(\gamma_1)|$ of the stable focus. In physical terms, that for increasing imaginary parts the real part of the leading ergodicity eigenvalue decreases indicates that the high-order harmonics of the fundamental angular frequency $|\Im(\gamma_1)|$ are more damped that low-order ones. On the other hand, the gap between the real parts of the ergodicity eigenvalues is a multiple of leading decay rate $-\Re(\gamma_1) = 1/\tau_{\gamma_1}$. This is why, when the delay d_1 is increased to its critical value d_c, the ergodicity eigenvalues get closer to the imaginary axis, resulting in critical slowing down. As a consequence, the spectral gap between the first ergodicity eigenvalue and the second gives a measure of the sensitivity of the system to perturbations (see also Chekroun et al., 2014; Lucarini, 2015). In the deterministic case, for a delay d_1 equal to the critical value d_c at which the system loses its stability, the spectral gap eventually

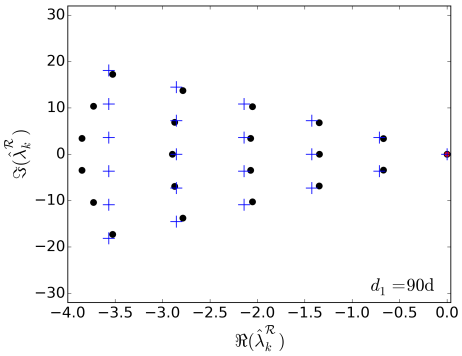

(a)

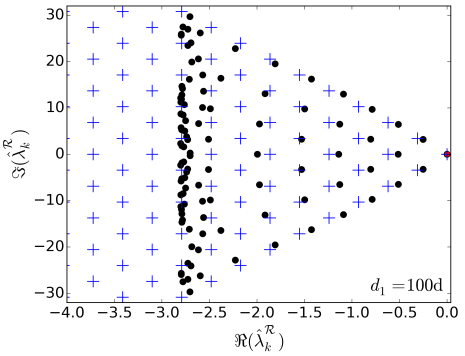

(b)

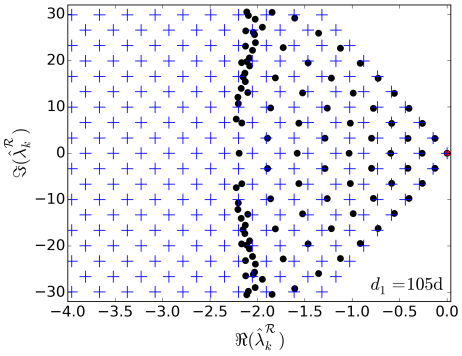

(c)

Figure 3.2: Leading reduced ergodicity eigenvalues (solid black dots) for the stochastic linear delayed oscillator (3.10) for a delay d_1 of (a) 90 days, (b) 100 days and (c) 105 days. The eigenvalues were approximated from transition matrices on the two-dimensional reduced space Y for a lag of 0.1 yr on a grid of 200-by-200 boxes spanning a square of ±4 standard deviations in both directions. The leading ergodicity eigenvalues calculated from formula (3.9) of conjecture 1 are also represented as blue pluses.

vanishes and any perturbation can result in a dramatic change in the statistics of the system (Gaspard et al., 1995). On the other hand, in the stochastic case considered here, noisy perturbations continuously perturb the deterministic part of the dynamics so that the system can become unstable before the spectral gap in the ergodicity eigenvalues has vanished (a more detailed discussion of this effect is given in the next section 3.3).

Remark 14. *That the quality of the estimation of the leading reduced ergodicity eigenvalues may be improved by increasing the lag τ. To the contrary, reduced ergodicity eigenvalues farther from the imaginary axis may be accessed by decreasing the lag (in which case the grid resolution should also be increased). A compromise should thus be found in choosing the lag τ for which the reduced transition matrix is estimated. One can also notice that the imaginary parts of the eigenvalues with large imaginary parts as well as the real parts of eigenvalues with large real parts tend to be underestimated.*

Remark 15. *That the reduced ergodicity eigenvalues agree so well with the analytical ones, even though the approximation is done on a two-dimensional space, can be understood by the fact that the dynamics are dominated by the leading complex pair of eigenvalues of the linear operator $\mathscr{A}$, which is separated from the rest of the spectrum and is associated with two eigenvectors spanning a two-dimensional space.*

3.2.3.3 *Ergodicity eigenvectors*

We have seen in chapter 2 that the forward ergodicity eigenvectors ψ_k^f, for the semigroup of transfer operators $\mathscr{L}_t$ w.r.t. the invariant measure, could be approximated by the left-eigenvectors of the reduced transition matrix $\hat{\mathbf{P}}_\tau^{\mathscr{R}}$ divided by its stationary density $\hat{\mathbf{m}}$, denoted $\psi_k^{\mathscr{R},f}(\tau)$, and that the backward ergodicity eigenvectors ψ_k^b by the right-eigenvectors of $\hat{\mathbf{P}}_\tau^{\mathscr{R}}$, denoted $\psi_k^{\mathscr{R},b}(\tau)$. Figure 3.3 represents the real parts of the leading reduced ergodicity eigenvectors $\psi_k^{\mathscr{R},f}(\tau)$ and $\psi_k^{\mathscr{R},b}(\tau)$ of the transition matrix $\hat{\mathbf{P}}_\tau^{\mathscr{R}}$ estimated above for a delay d_1 of 110 days (right before the loss of stability). As an exception, the first left-eigenvector of the transition matrix (fig. 3.3) is not divided by the stationary density $\hat{\mathbf{m}}$, which is thus represented. On the other hand, the first backward reduced ergodicity eigenvector $\psi_k^{\mathscr{R},b}(\tau)$ is the unique constant eigenvector, in agreement with the fact that $\hat{\mathbf{m}}$ is the unique stationary density, by construction. Moreover, recall from chapter 2 that if two observables f and g project strongly on the leading backward and forward ergodicity eigenvectors, respectively, then the correlation function $C_{f,g}(t)$ between these observables will decay slowly to zero, so that the mixing time is long. Here, only the real parts of the eigenvectors are plotted, because only real-valued observables are considered.

The represented eigenvectors reveal some interesting features. Firstly, the approximated stationary density, panel (a), is similar to that of the OU of section 2.3 (fig. 2.3(b))

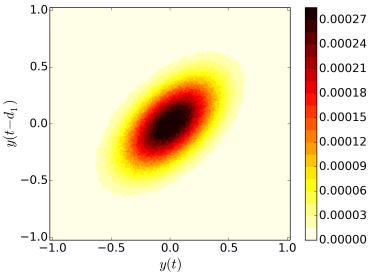

(a)

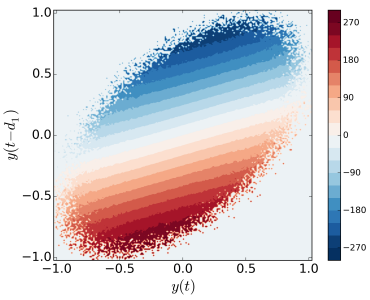

(b)

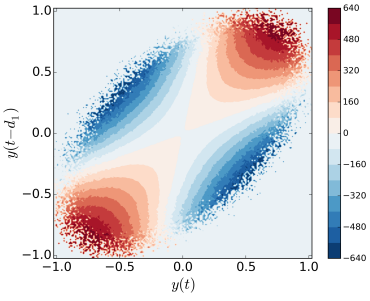

(c)

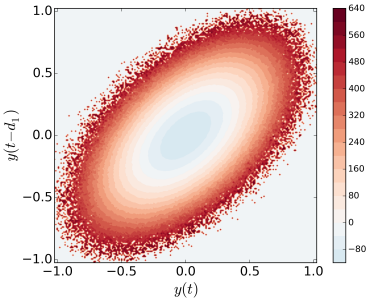

(d)

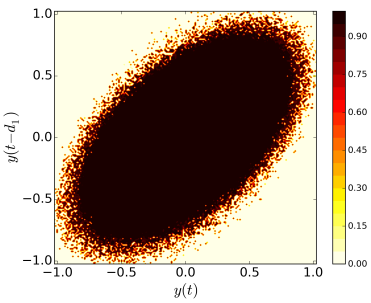

(e)

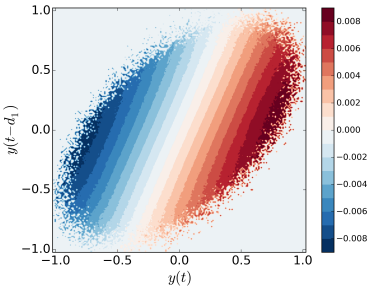

(f)

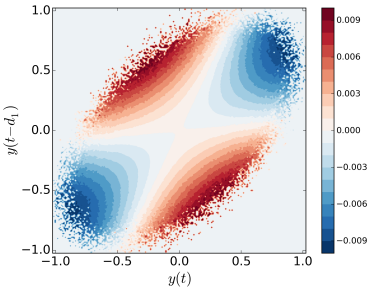

(g)

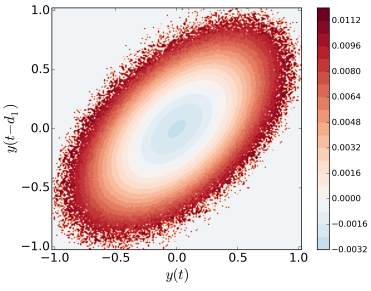

(h)

Figure 3.3: Real parts of the first four forward (left) and backwards (right) reduced ergodicity eigenvectors associated with the reduced ergodicity eigenvalues of figure 3.2 for the linear stochastic delayed oscillator (3.10) with a delay d_1 of 105 days. As an exception, panel (a) represents the stationary density $\hat{\mathbf{m}}$ of $\hat{\mathbf{P}}_\tau^{\mathscr{R}}$.

and both resemble a bivariate normal distribution. Moreover, the reduced ergodicity eigenvectors are qualitatively similar to polynomials in two dimension restricted to a compact support. This is in agreement with the results of Metafune et al. (2002, Section 3), who showed that the (generalized) ergodicity eigenvectors of a d dimensional OU are polynomials forming a complete orthogonal basis of $L^p_\mu(\mathbb{R}^d)$, $1 < p \leq +\infty$. Furthermore, eigenvectors associated to ergodicity eigenvalues farther from the imaginary axis have a smaller scale in the radial direction, while eigenvectors associated to ergodicity eigenvalues farther from the real axis have a smaller scale in the tangential direction. Interestingly, we will see in the following sections, that these ergodicity eigenvectors differ from those of nonlinear systems, allowing to distinguish a linear system from a nonlinear one.

Remark 16. *Even though each panel of figure 3.3 has a bounding box of the size of the domain of the grid on which the transition matrices are estimated, both the forward and backward reduced ergodicity eigenvectors have a compact support smaller than the size of the grid. In the presence of noise, however, their support is not expected to be bounded. As explained in remark 10 of chapter 2, this is a limitation of the numerical method used here which is due to the finite length of the time series used to estimate the transition matrices, implying that the region of the phase space covered by grid boxes which are not empty of realizations is compact.*

Remark 17. *As for Principal Component Analysis (PCA, e.g. von Storch and Zwiers, 1999, Chap. 13), care should be taken in the physical interpretation of the ergodicity eigenvectors, since each of them cannot be directly associated with a specific physical process. For example, the leading ergodicity eigenvalues represented in figure 3.4 are all associated with the leading complex pair of eigenvalues of the linear operator $\mathscr{A}$ and do not correspond to distinct physical processes.*

3.3 ANALYTICAL RESULTS ON THE ERGODICITY SPECTRUM OF THE STOCHASTIC HOPF

Before to analyze the ergodicity spectrum of the stochastic nonlinear oscillator and of the Zebiak-Cane model, both undergoing a Hopf bifurcation, we first study the changes in the ergodicity spectrum in a simple form of Hopf bifurcation. To our knowledge, the ergodicity spectrum of the Hopf bifurcation has only been studied in the deterministic case (Gaspard and Tasaki, 2001), most likely because the normal form of the stochastic Hopf is complicated (Arnold, 2003). However, we will see in this section that much can be learned about the ergodicity spectrum of a system undergoing a stochastic Hopf bifurcation from an analytical study of the Fokker-Planck equation associated with a simple form of stochastic Hopf. For this purpose, an SDE is derived by adding noise to the normal form of the deterministic Hopf bifurcation. This leads to a nonlinear Fokker-Planck equation which we do not attempt to solve directly. Instead, we make the approximation that the noise level is weak with respect to the radius

of the periodic orbit, and decompose the problem in the tangential direction and in the radial direction. The tangential problem corresponds to an advection-diffusion equation on the circle which can be solved analytically, while the problem in the radial direction is similar to that of the pitchfork bifurcation considered by Gaspard et al. (1995). While these results are not complete, they will prove very useful to give an interpretation to the ergodicity spectrum of the stochastic nonlinear delayed oscillator and of the Zebiak-Cane model, treated in the following sections 3.4 and 3.5, respectively.

3.3.1 *A simple form of the stochastic Hopf bifurcation*

Let us first derive a simple system undergoing a stochastic Hopf bifurcation. We start with the normal form of the Hopf bifurcation (Guckenheimer and Holmes, 1983) given by

$$\begin{aligned} dr &= \left(d\mu r + ar^3\right)dt \\ d\theta &= \left(\omega + c\mu + br^2\right)dt. \end{aligned} \tag{3.14}$$

To simplify the analysis (with a loss of generality which is not problematic for this study), we set $c = 0$, $b = d = 1$ and $a = -1$ (in order to consider the supercritical case). The parameter μ controls the stability of the invariant sets, while ω gives the angular frequency of infinitesimal oscillations (see also Strogatz, 1994). The ergodicity spectrum of the Hopf bifurcation as been studied analytically by Gaspard and Tasaki (2001) and we summarize some of their results here. For $\mu < 0$, only a stable fixed point exists with linear stability exponent $\mu \pm i\omega$ and the ergodicity eigenvalues are pyramidal, as for the OU and the linear delayed oscillator considered in sections 2.3 and 3.2, respectively. For $\mu > 0$, the fixed point becomes unstable and a stable periodic orbit Γ emerges with radius $R = \sqrt{\mu}$ and linear stability exponent $\gamma = -2\mu$. The ergodicity eigenvalues constitute an array of eigenvalues parallel to the imaginary axis, with their imaginary parts separated by a gap equal to the angular frequency ω and their real parts separated by the linear stability exponent γ. On top of this lies a pyramid of eigenvalues associated with the unstable fixed point (Gaspard and Tasaki, 2001, figure 2 and 3). In this case, the system is not mixing (cf. section 2.1), since the ergodicity eigenvalue zero is not the only one to have vanishing real part. Instead, there are infinitely many complex conjugate pairs of ergodicity eigenvalues lying on the imaginary axis, which correspond to the fundamental of the periodic orbit and its harmonics. That the system is not mixing can be understood by the fact that the dynamics along Γ is neutral (i.e neither contracting nor expanding) so that a distribution with support Γ is simply rotated by the dynamics but do not converge to the invariant measure (while a distribution transverse to Γ is attracted to Γ, hence the various lines of eigenvalues with non-vanishing real part parallel to the imaginary axis in Gaspard and Tasaki, 2001, figure 3).

With the addition of noise, however, a distribution supported by the attractor is diffused along and across the attractor, so that this distribution is expected to converge to the invariant measure at a rate dependent on the noise intensity and the radius R of Γ as well as on on the linear stability exponent γ of Γ. Thus, a typical system undergoing a Hopf bifurcation in the presence of noise is expected to be mixing, so that no other ergodicity eigenvalue than zero should lie on the imaginary axis.

For a more quantitative analysis, let us consider the normal form (3.14) with the addition of noise on each Cartesian coordinates $x = r\cos\theta$ and $y = r\sin\theta$, such that

$$\begin{aligned} dx = &\quad \big[(\mu - x^2 + y^2)x - \omega y\big]dt + q dW_1 \\ dy = &\quad \big[\omega x + (\mu - x^2 + y^2)y\big]dt + q dW_2, \end{aligned}$$

where W_1 and W_2 are two independent Wiener processes. By the change of variables to polar coordinate, the right hand side becomes

$$\begin{aligned} dx = &\quad \big[(\mu r - r^3)\cos\theta - \omega r\sin\theta\big]dt + q dW_1 \\ dy = &\quad \big[(\mu r - r^3)\sin\theta + \omega r\cos\theta\big]dt + q dW_2. \end{aligned}$$

Then, expanding the radius r with respect to x and y, considering that $(dW_i)^2 = dt$ is a first order differential and that $dW_1 dW_2 = 0$, one gets the differential

$$\begin{aligned} dr = &\quad \tfrac{\partial r}{\partial x}dx + \tfrac{\partial r}{\partial y}dy + \tfrac{1}{2}\tfrac{\partial^2 r}{\partial x^2}(dx)^2 + \tfrac{1}{2}\tfrac{\partial^2 r}{\partial y^2}(dy)^2 \\ d\theta = &\quad \tfrac{\partial \theta}{\partial x}dx + \tfrac{\partial \theta}{\partial y}dy + \tfrac{1}{2}\tfrac{\partial^2 \theta}{\partial x^2}(dx)^2 + \tfrac{1}{2}\tfrac{\partial^2 \theta}{\partial y^2}(dy)^2. \end{aligned} \tag{3.15}$$

Injecting $r = \sqrt{x^2 + y^2}$ and $\theta = \arctan(y/x)$ in (3.15) gives

$$\begin{aligned} dr = &\quad (\mu r - r^3)dt + q\cos\theta dW_1 + q\sin\theta dW_2 + \tfrac{q^2}{2r}dt \\ d\theta = &\quad \omega dt - \tfrac{q}{r}\sin\theta dW_1 + \tfrac{q}{r}\cos\theta dW_2. \end{aligned}$$

Thus, the system (3.14) with noise satisfies the SDE

$$d\eta = F(\eta)\,dt + \Sigma(\eta)\,dW \tag{3.16}$$

$$\text{with} \quad F(\eta) = \begin{pmatrix} \mu r - r^3 + \frac{q^2}{2r} \\ \omega \end{pmatrix}$$

$$\text{and} \quad \Sigma(\eta) = q\begin{pmatrix} \cos\theta & \sin\theta \\ -\frac{\sin\theta}{r} & \frac{\cos\theta}{r} \end{pmatrix},$$

where $\eta = (r, \theta)^T$ and $dW = (dW_1, dW_2)^T$. We can see that the noise is responsible for an additional drift term $\frac{q^2}{2r}$ in the radial direction. This term can be understood

by visualizing a periodic orbit Γ of radius R centered at O in the Oxy plane and figuring the impact of noise acting on the Ox direction on an initial state positioned at $(0,R)$ (i.e the noise is tangential to Γ at the position of the initial state on top of Γ). Whether the realizations of the noise are negative or positive, they will act as a centrifugal force pushing the state away from the center of Γ, with an average intensity increasing with the noise level q and with the curvature $1/R$ of Γ. On the other hand, the average effect of the noise in the tangential direction vanishes so that no additional drift appears in this direction. As a result, by taking $F(\eta) = 0$, one finds that, for any value of μ, there exists a periodic orbit Γ with radius $R = \sqrt{(\mu + \sqrt{\mu^2 + 2q^2})/2}$.

3.3.2 *Ergodicity spectrum of the stochastic Hopf*

The next step is to derive the Fokker-Planck equation associated with the SDE (3.16) (see chapter 2 and also Lasota and Mackey, 1994; Gardiner, 2009). The diffusion matrix is such that

$$\Sigma(\eta)\Sigma(p)^T = \begin{pmatrix} 1 & 0 \\ 0 & 1/r^2 \end{pmatrix},$$

so that it depends only on the radius. The Fokker-Planck equation for densities w.r.t. the Lebesgue measure is thus given by

$$\begin{aligned} \frac{\partial \rho(r,\theta)}{\partial t} = \quad & -\frac{\partial}{\partial r}\left[\left(\mu r - r^3 + \frac{q^2}{2r}\right)\rho(r,\theta)\right] - \frac{\partial}{\partial \theta}\left(\omega \rho(r,\theta)\right) \\ & + \frac{q^2}{2}\frac{\partial^2 \rho(r,\theta)}{\partial r^2} + \frac{1}{2}\left(\frac{q}{r}\right)^2 \frac{\partial^2 \rho(r,\theta)}{\partial \theta^2}, \end{aligned} \tag{3.17}$$

where the first line of the right hand side is the drift, with both a deterministic and a stochastic contribution and the second line is the diffusion. This is a parabolic Partial Differential Equation (PDE) with variable coefficients so that finding all the solutions of this equation is a very difficult problem. However, much can be said about the spectrum of the generator $\mathscr{G}$ defined by the right hand side of the Fokker-Planck equation (3.17). First, the density $p(r,\theta)$ of the invariant measure μ w.r.t. the Lebesgue measure is independent θ. Indeed, one can write the drift $\mu r - r^3 + q^2/(2r)$ in gradient form $-\frac{\partial}{\partial r}U(r)$, with a potential $U(r) = -\mu r^2/2 + r^4/4 - q^2 \log(r)/2$ depending only on the radius. The stationary solution of the Fokker-Planck equation for such systems is given by (Gardiner, 2009, Chap. 5.5)

$$p(r) = N e^{-U(r)/\sigma},$$

where N is a normalization constant and σ the diffusion coefficient equal to $q^2/2$, in our case. Thus, the stationary density of the SDE (3.16) is given by

$$p(r) = N r e^{\frac{\mu}{q^2} r^2 - \frac{r^4}{2q^2}},$$

To go further in unraveling the spectral properties of the Fokker-Planck equation (3.17), we decompose the generator $\mathscr{G}$ in a radial and an tangential component, as such

$$\begin{aligned} \mathscr{G} = & \quad \mathscr{G}_r + \mathscr{G}_\theta \\ \text{with} \quad \mathscr{G}_r u(r) = & \quad -\tfrac{\partial}{\partial r}\left[\left(\mu r - r^3 + \tfrac{q^2}{2r}\right)u(r)\right] + \tfrac{q^2}{2}\tfrac{\partial^2 u(r)}{\partial r^2}, \qquad (3.18) \\ \text{and} \quad \mathscr{G}_\theta v(\theta) = & \quad -\tfrac{\partial}{\partial \theta}\left(\omega v(\theta)\right) + \tfrac{1}{2}\left(\tfrac{q}{r}\right)^2 \tfrac{\partial^2 v(\theta)}{\partial \theta^2}. \qquad (3.19) \end{aligned}$$

The key step of our study is to notice that, if not for the term $(q/r)^2$ in front of the second order derivative in θ, the eigenvalues of $\mathscr{G}$ would be given by combinations of the eigenvalues of the radial operator $\mathscr{G}_r$ and of the tangential operator $\mathscr{G}_\theta$, while its eigenvectors would be given by products of their eigenvectors of $\mathscr{G}_r$ and $\mathscr{G}_\theta$. However, assuming that the control parameter μ is very large compared to the noise level q, so that the periodic orbit is very stable and noisy fluctuations transverse to it small, one can approximate the term $(q/r)^2$ in front of $\frac{\partial^2 \rho(r,\theta)}{\partial \theta^2}$ by the constant $(q/R)^2$, where R is the radius of the periodic orbit Γ. As a consequence, assuming in the following that $\mu/q^2 >> 1$, the spectrum of the generator $\mathscr{G}$ can be studied by calculating the spectra of each component $\mathscr{G}_r$ and $\mathscr{G}_\theta$ separately.

Remark 18. *Here, the spectral properties of the generator $\mathscr{G}$ of the semigroup of transfer operators $\mathscr{P}_t, t \geq 0$ acting on densities w.r.t. the Lebesgue measure are studied rather than that of the generator $\mathscr{G}_\mu$ of the semigroup of transfer operators $\mathscr{L}_t, t \geq 0$ acting on densities w.r.t. the invariant measure μ. This choice comes from the fact that the complete ergodicity spectrum will be calculated form the the Fokker-Planck equation (3.17) allowing to make some comparisons with the results obtained in the deterministic case by Gaspard and Tasaki (2001).*

3.3.2.1 *Ergodicity spectrum for the tangential operator $\mathscr{G}_\theta$*

The spectrum of the tangential operator $\mathscr{G}_\theta$ is the most accessible. Indeed, the latter is the infinitesimal generator of the advection-diffusion equation with periodic boundary conditions

$$\begin{aligned} \frac{\partial v(\theta)}{\partial t} = & \quad -\omega \tfrac{\partial}{\partial \theta} v(\theta) \quad + D\frac{\partial^2 v(\theta)}{\partial \theta^2} \qquad (3.20) \\ v(-\pi) = & \quad v(\pi) \\ \frac{\partial v(-\pi)}{\partial \theta} = & \quad \tfrac{\partial v(\pi)}{\partial \theta} \\ v(0,\theta) = & \quad v_0. \end{aligned}$$

where ω plays the role of a constant velocity and $D = \frac{1}{2}\left(\frac{q}{R}\right)^2$ is the diffusion coefficient. The solutions of this linear equation are known to take the form

$$v(\theta, t) = \sum_{k=-\infty}^{+\infty} h_k e^{(-Dk^2 + ik\omega)t} e^{-ik\theta}, \tag{3.21}$$

where the $h_k = -h_{-k}$ are determined by the initial condition v_0. Thus, the ergodicity eigenvalues, forward eigenvectors and backward eigenvectors corresponding to (3.19) are respectively given by

$$\begin{aligned} \lambda_{\theta,k} &= -k^2 \tfrac{1}{2}\left(\tfrac{q}{R}\right)^2 + ik\omega, \quad k \in \mathbb{Z} \\ \psi^f_{\theta,k}(\theta) &= e^{-ik\theta}/\sqrt{2\pi} \\ \psi^b_{\theta,k}(\theta) &= \psi^f_{\theta,k}(\theta). \end{aligned} \tag{3.22}$$

One can see that the real part of the kth eigenvalue $\lambda_{\theta,k}$ of $\mathscr{G}_\theta$ is proportional to the square of its rank k and to the square of the ratio of the noise level q with the radius R of Γ, while the imaginary part of $\lambda_{\theta,k}$ corresponds to the kth harmonic of the fundamental ω. Moreover, the eigenvectors are not dependent on the noise level q. Thus, the more intense the noise relatively to the radius of the periodic orbit, the stronger the mixing. In particular, taking q equal to 0, one recovers the family of ω-spaced purely imaginary eigenvalues of the non-mixing deterministic case (Gaspard and Tasaki, 2001).

Remark 19. *The first forward eigenvector gives the density of the invariant measure w.r.t. the Lebesgue measure. Here, it is constant, indicative that the Lebesgue measure is invariant for the advection-diffusion equation with periodic boundary conditions. This is in agreement with the fact that the dynamics on the periodic orbit is neutral. That is, there is no contraction nor expansion so that volumes are preserved as for conservative systems.*

Remark 20. *Even though the periodic orbit is circular, so that the correlation spectrum would reveal only one peak at the fundamental, ergodicity eigenvalues are found at the positions of every harmonics. The reason is that these eigenvalues are associated with the normal modes of (3.22). That a single peak at the fundamental frequency is visible for a trajectory along a circular periodic orbit Γ is due to the fact that the coordinates $(x(t), y(t)) = (R\cos\theta(t), R\sin\theta(t))$ parametrizing Γ are orthogonal to all but the second pair of conjugate eigenvectors.*

3.3.2.2 *Ergodicity spectrum for the radial operator $\mathscr{G}_r$*

The derivation of the spectrum of the radial operator $\mathscr{G}_r$ is more involved and will be carried only partially. We start by neglecting the diffusion term $\frac{q^2}{2}\frac{\partial^2 u(r)}{\partial r^2}$ in (3.18),

so that $\mathscr{G}_r$ reduces to the infinitesimal operator of the Liouville equation induced by the ODE

$$\begin{aligned} \frac{\partial r}{\partial t} = &\quad \mu r - r^3 + \tfrac{q^2}{2r} = F_r(r) \\ r(0) = &\quad r_0, \quad r_0 \in (0, +\infty). \end{aligned} \tag{3.23}$$

From the change of variable $s = r^2$ and using partial fractions, one finds that the solution $\phi_r(t)r$ of (3.23) for the initial condition r, is given by

$$\phi_r(t)r = \sqrt{\frac{s_+ - s_- \frac{r^2 - s_+}{r^2 - s_-} e^{\gamma t}}{1 - \frac{r^2 - s_+}{r^2 - s_-} e^{\gamma t}}}, \quad t \geq 0,$$

with $s_\pm = \frac{\mu \pm \sqrt{\mu^2 + 2q^2}}{2}$ and $\gamma = -2\sqrt{\mu^2 + 2q^2}$. One has that s_+ is the square of the fixed point R for (3.23) (i.e the radius of Γ) and γ is the linear stability exponent of (3.23) at R. We can see that, due to the addition of noise, the periodic orbit exists for any μ in $\mathbb{R}$ and that its stability increases with q. The latter can be understood by the fact that for $r < R$ the additional drift term $\frac{q^2}{2r}$ vigorously pushes the state towards the periodic orbit, while for $r > R$, it pushes the state away from the periodic orbit, but much more weakly.

Following the methodology of Gaspard et al. (1995), the next step to calculate the ergodicity spectrum corresponding to (3.23), is to find a decomposition in exponentials of time of the average at time t of g with respect to an initial density ρ_0, given by

$$\langle \rho_0, g \circ \phi_r \rangle = \int_0^{+\infty} \rho_0(r) g(\phi_r(t)r) dr.$$

To do so, we proceed by expanding $g(\phi_r(t)r)$ with respect to the variable $\xi = \frac{r^2 - s_+}{r^2 - s_-} e^{\gamma t}$ at $\xi = 0$ (i.e. where $r = R$), which yields

$$g(\phi_r(t)r) = \sum_{n=0}^{\infty} \frac{\xi^n}{n!} \frac{d^n}{d\xi^n} g\left(\sqrt{\frac{s_+ - s_- \xi}{1 - \xi}} \right) \Bigg|_{\xi=0}.$$

Next, taking the average of $g(\phi_r(t)r)$ with respect to ρ_0 at time t gives

$$\begin{aligned} \langle \rho_0, g \circ \phi_r \rangle = &\quad \textstyle\sum_{k=0}^{\infty} e^{k\gamma t} \left[\int_0^{+\infty} \frac{1}{n!} \left(\frac{r^2 - s_+}{r^2 - s_-} \right)^n \rho_0(r) dr \right] \\ &\left[\int_0^{+\infty} g(r) \frac{d^n}{\xi^n} \delta\left(r - \sqrt{\tfrac{s_+ - s_- \xi}{1 - \xi}} \right) \Big|_{\xi=0} dr \right], \end{aligned} \tag{3.24}$$

where δ is the Dirac distribution. We thus have obtained a spectral decomposition of the semigroup generated by the radial operator $\mathscr{G}_r$ and the ergodicity eigenvalues, forward eigenvectors and backward eigenvectors corresponding to (3.23), are respectively given by

$$\begin{aligned}
\lambda_{r,k} = &\quad k\gamma = -2k\sqrt{\mu^2+2q^2}, \quad k \in \mathbb{N} \\
\psi^f_{r,k}(r) = &\quad \tfrac{d^n}{\xi^n}\delta\left(r - \sqrt{\tfrac{s_+ - s_- \xi}{1-\xi}}\right)\Big|_{\xi=0} \\
\psi^b_{r,k}(r) = &\quad \tfrac{1}{n!}\left(\tfrac{r^2-s_+}{r^2-s_-}\right)^n.
\end{aligned}$$

As a result, the ergodicity eigenvalues $\lambda_{r,k}, k \in \mathbb{N}$ are given by multiples of the linear stability exponent $\gamma = -2\sqrt{\mu^2+2q^2}$, so that the gap between them increases with the control parameter μ and the noise level q. As a matter of fact, the more stable the periodic orbit, the faster do probability densities converge to the invariant distribution $\delta(r-R)$ (associated with the fixed point at the radius of the periodic orbit).

So far, our analysis of the spectrum of the radial operator $\mathscr{G}_r$ has neglected the diffusion term $\frac{q^2}{2}\frac{\partial^2 g(r)}{\partial r^2}$ in (3.18). This term is a second order partial derivative so that (3.18) constitutes a Sturm-Liouville problem difficult to solve analytically. However, the effect of the addition of the diffusion can be described at least qualitatively. First of all, when the nonlinear drift F_r of the the radial component (3.18) of the Fokker-Planck equation is linearized at R as $\tilde{F}_r(r) = \gamma r$ (with $r \in \mathbb{R}$ for convenience), one is left with an OU as studied in chapter 2. By the change of variable $z^2 = -\frac{\gamma}{q^2}r^2$ and by multiplying the eigenvalue problem $\mathscr{G}_r\psi^f_{r,k} = \lambda_k\psi^f_{r,k}$ by e^{-z^2}, one is left with a differential equation whose solutions are Hermite polynomials. It follows that the ergodicity spectrum of the linearized radial operator $\mathscr{G}_r$ is given by

$$\begin{aligned}
\lambda_{r,k} = &\quad k\gamma = -2k\sqrt{\mu^2+2q^2}, \quad k \in \mathbb{N} \\
\psi^f_{r,k}(r) = &\quad N_k H_k(-\gamma r/q)e^{-\frac{\gamma r^2}{q^2}} \\
\psi^b_{r,k}(r) = &\quad N_k^* H_k(-\gamma r/q),
\end{aligned} \tag{3.25}$$

where H_k is the kth physicists' Hermite polynomial and N_k and N_k^* are normalization constants. We have seen in section 2.3 that the noise level has no impact on the ergodicity eigenvalues of an OU. On the other hand, the singularities in the deterministic forward eigenvectors are smoothed by the diffusion, so that Dirac distributions are changed to Hermite polynomials with increasing spatial scale, as the noise level is increased (see also Gaspard et al., 1995). Here, the invariant density is given by the Gaussian $N_1\exp(-\frac{\gamma r^2}{q^2})$, by which the forward eigenvectors $\psi^f_{r,k}$ should be divided the get the eigenvectors with respect to the invariant measure.

Furthermore, it has recently been shown by Lan and Mezić (2013), for deterministic systems with a hyperbolic fixed point (or a periodic orbit), that the ergodicity eigenvalues of the nonlinear system are identical to the ergodicity eigenvalues of the linearization around the fixed point. However, this result is no longer true in the presence of noise. Indeed, in the stochastic case, the net effect of nonlinear terms of the form $-r^{2p+1}, p \in \mathbb{N}^*$ is to pull trajectories or densities towards the invariant measure at a faster rate than a linear term such as $-r$ would do, when $r > 1$. Thus, the addition of a nonlinear term $-r^{2p+1}$ to a linear system has the effect of pushing the ergodicity eigenvalues farther away from the imaginary axis as the noise level q is increased (as can be seen from the numerical results of Gaspard et al., 1995). In conclusion, one would expect the eigenvalues of $\mathscr{G}_r$ (in the nonlinear stochastic case) to be of the form

$$\lambda_k^r = -2k\sqrt{\mu^2 + 2q^2} - \mathscr{O}(q^2), \quad k \in \mathbb{N}. \tag{3.26}$$

To recapitulate, assuming that $\mu/q^2 >> 1$, the ergodicity eigenvalues associated with the Fokker-Planck equation (3.17) of the simple SDE (3.16) for the stochastic Hopf bifurcation can be obtained by summing pairwise each eigenvalue of the radial operator $\mathscr{G}_r$ with each eigenvalue of the tangential operator $\mathscr{G}_\theta$ calculated separately from (3.22) and (3.26), respectively. As for the ergodicity eigenvectors, they can be calculated as products of those of $\mathscr{G}_r$ and $\mathscr{G}_\theta$. These spectra will be used in the following sections 3.4 and 3.5 to interpret the reduced ergodicity spectra estimated for the stochastic nonlinear delayed oscillator and the stochastic Zebiak-Cane model, respectively.

3.4 APPLICATION TO THE STOCHASTIC NONLINEAR DELAYED OSCILLATOR

In light of the results on the ergodicity spectrum of the linear version of the stochastic delayed oscillator (3.10) analyzed in section 3.2.3 and of the stochastic Hopf calculated in the previous section 3.3, we now study the ergodicity spectrum of the nonlinear version

$$dy(t) = \big(a_0 y(t) + c_0 y(t)^3 + a_1 y(t - d_1)\big)\,dt + q\,dW(t), \tag{3.27}$$

of the stochastic delayed oscillator. The same values of a_0, a_1 and q are taken as for the linear case of section 3.2.3, with $a_0 = 2.2\ \mathrm{yr}^{-1}$, $a_1 = -3.9\ \mathrm{yr}^{-1}$ and $q = 0.1$. The coefficient c_0 in front of the cubic term is arbitrarily set to $-1\ \mathrm{yr}^{-1}$. Due to the third order term $c_0 y^3$ in (3.27), contrary to the linear delayed oscillator (3.10), stable solutions can exist for $a_0 > -a_1$ or for $d_1 > d_c$. Taking the left-hand side of (3.27) equal to 0, one finds that $y_0 = 0$ is a fixed point (as in the linear case) but that two other fixed points exist for $a_0 > -a_1$, given by

$$y_\pm = \pm\sqrt{-\frac{a_0 + a_1}{c_0}}. \tag{3.28}$$

The fixed point y_0 always exists, but gets unstable for $a_0 > -a_1$, independently of the delay. For $a_0 > -a_1$, the two symmetric fixed points y_- and y_+ emerge from the origin and are stable for small values of the delay d_1. Thus, a pitchfork bifurcation occurs at $a_0 = -a_1$ and the stability of the fixed points y_- and y_+ has been analyzed by Suarez and Schopf (1988).

Here, we are interested in the case where the instantaneous instability is smaller than the delayed damping, so that $a_0 < -a_1$, so that the fixed point y_0 is stable for short delays $d_1 < d_c$ as in section 3.2.3. When linearized around y_0, the deterministic part of the nonlinear delayed oscillator (3.27) reduces to the linear delayed oscillator of Battisti and Hirst (1989), studied in section 3.2. The characteristic equation (Dugard and Verriest, 1998, Chap. 1) of the deterministic part of (3.27) linearized around y_0 is thus given by

$$\gamma - a_0 - a_1 e^{-\gamma d_1} = 0, \tag{3.29}$$

so that the fixed point y_0 becomes unstable for $d_1 > d_c = \arccos(-a_0/a_1)/\sqrt{a_1^2 - a_0^2} \approx$ 110 days, with a characteristic period $P_{\gamma_c} = 2\pi/\sqrt{a_1^2 - a_0^2} \approx 2.0$ yr. Due to the stabilizing effect of the cubic term $c_0 y^3$, however, a Hopf bifurcation occurs at $d_1 = d_c$, so that a stable periodic orbit emerges for large delays $d_1 > d_c$. The period of the periodic orbit is determined by the relative strength of the positive feedback, measured by a_0, with respect to the strength of the delayed negative feedback, given by a_1. In physical terms, when the damping $-a_0$ is weak, e.g. when the effect of reflected Rossby waves is weak on the local anomaly, the oscillation takes more time to change phase so that its period is longer.

3.4.1 *Ergodicity eigenvalues*

One expects the ergodicity eigenvalues of the nonlinear stochastic delayed oscillator to be at least qualitatively similar to that obtained for the linear case in section 3.2.3 for a small delay $d_1 << d_c$ (i.e. far before the criticality) and to that obtained for the simple form of stochastic Hopf calculated in the previous section 3.3 for a large delay $d_1 << d_c$ (i.e. far after the criticality). However, for intermediate delays, we do not have access to the ergodicity spectrum of the stochastic nonlinear delayed oscillator analytically.

Instead, we apply the methodology of reduced transfer operators presented in chapter 2. The stochastic process governed by the SDDE (3.27) is simulated using the Euler-Maruyama scheme with a time step of 0.001 yr for 10^5 yr. We have seen in section 3.2.1 that an SDDE can be represented by an SDE on an (infinite-dimensional) Hilbert space $H = \mathbb{R}^d \times L^2([-d_1, 0), \mathbb{R}^d)$ (Da Prato and Zabczyk, 1996, Chap. 10). Thus, the transition matrices $\mathbf{P}_\tau^{\mathscr{R}}$ are estimated on a reduced space Y defined by the observation operator $\mathscr{R}$ such that $\mathscr{R}(X(t)) = (y(t), y(t-d_1))$, as for the linear case in section 3.2.3. The reduced space Y is discretized into 200-by-200 grid boxes

spanning ±4 standard deviations in both directions. The transition matrix $\mathbf{P}_\tau^{\mathscr{R}}$, giving a discrete approximation of the reduced transfer operator $\mathfrak{L}_\tau^{\mathscr{R}}$, is then estimated by the Maximum Likelihood Estimator (MLE) (2.16) for a lag τ of 0.05 yr. Finally, the reduced ergodicity eigenvalues $\hat{\lambda}_k^{\mathscr{R}}(\tau)$ are calculated according to (2.21), by taking the the complex logarithm divided by τ of the eigenvalues $\hat{\zeta}_k^{\mathscr{R}}(\tau), 1 \leq k \leq m$ of the estimated transition matrix $\hat{\mathbf{P}}_\tau^{\mathscr{R}}$.

The resulting spectra are represented in figure 3.4, for a lag d_1 of (a) 90 days (before the deterministic Hopf bifurcation), (b) 110 days (at the bifurcation), (c) 130 days and (d) 180 days (both after the bifurcation). The two horizontal dashed black lines at the bottom and the top of these plots represent the boundaries $\pm\pi/\tau$ of the imaginary parts of the approximated ergodicity eigenvalues, which arise from the fact that the imaginary part of the complex logarithm is calculated modulo 2π. In addition, the thin black line in panel (d) represents the linear regression to the reduced ergodicity eigenvalues of the parabola (3.22), obtained for the ergodicity eigenvalues of the tangential component $\mathscr{G}_\theta$ of the generator associated with the simple SDE (3.16) for the stochastic Hopf bifurcation.

On panel (a) of figure 3.4, a pyramidal array of eigenvalues reminiscent of that of the linear version of the delayed oscillator represented in figure 3.2 is found. This should not come as a surprise, since for such a short delay d_1 of 90 days compared to the noise level q, the fixed point y_0 of the deterministic nonlinear delayed oscillator (3.27) is strongly stable so that the dynamics is dominated by the linear terms. On the other hand, for a delay d_1 larger than 110 days (fig. 3.4(c,d)), the periodic orbit has emerged (as seen from the stationary density represented in the coming figure 3.7(a)). In particular, for the large delay d_1 of 180 days (fig. 3.4(d)), a single parabolic curve of eigenvalues is visible. As can be seen from the perfect fit of the thin black line to these eigenvalues, this result is in very good agreement with the analytical formula (3.22) found for the ergodicity eigenvalues corresponding to the tangential component of the simple form of stochastic Hopf. The regression coefficients yield a value of 3.6 yr^{-1} for the tangential pulsation ω and of 1.3 for the radius R, when taking $q = 0.1$. This value for R is in fact smaller than the radius of the periodic orbit (see fig. 3.7(a)). One possible explanation is that the noise level is effectively increased by the coarse-graining induced by the discretization of the reduced transfer operator $\mathfrak{L}_\tau^{\mathscr{R}}$ (see Froyland et al., 2013). Interestingly, for a smaller delay d_1 of 130 days (fig. 3.4(c)), three parabolic curves of eigenvalues are visible. This is explained by the fact the periodic orbit is less stable for $d_1 = 130$ days than for $d_1 = 180$ days, so that according to the analytical formula (3.26) obtained for the radial component of the simple form of stochastic Hopf for large delays, the gap between the real parts of the reduced ergodicity eigenvalues decreases with the delay (i.e. with the approach of the bifurcation). Finally, for the intermediate delay of 110 days (fig. 3.4(b)), the reduced ergodicity eigenvalues accumulate at the imaginary axis, and seems to constitute a smooth transition between the spectra for a delay d_1

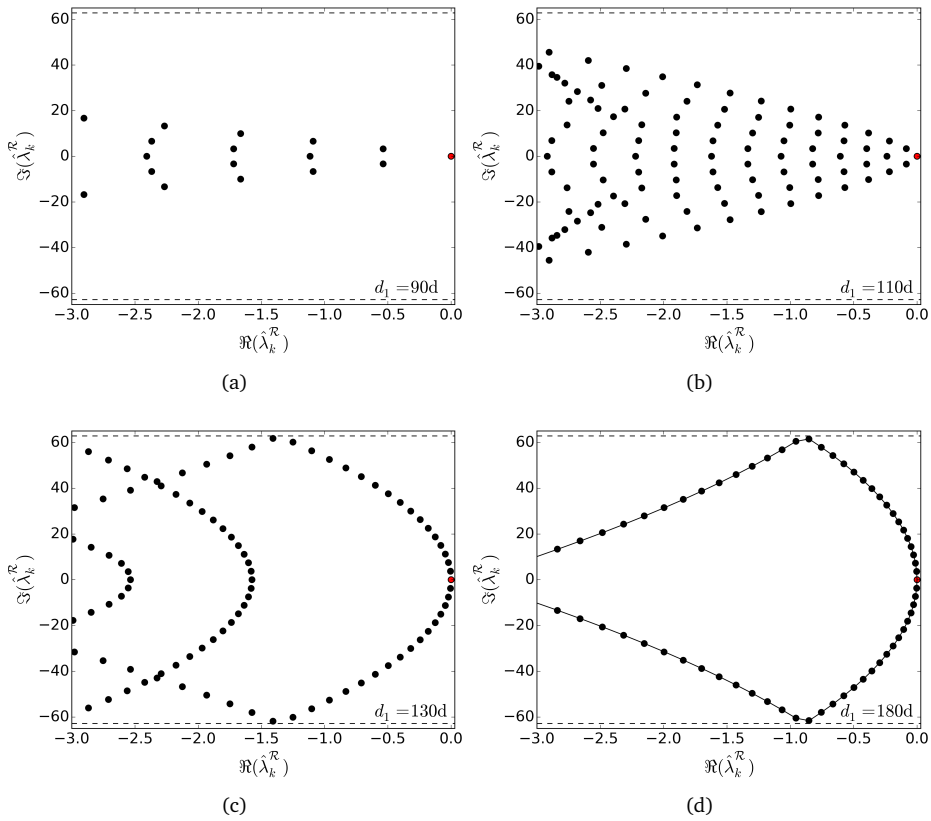

Figure 3.4: Reduced ergodicity eigenvalues of the stochastic nonlinear delayed oscillator (3.27) for a delay d_1 of (a) 90 days (before the deterministic Hopf bifurcation), (b) 110 days (at the bifurcation), (c) 130 days and (d) 180 days (both after the bifurcation). The eigenvalues were approximated from transition matrices on a two-dimensional reduced space with components $(y(t), y(t-d_1))$, for a lag of 0.05 yr on a grid of 200-by-200 boxes spanning a square of ±4 standard deviations in both directions.

shorter than the critical delay d_c and the spectra for $d_1 > d_c$. This approach of the reduced ergodicity eigenvalues to the imaginary axis is at the origin of the slowing down of the system at the approach of a criticality and is indicative of the weakening of its stability. We will see in the next section 3.5 that such reduced ergodicity spectra are also found for the stochastic Zebiak-Cane.

To conclude, the agreement of the reduced ergodicity eigenvalues for the stochastic nonlinear delayed oscillator (3.27) (fig. 3.4), with the analytical results of section 3.3 for the simple form of stochastic Hopf suggests that the method of approximation of the ergodicity spectrum stochastic evolution equations on a reduced space can provide a very powerful tool to study the evolution of statistics and the stability of dynamical systems.

3.4.2 *Ergodicity eigenvectors and correlation function*

To go further, let us now analyze the reduced ergodicity eigenvectors calculated from the transition matrices estimated in the previous subsection 3.4.1 and compare them with those obtained for the linear version of the stochastic delayed oscillator represented in figure 3.3. Figures 3.5, 3.6, and 3.7 represent the real parts of the leading forward (left panels) and backward (right panels) reduced ergodicity eigenvectors calculated from the estimated transition matrices $\hat{\mathbf{P}}_\tau^{\mathscr{R}}$, for a delay d_1 of 90 days (before the deterministic bifurcation), 110 days (at the bifurcation) and 130 days (after the bifurcation), respectively. Let us recall from chapter 2 that the forward reduced ergodicity eigenvectors $\psi_k^{\mathscr{R},f}(\tau)$ are calculated from the left eigenvectors of the transition matrix $\hat{\mathbf{P}}_\tau^{\mathscr{R}}$ divided by the stationary density $\hat{\mathbf{m}}$ with elements $\hat{m}_i = \#\{y_s \in B_i\}/\#\{y_s \in G\}$, while the backward reduced ergodicity eigenvectors $\psi_k^{\mathscr{R},b}(\tau)$ are calculated from the right eigenvectors of the transition matrix $\hat{\mathbf{P}}_\tau^{\mathscr{R}}$. Again, as an exception, panel (a) of each figure represents the stationary density $\hat{\mathbf{m}}$, itself. Recall also, from the spectral decomposition (2.11) of the correlation function, that if two observables project strongly on the leading backward and forward ergodicity eigenvectors, then their correlation function decays slowly to zero, so that the mixing time is long. Here, only the real part of the eigenvectors is plotted, because only real-valued observables will be considered.

Starting with the analysis of figure 3.5, for a small delay d_1 of 90 days, one can see that reduced ergodicity eigenvectors are similar to two-dimensional polynomials with compact support. This is in agreement with the fact that, for a small delay d_1 w.r.t the noise level q, the fixed point y_0 is strongly stable and the cubic term in (3.27) weak. Thus the system reduces to the stochastic linear delayed oscillator (3.10), which can be extended to an infinite-dimensional OU for which the eigenvectors of the leading part of the spectrum is indeed expected to be given by polynomials (Metafune et al.,

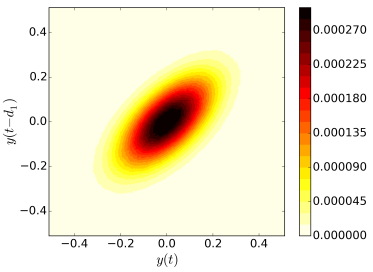

(a)

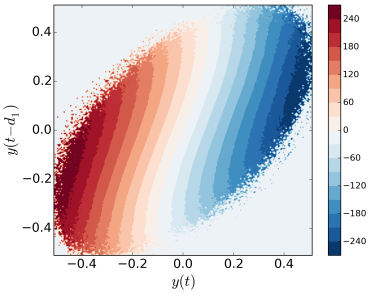

(b)

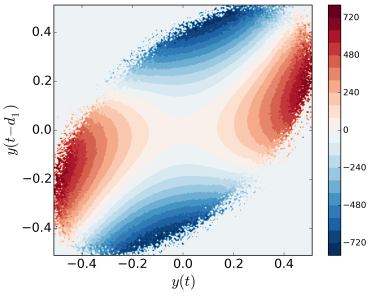

(c)

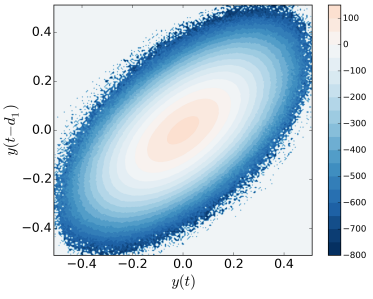

(d)

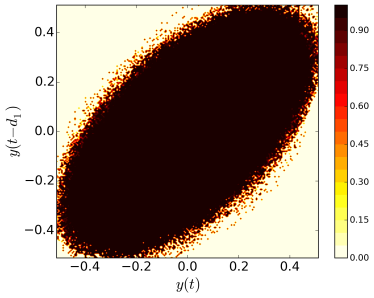

(e)

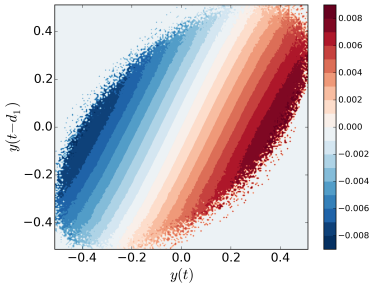

(f)

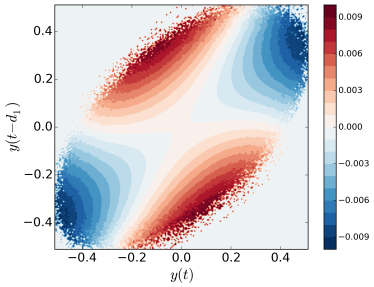

(g)

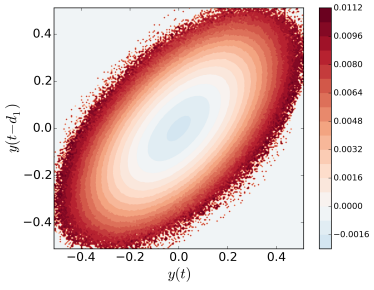

(h)

Figure 3.5: Real part of the first four forward (left) and backward (right) reduced ergodicity eigenvectors associated with the reduced ergodicity eigenvalues of figure 3.4(a), for the nonlinear stochastic delayed oscillator (3.27) with a delay d_1 of 90 days. As an exception, panel (a) represents the stationary density $\hat{\mathbf{m}}$ of $\hat{\mathbf{P}}_\tau^{\mathscr{R}}$.

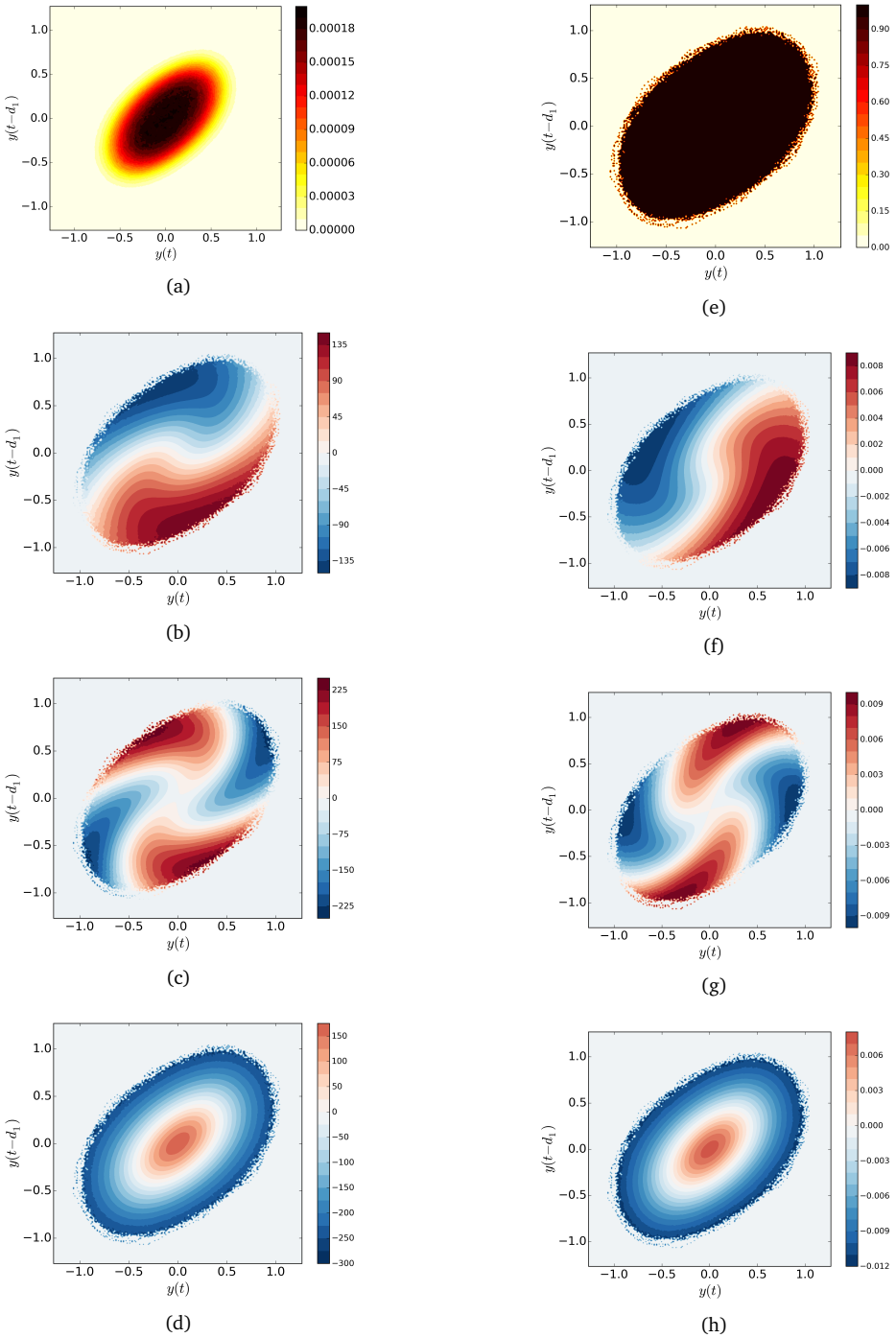

Figure 3.6: Real part of the first four forward (left) and backward (right) reduced ergodicity eigenvectors associated with the reduced ergodicity eigenvalues of figure 3.4(b), for the nonlinear stochastic delayed oscillator (3.27) with a delay d_1 of 110 days. As an exception, panel (a) represents the stationary density $\hat{\mathbf{m}}$ of $\hat{\mathbf{P}}_\tau^{\mathscr{R}}$.

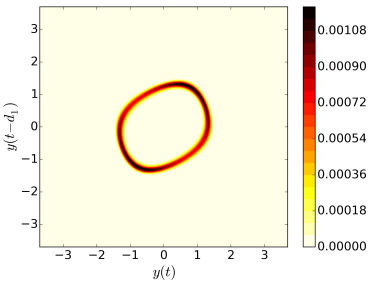

(a)

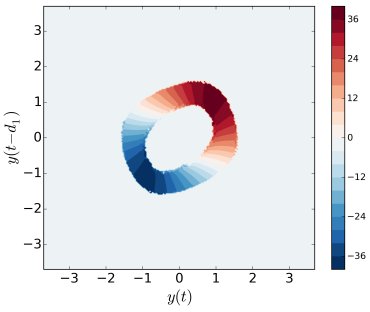

(b)

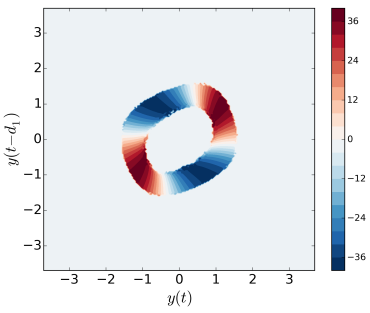

(c)

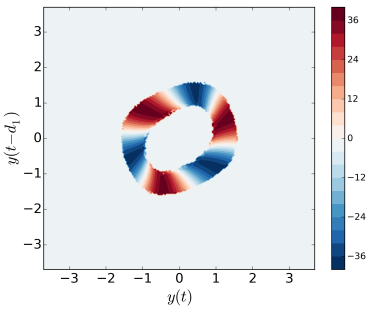

(d)

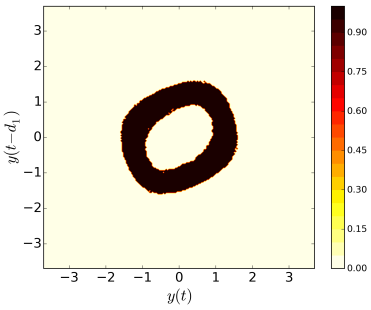

(e)

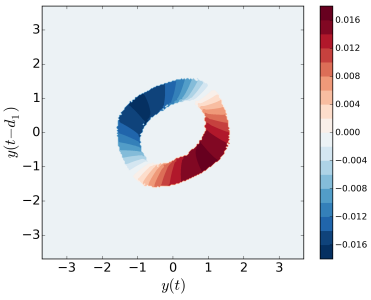

(f)

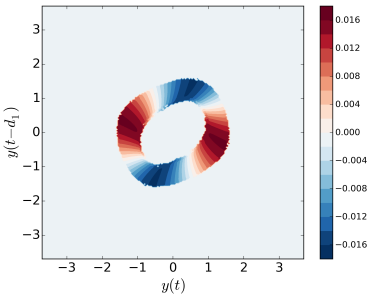

(g)

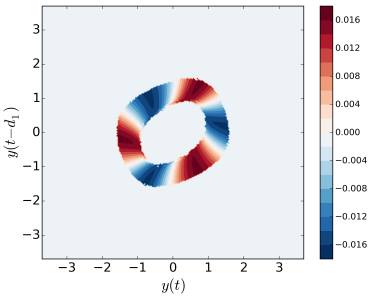

(h)

Figure 3.7: Real part of the first four forward (left) and backward (right) reduced ergodicity eigenvectors associated with the reduced ergodicity eigenvalues of figure 3.4(c), for the nonlinear stochastic delayed oscillator (3.27) with a delay d_1 of 130 days. As an exception, panel (a) represents the stationary density $\hat{\mathbf{m}}$ of $\hat{\mathbf{P}}_\tau^{\mathscr{R}}$.

2002). (see section 3.2). As seen in chapter 2, the fact that the reduced ergodicity eigenvectors have compact support is due to the finite length of the time series used to estimate the transition probabilities in $\hat{\mathbf{P}}_\tau^{\mathscr{R}}$.

For a large delay d_1 of 130 days (i.e after the deterministic bifurcation, figure 3.7), the periodic orbit is revealed. Furthermore, in the tangential direction, the ergodicity eigenvectors are similar to harmonic functions, in agreement with the eigenvectors (3.22) obtained analytically for the tangential component of the Fokker-Planck equation of the simple form of stochastic Hopf of section 3.3. In the radial direction, the ergodicity eigenvectors are almost constant, in agreement with the fact that they are associated with the first parabolic curve of ergodicity eigenvalues (fig. 3.4(c)), the eigenvectors of which are constant, according to (3.25). These results are, however, limited by the fact that the support of the eigenvectors is very narrow in the radial direction, due to the strong stability of the periodic orbit w.r.t. to the noise level and the finite length of the time series used to estimate the transition probabilities.

Last but not least, for an intermediate delay d_1 of 110 days (i.e at the deterministic Hopf bifurcation, fig. 3.6), very characteristic twisted patterns are revealed by the reduced ergodicity eigenvectors, which seem to correspond to a smooth transition from the eigenvectors for a small delay (before the criticality), represented figure 3.5, to those for a large delay (after the criticality), represented figure 3.7. These results could not be obtained from the analysis of an OU or on the stochastic Hopf. This reveals the potential of the methodology of reduced transfer operators presented in chapter 2 as a phenomenological yet more practical method to study stochastic bifurcations, in complement to stochastic normal forms (Arnold, 2003, Chap. 9). Moreover, the patterns described by these eigenvectors are very different from those found for the linear version (3.10) of the stochastic delayed oscillator, for a similar value of the delay, and represented figure 3.3. Neither do they correspond to the product of harmonic functions with polynomials as found in section 3.3 for the stochastic Hopf with large values of the control parameter. Thus, the reduced ergodicity eigenvectors of figure 3.6 reveal the nonlinear dynamics in action during the Hopf bifurcation and allow to discriminate linear from nonlinear dynamics in the presence of noise and, in the second case, from the subcritical from the supercritical situation.

Let us insist on this key point by analyzing the time series from which the reduced ergodicity spectra have been calculated and the corresponding correlation functions. Having calculated the left and right eigenvectors of the transition matrices, it is possible to calculate the reconstruction of the correlation function for different lags solely from the spectrum of the single transition matrix $\hat{\mathbf{P}}_\tau^{\mathscr{R}}$. Indeed, following section 2.2.3, the transition matrix correlation function $\tilde{C}_{f,g}(t)$, for two observables f and g in the two-dimensional reduced space, can be approximated as such

$$\tilde{C}_{f,g}(t) \approx (\mathbf{f}\mathbf{D}(\hat{\mathbf{m}})\hat{\mathbf{F}}_\tau^{\mathscr{R}})e^{t\hat{\Lambda}_\tau^{\mathscr{R}}}(\hat{\mathbf{E}}_\tau^{\mathscr{R}}\mathbf{g}^*) - (\mathbf{f}\hat{\mathbf{m}})(\hat{\mathbf{m}}\mathbf{g}^*), \tag{3.30}$$

where $\hat{\mathbf{E}}_\tau^{\mathscr{R}}$ and $\hat{\mathbf{E}}_\tau^{\mathscr{R}}$ are respectively the left and right eigenvectors of the transition matrix $\hat{\mathbf{P}}_\tau^{\mathscr{R}}$ and $e^{t\hat{\Lambda}_\tau^{\mathscr{R}}}$ is the diagonal matrix with elements $e^{t\hat{\lambda}_k^{\mathscr{R}}(\tau)}, 1 \leq k \leq n$. The

spectral reconstruction of the autocorrelation function $\tilde{C}_{f,f}(t)$, taking as observable simply $f(y) = y$, from the previously defined transition matrix $\hat{\mathbf{P}}_\tau^{\mathscr{R}}$, for $\tau = 0.05$, is represented in figure 3.8 by a dashed green line, for a delay of (a) 90 days, (b) 110 days and (c) 130 days. On top of this is also plotted the sample autocorrelation function $\hat{C}_{f,f}(t)$ (see chapter 2) with a thick blue line. To give an impression of the dynamics behind these correlation functions, corresponding snippets of the simulated time series are also represented in panels (d) to (f).

As a first remark, the spectral reconstruction of the transition matrix correlation function $\tilde{C}_{y,y}(t)$ is in very good agreement with the sample correlation function $\hat{C}_{y,y}(t)$, even though only the spectrum of a transition matrix at a single lag was used, assuming that the semigroup property and a fortiori the spectral mapping theorem holds, for (2.24) to give a good approximation of the full decomposition (2.23). This is an indication that at least the leading ergodicity eigenvalues are robust to the lag τ chosen to estimate the transition matrix $\hat{\mathbf{P}}_\tau^{\mathscr{R}}$ and that the true ergodicity eigenvalues are captured (a more thorough test would be to directly calculate the reduced ergodicity spectrum for different lags as in chapter 5).

However, much more can be learned from the spectral properties of transfer operators than from the correlation function or the stationary density alone. Indeed, we have seen that the ergodicity spectrum allows to separate the dynamics of statistics into characteristic time-scales (see fig. 3.4) and patterns (see fig. 3.5, 3.6 and 3.7). As an important example, it is difficult to qualitatively discriminate the subcritical case $d_1 = 90$ days from the critical case $d_1 = 110$ days just from the corresponding times series and correlation functions, represented figure 3.8(a, d) and 3.8(b, c), respectively. To the contrary, the twisted eigenvectors of figure 3.6 for $d_1 = 110$ days (at the criticality) are markedly different from those of figure 3.5 for $d_1 = 90$ (before the criticality). Thus, it appears that the reduced ergodicity eigenvectors allow to discriminate a stochastic system with linear dynamics from a system in which nonlinear effects are important, such as when close to a bifurcation. This important point to understand the nature of ENSO is supported by the following section 3.5, where a similar analysis is performed for the Zebiak-Cane model, and will be discussed in greater details in section 3.6.

3.5 APPLICATION TO THE ZEBIAK-CANE MODEL

In order learn more about the ergodicity spectrum associated with ENSO dynamics, we now apply the methodology of reduced transfer operators of chapter 2 to the stochasticly forced Zebiak-Cane model, a more realistic model of ENSO than the stochastic nonlinear delayed oscillator of the previous section 3.4. These results will also illustrate the applicability of the method to Galerkin approximations of (infinite-dimensional) PDEs. We start by describing the stochastic version of the fully-coupled Zebiak-Cane model, in which a Hopf bifurcation occurs, and show that while

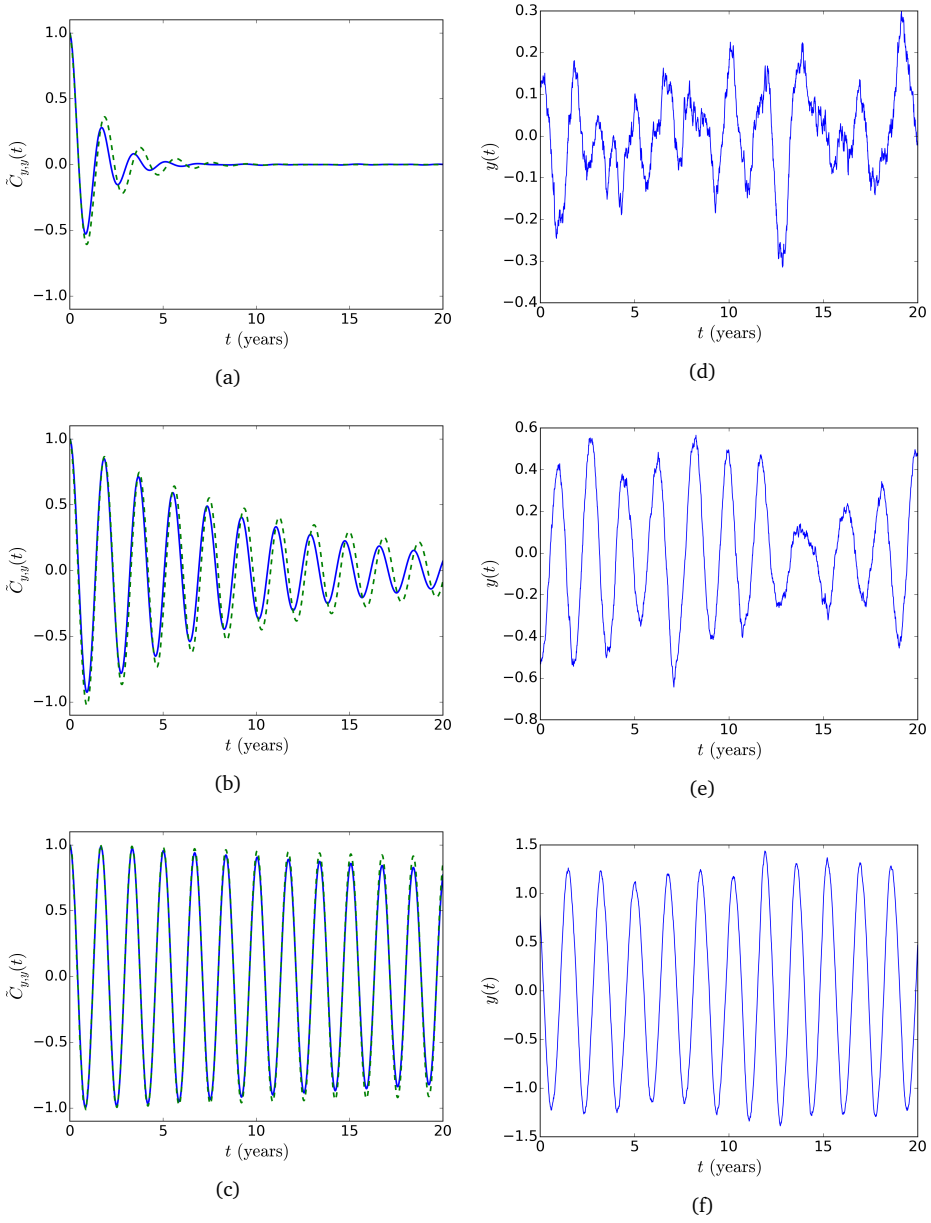

Figure 3.8: Correlation functions (left) and time series snippets (right) for the stochastic nonlinear delayed oscillator with a delay of 90 days (top), 110 days (middle) and 130 days (bottom). More precisely, the left panels represent the sample correlation function $\hat{C}_{y,y}(t)$ (thick blue line) and the spectral reconstruction of the transition matrix correlation function $\tilde{C}_{y,y}(t)$ (green dashed line), calculated according to (2.24) from the eigenvectors of the transition matrix $\hat{\mathbf{P}}_{\tau}^{\mathscr{R}}$, $\tau = 0.05$.

the ergodicity eigenvalues of the model are comparable to those obtained for the stochastic nonlinear delayed oscillator and allow to understand the phenomenon of noise-induced oscillations described by Roulston and Neelin (2000), the reduced ergodicity eigenvectors show some interesting differences due to nonlinear effects.

3.5.1 *Stochasticly-forced fully-coupled Zebiak-Cane model*

The Zebiak-Cane model is a 1.5-shallow-water ocean model with an embedded mixed layer coupled to a steady-state linear shallow-water atmosphere, on an equatorial beta plane (for a detailed description, see Zebiak and Cane, 1987). Variables are expanded into spectral basis functions, with 30 Chebychev polynomials in the zonal direction and 31 Hermite functions in the meridional direction. For this study, we use the fully-coupled version of the Zebiak-Cane model (van der Vaart et al., 2000) in which not only the anomalies but also the mean fields of the ocean and the atmosphere are coupled, allowing to get rid of spurious stable solutions (Neelin and Dijkstra, 1995). The long-term dynamics of this model are largely determined by the adimensional coupling parameter μ between the ocean and the atmosphere. For low values of μ and a standard choice of the other parameters, only damped solutions exist, converging to a stable fixed point. However, for a coupling larger than the critical value $\mu_c \approx 2.85$, a supercritical Hopf bifurcation occurs at which a periodic orbit emerges with a period of 3 to 4 years, reminiscent of ENSO.

Of great interest for the understanding of the nature of ENSO is the impact of a stochastic wind forcing, representing fast atmospheric processes such as westerly wind-bursts, on the tropical ocean-atmosphere dynamics. In particular, Roulston and Neelin (2000) have shown that, in the Zebiak-Cane model, a stochastic wind-forcing is able to excite oscillations with a similar period as ENSO before the criticality, i.e for $\mu < \mu_c$, in particular when the noise has a red spectrum (see also Dijkstra, 2013, Chap. 8). Following their methodology, we have added a stochastic wind-forcing to the ideal external wind-stress (i.e. to the component of the wind which is not in response to the SST anomalies). To do so, the spatial pattern of the stochastic wind-forcing was calculated from observations as the first Empirical Orthogonal Function (EOF) of observed pseudo wind stress anomalies, with the seasonal cycle removed as well as the linear contribution from observed SST anomalies. In this study, we have chosen to modulate this spatial pattern with white noise with equipartition of variance over all frequencies. The level of the noise, calculated as the spatial average of the standard deviation of the adimensional stochastic wind-forcing, was given a value of 0.05 (see van der Vaart et al., 2000; Roulston and Neelin, 2000),relatively close to observations (the precise of value of the noise level is not important for the qualitative analysis which follows).

Several simulations of the model in the described configuration were run for 700 years, with an integration time step of 5 days and for different values of the control

parameter μ. Examples of time series of SST averaged over the eastern part of the basin with spin-up are shown in the left panels of figure 3.9, for a coupling parameter of 2.5 (before the Hopf bifurcation) with noise, of 3.5 (after the bifurcation) with noise, and of 3.5 without stochastic wind-forcing added, respectively. The corresponding periodograms estimating the power spectra (see chapter 2) of each time series of SST are also shown in the left panels of figure 3.9. In the strongly coupled deterministic case (lower panels of figure 3.9), the time series converges quickly to a periodic orbit, revealed by the corresponding periodogram composed of a sharp peak at the fundamental frequency, corresponding to a period of 3.6 years, and of its harmonics. For the same value of the coupling but with stochastic wind-forcing added (middle panels of figure 3.9), the fundamental frequency associated with the periodic orbit persists but the peaks associated with each harmonic are weaker and broader, in particular for high frequencies. For a coupling μ of 2.5, below its critical value μ_c, the system would converge to a stable fixed point, if not for the addition of noise. However, as can be seen on the upper panels of figure 3.9, noise-induced oscillations at the frequency of the deterministic periodic orbit are excited by the stochastic wind forcing, in agreement with the results of Roulston and Neelin (2000). In light of the theory presented in chapter 2, we will see, in the following subsection 3.5.2, that these changes in the statistical properties of the model are the result of changes in the ergodicity spectrum associated to it.

3.5.2 *Ergodicity spectrum in the Zebiak-Cane model*

In order to characterize the phenomenon of noise-induced oscillations described in the previous section 3.5.1 and to relate the dynamics of the Zebiak-Cane model to those of the stochastic nonlinear delayed oscillator studied in section 3.4, we now calculate reduced ergodicity spectra for the Zebiak-Cane model. Even if the Zebiak-Cane can be considered as a model of intermediate complexity, it is nonetheless constituted of several hundreds of degrees of freedom. Thus, in order to estimate the transition matrices from which the ergodicity spectrum will be calculated, we define a two-dimensional observation operator $\mathscr{R}$, with the SST averaged in the eastern part of the basin as first component and the thermocline depth averaged over the western part of the basin as second component (this is known to be a good observation operator to capture the periodic dynamics, see e.g van der Vaart et al., 2000). The so-defined reduced space Y is then discretized into 100-by-100 grid boxes spanning a rectangle of $[-5,3] \times [-4,4]$ standard deviations, and for a lag τ of one month (a coarser grid resolution is used here compared to the previous examples due to limitations in the computation of time series longer than 700 years in this model). In figure 3.10 are represented the leading reduced ergodicity eigenvalues calculated from estimated transition matrices $\hat{\mathbf{P}}_\tau^{\mathscr{R}}$ for a value of the coupling μ of (a) 2.5 and

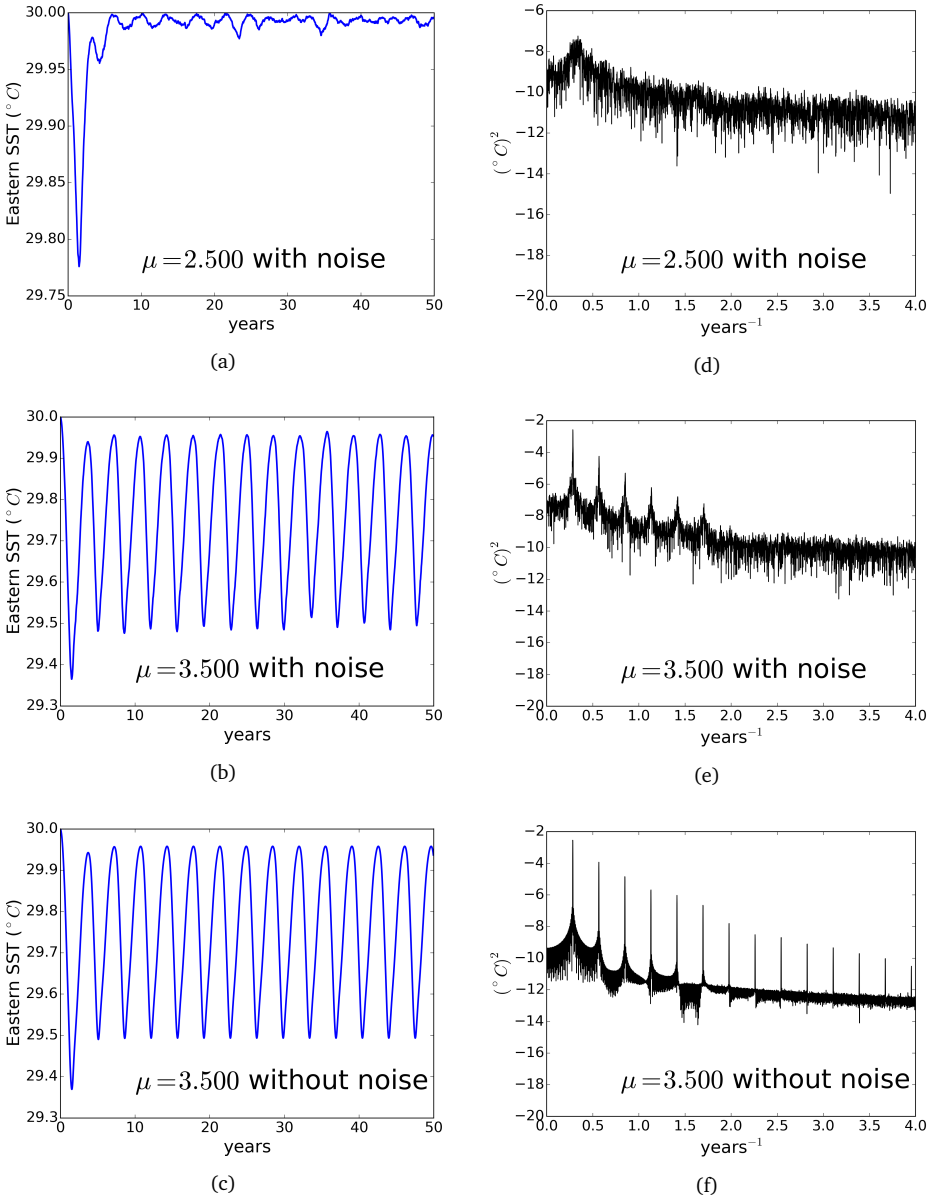

Figure 3.9: Time series (left) and periodograms (right) of the eastern SST index for a coupling μ of 2.5 with noise (top), of 3.5 with a noise (middle) and of 3.5 without noise (bottom).

(b) 2.8 (both before the deterministic Hopf bifurcation) and of (c) 2.9 and (d) 3.5 (both after the bifurcation), with stochastic wind forcing.

As a first observation, one recovers in figure 3.10(a) and (b) the familiar pyramid of eigenvalues associated with a stable focus point, also found in figures 2.3, 3.2 and 3.4(a) for the OU, the linear and the nonlinear delayed oscillators, respectively. As expected, as the control parameter (μ, in this case) is increased towards its critical value at which a Hopf bifurcation occurs, the secondary eigenvalues get closer and closer to the imaginary axis, indicative of the slowing down of the system due to the weaker stability of the fixed point. Let us remark that the real part of the eigenvalues far from the imaginary axis and close to the real axis are larger (in absolute value) compared to what would be expected from the ergodicity eigenvalues associated to a linear stable focus point. However, this difference increases close to the criticality, as can be seen in figure 3.10(b) for $\mu = 2.8$. Thus, it seems that this effect is not entirely due to the approximation method but rather to the nonlinearities excited by the noise close to the criticality (see section 3.3). Secondly, for large μ (fig. 3.10(d)), the reduced ergodicity eigenvalues follow a parabolic curve. According to the analytical results of section 3.3 for the stochastic Hopf and as found in the case of the stochastic nonlinear delayed oscillator of section 3.4 (fig. 3.4(c) and (d)), these eigenvalues are associated to the stochastically-forced periodic orbit. Interestingly, for a coupling μ close to its critical value $\mu_c \approx 2.85$ (fig. 3.10(b) and (c)), the ergodicity eigenvalues appear to undergo a smooth change between the clear pyramidal array found far before the bifurcation (fig. 3.10(a)) and the clear parabolic curves found after the bifurcation (fig. 3.10(d)). This transition differs from the case of the normal form of the deterministic Hopf bifurcation considered in (Gaspard and Tasaki, 2001), for which a continuous spectrum resulting in an algebraic decay of correlations exists at the bifurcation. This difference comes from the smoothing effect of the noise which introduces diffusion resulting in a non-vanishing mixing event at the criticality and stabilizes the system. Once again, such a result is made possible thanks to the approximation of the ergodicity spectrum from reduced transition matrices. In summary, the gap between the real parts of the ergodicity eigenvalues increases as the attractor (or the statistical steady-state) of the system becomes more and more stable. These results thus show that the characteristic statistical properties of both models of ENSO considered in this study, the Zebiak-Cane (Zebiak and Cane, 1987; van der Vaart et al., 2000) and the nonlinear delayed oscillator (Suarez and Schopf, 1988), are comparable and can be understood in terms of the ergodicity spectrum of a system undergoing a Hopf bifurcation (cf. section 3.3).

In addition, the ergodicity spectra represented in figure 3.10 allow to understand the power spectra and the phenomenon noise-induced oscillations presented in the previous section 3.5.1. Indeed, as can be understood from the decomposition of the correlation spectrum (2.12), each spectral peak in the periodograms represented in figure 3.9(d) and (e) is associated to a particular ergodicity eigenvalue represented

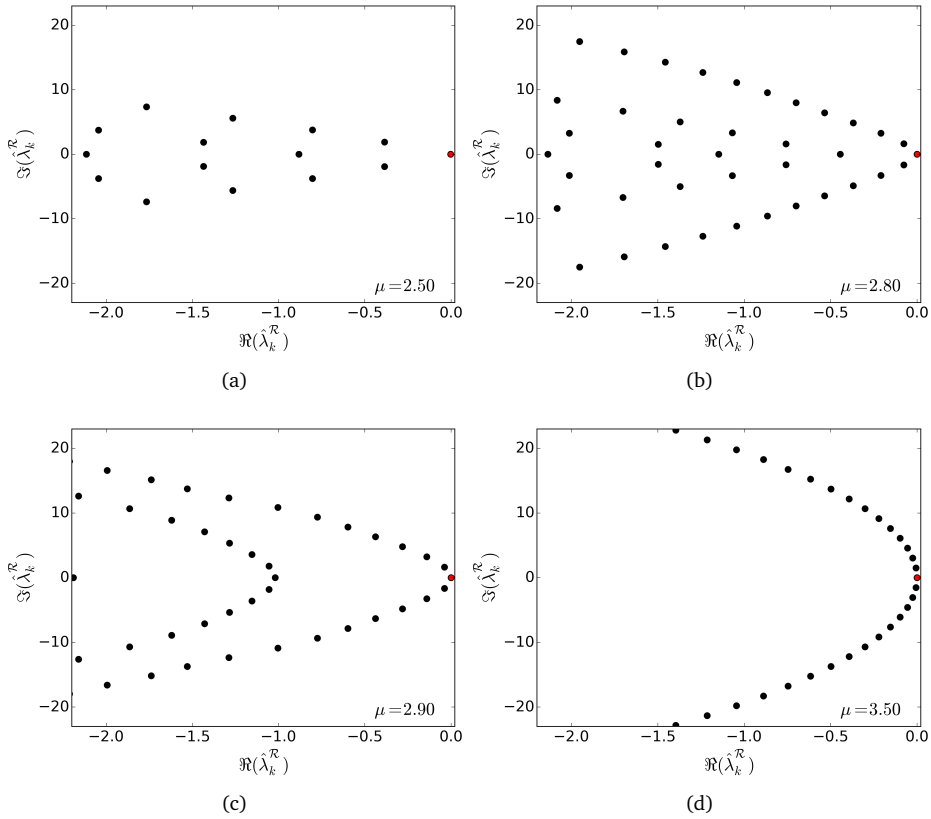

Figure 3.10: Leading part of the reduced ergodicity eigenvalues for the Zebiak-Cane model with a coupling μ of (a) 2.5 and (b) 2.8 (both before the deterministic Hopf bifurcation) and of (c) 2.9 and (d) 3.5 (both after the bifurcation). These eigenvalues were calculated from transition matrices on a two-dimensional reduced space composed the eastern SST and the western thermocline depth, for a lag of one month and a grid of 100-by-100 boxes spanning a rectangle of $[-5,3] \times [-4,4]$ standard deviations.

in figure 3.10(a) and (d), respectively. More precisely, for $\mu = 3.5$, the periodic orbit is very stable to noisy perturbations, so that the parabolic curve of eigenvalues of figure 3.10(d) is relatively flat and close to the imaginary axis, resulting in sharp peaks in the periodogram of figure 3.9(e). This periodogram is similar to the one of figure 3.9(f) for the deterministic case, for which, according to the results of Gaspard and Tasaki (2001), the leading ergodicity eigenvalues should have vanishing real parts. As the coupling parameter is decreased (or as the noise level is increased), however, the leading parabolic curve of eigenvalues sharpens, so that the leading eigenvalues get farther from the imaginary axis, in particular those with large imaginary parts. This results in the weakening and the spectral broadening of the peaks in the periodograms of figure 3.9(d) and (e), especially for high-order harmonics. However, even when the periodic orbit has disappeared, for $\mu = 2.5$, oscillations can still be excited by the noise (as can be seen figure 3.9(a) and (b)), since the leading ergodicity eigenvalues represented in figure 3.10(a) have non-vanishing imaginary parts. Yet, as the real part of the leading complex pair of eigenvalues decreases with the critical parameter μ, a stronger stochastic forcing is required in order to excite these oscillations.

Finally, the ergodicity eigenvectors corresponding to the ergodicity spectra represented in figure 3.10 (a) ($\mu = 2.5$), (b) ($\mu = 2.8$) and (d) ($\mu = 3.5$) are plotted in figures 3.11, 3.12 and 3.13, respectively. One can see that there is a degree of similarity between these eigenvectors and those of the stochastic nonlinear delayed oscillator, represented in figures 3.5, 3.6 and 3.7 in the previous section 3.4. In particular, for a small value of the coupling parameter (i.e before the criticality, fig. 3.11), the reduced ergodicity eigenvectors resemble two-dimensional polynomials with compact support, in agreement with the results of (Metafune et al., 2002) for finite-dimensional OUs. For a large value of the coupling parameter (i.e after the criticality, fig. 3.13), the periodic orbit is revealed and the eigenvectors are similar to harmonic functions in the tangential direction, in agreement with the results on the stochastic Hopf obtained in section 3.3. More interestingly, for an intermediate value of the coupling parameter (i.e at the criticality, fig. 3.13), the patterns described by the eigenvectors have the same twisted characteristic as those of the stochastic nonlinear delayed oscillator for intermediate delays, represented figure 3.6. However, the patterns are concentrated towards the fixed point with a value of $30°C$ for the SSTs and skewed towards stronger negative anomalies. This can be physically understood by the fact that, in this model, the SST tend to relax to the radiative equilibrium temperature T_E set to 30°, while, during a La Niña event, the ocean states gets cooler. As a conclusion, the reduced ergodicity eigenvectors allow to distinguish the dynamics of the Zebiak-Cane from the simpler dynamics of the stochastic delayed oscillator, in particular close to the bifurcation.

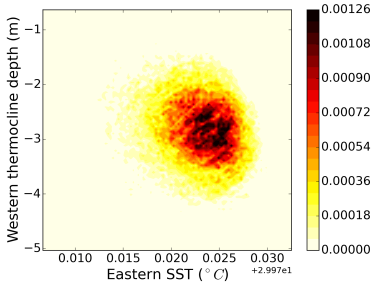

(a)

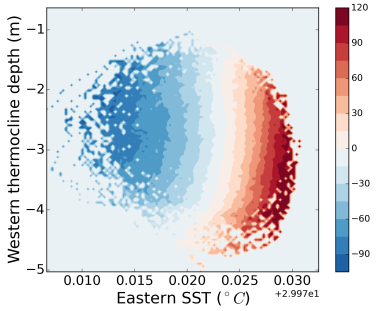

(b)

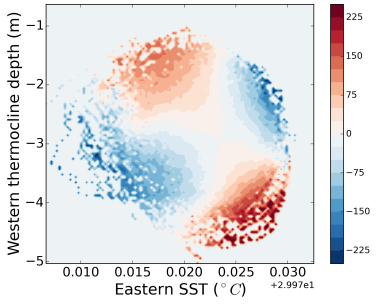

(c)

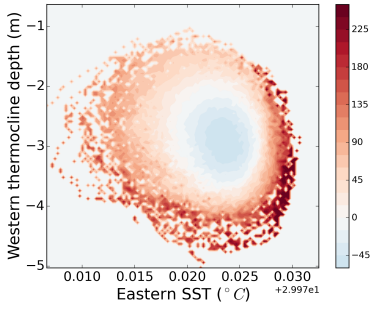

(d)

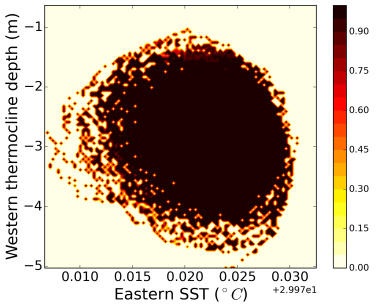

(e)

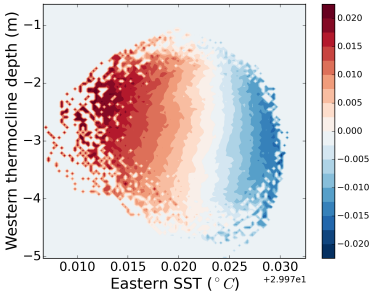

(f)

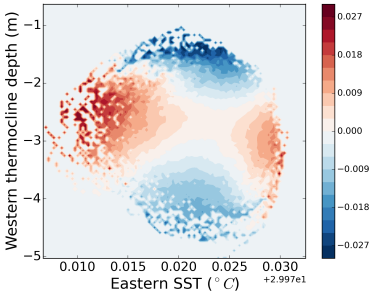

(g)

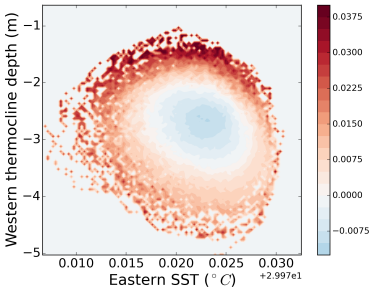

(h)

Figure 3.11: Real part of the first four forward (left) and backward (right) reduced ergodicity eigenvectors associated with the reduced ergodicity eigenvalues represented in figure 3.10(a) for the stochastic Zebiak-Cane model with a coupling μ of 2.5. As an exception, panel (a) represents the stationary density $\hat{\mathbf{m}}$ of $\hat{\mathbf{P}}_{\tau}^{\mathscr{R}}$.

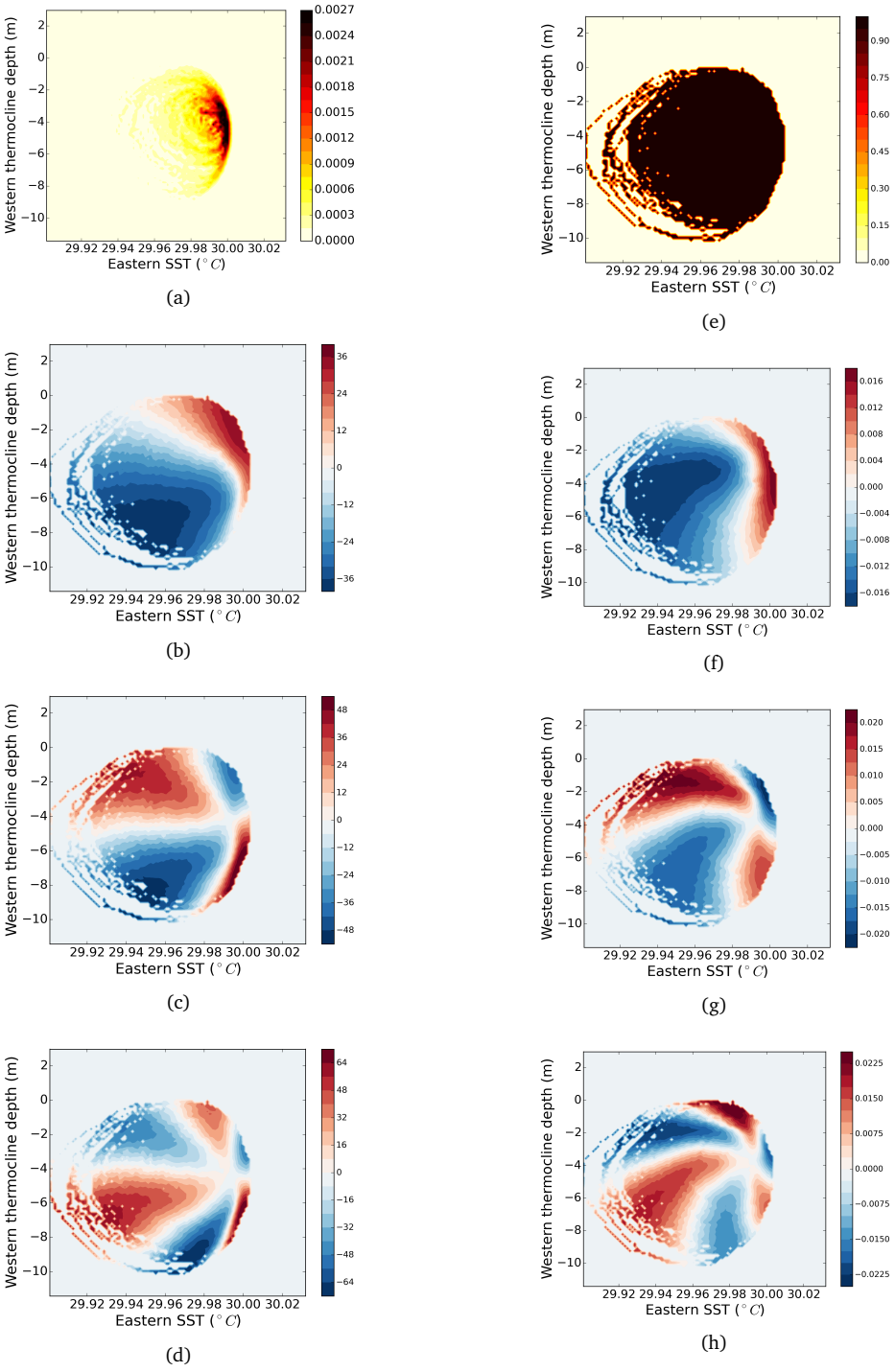

Figure 3.12: Real part of the first four forward (left) and backward (right) reduced ergodicity eigenvectors associated with the reduced ergodicity eigenvalues represented in figure 3.10(b) for the stochastic Zebiak-Cane model with a coupling μ of 2.8. As an exception, panel (a) represents the stationary density $\hat{\mathbf{m}}$ of $\hat{\mathbf{P}}_{\tau}^{\mathscr{R}}$.

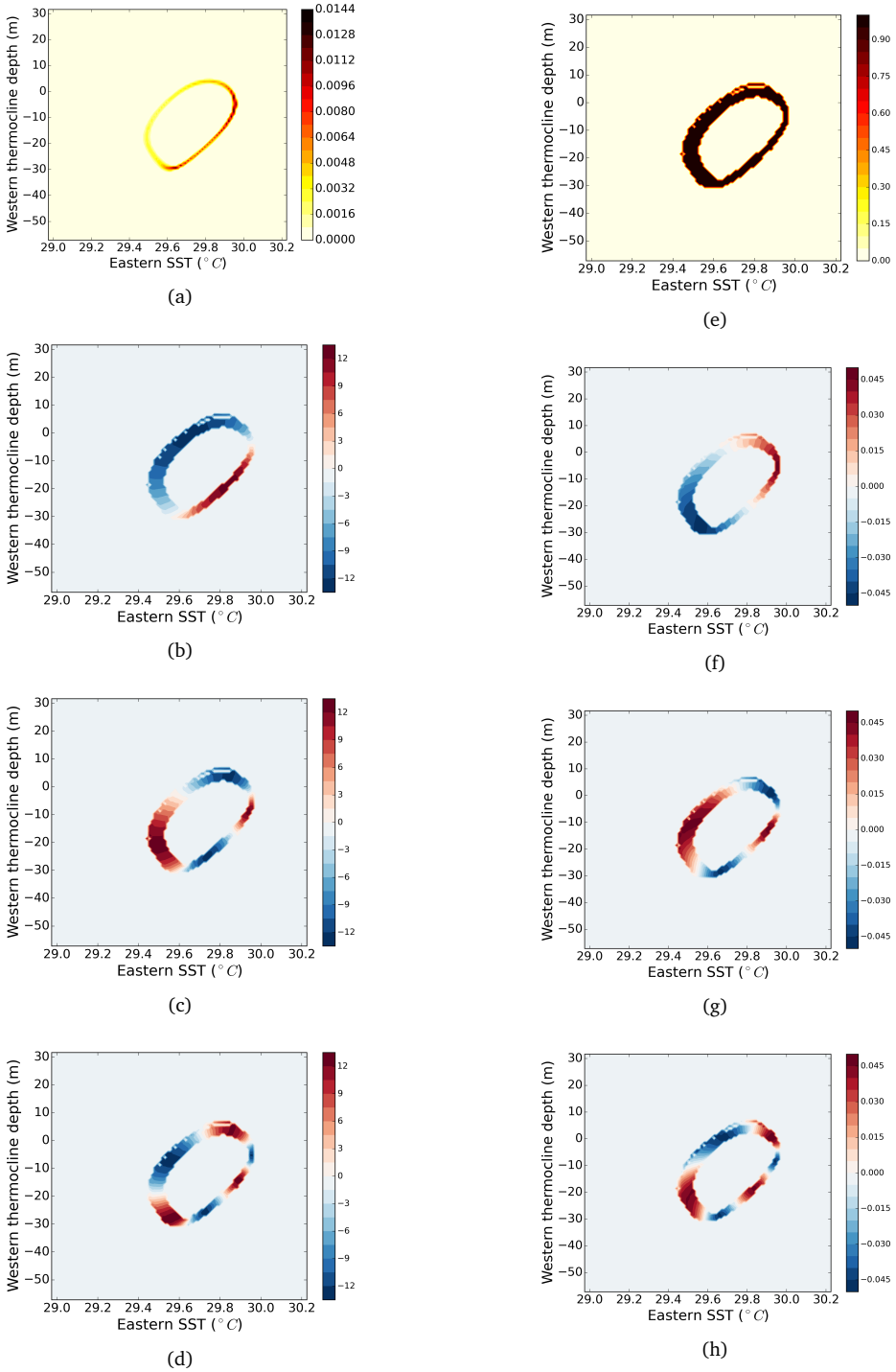

Figure 3.13: Real part of the first four forward (left) and backward (right) reduced ergodicity eigenvectors associated with the reduced ergodicity eigenvalues represented in figure 3.10(d) for the stochastic Zebiak-Cane model with a coupling μ of 3.5. As an exception, panel (a) represents the stationary density $\hat{\mathbf{m}}$ of $\hat{\mathbf{P}}_{\tau}^{\mathscr{R}}$.

3.6 SUMMARY AND DISCUSSION

On the mathematical side, the present study represents a first attempt to analyze the ergodicity spectrum of nonlinear SDDEs and PDEs undergoing a Hopf bifurcation. From a simple SDE derived from the normal form of the Hopf bifurcation to which noise is added, it is found that the ergodicity spectrum far after the criticality (i.e once the periodic orbit has emerged) is the product of a tangential and a radial contribution. The former is due to diffusion along the periodic orbit and is constituted of ergodicity eigenvalues proportional to the square of their rank and to the square of the ratio of the noise level over the radius of the periodic orbit, resulting in a characteristic parabolica-shaped spectrum. The later is due to contraction towards the periodic orbit and is akin to that found for a pitchfork bifurcation by Gaspard et al. (1995).

These analytical results compare well with the one found numerically for the delayed oscillator (an SDDE Suarez and Schopf, 1988) and the Zebiak-Cane model (the Galerkin approximation of a PDE van der Vaart et al., 2000). The ergodicity spectrum is approximated following the methodology of reduced transfer operators as presented in section 2.2. Far below the criticality a pyramidal spectrum is found, as for the OU with complex eigenvalues studied in section 2.3, while far above the criticality a parabolic spectrum is found, in agreement with the analytical results. In between, the spectrum experiences a smooth transition from the sub- to the supercritical case, which could not have been found analytically. These results thus suggest that the reduced ergodicity spectrum provides a direct and more phenomenological approach to the study of stochastic bifurcations.

On the physical side, one of the open fundamental questions in the application of ENSO theory is on the initiation of each particular event. In one extreme view, an event occurs because noise, in particular due to Westerly Wind Burst (WWBs), excites a large-scale SST pattern which is then amplified by Bjerknes' feedbacks. In the absence of the noise, in this view, the event would not have occurred. In another extreme view, an event occurs because infinitesimal SST anomalies would be amplified due to Bjerknes' feedbacks and noise (WWBs) is totally irrelevant for the initiation of the event.

In the deterministic Zebiak-Cane model, the two extreme regimes are separated by a critical value of the coupling strength μ_c associated with a Hopf bifurcation. For $\mu < \mu_c$ no event occurs and for $\mu > \mu_c$ a sustained oscillation occurs. We have shown here that one can also distinguish the different types of statistical behavior by looking at the reduced ergodicity spectrum. Indeed, far below the criticality, a pyramid of eigenvalues is present and the eigenvectors are similar to polynomials, whereas far above the criticality a parabolically shaped spectrum occurs associated with harmonic eigenvectors. Such ergodicity spectra allow to understand the correlation or power spectra of observables. For $\mu > \mu_c$, each ergodicity eigenvalue is associated with one harmonic of the periodic orbit. The imaginary part of an ergodicity eigenvalue corresponds to the frequency of the harmonic, while its non-vanishing real part

is due to diffusion resulting in a broadening of the spectral peak. When $\mu < \mu_c$, the oscillatory behavior can be excited by the noise because the leading ergodicity eigenvalues are close enough to the imaginary axis and have non-vanishing imaginary parts.

For a range of control parameter values around the critical value at which the deterministic bifurcation occurs, the ergodicity eigenvalues and eigenvectors undergo a smooth transition from the sub- to the supercritical case, so that one cannot say whether the bifurcation has yet occurred or not. However, the ergodicity eigenvectors are very different from the linear case so that it is at least possible to say that the system is nonlinear and close to a bifurcation. Furthermore, the Zebiak-Cane model ergodicity eigenvalues behave similar as simple delayed oscillator models, which provides additional (and more abstract) support that a delayed oscillator mechanism explains ENSO cycles.

In the application of these results to observations, one limitation that immediately appears is the length of the data (such as SST and thermocline depth) which is needed to reliably determine the ergodicity spectrum. However, long control runs from General Circulation Models (GCMs) could be used to calculate the ergodicity spectrum. Another approach applicable to observations would be to extract an Empirical Model Reduction (EMR, Kondrashov et al., 2015) from twentieth century observations of SST and to calculate the ergodicity spectrum from a long run of the EMR.

Another application is to develop early warning signals of transitions, such as associated with a range of different bifurcation phenomena. These can be based on single time series, such as the lag-1 autocorrelation or the variance (Lenton, 2011), or on multiple time series, such as the recently developed network indicators (van der Mheen et al., 2013; Feng et al., 2014). The approach of a bifurcation is inevitably related to at least one of the ergodicity eigenvalues approaching the imaginary axis. In the reduced transfer operators approach arises the issue of choosing the optimal observation operator so as for the reduced spectral gap to give an upper bound as sharp as possible to the true spectral gap (see *reduced spectral gap theorem*, in chapter 2). Although this may be highly application dependent, it will be an interesting topic for further research.

4

CHAOTIC ATTRACTOR CRISIS, STABILITY AND RESPONSE

The destruction of a chaotic attractor leading to a rough change in the dynamics of a system as a control parameter is smoothly varied is studied. While bifurcations involving nonchaotic invariant sets, such as fixed points or periodic orbits, can be characterized by a Lyapunov exponent crossing the imaginary axis, little is known about the changes in the Lyapunov spectrum of chaotic attractors during a crisis, notably because chaotic invariant sets have positive Lyapunov exponents and that Lyapunov eigenspaces vary on the invariant set. However, one would expect the critical slowing down of trajectories observed at the approach of a classical bifurcation to persist in the case of a chaotic attractor crisis. The reason is that, as the system becomes susceptible to the physical instability mechanism responsible for the crisis, it turns out to be less and less resilient to exogenous perturbations and to spontaneous fluctuations due to other types of instabilities on the attractor.

The statistical physics framework, extended to nonequilibrium systems, is particularly well suited for the study of global properties of chaotic systems. In particular, the semigroup of transfer operators governing the finite time evolution of probability distributions in phase space and its spectrum, the ergodicity spectrum, characterizes both the relaxation rate of distributions to a statistical steady state and the stability of this steady state to perturbations. If critical slowing down indeed occurs in the approach to an attractor crisis, the gap in the ergodicity spectrum (between the leading eigenvalue and the secondary ones) is expected to shrink.

Here we use a high dimensional, chaotic climate model system in which a transition from today's warm climate state to a snow-covered state occurs. This transition is associated with the destruction of a chaotic attractor as the solar constant is decreased. We show that critical slowing down develops in this model before the destruction of the chaotic attractor and that it can be observed from trajectories along the attractor. In addition, we demonstrate that the critical slowing down can be traced back to the shrinkage of the leading eigenvalues of coarse-grained approximations of the transfer operators, constructed from a long simulation of the model system, and that these eigenvalues capture the fundamental features of the attractor crisis.

4.1 INTRODUCTION

Much progress has been achieved during the last decades regarding bifurcation theory of low-dimensional dynamical systems and the emergence of aperiodic behavior and sensitive dependence to initial conditions, or chaos, when a parameter of the system is changed. Examples include changes in the Rayleigh number in hydrodynamics (Lorenz, 1963) or in the solar constant in climate science (Saltzman, 2002). Much less is known, however, on the sudden appearance or destruction of chaotic attractors. The review by Grebogi et al. (1983) provides a good starting point regarding the topological description of attractor crisis and the statistics of chaotic transients. However, little is known regarding the changes in statistical properties of high-dimensional chaotic systems undergoing an attractor crisis.

While it is a classical result that bifurcations involving nonchaotic invariant sets are associated with Lyapunov exponents crossing the imaginary axis and with the critical slowing down of trajectories (Strogatz, 1994), what happens before a chaotic attractor is destroyed is less understood. One reason for this is that the Lyapunov spectrum of high-dimensional systems is virtually inaccessible, either analytically or numerically. However, one would still expect critical slowing down to occur before the destruction of a chaotic attractor when the control parameter approaches its critical value at which the crisis occurs. The system must take more and more time to recover from exogenous perturbations and also from spontaneous fluctuations due to instabilities on the attractor. To make the distinction clear between the low-dimensional case and the chaotic case, we will here prefer the term “attractor crisis" rather than "bifurcation". We will also avoid the term “tipping point", often used in geophysics, because, even though a clear definition has been given in Lenton et al. (2008), its mathematical characterization remains vague and may refer to different concepts such as bifurcation, phase transition (Le Bellac et al., 2004) or catastrophe (Arnold, 1986).

For high-dimensional chaotic systems, geometrical approaches soon become intractable. However, statistical physics methods developed for nonequilibrium systems can become very fruitful (Eckmann and Ruelle, 1985; Young, 2002; Gallavotti and Lucarini, 2014), as already seen in chapter 3 in the context of stochastic evolution equations. Following the ground-breaking ideas of Boltzmann, a steady state is described as a time invariant probability measure (a statistical steady state) rather than a point in phase space. It is a fundamental property of nonequilibrium systems that the invariant measure is supported on a strange attractor with dimensionality lower than that of the phase space. This is the result of a contraction rate of the phase space that is positive on average and indicates the presence of a positive rate of entropy production (Ruelle, 1989a; Gallavotti and Lucarini, 2014). While most results concerning nonequilibrium mechanics have been found for the particular case of smooth uniformly hyperbolic systems (Young, 1998), their applicability to more general physical systems with a large number of degrees of freedom and exhibiting

chaotic dynamics has been motivated by the *Chaotic Hypothesis* in Gallavotti and Cohen (1995) (see also (Gallavotti and Lucarini, 2014)).

In the particular, yet physically highly relevant, case of mixing systems, probability distributions converge to a unique invariant measure (Lasota and Mackey, 1994). As seen in chapter 2 in the context of stochastic systems, how such relaxation occurs is described by the spectrum of transfer operators (see definitions (2.4) and (2.3)) governing the evolution of distributions by the dynamics (Ruelle, 1986a; Gaspard, 1998; Baladi, 2000). If a system close to undergo a crisis experiences a slowing down, the relaxation time of densities to the invariant measure must become very long, because trajectories take more and more time to converge to the more and more weakly attracting invariant set. We have seen an example of such situation in chapter 3 for the stochastic Hopf bifurcation. Since this relaxation time can be traced back to the inverse of the real part of the eigenspectrum of the transfer operators, the latter must thus get closer and closer to the imaginary axis as the crisis is approached. This simple idea is also supported by the fact that the gap between the leading eigenvalue of the transfer operators (associated with the invariant measure) and the secondary eigenvalues, which is related to the hyperbolicity of the system, gives a measure of the size of the perturbation for which one can expect the response of the system to be smooth (Butterley and Liverani, 2007; Ruelle, 2009; Lucarini, 2015). Since the response of a system at the crisis is definitely rough as an infinitesimal perturbation can lead to an attractor change, the gap in the eigenspectrum of the transfer operators is expected to shrink at the crisis.

One should not that in the dissipative deterministic case, the ergodic theory is very delicate, since strange attractors can be fractal and the eigenvectors of the transfer operators singular with respect to the Lebesgue measure due to the positive average contraction rate of volume in phase space associated with a positive entropy production. For some smooth uniformly hyperbolic systems, the discrete spectrum of the semigroup of transfer operators acting on Banach spaces, taking into account the dynamics of contraction and expansion on the stable and unstable manifolds, has been shown to be stable to perturbations (Gouëzel and Liverani, 2006; Butterley and Liverani, 2007) and is accessible via numerical schemes (Froyland, 2007). Moreover, we have seen in chapter 2 following the methodology of Chekroun et al. (2014) that the leading part of the ergodicity spectrum of high-dimensional systems can also be estimated numerically, but is dependent on the appropriate choice of an observation.

In this study, we explore the properties of an attractor crisis by taking an example from climate physics. This field has motivated many new concepts in dynamical systems theory and statistical mechanics. Prominent examples are the case of chaos itself (Lorenz, 1963), the use of stochastic dynamical systems (Hasselmann, 1976; Saltzman, 2002), the interpretation of complex climatic features using bifurcation theory (Dijkstra and Ghil, 2005; Dijkstra, 2005), the study of predictability of chaotic flows with its practical implications (Kalnay, 2003), methods for studying multiscale systems and developing parameterizations (Majda et al., 2001; Wouters and Lucarini,

2012, 2013; Franzke et al., 2015), and the use of response theory for studying how the climate responds to forcing (Gritsoun and Branstator, 2007; Abramov and Majda, 2007; Lucarini and Sarno, 2011; Lucarini et al., 2014; Ragone et al., 2015).

There are many indications that the climate of our planet is multistable, i.e. the present astronomical conditions are compatible with two climatic regimes, the present-day state, and the so-called Snowball state, whereby the Earth experiences extremely cold conditions. Paleoclimatological studies support the fact that in the distant past (about 700 Mya) the Earth was in such a Snowball state, and it is still a matter of debate which mechanisms brought the planet in the present warm state. Note that the issue of multistability is extremely relevant for the present ongoing investigations of habitability of exoplanets (Lucarini et al., 2013). Multistability is found for climate models across a hierarchical ladder of complexity, ranging from simple Energy Balance Models (Budyko, 1969; Sellers, 1968; Ghil, 1976) to fully coupled global circulation models (Pierrehumbert et al., 2011; Voigt and Marotzke, 2010). The robustness of such features is tied to the presence of an extremely powerful positive feedback which controls the transitions between the two competing states, the so-called ice-albedo feedback. The presence of a positive anomaly in ice cover favors a decrease of the absorbed radiation, because ice effectively reflects incoming solar radiation. This leads to a decrease in the surface temperature, which favors the formation of ice.

The Planet Simulator (PlaSim) (Fraedrich et al., 2005b,a) is a model displaying chaotic behavior. The model is complex enough to represent the main physical mechanisms of climate multistability, yet sufficiently fast to perform extensive numerical simulations (Lucarini et al., 2010; Boschi et al., 2013). In the present study, we demonstrate that critical slowing down is observed in PlaSim before the destruction of the chaotic attractor corresponding to a warm climate. This slowing down is visible for observables supported by the attractor (thus from simulations which have already converged to the attractor, without having to perturb the system). The slowing down is described by the leading eigenvalues of coarse-grained approximations of the transfer operators, constructed from a long simulation of the dynamical system and capturing the fundamental features of the attractor crisis.

Section 2 below briefly describes the climate model as well as the set up of different simulations for varying values of the control parameter. The spectral theory of transfer operators and the link to the slow decay of correlations associated with critical slowing down is described in section 3. This section contains also a presentation of the numerical method used to approximate the spectrum of transfer operators. The results are presented in section 4, where critical slowing down is shown to occur in the model as the attractor crisis is approached and to be associated with the approximated leading eigenvalues of the transfer operators getting closer to the imaginary axis. The results are summarized in section 5 where we explain the observed critical slowing down from the theory of boundary crisis (Grebogi et al., 1983) and discuss

its applications to response theory and the design of early-warning indicators of the crisis.

4.2 MODEL AND SIMULATIONS

As mentioned above, the attractor crises corresponding to the transition between warm states and snowball climate states has been replicated with qualitatively similar feature in a variety of models of various degrees of complexity. Given the goals of this study, we need a climate model that is simple enough to allow for an exploration of parameters in the vicinity of the attractor crisis and complex enough to feature essential characteristics of high-dimensional, dissipative, and chaotic systems, as the existence of a limited horizon of predictability due to the presence of instabilities in the flow. We have opted for using PlaSim, a climate model of so-called intermediate complexity. This model has already been used for several theoretical climate studies and provides an efficient platform for investigating climate transitions when changing boundary conditions and parameters.

4.2.1 *The Planet Simulator (PlaSim)*

The dynamical core of PlaSim is based on the Portable University Model of the Atmosphere PUMA (Fraedrich et al., 1998). The atmospheric dynamics is modeled using the primitive equations formulated for vorticity, divergence, temperature and the logarithm of surface pressure. Moisture is included by transport of water vapor (specific humidity). The governing equations are solved using the spectral transform method (Eliasen et al., 1970; Orszag, 1970). In the vertical, nonequally spaced sigma (pressure divided by surface pressure) levels are used. The parametrization of unresolved processes consists of long- (Sasamori, 1968) and short- (Lacis and Hansen, 1974) wave radiation, interactive clouds (Stephens et al., 1978, 1984; Slingo and Slingo, 1991), moist (Kuo, 1965, 1974) and dry convection, large-scale precipitation, boundary layer fluxes of latent and sensible heat and vertical and horizontal diffusion (Louis, 1979; Louis et al., 1981; Laursen and Eliasen, 1989; Roeckner et al., 1992). The land surface scheme uses five diffusive layers for the temperature and a bucket model for the soil hydrology. The oceanic part is a 50 m mixed-layer (swamp) ocean, which includes a thermodynamic sea ice model (Semtner, 1976).

The horizontal transport of heat in the ocean can either be prescribed or parametrized by horizontal diffusion. In this case, we consider the simplified setting where the ocean gives no contribution to the large-scale heat transport. While such a simplified setting is somewhat less realistic, the climate simulated by the model is definitely Earth-like, featuring qualitatively correct large scale features and turbulent atmospheric dynamics. Beside standard output, PlaSim provides comprehensive diagnostics for the nonequilibrium thermodynamical properties of the climate sys-

tem and in particular for local and global energy and entropy budgets. PlaSim is freely available including a graphical user interface facilitating its use. PUMA and PlaSim have been applied to a variety of problems in climate response theory (Ragone et al., 2015), entropy production (Lucarini and Pascale, 2014; Fraedrich and Lunkeit, 2008), and in the dynamics of exoplanets (Lucarini et al., 2013).

4.2.2 *Attractor crisis and instability mechanism*

In Lucarini et al. (2010) and Boschi et al. (2013), a parameter sweep in PlaSim is performed by changing the solar constant. The resulting changes in the Global Mean Surface Temperature (GMST) are represented in figure 4.1, taken from Boschi et al. (2013). For a large range of values of the solar constant there are two distinct statistical steady states, which can be characterized by a large difference — of the order of 40-50 K — in the value of the GMST. The upper branch in figure 4.1 corresponds to warm (W) climate conditions (akin to present day) and the lower cold branch represents snowball (SB) states. The W branch is depicted with a thin line, whereas the SB branch is depicted with a thick line. In the SB states, the planet is characterized by a greatly enhanced albedo due to a massive ice-cover.

The actual integration of the model is performed by starting from present-day climate conditions and decreasing the value of S, until a sharp W $\rightarrow$ SB transition is observed, corresponding to the attractor crisis, occurring at $S \approx 1263(Wm^{-2})$. The critical value of the solar constant needed to induce the onset of snowball conditions basically agrees with that found in Poulsen and Jacob (2004) and in Voigt and Marotzke (2010) (see also, Wetherald and Manabe, 1975, Fig. 5). The SB state is realized for values of the solar constant up to $S \approx 1433(Wm^{-2})$, where the reverse SB $\rightarrow$ W transition occurs. Hence, in the model there are two rather distinct climatic states for the present day solar irradiance (Voigt and Marotzke, 2010).

These W - SB transitions are induced by the ice-albedo positive feedback (Budyko, 1969; Sellers, 1968) which is strong enough to destabilize both W and SB states. The main ingredient of this feedback is the increase in the albedo (i.e. the fraction of incoming solar radiation reflected by a surface) due to the presence of ice. When a negative (positive) perturbation in surface temperature results in temperatures below (above) the freezing point ($T_f \approx 271.8K$, for sea ice), ice is formed (melts). Because of the larger albedo of the ice compared to ocean or land surfaces, this increase (decrease) in the ice-cover extent leads to a decrease (increase) of the surface temperature, further favoring the formation (melting) of ice. The dominant damping processes of this growth mechanism include the local decrease of emitted long-wave radiation with decreasing temperatures and the meridional heat transport from the equator to the poles. However, as the solar constant is decreased to criticality, these negative feedbacks are not sufficient to damp the ice-albedo feedback and the transitions occur.

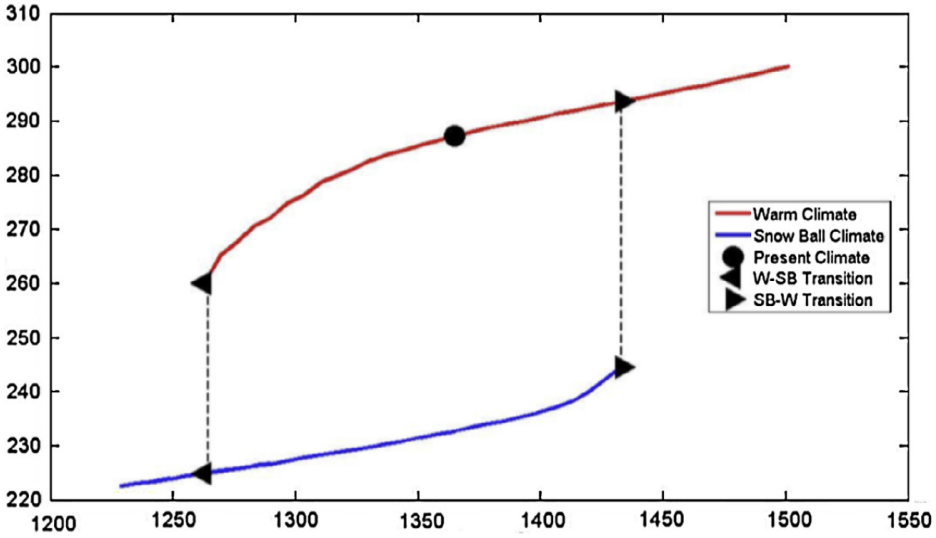

Figure 4.1: Hysteresis plot of the GMST (in Kelvin) for a varying solar constant S (in $W\,m^{-2}$) in PlaSim. Figure from Boschi et al. (2013).

In more idealized models (Scott et al., 1999) or, in general, in non-chaotic models (Lucarini et al., 2007), bistability is typically associated with the presence of two stable fixed points separated by a saddle node, and the loss of a fixed point is related to a bifurcation determining the change in the sign of one eigenvalue of the system linearized around the fixed point. In the present case, instead, the two branches define the presence of two parametrically modulated (by the changes in the value of the solar constant) families of disjoint strange attractors, as in each climate state the dynamics of the system is definitely chaotic. This is suggested by the fact that, for example, the system features variability on all time scales (Schalge et al., 2013) which corresponds, to having intransitive climate conditions (Lorenz, 1967; Peixoto and Oort, 1992). The loss of stability occurring through the W $\rightarrow$ SB and SB $\rightarrow$ W transitions is related to the catastrophic disappearance of one of the two strange attractors (Grebogi et al., 1983). Near the transitions, the system features quasi-transitive climate conditions, where long transients can be observed.

4.2.3 *Set-up of long simulations for varying solar constant*

While the studies in Lucarini et al. (2010) and Boschi et al. (2013) were focused on the thermodynamic properties of the model solutions along the two branches of statistical steady state, we here focus on the changes in the characteristic evolution of statistics (see chapter 2) along the warm branch as the solar constant S is decreased

to its critical value $S_c = 1263(Wm^{-2})$. The reduced transition matrix method presented in chapter 2 requires very long time series of observables. The model is hence ran for 10,000 years in the configuration presented section 4.2.1 and for 12 different fixed values of the solar constant, ranging from the critical value S_c to 1360 (Wm^{-2}) (approximately the present day value).

The initial state of each simulation is taken in the basin of attraction of the warm state. While this is difficult to guarantee, taking as initial state the annual mean of the 100th year of a simulation for a solar constant as high as 1450 (Wm^{-2}) (i.e for which only the warm state exists) resulted in the convergence to the warm state for each of the 14 values of S. A spin-up of 200 years was more than enough for the simulations to converge to the statistical steady state (facilitated by the fact that the ocean has no dynamics). Preparing for the analysis of section 4.3, this spin-up period was removed from the time series. The time series for each observable is subsequently sub-sampled from daily to annual averages, in order to focus on interannual-to-multidecadal variability and to avoid having to deal with the seasonal cycle.

4.3 SLOWING DOWN AND ERGODICITY SPECTRUM

The long simulations described in section 4.2.3 are now used to study the statistical changes occurring along the warm branch of statistical steady states as the solar constant is decreased towards its critical value S_c. Before applying the reduced transition matrix method presented in chapter 2, it is first of all shown that critical slowing down can be observed before the crisis. Note that we have discarded all results relative to values of the solar constant smaller than $1265(Wm^{-2})$, because the sea-ice cover (a discontinuous observable) becomes very sensitive to the spatial resolution of the model close to criticality. This results in spurious meta-stable states with different number of grid boxes covered by sea ice.

4.3.1 *Changes in the statistical steady state*

We start by discussing the statistics of a few observables to stress their key role in the ice-albedo feedback, the instability mechanism responsible for the attractor crisis (see section 4.2.2). Based on physical grounds, the following observables will be used:

- the global fraction of Sea Ice Cover (SIC) in the Northern Hemisphere (NH),
- the Mean Surface Temperature (MST) averaged around the Equator (Eq, i.e. from $15°S$ to $15°N$),

The SIC is the primary variable involved in the ice-albedo feedback as an ice-covered ocean has a much bigger albedo than an ice-free ocean. Sea ice forms when the surface temperature is below the freezing point ($T_f \approx 271.8K$) motivating the choice

of a surface temperature indicator. Furthermore, the MST at the equator is an indicator of the amount of heat stored in the ocean at low latitudes (indeed, because the ocean is slab, the temperature of the water column is uniform and proportional to its heat content) and that can potentially be transported to high latitudes through horizontal diffusion in the Ocean or, indirectly, through the general circulation of the Atmosphere.

The sample mean (from the long simulations) of these observables are represented in figure 4.2(a-b), allowing us to recap the changes in the climate steady state (Lucarini et al., 2010; Boschi et al., 2013). As the solar constant is decreased, less thermal Outgoing Longwave Radiation (OLR) is necessary to balance the Incoming Shortwave Radiation (ISR) from the sun, so that, as predicted by the Stefan-Boltzmann law of black bodies, the temperature of the Earth cools down, explaining the decrease in the Eq MST (Fig. 4.2(b)). The cooling of the surface of the Earth induces an increase of the extent of the sea ice towards low latitudes, further weakening the amount of absorbed solar radiation and strengthening the cooling. These changes in the mean of these observables are smooth, almost linear. Only for a value of the solar constant smaller than $1280(Wm^{-2})$ does the increase in NH SIC strengthen.

However, the sample variance (Fig. 4.2(c-d)) and skewness (Fig. 4.2(e-f)) experience rougher changes with the solar constant. Indeed, the variance of the NH SIC and Eq MST increases dramatically for $S < 1300(W/m^2)$. This increase indicates that the ice-albedo feedback is less and less damped as the criticality is approached. Thus, an anomaly in, for instance, the surface temperature can lead to an increase in the SIC which will be less easily damped by heat transport from a cooler equator. To stress the relationship between the NH SIC and the Eq MST, their joint Probability Density Function (PDF, calculated from the first eigenvector of the transition matrices estimated in the next section 4.3.3, yielding exactly the same results as binned estimates, see chapter 2) is plotted figure 4.3, for decreasing values of the solar constant. Apart from the changes in the mean and the increase in the variance (the axis of each panel have the same scaling), these plots show that while for $S = 1300(Wm^{-2})$ (panel (a)) the NH SIC and Eq MST are not correlated and normally distributed, their distribution becomes more and more tilted and skewed as the solar constant is decreased (panel (b-d)). This increase in the skewness of the NH SIC and Eq MST is also visible figure 4.2(e-f) from which one can verify that positive values of the NH SIC and negative values of the Eq MST are favored as the criticality is approached. This asymmetry is in agreement with the fact that as the ice-albedo feedback is less and less damped, larger excursions of the SIC to low latitudes and concomitant cooler temperatures are permitted.

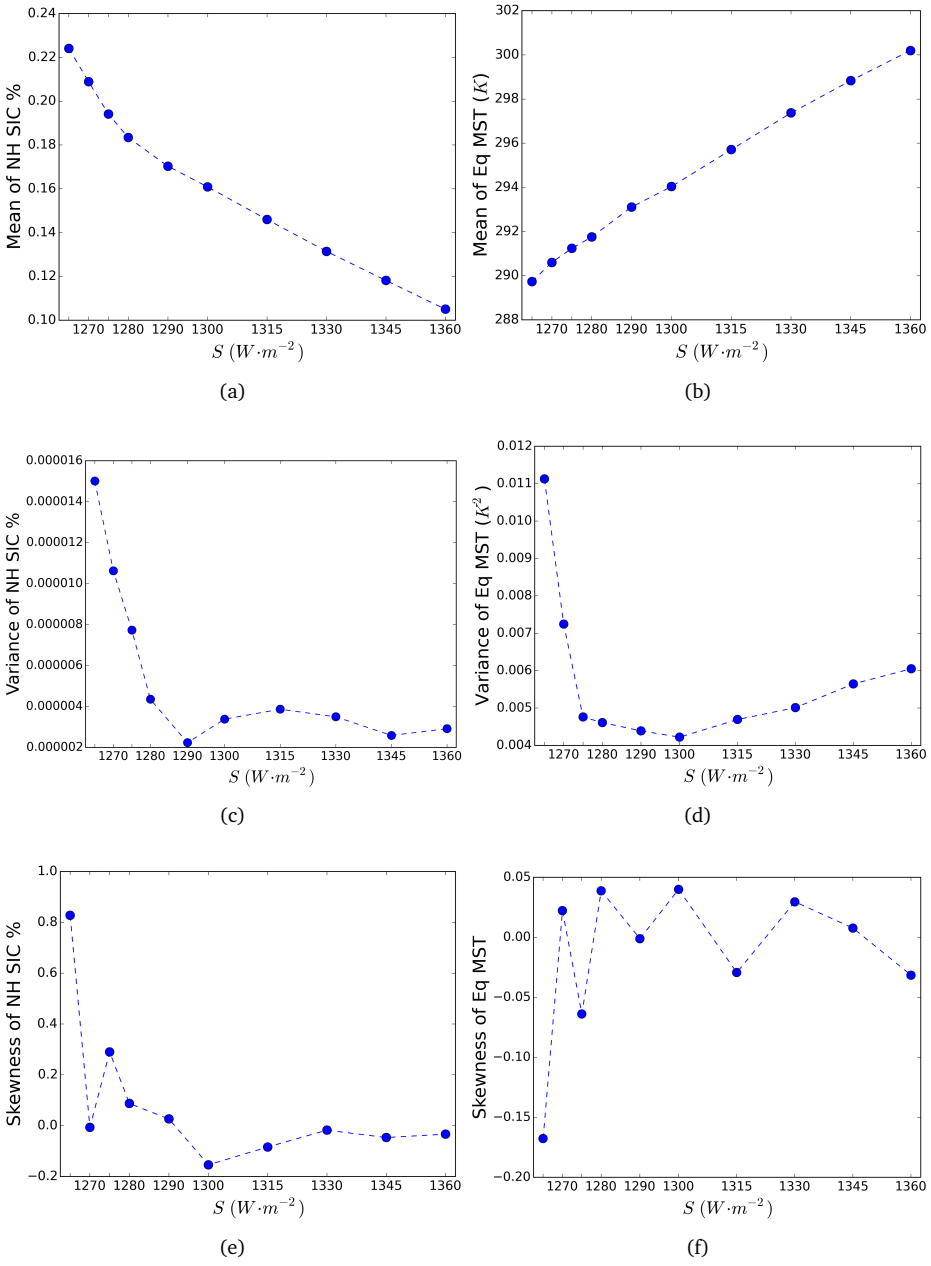

Figure 4.2: Sample mean (a-b), variance (c-d) and skewness (e-f) of yearly averages of the NH SIC fraction (top) and the Eq MST in Kelvin (bottom), versus the solar constant S (Wm^{-2}).

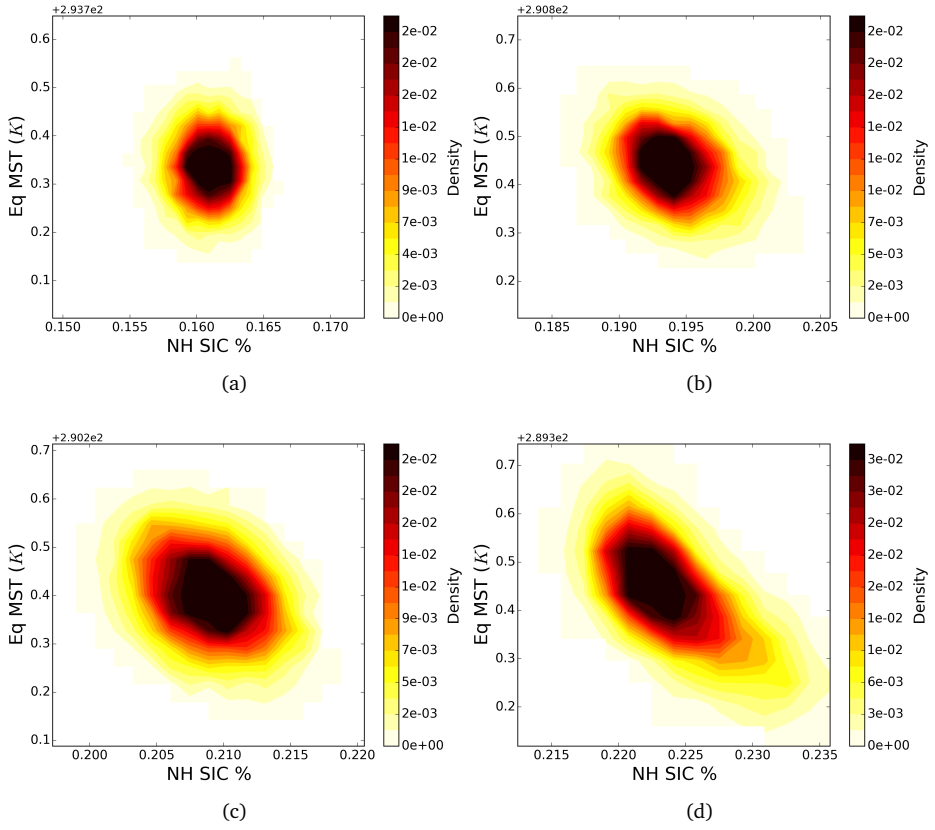

Figure 4.3: Joint PDFs of the NH SIC and Eq MST for (a) $S = 1300(Wm^{-2})$, (b) $S = 1275(Wm^{-2})$, (c) $S = 1270(Wm^{-2})$ and (d) $S = 1265(Wm^{-2})$, corresponding to the first eigenvector of the transition matrices estimated in section 4.3.3. The scaling of the axis is the same for each panel and is taken so as to span -3 to +3 standard deviations of the NH SIC and the Eq MST for $S = 1265(Wm^{-2})$.

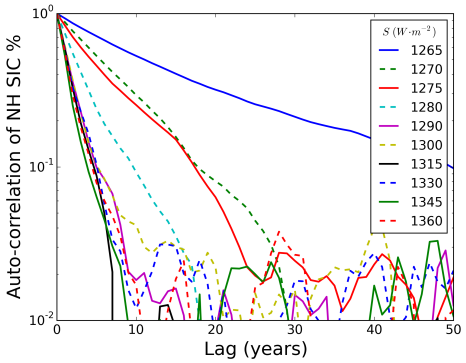

(a)

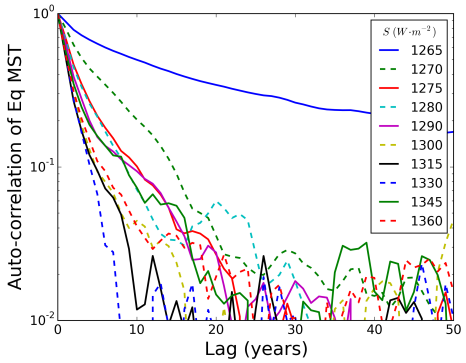

(b)

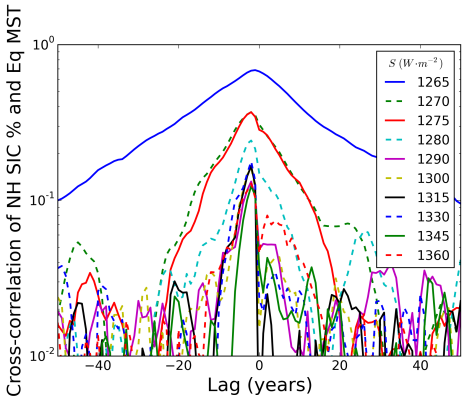

(c)

Figure 4.4: (a) ACF of the NH SIC, (b) ACF of the Eq MST and (c) CCF (in absolute value) of the NH SIC and Eq MST, for different values of the solar constant; note that the ordinate has a logarithmic scale.

4.3.2 *Critical slowing down*

Section 4.3.1 revealed the changes in the moments of the steady state along the warm branch, which could be linked to the physical mechanism of ice-albedo feedback. We now show that, consistent with the increase in variance and skewness of the NH SIC and Eq MST, their decorrelation time also increases. For this purpose, the sample AutoCorrelation Function (ACF) and CrossCorrelation Function (CCF) of these observables, defined by (2.19), are calculated from the simulations presented in section 4.2.3 and shown in figure 4.4. Note that, because the NH SIC and Eq MST are mostly anti-correlated, the absolute value of the CCF between NH SIC and the Eq MST is plotted in figure 4.4(c).

From the rather linear dependence of the correlation functions with the lag, we observe that the correlation functions are dominated by an exponential with slow decay

rate in the spectral decomposition (2.11). In light of this decomposition, the fact that the correlation functions in figure 4.4 show different decay rates depending on the choice of the observables is indicative that these observables project differently on the eigenvectors of the transition semigroups. For example, that the ACFs for the NH SIC (Fig. 4.4.a) decay more slowly that the ACFs for the Eq MST (Fig. 4.4.b) suggests that the NH SIC projects more strongly on the part of the spectrum of the semigroup of transfer operators close to the imaginary axis than the Eq MST. Furthermore, no oscillatory behavior is found in the correlation functions, indicative that the leading ergodicity eigenvalues on which the observables project must have vanishing imaginary part. Note also the strong correlations between the NH SIC and the Eq MST figure 4.4(c), in agreement with the PDFs of figure 4.3.

Most importantly, the correlation functions decay more and more slowly as the solar constant is decreased towards its critical value. Critical slowing down is thus apparent before the attractor crisis in this model, even when the unperturbed evolution of the system alone is observed (i.e., from time series converged to the attractor). This result can be explained in physical terms by the fact that, as the criticality is approached, spontaneous fluctuations, such as a temperature anomalies caused by instabilities in the atmosphere, are able to trigger the ice-albedo feedback. Mathematically, the slowing down and the chaotic attractor crisis cannot simply be understood in terms of a Lyapunov exponent becoming positive, as in Gaspard et al. (1995) and Gaspard and Tasaki (2001) for the normal forms of the pitchfork and Hopf bifurcations. Indeed, estimates in Schalge et al. (2013) suggest that the dynamical core of PlaSim possesses many positive Lyapunov exponents. As will be discussed in section 4.4, the slowing down can be explained by the approach of the stable manifold of a repeller colliding with the attractor at the crisis.

4.3.3 *Changes in the spectrum of transfer operators*

The spectral theory of transition semigroups presented in chapter 2 and the results obtained in chapter 3 for the stochastic Hopf bifurcation suggests that the slowing down observed before the attractor crisis can be explained by the approach of the spectrum of the semigroup of transfer operators, the ergodicity spectrum, towards the imaginary axis. To test this theory here, we apply the method of reduced transfer operators presented in chapter 2 and estimate transition matrices from the time series of the NH SIC and the Eq MST, observables selected for being most sensitive to the slowing down (as can be seen figure 4.4) and most relevant in terms of ice-albedo feedback (see section 4.3.1).

Remark 21. *Even though the methodology applied here is technically the same as the one presented in chapter 2 and applied in chapter 3 in a stochastic context, the outcome of the method in this deterministic case is expected to differ in two fundamental ways.*

The first difference is that, in the deterministic case considered here and contrary to the stochastic case, one cannot expect to resolve motions of contraction towards the attractor, since the transition probabilities are estimated from a unique long time series with spin-up (or transient) removed. Taking the simple example of a stable periodic orbit, one can see that, after a transient period of convergence to the periodic orbit, the trajectory will only feel the neutral dynamics on the periodic orbit and not the dynamics of contraction to it. Thus, with our method, only the ergodicity eigenvalues corresponding to dynamics along the unstable manifold can be hoped to be approximated, as opposed to the ergodicity eigenvalues corresponding to dynamics along the stable manifold (see also Ruelle, 2009; Cessac and Sepulchre, 2007). However, we have seen in figure 4.4 that the slowing down could be observed from the evolution of observables in steady state. This can be explained in physical terms by the fact that the primary mechanism of instability leading to the destruction of the attractor, the ice-albedo feedback, is not only activated by exogenous perturbations but also by spontaneous fluctuations along the attractor (i.e., internal variability, in climatic jargon). Thus, it is expected that the ergodicity eigenvalues associated with dynamics along the attractor should be affected by the approach of the attractor crisis.

The second difference is that, because of the coarse graining induced both by the projection of the dynamics on a reduced space (Chekroun et al., 2014) and by the Galerkin approximation (Froyland et al., 2013), the rate of decay of correlations measured by the spectral gap of the reduced transition matrices will overestimate the true rate of decay of correlations as measured by the spectral gap in the true ergodicity spectrum. The part of this effect due to the projection of the dynamics on a reduced space was already stressed in chapter 2 by the reduced spectral gap theorem. However, this is even more pathological in the deterministic case since, as a consequence of the coarse graining introducing spurious diffusion, the rate of decay of correlations measured by the reduced spectral gap will be increased by the exponential divergence of nearby trajectories. Thus, as discussed by Ruelle (1986b) at the end of his article, the time lag at which the decay of correlations is measured and, a fortiori, for which the transition matrices are estimated should be short relatively to the logarithm of the size of the perturbation induced by the coarse graining divided by the largest characteristic exponent. In our case, this would constitute a major restriction, since atmospheric baroclinic instability is expected to be associated with Lyapunov exponents corresponding to a time scale of only a few days, while the ice-albedo feedback dynamics has a time scale of several years. However, let us argue that, as supported by the correlation functions of figure 4.4, such a restriction can be weakened depending of the observables. Indeed, such an observable such as the NH SIC is barely affected by fast processes such as atmospheric baroclinic instabilities. Thus, by choosing such slow observables, one can hope to get a reasonable approximation of the spectral gap of the ergodicity spectrum by choosing an observation operator such that the leading ergodicity eigenvectors project significantly on the reduced space which it defines.

We first consider a one dimensional reduced space defined from the NH SIC or the Eq MST alone. A grid of 50 boxes spanning the interval $[-5\sigma, 5\sigma]$, where σ is the standard deviations of each observable, is taken. The width of the domain is chosen so as to avoid boundary effects which tend to result in a spectrum spuriously too far from the imaginary axis. The choice of the number of boxes is a trade-off between the resolution of short spatial and temporal scales and the quality in the estimates of the transition probabilities by the Maximum Likelihood Estimator (MLE) (2.16). A lag of one year was chosen (i.e., at the sampling frequency of the time series) which should allow us to determine the eigenvalues corresponding to time scales as short as one year. However, it is shown in A that our results are relatively robust to changes in the grid, the lag and to the sample size.

The leading eigenvalues of the transition matrices estimated for different values of the solar constant are represented in figure 4.5 for the NH SIC. The first eigenvalue, represented in red, is always 0 and is associated with the invariant density of the transition matrix, which is a projection of the actual invariant measure of the system. The slowest relaxation time in the series of exponentials in (2.11) is determined by the real part of the second eigenvalue and is given in the upper-right corner of figure 4.5. Finally, the first five secondary eigenvalues are represented in blue to help following their evolution. The main result here is that, in agreement with the slower decay of correlations of the NH SIC observed in figure 4.4(a), the leading secondary eigenvalues get closer and closer to the imaginary axis, as the solar constant nears its critical value. Furthermore, that the leading eigenvalues have vanishing imaginary part agrees with the fact that no periodicity is found in the correlation functions represented figure 4.4(a).

For a more detailed analysis, the real part of the four leading secondary eigenvalues for the NH SIC and for the Eq MST are plotted figure 4.6(a) and (b), respectively. Furthermore, the corresponding plot for the transition matrices estimated using the two dimensional space composed of both the NH SIC and the Eq MST is also shown in figure 4.6(c). For this two dimensional observable, a coarser grid of 25×25 boxes was used, because of the higher dimension of the reduced space compared to the one dimensional case. In fact, the PDFs represented figure 4.3 were calculated as the first left eigenvector of these transition matrices (see chapter 2). To these plots are added the sample decorrelation rates of the observables, calculated from the sample ACFs or CCFs as $\gamma_{i,j} = \log(|C_{f_i,f_j}(\tau)|)/\tau$, where $C_{f_i,f_j}(\tau)$ is the sample ACF or CCF with observable f_i leading observable f_j by a lag τ. Here the lag τ was chosen as 1 year, the same as for the estimation of the transition matrices. For example, $\gamma_{1,2}$ in figure 4.6(c) shows the sample decorrelation rate with the NH SIC leading the Eq MST by 1 year.

The plots in figure 4.6 confirm the approach of the imaginary axis by the leading secondary eigenvalues for the NH SIC, the Eq MST and the (NH SIC, Eq MST), as

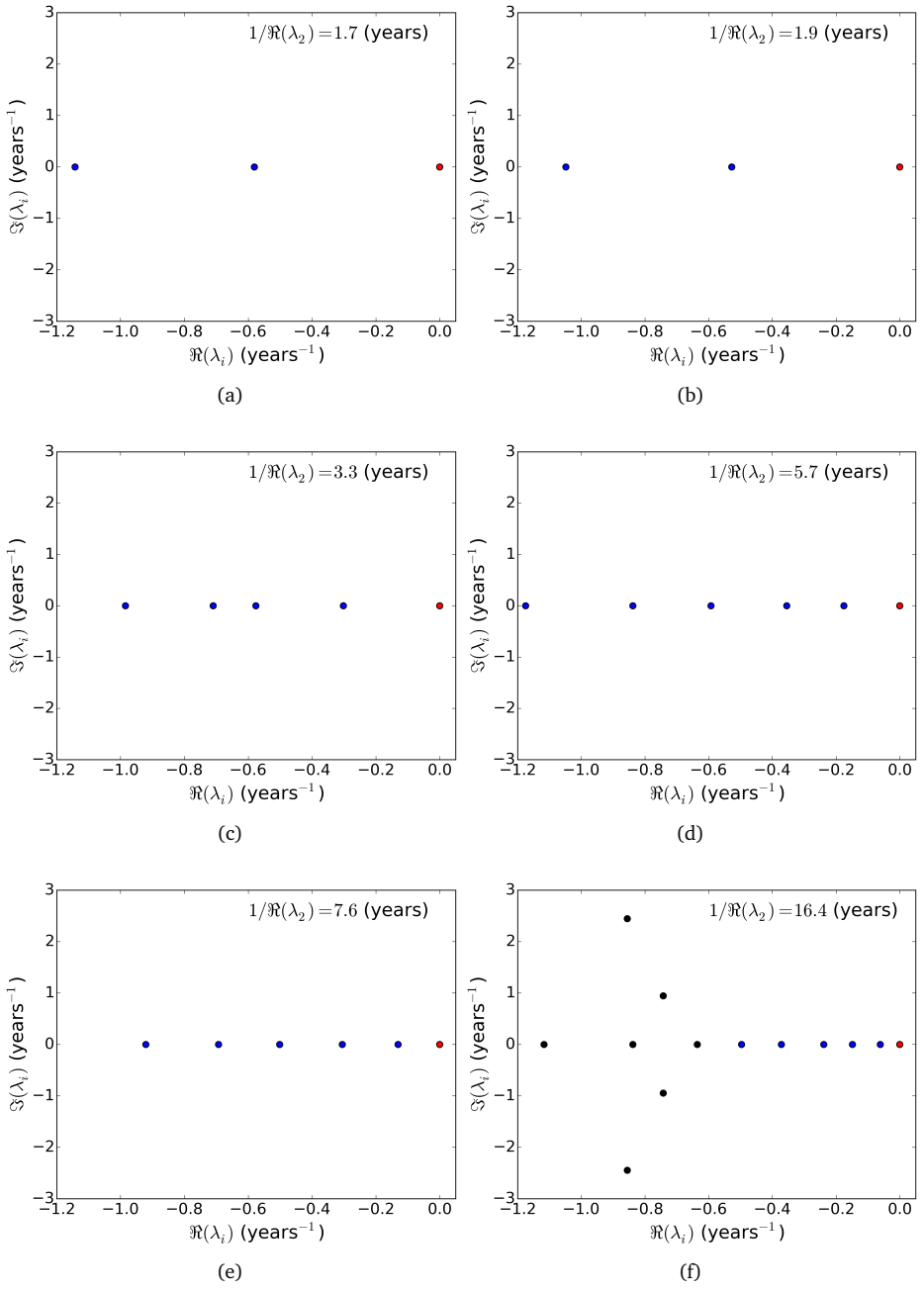

Figure 4.5: Reduced ergodicity spectra of the NH SIC for a solar constant of (a) 1360, (b) 1290, (c) 1280, (d) 1275, (e) 1270 and (f) 1265 (Wm^{-2}). The first eigenvalue, which is zero, is represented in red, while the first 5 secondary eigenvalues are represented in blue. The slowest relaxation time in the series of exponentials in (2.11) is determined by the real part of the second eigenvalue and is given in the upper-right corner of the panels.

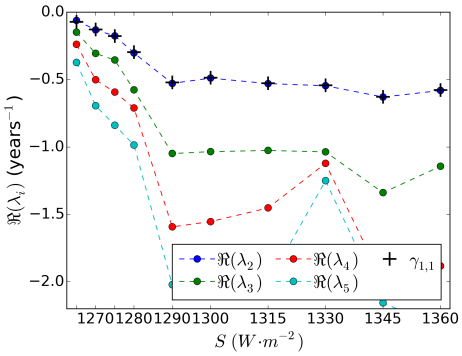

(a)

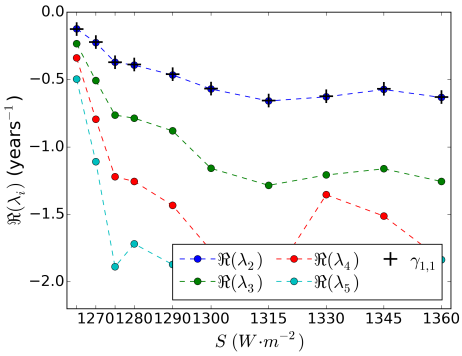

(b)

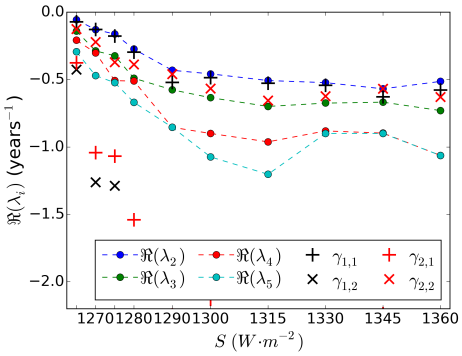

(c)

Figure 4.6: Real part of the four leading secondary eigenvalues for (a) the NH SIC and (b) the Eq MST and (c) the (NH SIC, Eq MST), versus the solar constant. The sample decorrelation rates $\gamma_{i,j}$ between the observables are also represented as black and red crosses.

the solar constant is decreased to its critical value. In particular, the time scale associated with the second eigenvalue for the (NH SIC, Eq MST) transition matrices increases from about 2 years to more than 17 years right before the crisis, yielding a quantitative measure of the critical slowing down associated with the disappearance of the attractor. Moreover, for $S < 1290(Wm^{-2})$, the increase of the real parts is almost linear and is reminiscent of the results found for deterministic bifurcations of low-dimensional systems (Gaspard et al., 1995; Gaspard and Tasaki, 2001) as well as for the stochastic Hopf bifurcation treated in chapter 3. Overall, these changes are in agreement with the slower decay of the ACFs and CCFs shown in figure 4.4. In particular, one can see that the maximum sample decorrelation rates coincide very well with the real part of the second eigenvalue as predicted by (2.11). This, however, will depend on how well the observables project on the eigenvectors associated with the second eigenvalue, i.e on how large is the term $\langle f, \psi_2^* \rangle \langle \psi_2, g \rangle$ in (2.11) (for instance, if the observable project very strongly on the third eigenvectors compared to the second, the decorrelation rate may coincide better with the real part of the third eigenvalue than the second).

Remark 22. *The ability of the reduced ergodicity spectrum to approximate the spectrum of the full transfer operators depends on the choice of the observation operator $\mathscr{R}$. In this study, however, we are particularly interested in the spectral gap between the first and the second ergodicity eigenvalues. According to the reduced spectral gap theorem of chapter 2, the spectral gap between the reduced ergodicity eigenvalues gives an upper bound to the true spectral gap. Thus, a small reduced spectral gap is necessarily associated with small spectral gap between the true ergodicity eigenvalues.*

4.4 SUMMARY AND DISCUSSION

Motivated by the question whether critical slowing down can be observed in a chaotic system undergoing an attractor crisis and whether this slowing down can be explained in terms of spectrum of operators governing the dynamics of statistics, we have taken as test bed a high-dimensional chaotic climate model undergoing a change of attractor as a control parameter is varied.

Correlation functions estimated from long simulations of the model have revealed that a slowing down indeed occurs as the critical value of the control parameter is approached. Importantly, the slowing down could be seen from the evolution of observables in steady state, without having to perturb the system away from the attractor. This could be explained in physical terms by the fact that the primary mechanism of instability leading to the destruction of the attractor, the ice-albedo feedback, is not only activated by exogenous perturbations but also by spontaneous fluctuations along the attractor (i.e., internal variability, in climatic jargon). This aspect, related to the presence of positive Lyapunov exponents associated with unstable processes,

makes the treatment of deterministic chaotic systems intrinsically more interesting than that of simpler systems featuring fixed points or periodic orbits as attractors.

The topological explanation of this phenomenon is less straightforward, but the study in Bódai et al. (2013) suggests that the observed critical slowing down could be related to the approach of the attractor by a repeller, eventually leading to the crisis. They show that in a simple, yet physically relevant, energy model able to reproduce accurately the snowball/snowfree bistability system the attractor crisis is due to the collision of the attractor of the warm steady state with a repelling invariant set (the so-called "edge state"). Such mechanism has been extensively described in Grebogi et al. (1983) for low-dimensional systems such as the Hénon map or the Lorenz flow and also in Schneider et al. (2007) for high-dimensional hydrodynamic flows. In these studies, several attractors coexist for a large range of parameter values, as in PlaSim, and it is shown that their basins of attraction are separated by the stable manifold of a repeller, while the closure of the unstable manifold of the repeller lies on the attractors (the simplest example of this situation would be two stable fixed points separated by a saddle node). Furthermore, as the control parameter is varied towards its critical value one of the attractors gets dangerously close to the stable manifold of the repeller, eventually colliding with it at the crisis. There, one of the attractors is destroyed and becomes part of the basin of attraction of the other.

Recently the edge state has been constructed also for a simplified climate model incorporating the dynamical core of PlaSim and a simplified representation of the oceanic transport and of the ice-albedo feedback (Lucarini and Bódai, 2015). For this case, the above mentioned mechanism of attractor crisis has been confirmed in detail. We are therefore led to think that the edge state exists also in the PlaSim configuration adopted here. The critical slowing down observed at the approach of the crisis could thus be explained by the influence of the stable manifold of the edge state on the dynamics on the attractor. Indeed, trajectories along the attractor approaching the region in which the stable manifold of the edge state is close are expected to spend more and more time in this region, resulting in an increase of the correlations (and thus of predictability). Note that understanding the properties of the edge state is key to predicting the features of the noise induced transitions across the two basins of attractions.

The second step of this study was to verify that the slowing down of the decay of correlations can be described in terms of spectrum of transfer operators, relying on approximations by Markov transition matrices acting on a reduced space. Approximating this spectrum for systems with competing time scales can reveal much reacher dynamics than by the estimation of the decorrelation rates alone. Of course, one cannot expect to recover the discrete part of the spectrum of transfer operators very accurately with such coarse-grained representations. However, with an appropriate choice of observable one can expect to get good estimates of the leading eigenvalues as supported by the reduced spectral gap theorem of chapter 2. The observable should be such that the leading ergodicity eigenvectors project well on reduced space

defined by the observable. However, these eigenvectors are difficult to access and the choice of the observable should eventually be guided by the behavior of its correlation functions and by an understanding of the fundamental physical mechanisms responsible for the slow dynamics. Moreover, if the reduced space on which the transition matrices are estimated is defined by an observable which is such that its correlation functions decay slowly, unresolved fluctuations (i.e orthogonal to the reduced space) are more likely to experience a correlation decay faster than the observable itself and could thus be approximated by a decorrelated noise. In this case, the evolution of the observable could be modeled by a stochastic process on the reduced space and the evolution of densities in this space would itself be governed by the semigroup of transfer operators of the stochastic process (see chapter 5 for a detailed discussion).

Contrary to the changes in the statistical moments of observables (cf. section 4.3.1), which are expected to vary depending on the topology of the attractor, the approach of the spectrum of the semigroup of transfer operators to the imaginary axis responsible for the slowing down as an attractor crisis is approached is expected to be rather general. It is based on both the physical idea that the instability mechanism becomes more and more easy to trigger by spontaneous fluctuations along the chaotic attractor and on the discussion on the collision with an edge state. In fact the narrowing of the spectral gap between the eigenvalue 0 and the secondary eigenvalues of the semigroup is an indicator that the radius of convergence of the series expansion of the perturbed invariant measure shrinks (Kato, 1995; Lucarini, 2015). In other words, the size of the perturbation for which response theory applies (Ruelle, 2009) vanishes at the criticality, accordingly to the fact that a dramatic change in the statistics occurs during the attractor crisis.

Finally, we have seen in section 4.3.3, that the change in the spectrum of the semigroup of transfer operators (and, a fortiori, in the decorrelation rates) is very smooth before the crisis, in agreement with the analytical results in Gaspard et al. (1995) and Gaspard and Tasaki (2001) for low-dimensional systems. Invoking the chaotic hypothesis, such numerical results could be explained by the differentiability of the spectrum of Anosov systems, proved in Gouëzel and Liverani (2006) for appropriate Banach spaces. The fact that critical slowing down can be observed from long time series of a high-dimensional chaotic system suggests that classical early warning indicators such as the lag-1 autocorrelation (Held and Kleinen, 2004), could be used to detect a chaotic attractor crisis from observations. However, the smoothness in the change of the spectrum of the semigroup of transfer operators suggests that autocorrelation-based indicators cannot be expected to give a very strong signal at the approach of an attractor crisis. This analysis thus shows, that even though the methodology presented chapter 2 is too demanding in terms of data to apply it to observations and use the spectral gap as an early-warning indicator of a crisis, it is very well suited to understand and design such indicators in the more general context of high-dimensional chaotic (and also stochastic) systems than the one of AR(1)

processes for which the lag-1 autocorrelation indicator was originally developed in Held and Kleinen (2004). This will be discussed in more details in chapter 6.

5

LOW-FREQUENCY ATMOSPHERIC VARIABILITY: A TRANSFER OPERATOR APPROACH TO META-STABILITY AND EARLY WARNINGS

The existence of persistent midlatitude atmospheric flow regimes with time scales larger than 5-10 days and indications of preferred transitions between them motivates to develop early warning indicators for such regime transitions. In this chapter, we use a hemispheric barotropic model together with estimates of transfer operators on a reduced phase space to develop an early warning indicator of the zonal to blocked flow transition in this model. It is shown that, the spectrum of the reduced Markov operator can be used to study the slow dynamics of the flow as well as the non-Markovian character of the reduction. The slowest motions are thereby found to have time scales of three to six weeks and to be associated with meta-stable regimes (and their transitions) which can be detected as almost-invariant sets of the transfer operator. From the energy budget of the model, we are able to explain the meta-stability of the regimes and the existence of preferred transition paths. Even though the model is highly simplified, the skill of the early warning indicator is promising, suggesting that the transfer operator approach can be used in parallel to an operational deterministic model for stochastic prediction or to assess forecast uncertainty.

5.1 INTRODUCTION

The midlatitude atmospheric flow is considered to be a chaotic dynamical system for which predictability is limited (Lorenz, 1969; Leith, 1978; Simmons and Hollingsworth, 2002). Although the behavior of this flow is dominated by weather systems on short time scales caused by baroclinic instability, strong variability on time scales longer than 5-10 days, with a predominantly barotropic structure, is also observed (James, 1994). It has been argued that at least part of the observed low-frequency variability can be explained by recurrent and persistent atmospheric regimes (Mo et al., 1988; Kimoto and Ghil, 1993; Smyth et al., 1999) such as the North Atlantic Oscillation (NAO) and blocking events (Plaut and Vautard, 1994; Ghil and Robertson, 2002).

Many studies identifying atmospheric regimes use algorithms relying on the recurrence property of these regimes such as the k-means (Mo et al., 1988; Kondrashov et al., 2004) and the Gaussian mixture algorithms (Smyth et al., 1999; Smyth, 1999). Other studies make use of persistence properties, for example leading to Hidden Markov Models (Majda et al., 2006; Franzke et al., 2008). Most of these techniques rely on the reduction of the high-dimensional phase space to a few dimensions.

The existence of weather regimes in General Circulation Models (GCM) and in reanalysis has been questioned for some time (Stephenson et al., 2004; Christiansen, 2007; Fereday et al., 2008). Using the Integrated Forecast System (IFS) of the European Centre for Medium-Range Weather Forecasts (talk), it was shown (Dawson et al., 2012; Jung et al., 2005; Dawson et al., 2014) that it was necessary to use a spatial resolution of T1279 (16 km), or to include stochastic parametrizations, in order for the atmospheric regime behavior to occur. This suggests that although the atmospheric regimes are large-scale low frequency motions, the faster small-scale motions (either explicitly resolved or included as random perturbations) are important to simulate them.

The barotropic structure of midlatitude low-frequency variability has motivated early studies using low-order barotropic models. Charney and DeVore (1979) have shown that such regimes could manifest themselves in highly truncated spectral barotropic models as stable fixed points representative of different solutions of a standing Rossby wave over topography. Flow regimes and spontaneous transitions have been observed in laboratory experiments using rotating annulus experiments for a barotropic fluid with topography (Weeks et al., 1997) and for a two-layer shear flow (Williams, 2003; Williams et al., 2004, 2005, 2008). In (Weeks et al., 1997), a zonal flow and blocked flow were found for different values of the Rossby number, and spontaneous transitions between the two were observed for intermediate values of the Rossby number. They suggested that these transitions were associated with the existence of two basins of attraction connected by heteroclinic orbits.

A scenario of chaotic itinerancy (Kaneko, 1991; Itoh and Kimoto, 1996) permitted by heteroclinic connections is supported by the study of Crommelin et al. (2004) us-

ing a 6-mode barotropic model. For specific values of the forcing parameter, the two stable fixed points of the zonal and blocked regimes merge with a periodic orbit (due to barotropic instability), yielding a heteroclinic connection. Although such a specific situation is unlikely to exist in the real atmosphere, Crommelin (2003) found evidence of ruins of such a heteroclinic connection in a hemispheric barotropic model with realistic topography and forcing (Selten, 1995), manifested by the presence of preferred transition paths. Regime behavior was also found in more realistic barotropic (Legras and Ghil, 1985; Branstator and Opsteegh, 1989; Crommelin, 2003) and multilayer quasi-geostrophic models (Itoh and Kimoto, 1996; Kondrashov et al., 2004). Because these models exhibit chaotic behavior, the regimes are no longer identified by stable fixed points but rather as neighborhoods in the phase space where trajectories tend to persist, motivating their denomination as meta-stable regimes.

In the laboratory experiments by Williams (2003), it is the inertia-gravity waves which are responsible for the regime transitions when the flow is baroclinically unstable. Such waves and barotropic disturbances occur in the real atmosphere together with baroclinically unstable synoptic weather systems, so that it is not yet clear if one disturbance is more important than the other in inducing certain regime transitions. All these possible mechanisms suggest, however, that the variability of the midlatitude atmospheric circulation can be captured by a deterministic model with multiple basins of attraction 'forced' by random perturbations representative of high-frequency eddies.

This multi-scale property of the climate system motivates a stochastic-modeling approach (Gardiner, 2009) to climate variability (Penland, 2003). Stochastic climate modeling often relies on a time-scale separation where the state vector is decomposed into a slow climate component and fast weather fluctuations. These fast fluctuations are not resolved explicitly but their aggregated effect is represented by a noise term. The system is thus modeled by a Stochastic Differential Equation (SDE) (Gardiner, 2009) with in general nonlinear deterministic terms and additive and/or state-dependent noise terms (Majda et al., 1999, 2001; Franzke et al., 2005; Franzke, 2014). When the time-scale separation assumption is violated, the Mori-Zwanzig formalism shows that a non-Markovian term representative of the memory effect induced by past interactions between the resolved and the unresolved variables has to be added (Chorin and Hald, 2009; Darve et al., 2009; Wouters and Lucarini, 2013; Kondrashov et al., 2015). Stochastic modeling has been applied to many problems in climate science, such as subgrid-scale parametrization, uncertainty quantification and data assimilation (Palmer and Williams, 2009; Franzke, 2014).

When randomness is present in a dynamical system, whether it is because of uncertainty in the initial state of chaotic systems or because of a stochastic forcing, it is of interest to study the evolution of probability densities in phase space by the flow rather than that of individual trajectories (Lasota and Mackey, 1994). We have seen in chapter 2 that the evolution of densities is governed by the semigroup of transfer operators whose spectrum, the ergodicity spectrum, gives valuable information

on the slow dynamics of the system. In particular, the leading ergodicity eigenvalues are associated with a slow correlation decay, which can be due to meta-stability (Froyland and Padberg-gehle, 2014).

The main purpose of the present study is to develop an early warning indicator of transitions between atmospheric flow regimes. A traditional method that gives an early warning of a sudden transition is the use of the critical slow down of the system when it gets close to a bifurcation point (Scheffer et al., 2009). However, in a high-dimensional model such as that used in (Crommelin, 2003) it is too simplistic to reduce the topology of the system to one or more stable fixed points. Recently, it was shown that complex networks can reveal information on nearby simple bifurcations in high-dimensional dynamical systems (van der Mheen et al., 2013). Near bifurcation points, the topology of the network changes drastically and early warning indicators for transitions were developed based on these topological changes (Viebahn and Dijkstra, 2014; Feng et al., 2014; Tirabassi et al., 2014).

In this study, we base the early warning indicator on the evolution of probability densities with respect to meta-stable regimes in a reduced phase space of the barotropic model used in Crommelin (2003). To study the slow dynamics in this phase space and to evaluate the effect of memory induced by the reduction, the spectrum of transfer operators estimated for different lags is analyzed. Meta-stable regimes are subsequently detected from the transfer operator at a carefully chosen lag. An early warning indicator of transition to the blocked regime is developed from the transfer operator making use of the existence of preferred transition paths between the regimes. To test the quality of the early warning indicator, a traditional method employing the Peirce skill score (Peirce, 1884; Stephenson, 2000; Thornes and Stephenson, 2001) is used. Finally, a study of the energy budget of the barotropic model is performed, where particular attention is given to the conversion of mean kinetic energy to eddy kinetic energy by Reynolds' stresses, to provide a physical background to the early warning indicator.

5.2 REDUCTION OF THE T21-BAROTROPIC MODEL

5.2.1 *Model and data*

Transitions between zonal and blocked regimes of the northern hemisphere atmospheric circulation are here investigated using a barotropic model (Selten, 1995; Crommelin, 2003; Franzke et al., 2005). The dimensionless equation of the model, expressed in terms of the streamfunction ψ (representing the non-divergent flow) and using the mean radius of the Earth and the inverse of its rotation rate as horizontal and temporal scale, is given by the barotropic vorticity equation (BVE)

$$\frac{\partial \nabla^2 \psi}{\partial t} = -\mathscr{J}(\psi, \nabla^2\psi + f + h_b) - k_1\nabla^2\psi + k_2\nabla^8\psi + \nabla^2\psi^*, \tag{5.1}$$

where $\mathscr{J}$ denotes the Jacobian operator, f the Coriolis parameter, h_b the scaled orography, k_1 the Ekman damping coefficient, k_2 the coefficient of scale-selective damping and $\nabla^2\psi^*$ the prescribed vorticity forcing. The adimensional orography h_b is related to the one of the real Northern Hemisphere h'_b by

$$h_b = 2A_0 \frac{h'_b}{H} \sin\phi_0, \tag{5.2}$$

where $\phi_0 = 45°\text{N}$, $A_0 = 0.2$ is a factor determining the strength of the surface winds that blow across the topography, and H is a scale height of 10 km.

The BVE is projected onto spherical harmonics, triangularly truncated at the 21^{st} mode (T21). The spherical harmonic coefficients are chosen such that the model is hemispheric with no flow across the equator, resulting in a system of 231 Ordinary Differential Equations (ODE), which are integrated using a fourth order Runge-Kutta numerical scheme. Following (Selten, 1995), the Ekman damping time scale and the scale-selective damping time scale were chosen as 15 days and 3 days (for wavenumber 21), respectively, so as to adequately reproduce the observed mean and variance of the 500hPa Northern-Hemisphere 10-day mean relative vorticity. The vorticity forcing $\nabla^2\psi^*$ is calculated from ECMWF reanalysis data of wintertime 500hPa relative vorticity from 1981 to 1991, in order for the first two moments of the simulated relative vorticity to be as close as possible to the observed relative vorticity. The term $\nabla^2\psi^*$ is calculated (Roads, 1987; Selten, 1995) according to

$$\nabla^2\psi^* = \mathscr{J}(\psi_{cl}, \nabla^2\psi_{cl} + f + h_b) + k_1\nabla^2\psi_{cl} - k_2\nabla^8\psi_{cl} + \overline{\mathscr{J}(\psi', \nabla^2\psi')}, \tag{5.3}$$

where ψ_{cl} is the mean of the observed streamfunction. The quantity ψ' is the deviation of the 10-day running mean observed streamfunction from ψ_{cl}. The present study relies on a 500,000-day-long simulation using an integration time step of 30 minutes, with daily output and a spin-up of 5,000 days removed.

5.2.2 *Phase space reduction*

In order to investigate the presence of meta-stable regimes and preferred transition paths, it is important to define a proper reduction of the 231-dimensional phase space (see chapter 2). This is usually done by projecting the state vector on a low-dimensional basis of orthogonal vectors such that the variance of the projected state vector is maximized. In practice, this can be achieved by an Empirical Orthogonal Function (EOF, e.g von Storch and Zwiers, 1999, Chap. 13) analysis of the streamfunction normalized by the kinetic energy norm (Crommelin, 2003; Franzke et al., 2005). The streamfunction patterns of the three leading EOFs are represented in figure 5.1 and explain 36.7% of the total variance. The first EOF is related to the Arctic Oscillation (AO), blocking events and the strength of the polar vortex (Crommelin,

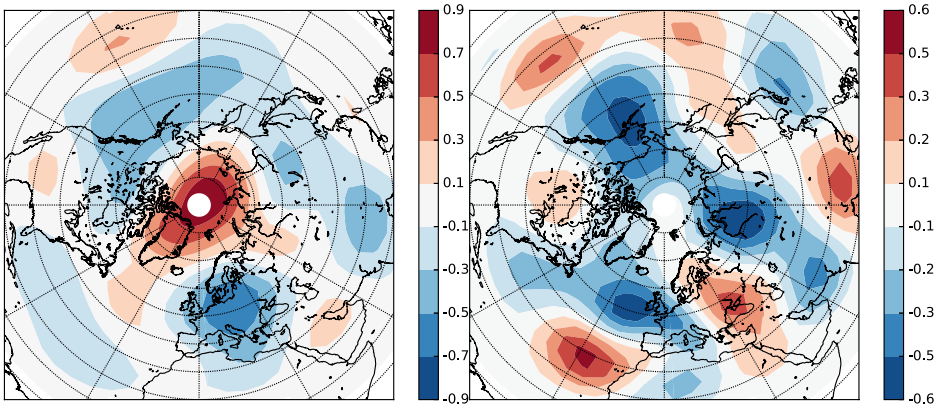

(a) (b)

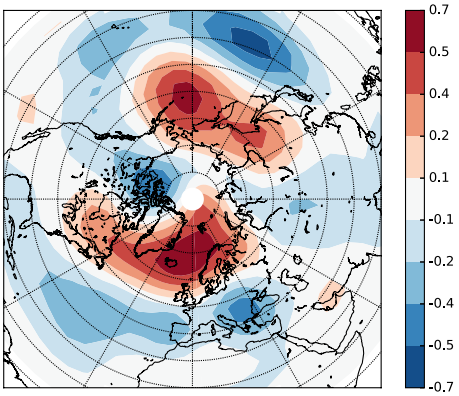

(c)

Figure 5.1: Dimensionless streamfunction of the three leading EOFs of the barotropic model. EOF 1 (a), EOF 2 (b) and EOF 3 (c) that explain 21.4%, 8.5% and 6.8% of the variance, respectively.

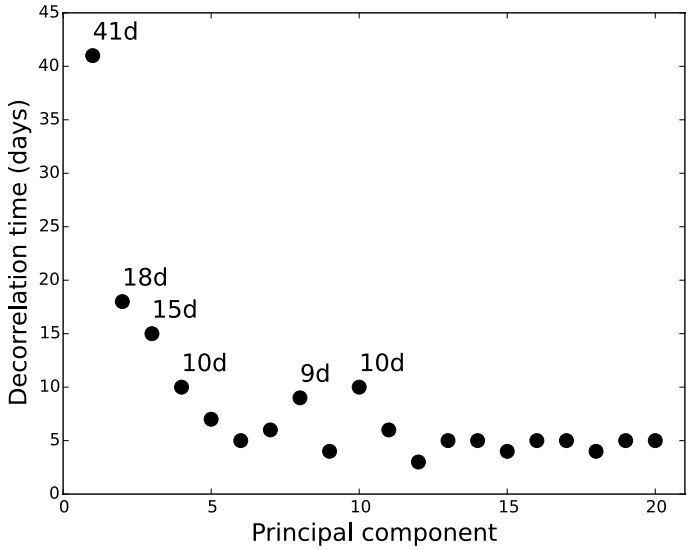

Figure 5.2: Decorrelation times (in days) of the 20 leading principal components.

2003). As it shows a dipole-like pattern over the Atlantic basin, the third EOF has been associated with the North Atlantic Oscillation (NAO).

For the purpose of this study, special care must be given to the choice of the EOFs used to define the reduce phase space. Indeed, the presence of meta-stable regimes and the transitions between them should not be hidden by the projection. Furthermore, for the sake of time-scale separation between the motions in the reduced phase space and the unresolved ones and in order to capture the leading ergodicity eigenvalues, it is important for the principal components of the selected EOFs to show decorrelation times as large as possible compared to the other principal components. These decorrelation times, defined as the lag after which the autocorrelation function has decayed to $1/e$ of its value at lag 0, are plotted in figure 5.2 for the 20 leading principal components. Largest decorrelation times are found for principal components 1, 2 and 3 (41, 18 and 15 days, respectively), while other principal components have a decorrelation time shorter than 10 days (with many smaller than 5 days). Because Crommelin (2003) has shown that meta-stability was mainly visible on the first principal component (pc_1), while transition between the meta-stable regimes occurred through low and high values of principal component pc_3, we have chosen to define the reduced phase space Y as the $(\mathrm{EOF}_1, \mathrm{EOF}_3)$ plane. The projection of the state vector $x \in H$ on the reduced phase space Y is then given by the observation y obtained by $\mathscr{R} : \mathbf{x}_t \mapsto \mathbf{y}_t = (\mathrm{pc}_1(t), \mathrm{pc}_3(t))$.

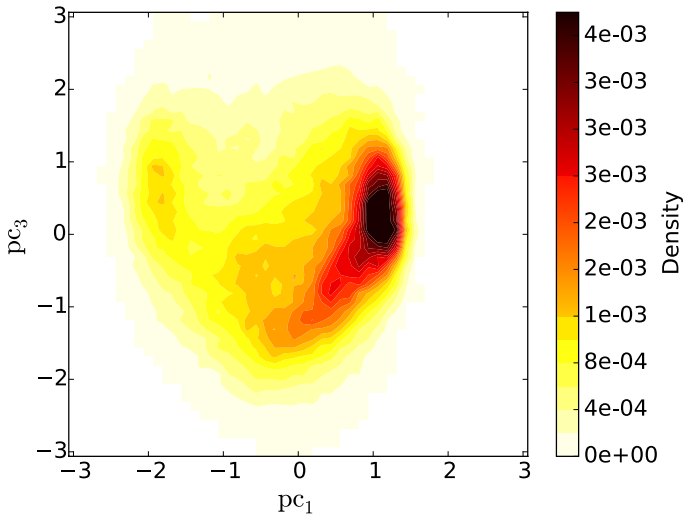

Figure 5.3: Probability density function of the first and third leading principal components normalized by their respective standard deviations and discretized using 50×50 grid boxes.

The two-dimensional normalized histogram of pc_1 and pc_3 for the 500,000-day-long simulation is (cf. figure 5.3) similar to figure 7 in (Crommelin, 2003). To estimate the histogram, principal components pc_1 and pc_3 were normalized by their respective standard deviations and the $(\mathrm{EOF}_1, \mathrm{EOF}_3)$ plane was discretized into a grid G of 50×50 boxes spanning a $[-3,3] \times [-3,3]$ square. Grid boxes at the boundary are extended so that all realizations belong to the grid. Furthermore, if a box contains no realization, it is removed from the grid, as it is not likely to support part of the projection of the attractor. This resulted in a grid of $m = 1577$ boxes containing on average 314 realizations and such that 80% of the boxes contain at least 20 realizations. The components h_i of the normalized histogram $\mathbf{h}$ for grid box B_i are then calculated as the likelihoods $\hat{\mathbb{P}}(y_t \in B_i) = \#\{y_t \in B_i\}/\#\{y_t \in G\}$, where $\#\{y_t \in B_i\}$ is the number of realizations of the observable y in box B_i and $\#\{y_t \in G\}$ is the total number of realizations.

The histogram in figure 5.3 shows two local maxima indicative of the presence of recurrent or persistent regimes. These regimes will be precisely defined in section 5.3.3. For now, following Crommelin (2003), we associate the local maximum for negative pc_1 to the blocked regime (since it corresponds to high pressure over northwestern Europe) and the maximum for positive values of pc_1 to the zonal regime. Crommelin (2003) also showed that the transitions from the zonal to the blocked

regime were preferably going through negative values of pc_3, interpreted as the positive phase of the NAO.

The dynamics of the state vector x of the barotropic model on the phase space X are deterministic and Markovian. However, application of the Mori-Zwanzig formalism (Chorin and Hald, 2009; Darve et al., 2009; Kondrashov et al., 2015) indicates that in a closed model of the dynamics of the observable y, memory terms accounting for past interactions between the resolved and the unresolved variables have to be included together with an, in general nonwhite, noise term. Under the assumption that the time scales of the resolved variables are slower by several orders of magnitude than those of the unresolved variables, these memory terms can be neglected (Givon et al., 2004; Majda et al., 2001). As can be seen in figure 5.2, the decorrelation time of the unresolved variables pc_2 is not smaller that the one of the resolved variables pc_1 and pc_3 and hence time-scale separation does not apply and memory effects should be considered. Following the methodology of chapter 2, we show in section 5.3 how transfer operator techniques can provide detailed information on this issue.

5.3 SPECTRAL PROPERTIES, MEMORY AND ALMOST-INVARIANT SETS

The semigroup of transfer operators is now analyzed to study the dynamics associated with the meta-stable regimes. Because, the high dimensionality of the phase space of the barotropic model ($d = 231$) prohibits the direct approximation of the semigroup of transfer operators and since, as described in section 5.2.2 and in Crommelin (2003), the dynamics relevant to transitions between meta-stable regimes predominantly occur in the reduced phase space $Y = (\mathrm{EOF}_1, \mathrm{EOF}_3)$, we instead estimate the transition matrix approximating the reduced Markov operator on the reduced phase space Y (see chapter 2). Accordingly, we have discretized the reduced phase space Y using exactly the same 50×50 grid as for the histogram as in section 5.2.2. Then, the matrices $P_\tau^{\mathscr{R}}$ were estimated using the Maximum Likelihood Estimator (MLE) of chapter 2 from the 500,000-day-long time series of $\mathbf{y}$ and for different lags τ. Importantly, $\hat{P}_\tau^{\mathscr{R}}, \tau \geq 0$ need not be a semigroup because (i) the partial observation of the system introduces memory effects (Darve et al., 2009; Chorin and Hald, 2009), (ii) the Galerkin approximation adds numerical diffusion (Froyland et al., 2013) and (iii) the estimation of transition probabilities from a time series of limited length is prone to sampling errors (cf. section 5.3 below).

5.3.1 *Spectral properties and slow dynamics*

For this purpose, we calculate the reduced ergodicity eigenvalues $\hat{\lambda}_k^{\mathscr{R}}(\tau)$ associated with $\hat{P}_\tau^{\mathscr{R}}$ for τ ranging from 1 to 39 days. The rates $r_k(\tau) = -\Re(\hat{\lambda}_k^{\mathscr{R}}(\tau))$ corresponding to the 10 leading eigenvalues different from zero of each $\hat{P}_\tau^{\mathscr{R}}$ are represented fig-

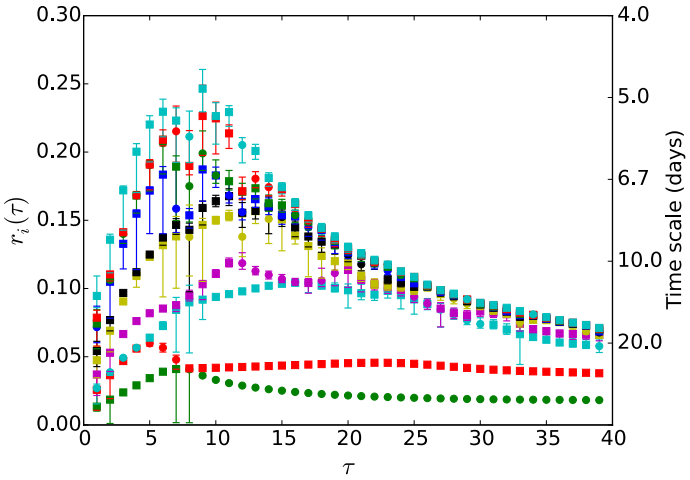

Figure 5.4: Rates $r_k(\tau)$ corresponding to the 10 leading eigenvalues different from unity of each $\hat{P}_\tau^{\mathscr{R}}$, with the lag τ as abscissa and the (cyclic) coloring giving the rank of the rate. A complex pair of eigenvalues is represented by one square for the two conjugates. The error bars represent 99% confidence intervals estimated from a thousand surrogate transition matrices by applying the bootstrap method described in Appendix B.1.

ure 5.4 with the lag τ as abscissa and the (cyclic) coloring distinguishing the rank of the rate. A complex pair of conjugate eigenvalues is represented by one square for the two conjugates. The error bars represent 99% confidence intervals estimated from a thousand surrogate transition matrices by applying the bootstrap method described in Appendix B.1.

Our first observation concerns the small width of the confidence intervals (some are even hidden by the marker size). These intervals evaluate the robustness of the estimates to the limited length of the time-series. The largest intervals occur when two rates almost overlap, so that one of them may appear or disappear in the surrogates, resulting in a change of rank for all higher-rank rates. In our case, large confidence intervals are thus usually indicative of an uncertainty in the existence of two close but distinct rates or of only one (as for the leading rates at $\tau = 7$ or 8, for example). Moreover, Appendix B.1 shows that at least the three leading rates are very robust to changes in the the grid resolution, ranging from a 10×10 grid to a 100×100 grid, compared to the original 50×50 grid.

Being confident on the robustness of the rates to the sampling as well as to the grid resolution, we now turn to a detailed analysis of the results in figure 5.4. First, we can see that the two rates closest to zero, the leading rates in red and green,

are well separated from the rest of the spectrum after a lag between 5 and 10 days. One of these rates derives from a real eigenvalue (the circle), the other represents a pair of complex conjugate eigenvalues (the square); they exchange rank at a lag of 8 days. We can calculate an indicative time scale associated with each rate as the inverse of the rate. Whether this time scale corresponds, to a good approximation, to a decorrelation time is not the matter of this study. For a lag of 15 days, the first rate (in green) and the second rate (in red) correspond to a time scale of 40 and 23 days respectively. Furthermore, the second rate is separated from the third (in cyan) by a gap of 13 days. This time-scale separation suggests that the reduced dynamics are slowly mixing due to the presence of meta-stable regimes responsible for low-frequency variability (Dellnitz and Junge, 1997; Froyland and Dellnitz, 2003; Chekroun et al., 2014). This confirms the work on meta-stable atmospheric regimes in this model by Crommelin (2003); we will see in section 5.3.3 how such regimes can be more objectively detected.

The second important feature, relevant to the problem of stochastic prediction of section 5.4.2, is the relative constance of the two leading rates for lags larger than 8 days. We can say that the slow dynamics associated with these rates "behave as Markovian", by which we mean that looking only at these rates, one cannot disprove the semigroup property, even though the dependance on the lag of the other rates is clearly indicative that $\{\hat{P_\tau}\}_{\tau\geq 0}$ cannot constitute a semigroup. Thus, the two leading rates do not seem to be affected by memory effects due to the partial observation of the system or by estimate errors, since one would not expect them to be constant otherwise.

From the separation of the two leading rates from the other rates as well as their relative independence on the lag τ for lags larger than 8 days, we expect 8 days to be the minimum lag for which the transition matrix $\hat{P}_{\tau=8}$ is likely to predominantly resolve the dynamics associated with the meta-stable regimes. Consequently, the following developments will rely mostly on the transition matrix $\hat{P}_{\tau=8}$. Such strategy for the choice of the lag is similar to the one of DelSole (2000) and Berner (2005), who look directly at the decorrelation rate of their time series to infer for which lag they should estimate the drift and diffusion coefficients of the Fokker-Planck equation they want to approximate. In our case, however, all the rates associated with the dominant eigenvalues of the transfer operators are considered and not only the decorrelation rate of the time series alone. Let us also acknowledge that the SMT has been used in Crommelin and Vanden-Eijnden (2011) to estimate the spectrum of the generator associated with a Fokker-Planck equation, in Froyland et al. (2013) to compare approximates of transfer operators and generators of low-dimensional dynamical systems and in Franzke et al. (2008) to test the meta-stability of Hidden Markov Models. However, we do not know other studies using the SMT to test the "Markovianity" of reduced systems, even though the τ-test in **?** serves a similar purpose in the context of Linear Inverse Modeling.

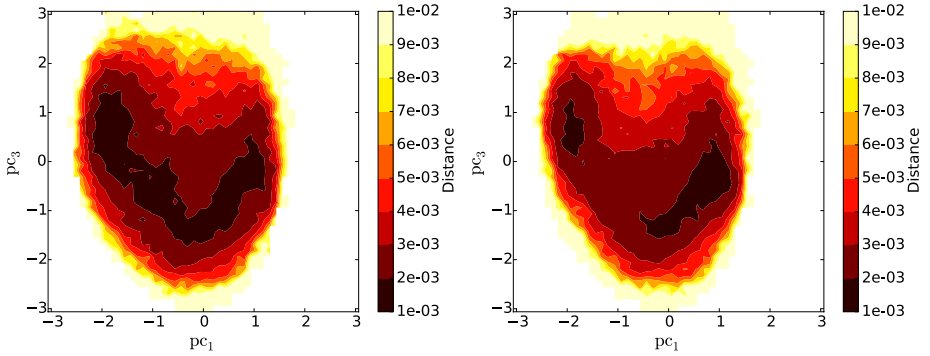

(a) (b)

Figure 5.5: The value at each grid point represents the distance, for an initial density of 1 at this grid point, between the density f_{8k}^{pow} transferred by the k^{th} power of $\hat{P}_8$ and a density f_{8k}^{long} transferred by $\hat{P}_{k\times 8}$ for (a) $k=2$ and (b) $k=4$.

5.3.2 *Further validation of the semigroup property*

We further test to which extent the semigroup property is violated for special cases of powers k of $\hat{P}_\tau$ and the corresponding matrices $\hat{P}_{k\times\tau}$. Rather than directly calculating a distance between the matrices $(\hat{P}_\tau^{\mathscr{R}})^k$ and $\hat{P}_{k\times\tau}$, we prefer to calculate, for an initial density f_0, the distance between the density $f_{k\tau}^{\text{pow}} = f_0(\hat{P_\tau})^k$ transferred by the k^{th} power of $\hat{P_\tau}$ and the density $f_{k\tau}^{\text{long}} = f_0\hat{P}_{k\times\tau}$ transferred by $\hat{P}_{k\times\tau}$. We use the distance $d(f,g) = \sqrt{\sum_{i=1}^m \pi_i(f_i-g_i)^2}$, which is a sum of squared errors between the components of f and g, weighted by the likelihoods $\hat{\mathbb{P}}(y_t \in B_i)$, so that errors in grid boxes less likely to be reached by the Markov process are given less weight. The distances $d(f_{k\tau}^{\text{pow}}, f_{k\tau}^{\text{long}})$ have been calculated for a set of m initial densities associated with each grid box in $\{B_i\}$, so that the density associated with box B_j integrates to 1 in B_j and to zero elsewhere. The distances are represented figure 5.5a and b for a lag τ of 8 days and for a multiplicator k of 2 and 4, respectively (dark colors indicate small distance).

To explain the nature of the violation of the semigroup property, let us recall that there exists only three possible candidates, namely (i) the partial observation of the dynamical system, (ii) the coarse-graining induced by the Galerkin approximation and (iii) sampling errors. Furthermore, it is shown in Appendix B.2, that the distances plotted figure 5.5 are not affected by the use of twice as more samples and that they only decrease slightly when the resolution increases (and vice versa). Thus, we can

say that positive distances in figure 5.5 are mostly the consequence of memory effects induced by the partial observation of the high-dimensional barotropic model.

We can observe that these memory effects are mostly important where the stationary density is small (figure 5.3) and thus, where trajectories are less likely to pass by. The denser regions which are associated with meta-stability, as will be seen section 5.3.3, seem to be less affected by memory effects. This result is in agreement with the relative constancy with lag of the leading rates, also associated with meta-stability. Such memory effects, as well as the dependence on the lag of the spectral gap between the leading rates, should be put in perspective with stochastic modeling with Stochastic Differential Equations (SDE) and based on time-scale separation (Majda et al., 1999, 2001; Franzke, 2014). Indeed, in such models, one seeks a reduced basis for the decorrelation time of the resolved variables to be much longer than the one of the unresolved variables, in order to be able to neglect the memory effects made explicit by the Mori-Zwanzig formalism (Darve et al., 2009; Chorin and Hald, 2009). If the transition matrices on the reduced phase space do not directly help in the choice of the basis on which the dynamical system can be optimally reduced, their rates can give insights on the impact of the reduction on the resolved variables.

5.3.3 *Meta-stable regimes as almost-invariant sets*

We have seen, section 5.3.2, that the two leading rates of figure 5.4 are close to zero and that a large spectral gap separates them from the rest of the rates, a configuration indicative of the presence of meta-stable regimes. This characteristic of meta-stability or persistence allows to formally define these regimes as almost-invariant sets (Dellnitz and Junge, 1997; Froyland and Dellnitz, 2003). We now give an extension of the definition of almost-invariant sets to sets in the reduced phase space and present an algorithm to detect them from a transition matrix $\hat{P}_\tau^{\mathscr{R}}$.

A set A of the phase space H is almost-invariant if $S_\tau^{-1}(A) \approx A$, so that

$$\mathbb{P}_\mu(S_\tau x \in A | x \in A) \approx 1. \tag{5.4}$$

Reformulating, the probability for a trajectory starting in a set A to leave this set after a lag τ is almost-zero. These sets are thus associated with persistent or meta-stable regimes.

In the case of almost-invariant sets in the reduced phase space, we are interested in almost-invariant sets E of Y, such that (see chapter 2)

$$\mathbb{P}_\mu(\mathscr{R}(S_\tau x) \in E | \mathscr{R}(x) \in E) \approx 1 \iff \mathbb{P}_\mu(S_\tau x \in h^{-1}(E) | x \in h^{-1}(E)) \approx 1. \tag{5.5}$$

This important result states that if a set E is almost-invariant in the reduced space Y, its pre-image $h^{-1}(E)$ in H is almost-invariant to the flow S_τ. In other words, almost-invariant sets in the reduced phase space are images of almost-invariant, yet coarser,

sets in the full phase space. Of course, these coarse-grained almost-invariant sets may not be optimal, in the sense that other, more strongly almost-invariant sets (w.r.t (5.4)) may exist but are filtered out by the observable h in the same way RP resonances can be filtered out by h.

Based on these considerations, the transition matrix $\hat{P}_{\tau=8}$ was used to define the meta-stable regimes objectively. For the detection of almost-invariant sets (see also, Dellnitz and Junge, 1997; Froyland and Dellnitz, 2003; Froyland and Padberg, 2009) we use an optimal Markov chain reduction (Deng et al., 2011; Rosvall and Bergstrom, 2008) with respect to the relative entropy rate Cover and Thomas (1991). This type of Markov chain reduction is particularly well suited for the detection of dense almost-invariant sets (highly recurrent), since it attempts to minimize the distance between a density transferred by the reduced transition matrix (giving the transition probabilities between the almost-invariants, see below) and the same density transferred by the original transition matrix. The optimization was implemented using the greedy algorithm from network theory (Clauset et al., 2004), where the grid boxes are iteratively merged to give coarser and coarser almost-invariant sets.

In accordance with the bimodality of the histogram (figure 5.3), we have chosen to look for a number of almost-invariant sets p of 2. These two sets are plotted in figure 5.6, such that all grid boxes in green belong to the first almost-invariant set and all grid boxes in blue belong to the second one. For the family of almost-invariant sets $\{E_\beta\}$, the 2-by-2 reduced transition matrix $\hat{Q}_{\tau=8,}$, such that $(\hat{Q}_{\tau=8})_{\beta\gamma} = \hat{\mathbb{P}}(y_{t+\tau} \in E_\gamma | y_t \in E_\beta)$, and its stationary density η, such that $\eta_\beta = \hat{\mathbb{P}}(y_t \in E_\beta)$, are found to be

$$\hat{Q}_{\tau=8} = \begin{pmatrix} 0.79 & 0.21 \\ 0.14 & 0.86 \end{pmatrix}, \quad \eta = \begin{pmatrix} 0.27 \\ 0.73 \end{pmatrix}, \tag{5.6}$$

the second almost-invariant set (in blue) being almost three times as dense as the first one (in green).

The algorithm is designed to find almost-invariant sets whose union covers the entire grid. However, in view of the early warning problem discussed in section 5.4, we need to find a restriction of the definition of the regimes $\{R_\beta\}$ to smaller regions of the grid so that the likelihood $\hat{\mathbb{P}}(y_t \in R_\beta)$ to be in any regime R_β becomes smaller than one (Kharin and Zwiers, 2003). To do so, we selected, for each almost-invariant set E_β, their grid boxes B_i maximizing the likelihood $\hat{\mathbb{P}}(y_t \in B_i, y_{t+\tau} \in E_\beta, y_{t-\tau} \in E_\beta)$ of a realization of $\mathbf{y}$ to be in B_i and to come from and go to the same almost-invariant set E_β, until a sufficiently large number of boxes have been attributed to the regime R_β to have $\hat{\mathbb{P}}(y_t \in R_\beta) = \hat{\mathbb{P}}(y_t \in E_\beta)/2$ (until half of the almost-invariant set has been selected in terms of stationary density π). These restrictions are plotted in dark green and dark blue (Fig. 5.6) and define the blocked and zonal regimes, respectively. The probability to stay in the so-defined blocked and zonal regimes after 8 days is of 66% and 70%, respectively.

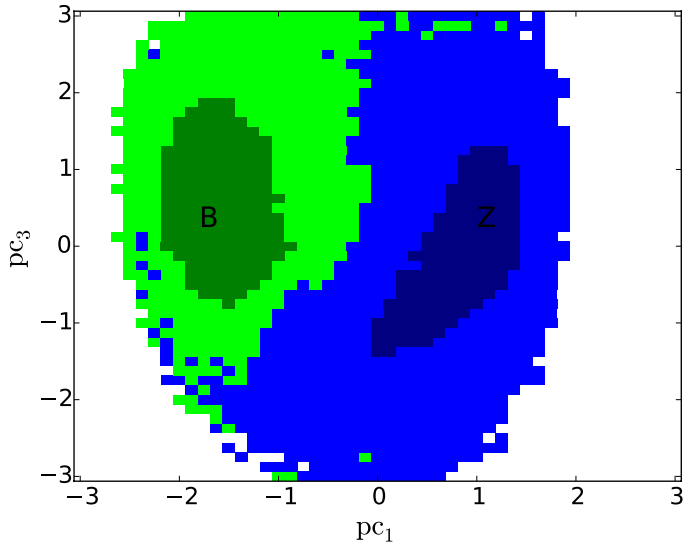

Figure 5.6: Two almost-invariants sets and their restrictions (in dark colors) corresponding to the blocked and the zonal regime, respectively.

It is shown in the Appendices B.1, B.2 and B.3 that these regimes are relatively robust to the limited length of the time series, to the grid resolution and to the lag, respectively. Their definition together with the transition matrices $\{\hat{P}_\tau^{\mathscr{R}}\}$ are used in section 5.4 to define an early warning indicator of a transition to the blocking regime.

5.4 PREFERRED TRANSITION PATHS AND EARLY WARNING

5.4.1 *Preferred transition paths*

Having defined the regimes, we now study the transitions between them. Following Branstator and Berner (2005), we first plot the mean tendencies of the normalized principal components pc_1 and pc_3. The tendencies were calculated for each principal component using a finite difference scheme such that $\Delta\mathrm{pc}_i(t) = (\mathrm{pc}_i(t+\Delta t) - \mathrm{pc}_i(t))/\Delta t$, where $\Delta\mathrm{pc}_i$ is the approximate tendency of the i^{th} principal component and Δt is the time step. An estimate of the mean tendency for each grid box was then calculated by averaging over all the realizations of $\mathbf{y}$ in this grid box.

The mean tendency for a time step Δt of 8 days is plotted figure 5.7. It can be seen as a composition of a clockwise rotation and two sinks. This result corroborates both the meta-stability of the regimes and the existence of preferred transition paths

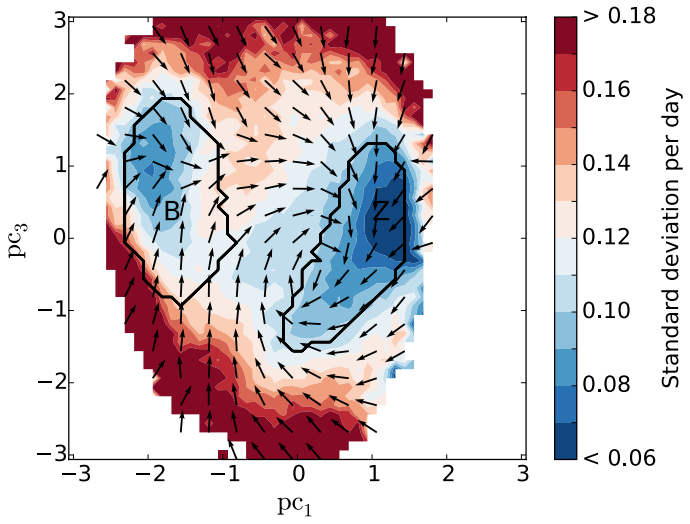

Figure 5.7: Mean tendency of the normalized principal components calculated using centered differences for $\Delta t = 8$ days. Arrows represent the direction and the colors represent the magnitude (in standard deviation per day). As for the following figures, the black contours delimitate the blocked regime, marked by the letter B, and the zonal regime, marked by the letter Z.

between them, reminiscent of a pseudo-periodic orbit (Plaut and Vautard, 1994; Crommelin, 2003). Indeed, the rotation is such that typical trajectories leaving the zonal regime (blocked regime) to go to the blocked regime (zonal regime) transit through negative values (positive values) of pc_3. Furtermore, the correspondence between the sinks with low values of mean tendency and the regimes is striking, in particular for the zonal regime. We have seen in section 5.3.2 that the memory effects are relatively weak in the region of the regimes. In the limit when these effects can be neglected, the reduced dynamics can be modeled by an SDE and the mean tendency gives an approximation of the drift term involved in the Fokker-Planck equation (together with diffusion, not calculated here, Berner, 2005; Gardiner, 2009) which generates the semigroup of transfer operators associated with the SDE. The correspondence between weak tendency and almost-invariance is thus not coincidental.

To further support the existence of preferred transition paths from one regime to the other, we have calculated, for each grid box, the likelihood $\hat{P}_{ZB}$ ($\hat{P}_{BZ}$) that a trajectory starting in the zonal regime (blocked regime) and passing through this grid box reaches the blocked regime (zonal regime) before the zonal regime (blocked regime). Such likelihoods are sometimes referred to as committers in molecular dy-

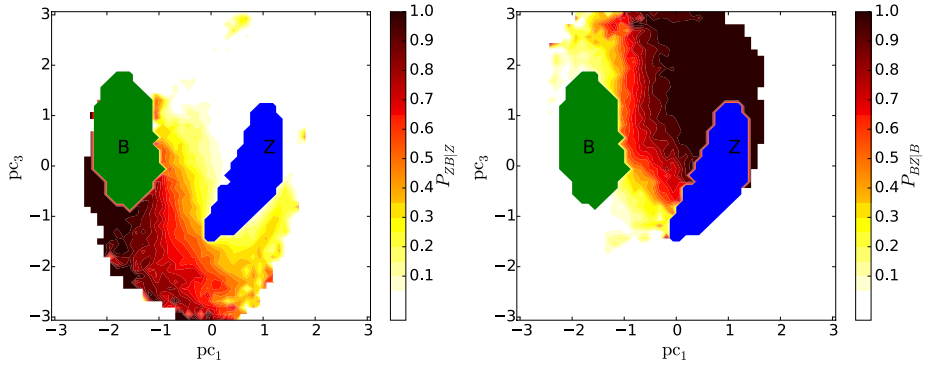

(a) (b)

Figure 5.8: Likelihood, for each grid box, to reach (a) the blocked regime before the zonal regime and (b) the zonal regime before the blocked regime.

namics (see e.g. Schütte and Marco Sarich, 2013) and can be used for the detection of meta-stable regimes as well.

The resulting likelihoods are plotted in figure 5.8. In agreement with the tendency, the trajectories going from the zonal to the blocked regime are more likely to do so through low values of the 3^{rd} principal component while trajectories going from the blocked to the zonal regime favor high values of the 3^{rd} principal component.

5.4.2 *Early warning indicator*

The presence of preferred transition paths from the zonal to the blocked regime, as well as the weak mixing associated with the existence of rates close to zero (cf. section 5.3.1), suggests that there is potential skill in predictability of transitions to the blocked regime. Note that more than trying to predict when a trajectory will leave the zonal regime, we want to use the fact that trajectories leaving the zonal regime are more likely to go to the blocked regime if they transit through negative values of pc_3. We therefore use the transition matrices for different lags to provide an approximation of the transfer of densities in the reduced phase space by the flow and to build an early-warning indicator of transitions to the blocked regime.

The quality of the indicator will depend on (i) the predictability of the full system (in terms of sensitive dependence to initial conditions or rate of decay of correlations) and (ii) the validity of the Markov approximation for the reduced dynamics. While the former is determined by the dynamical system alone, the latter depends on the choice of the observable. We have seen in section 5.3 that the violation of the

semigroup property indicates that the reduced dynamics are overall non-Markovian. However, the constancy of the leading rates also indicates that motions associated with the meta-stable regimes behave as Markovian, suggesting that densities transferred by the estimated transition matrices could be used to give a probability of reaching one of the regimes.

The early-warning indicator is thus designed as such. Whenever the observed trajectory (in our case, the simulation) leaves the zonal regime, we define an initial density $f_{B_i,\tau=0}$, integrating to 1 over grid box B_i to which the last observation belongs and to zero elsewhere (one could instead define an initial density spreading over several boxes to account for uncertainties in the observation). Next, the Markov approximation $f_{B_i,\tau=1}$ of the transfer of $f_{B_i,\tau=0}$ by the flow after a lag τ of 1 day is calculated as $f_{B_i,\tau=0}\hat{P}_{\tau=1}$. We then calculate the likelihood $\hat{\mathbb{P}}(y_{\tau=1} \in R_{\text{block}} | y_0 \in B_i) = \sum_{B_j \in R_{\text{block}}} (f_{B_i,\tau=1})_j$ for a realization y_{t+1} to belong to the blocking regime knowing that y_t belongs to grid box B_i. If this estimated probability exceeds a given critical probability p_c, an alarm of transition to the blocked regime after a lag τ_{alarm} of 1 day is given. Otherwise, the same process is repeated for $\tau = 2, 3, \ldots$ until an alarm is given or a limit lag $\tau_{\max}$ is reached, after which we wait for the next observation to run the forecasting system.

To illustrate this process we show in figure 5.9 the transferred density for grid box 314 marked as a blue square and lying in the region of preferred transition paths between the zonal and the blocked regimes. This initial density $f_{B_{i=314},\tau=0}$, is plotted alone panel d). The densities $f_{B_{i=314},\tau=4}$, $f_{B_{i=314},\tau=8}$ and $f_{B_{i=314},\tau=16}$ transferred using the transition matrices $\hat{P}_{\tau=4}$, $\hat{P}_{\tau=8}$ and $\hat{P}_{\tau=16}$ are plotted panel (a), (b) and (c), respectively. The densities $f_{B_{i=314},\tau=2\times4}$ and $f_{B_{i=314},\tau=2\times8}$ transferred using the square of the transition matrices $\hat{P}_{\tau=4}$ and $\hat{P}_{\tau=8}$ are also plotted panel e) and f), respectively, to show how the semigroup property can be violated. The corresponding likelihoods to reach the blocked regime are written in the top left of each panel.

We can see that if a critical probability p_c of 0.3 would be chosen, an alarm of transition to the blocking regime would be raised for $\tau = 8$ days (figure 5.9b), as described in the previous paragraph. Figure 5.10 shows the grid boxes for which an alarm would be given if a critical probability p_c of 0.3 was used and the respective lag τ_{alarm} after which the transition is predicted to occur. In this case, alarms are mainly flagged for trajectories passing through grid boxes close to the blocked regime or in the region of low principal component pc_3.

The quality of the early warning indicator of transition to the blocked regime was tested over all trajectories starting when leaving the zonal regime and ending when reaching any of the regimes. In order to take into account sampling errors in the estimation of the transition matrices, the test was performed on a second 500,000-day-long simulation which was ran taking as initial state the last state of the original simulation from which the transition matrices were estimated. Out of the 11759

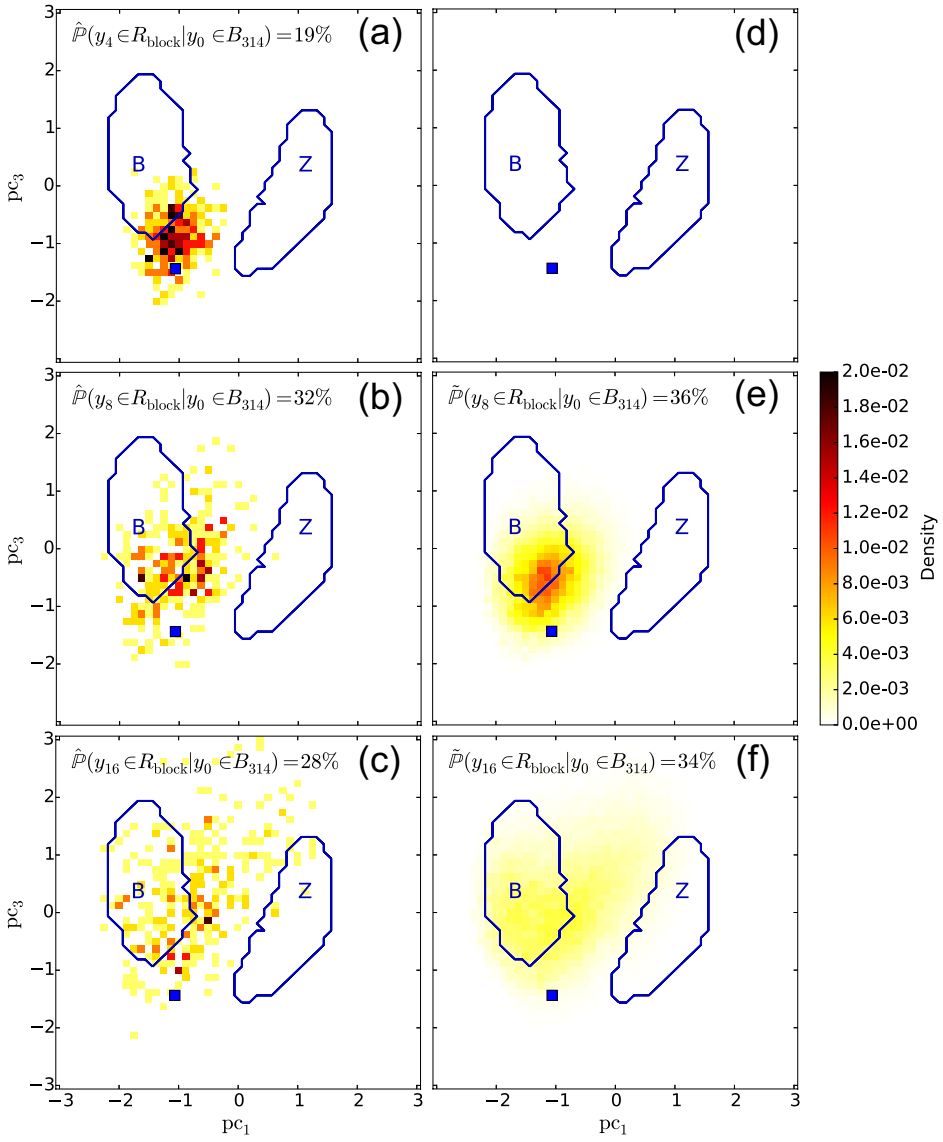

Figure 5.9: Approximation $f_{B_{i=314},\tau}$ of the transfer of the initial density $f_{B_{i=314},\tau=0}$ for a lag τ of (a) 4 days, (b) 8 days and (c) 16 days. The initial density is plotted in panel (d), integrating to one over box $B_{i=314}$ and to zero elsewhere. The densities transferred using the square of $\hat{P}_{\tau=4}$ and of $\hat{P}_{\tau=8}$ are plotted panel (e) and (f), respectively. The corresponding likelihoods to reach the blocked regime are written in the top left of each panel.

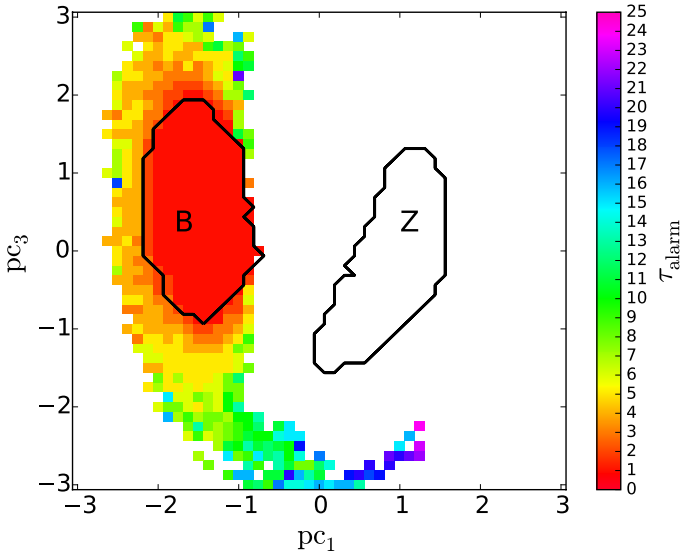

Figure 5.10: Predicted time of transition to the blocked state τ_{alarm}, in days, for each grid box where an alarm is given for a critical probability p_c of 0.3.

trajectories starting from the zonal regime, 1993 reached the blocked regime, which we call an *occurrence* event (O), while 9766 reached the zonal regime, which we call a *nonoccurrence* event ($\overline{\text{O}}$).

When testing a forecast system, one is interested in how many alarms (A) were given when the event actually occurred, the number of so-called *hits*, and how many did not occur, the number of so-called *false alarms*. In the case of a hit, the event occurs at a given time τ_{occ} after the alarm is given, so that not only the occurrence of the event should be forecasted, but also when it will occur. For easy reference, the different cases are shown in Table 5.1. For example, a forecast that a blocking event will occur in a month although it will truly occur only a week later is not of much help. For the purpose of assessing the skill of a forecast not only in terms of occurrence but also in terms of precision of the forecasted date of occurrence, we need to define a tolerance ϵ, in days, such that a hit (H) is granted only when an alarm is given with a prediction time τ_{alarm} such that $\tau_{\text{occ}} - \epsilon \leq \tau_{\text{alarm}} \leq \tau_{\text{occ}} + \epsilon$. If, however, the event is predicted to happen too early ($\tau_{\text{alarm}} < \tau_{\text{occ}} - \epsilon$), it is counted as a *false alarm of type II* (FA2), while if the event is predicted to happen too late ($\tau_{\text{alarm}} > \tau_{\text{occ}} + \epsilon$), it is counted as a *missed alarm of type II* (MA2). When the event did not occur and no alarm ($\overline{\text{A}}$) was given, we count a *correct rejection* (CR). When an event occurs but no alarm is given, we count a *missed alarm of type I* (MA1) and

Table 5.1: Overview of the different cases which can occur depending on the alarm given and the event occurring.

	A	A	A	$\overline{\text{A}}$
	$\tau_f < \tau_o - \epsilon$	$\lvert\tau_f - \tau_o\rvert \leq \epsilon$	$\tau_f > \tau_o + \epsilon$	
O	FA2	H	MA2	MA1
$\overline{\text{O}}$	FA1	FA1	FA1	CR

when an event is predicted but does not occur, we count a *false alarm of type I* (FA1).

To assess the skill of the forecasts based on the categories defined in Table 5.1, we adapted the original Peirce skill score (PSS) (Peirce, 1884; Stephenson, 2000) to forecasts including the time of occurrence. In our case, we define the PSS as

$$S_{Peirce}(p_c) = \text{HR}(p_c) - \text{FAR}_1(p_c),$$

where $\text{HR}(p_c) = \text{H}(p_c)/\text{O}(p_c)$ is the hit rate, defined as the ratio of the number of hits over the number of occurrences, and $\text{FAR}_1(p_c) = \text{FA1}(p_c)/\overline{\text{O}}(p_c)$ is the false alarm rate of type I. The hit rate gives the likelihood of giving an alarm when the event occurs, while the false alarm rate of type I gives the likelihood that an alarm is given but the event does not occur. If the hit rate exceeds the false alarm rate the PSS is positive and the forecast has skill. A PSS of 1 is reached for a perfect forecast, when alarms are only raised when an event will actually occur and with the right predicted time of occurrence.

The PSS is plotted figure 5.11 versus the critical probability p_c and for different tolerances ϵ. A tolerance of ∞ means that the precision of the predicted date of occurrence is not taken into account in the skill score. It is evident that as the tolerance increases, the skill score increases as well. The PSS reaches a maximum for a critical probability around 0.5, depending on the tolerance. Such scores have to be put in perspective with the predicted time of occurrence τ_{alarm}. Indeed, a successful prediction of occurrence of a blocking event 1 day ahead is counted as a hit, but is not of much practical use. For this reason, we have also represented the average prediction time τ_{alarm} as a black dashed line on the same figure 5.11. It is of around two weeks for a critical probability of 0.3 and around one week for a critical probability of 0.45. Thus, depending on the final purpose of the forecast system, a compromise has to be found between the skill of the forecast system and how many days ahead an event is predicted on average. Choosing a critical probability of 0.3 would give a reasonably good skill score of 0.4 (better than a no-skill forecast) with an average prediction time of 2 weeks.

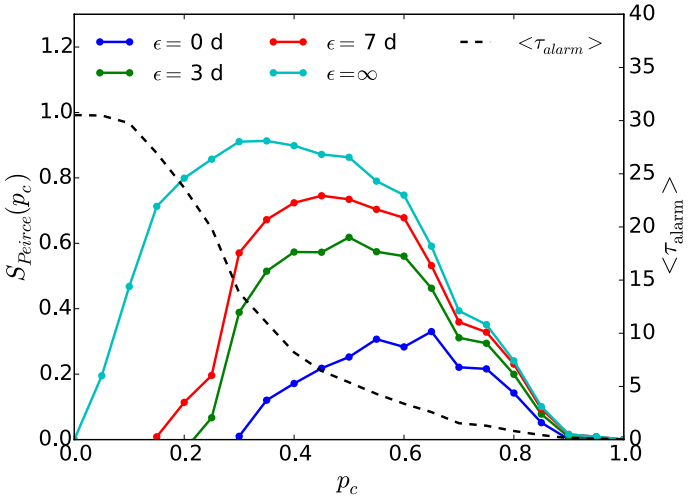

Figure 5.11: Peirce skill score of the probability forecast of reaching the blocked regime versus the critical probability p_c for different tolerances ϵ (straight lines). The average time lag in days for which an alarm is given is also plotted in black dashed line.

To summarize, the main advantage of a forecast system relying on the transfer of densities is that it constitutes a very cheap way to account for the sensitive dependence on initial conditions of a chaotic dynamical system.

5.5 ENERGETICS OF THE TRANSITIONS

In this section we focus on the remaining question on how the dynamics of the barotropic model can explain (i) the persistence of each regime and (ii) the preferred transition paths from the zonal to the blocked regime through high values or pc_3.

To help clarifying these issues the hemispheric energy budget of the model is studied. First, the fields are decomposed in a $\bar{\tau} = 8$ days running mean and a deviation from it. This decomposition yields for the streamfunction

$$\psi = \overline{\psi} + \psi' \quad \text{with} \quad \overline{\psi} = \frac{1}{\bar{\tau}} \int_{t-\bar{\tau}/2}^{t+\bar{\tau}/2} \psi \, dt'. \tag{5.7}$$

Inserting (5.7) into equation (5.1)and applying the running mean gives the equation of the mean relative vorticity

$$\frac{\partial \nabla^2 \overline{\psi}}{\partial t} + \mathcal{J}(\overline{\psi}, \nabla^2 \overline{\psi} + f + h) + \overline{\mathcal{J}(\psi', \nabla^2 \psi')} = -k_1 \nabla^2 \overline{\psi} + k_2 \nabla^8 \overline{\psi} + \nabla^2 \psi^*. \tag{5.8}$$

Subtracting (5.8) from (5.1) gives the equation of the deviation from the running mean as

$$\frac{\partial \nabla^2\psi'}{\partial t} + \mathcal{J}(\overline{\psi}, \nabla^2\psi') + \mathcal{J}(\psi', \nabla^2\overline{\psi} + f + h)$$
$$+\mathcal{J}(\psi', \nabla^2\psi') - \overline{\mathcal{J}(\psi', \nabla^2\psi')} = -k_1\nabla^2\psi' + k_2\nabla^8\psi'. \tag{5.9}$$

In order to obtain the equation of the hemispheric average of the mean kinetic energy $\overline{E} = < \frac{\overline{u}^2+\overline{v}^2}{2} >$, with $< \cdot >$ denoting the hemispheric average $\frac{1}{2\pi}\int_0^{2\pi}\int_0^{\pi/2} \cdot \cos\phi \, \mathrm{d}\phi \, \mathrm{d}\lambda$, equation (5.8) is multiplied by $\overline{\psi}$ and averaged hemispherically, giving

$$\frac{\partial \overline{E}}{\partial t} = < \overline{\psi}\, \overline{\mathcal{J}(\psi', \nabla^2\psi')} > -2k_1\overline{E} - k_2 < \overline{\psi}\nabla^8\overline{\psi} > - < \overline{\psi}\nabla^2\psi_* > . \tag{5.10}$$

The first term on the right hand side is equal to the opposite of the sum of the Reynolds' stress terms which represent a conversion of mean to eddy kinetic energy. Finally, multiplying (5.9) by ψ', applying the running mean and averaging over the hemisphere gives the equation of the global eddy kinetic energy $E' = < \frac{\overline{u'^2}+\overline{v'^2}}{2} >$

$$\frac{\partial E'}{\partial t} = - < \overline{\psi}\overline{\mathcal{J}(\psi', \nabla^2\psi')} > -2k_1E' - k_2 < \psi'\nabla^8\psi' > . \tag{5.11}$$

The terms in the equations (5.10) and (5.11) were calculated from the model simulation results and we could verify that the calculated tendencies equated the sum of the right hand side terms but for a small error of up to 13% of the standard deviation of the tendencies due to the running average of a deviation not being exactly zero.

The energetics of the transitions can be studied by plotting the kinetic energies (Fig. 5.12) and the terms in the energy budget (Fig. 5.13) averaged for each grid box of the reduced phase space. To these plots, a 200 days long trajectory transiting smoothly from the zonal to the blocked regime is added in green, starting with a black square and ending with a black triangle. It is first interesting to notice that low values of E' coincide rather well with our definition of the regimes (Fig. 5.12b). That fact that the eddies are weak in the neighborhood of the regimes is mostly explained by low values of conversion to eddy kinetic energy (Fig. 5.13c), in particular for the zonal regime, and additionally by a negative forcing for the blocked regime (Fig. 5.13c-d). This stabilization of the flow in the region of the regimes is a good physical candidate to explain their persistence.

We have seen (section 5.4), that typical trajectories from the zonal to the blocked regime transit through the region of negative pc_3. Figures 5.12 and 5.13 allow us to give a typical scenario for such a transition. Each step of the following scenario is marked in figures 5.12 and 5.13 by the corresponding number.

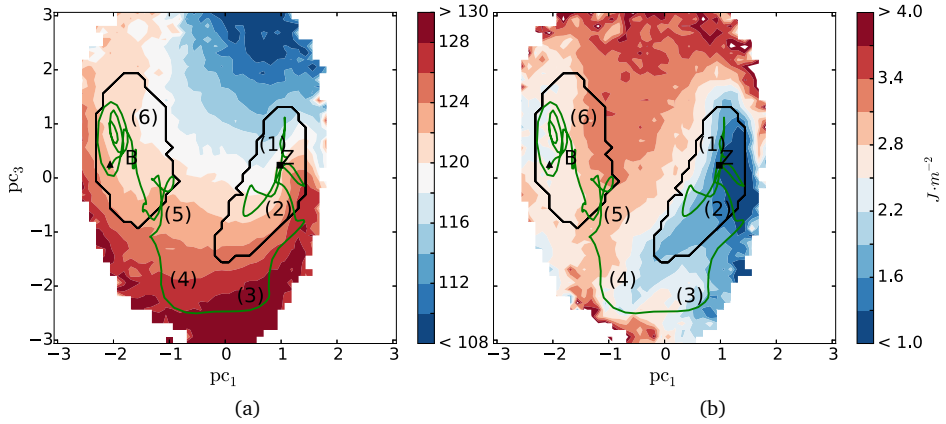

Figure 5.12: (a) Hemispheric mean kinetic energy $\overline{E}$ in Jm^{-2}, (b) Hemispheric eddy kinetic energy E' in Jm^{-2}. The green line, starting with a black square and ending with a black triangle, represents a 200 days long trajectory transiting from the zonal to the blocked regime.

1. Starting in the zonal regime, the Reynolds' stress terms are small and the mean flow is stable. However, the positive forcing induces an increase of the mean kinetic energy $\overline{E}$.

2. As $\overline{E}$ increases and the forcing persists, the trajectory evolves to lower value of pc_3 and eventually leaves the zonal regime.

3. The trajectory then reaches a region of pc_1 close to zero and low pc_3. The forcing is still strong but the Reynolds stress terms begin to increase because the strongly sheared flow becomes barotropically unstable for lower values of pc_3, so that the total eddy kinetic energy E' continues to increase.

4. As the trajectory reaches lower values of pc_1, the forcing reverses but the Reynolds' stress terms continue to increase as the barotropic eddies which emanated at the previous step develop, so that $\overline{E}$ is converted to E' which continues to increase.

5. The trajectory then goes to larger values of pc_3 where the forcing is negative and energy is removed both from the mean flow and from the eddies so that the barotropic eddies decay.

6. The trajectory eventually reaches the blocked regime for lower values of pc_1 where E' decreases due to the negative forcing coincident with relatively small Reynolds' stress terms. The mean flow is once again relatively stable, although

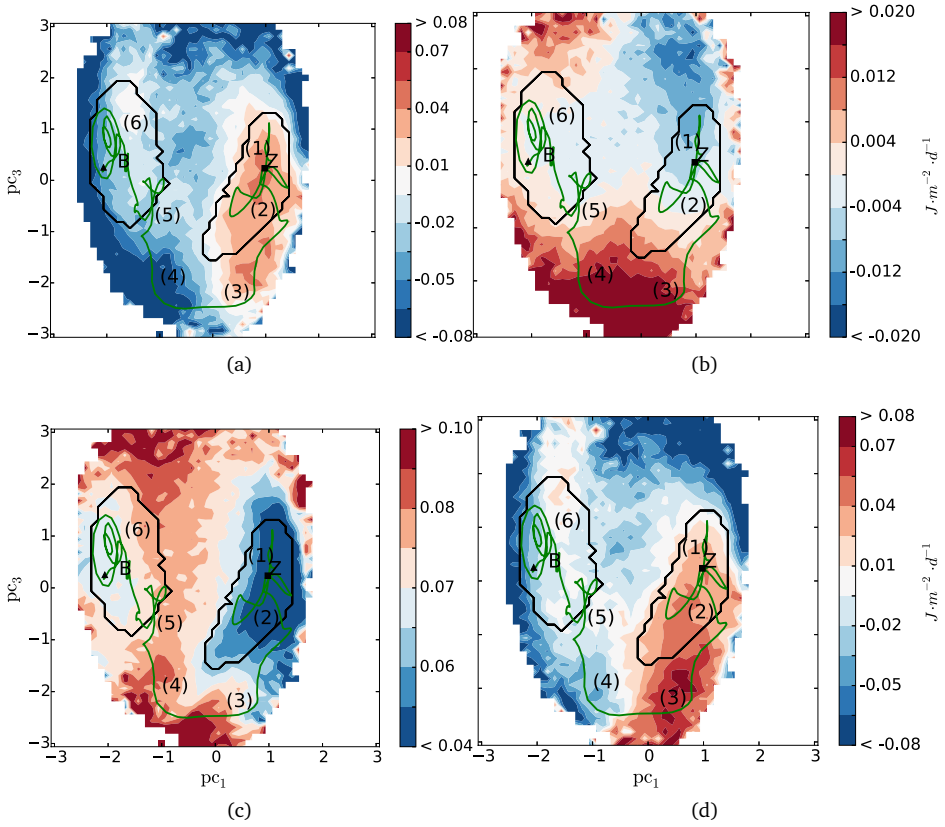

Figure 5.13: (a) Tendency of the hemispheric mean kinetic energy in $Jm^{-2}day^{-1}$, (b) Tendency of the hemispheric eddy kinetic energy in $Jm^{-2}day^{-1}$, (c) Hemispheric Reynold's stresses (conversion from mean to eddy kinetic energy when positive) in $Jm^{-2}day^{-1}$, (d) Sum of hemispheric forcing and dissipation in $Jm^{-2}day^{-1}$. The green line, starting with a black square and ending with a black triangle, represents a 200 days long trajectory transiting from the zonal to the blocked regime.

not as much as for the zonal regime, as can be seen for the relatively large Reynolds stress terms in the region of largest pc_1 inside the blocked regime.

This scenario is consistent with the mechanisms of chaotic itinerancy (Itoh and Kimoto, 1996), heteroclinic connections (Weeks et al., 1997; Crommelin, 2003) and almost-invariant sets bounded by invariant manifolds (Froyland and Padberg, 2009). Indeed, when the reduced state is in the zonal regime, the flow is relatively stable as it belongs to what would be the basin of attraction of the zonal regime. However, as it moves towards the neighborhood of positive forcing, energy is given to the mean flow, the horizontal shear increases and the flow becomes unstable to small perturbations. The increasing Reynolds' stress term indicates that the perturbation grows, starts to interact with the mean flow and enables the state to leave the basin of attraction of the zonal regime.

5.6 SUMMARY AND DISCUSSION

Using concepts of transfer operators of dissipative dynamical systems, stochastic reduction and meta-stable regimes, we developed an early warning indicator of midlatitude atmospheric regime transitions. It was applied here to the transitions between a zonal and blocked flow in a barotropic hemispheric atmosphere model.

Transfer operators yield the evolution of densities induced by the flow. Markov operators have been estimated on the reduced phase space to approximate the point spectrum of the generator of the transfer operators, namely the ergodicity spectrum. Their approximation for different lags have been used to assert the presence of slow dynamics associated with meta-stable regimes and the impact of memory effects on these motions. The presence of rates close to zero and separated from the rest of the spectrum supports the existence of almost-invariant sets associated with meta-stable regimes and with time scales of three to six weeks. Furthermore, the relative constancy of these rates showed that memory effects are weak in the meta-stable regimes and along the transition path from the zonal to the blocked regime.

In order to objectively define these regimes, we have developed an algorithm for the computation of almost-invariant sets based on earlier work in (Dellnitz and Junge, 1999; Froyland and Dellnitz, 2003; Froyland and Padberg, 2009), as well as on optimal Markov chain reduction (Deng et al., 2011; Rosvall and Bergstrom, 2008) and greedy optimization in networks (Clauset et al., 2004). The algorithm attempts to minimize a measure of the distance between the reduced Markov operator (giving the transition probabilities between the almost-invariants) and the original one and allows the detection of sets which are both recurrent and persistent. The algorithm has enabled us to robustly define the blocked and the zonal regimes.

Compared to spectral almost-invariant detection algorithms such as developed earlier by (Dellnitz and Junge, 1997, 1999; Froyland and Dellnitz, 2003; Froyland and Padberg, 2009), which are based on the decomposition of the leading eigen-

vectors of the transfer operator into characteristic functions supporting the almost-invariant sets, our algorithm is expected to perform better in the detection of more than two almost-invariant sets, since the latter uses an aggregative implementation rather than a divisive one like the spectral algorithms. For example, a similar algorithm (Rosvall and Bergstrom, 2008) has been used for the detection of a dozen of communities, associated with spatial patterns of variability, in a correlation network of sea surface temperature (Tantet and Dijkstra, 2014). In this study, we were only interested in the bi-partition problem and our algorithm showed comparable performance in terms of invariance with respect to that in (Froyland and Padberg, 2009).

The transfer operator based algorithms are also comparable to Hidden Markov Models (HMM, Majda et al., 2006; Franzke et al., 2008), with the difference that the former are nonparametric (no assumption is made on the distribution of the reduced states). Contrary to HMM, our algorithm detects hard clusters (nonoverlapping sets) and takes as input the transfer operator rather than directly the time series of the observable. In theory, it would be possible to adapt the algorithm to soft clustering (to allow overlapping between the clusters) but the optimization problem would become harder as it would necessitate another algorithm than the (combinatorial) greedy algorithm.

The energy budget of the model showed that striking similarities exist between regions of low EKE and regions of almost-invariance, weak tendency and small memory effects. Low EKE is indicative of stability of the mean flow and thus of almost-invariance, low tendency as well as weaker memory effects due to the small amplitude of the faster unresolved variables.

The early warning indicator is based on a forecasting scheme involving the evolution of densities by the estimated transfer operator in a two-dimensional reduced phase space spanned by two EOFs of the model. It relies on the Markov approximation of the evolution of an initial density in the neighborhood of the latest observation of the system and on the estimation of the probability to reach the blocked regime. A warning is broadcasted for a lag τ_{alarm} if this probability exceeds a prescribed critical probability. The quality of the early warning indicator, as measured by the Peirce Skill Score, is highest for a critical probability of about 0.5 but a smaller critical probability of 0.3 allows to emit warnings two weeks ahead of the event, on average. A next step is to investigate how this promising indicator would perform for more realistic models of atmospheric flow transitions.

While the model here has obvious deficiencies (e.g. the lack of the representation of baroclinic instability), it is one of the midlatitude atmospheric models for which regime transitions are found and hence forms a nice test model for the development of the early warning indicator. The computational procedure can in principle be carried out with a General Circulation Models (GCM) exhibiting regime behavior (Dawson et al., 2012, 2014), if sufficiently long simulations can be performed. Note that in our case, we used a 500,000-day-long simulation ($\sim$ 1300 years) to assure the signi-

ficance of our statistics. However, the dominant part of the spectrum was found to be robust to the use of only 50×365 samples which is the typical size of an operational GCM or a reanalysis record. The question remains if the transfer operator based early warning indicator would perform well with nearly Gaussian GCM or observational data (Dawson et al., 2012, 2014; Majda et al., 2006), where it is not clear whether preferred transition paths between the meta-stable regimes exist.

Another application could be to estimate transfer operators from a long run of an operational weather prediction GCM and use these operators in parallel with a deterministic run of the GCM, in order to account for both uncertainty in the deterministic forecast (Palmer et al., 2005), and to give an early warning indicator of transition to a new meta-stable regime.

Finally, the early warning indicator presented here certainly extends those based on critical slowdown (Scheffer et al., 2009), such as the increase in variance and lag-1 autocorrelation, which definitely have problems in high-dimensional phase space. Even the network based indicators (van der Mheen et al., 2013; Viebahn and Dijkstra, 2014; Feng et al., 2014; Tirabassi et al., 2014) are not readily extended to high-dimensional systems. It is therefore hoped that the techniques in this chapter will find application in many types of chaotic high-dimensional systems as found in physics and engineering.

6

GENERAL SUMMARY AND DISCUSSION

Some applications of ergodic theory and nonequilibrium statistical physics to climate were presented in this work. The focus was on transfer operators governing the evolution of statistics by the dynamics. In particular, we have argued that the spectrum of these operators, the ergodicity spectrum, allows to characterize climate variability and response to forcing. We have started our demonstration with known theoretical results supporting the application of transfer operators to the study of high-dimensional chaotic or stochastic systems, such as climate. In particular, the gap between the leading eigenvalues of the transfer operators is directly related to the sensitivity of the system to perturbation. The practical applicability of the theory was then shown to be made possible by the reduction method introduced by Chekroun et al. (2014) to the climate community. Indeed, transfer operators act on functions of a state living in a possibly high-dimensional phase space. Instead, the reduction method allows to approximate the transfer operators by their projections acting on functions on a reduced phase space. Supporting the applicability of the reduction method to the study of the stability of a dynamical system, it was shown for the first time that the spectral gap calculated from reduced transfer operators gives an upper bound to the true spectral gap of the transfer operators.

Our first application was concerned with an Ornstein-Uhlenbeck process (OU). The first goal of this short study was to test the reduction method on a simple stochastic system of relevance to climate (Hasselmann, 1976). Second, it allowed to present known results regarding the ergodicity spectrum of an OU, proved by Metafune et al. (2002), which were subsequently used to give novel analytical formulas for the ergodicity spectrum of linear Stochastic Delay Differential Equations (SDDEs). These results were directly applied to the analysis of a simple yet very insightful stochastic delayed oscillator model of El Niño-Southern Oscillation (ENSO) (Battisti and Hirst, 1989). The ergodicity spectra obtained analytically and through the reduction method were found to be in very good agreement with each other and to characterize the periodicity and the stability of the system. The nonlinear case was then treated, supported by novel results on a simple form of stochastic Hopf bifurcation. Such a bifurcation is found both in the stochastic nonlinear delayed oscillator (Suarez and Schopf, 1988) and in the stochastic Zebiak-Cane model (Zebiak

and Cane, 1987; van der Vaart et al., 2000; Roulston and Neelin, 2000). The developments on the simple form of stochastic Hopf thus allowed to give a good interpretation of the behavior of the reduced ergodicity spectra in this model. In particular, as expected from the theory, it was found that the ergodicity spectrum shrinks to the imaginary axis at the approach of the bifurcation, resulting in the critical slowing down of the system.

These developments allowed to gain some insights regarding the relationship between the ergodicity spectrum and the stability of a system. These first applications dealt with high-dimensional yet nonchaotic problems. On the other hand, the aim of our second application was to show that much could be learned regarding the stability of a high-dimensional and chaotic system from the reduced ergodicity spectrum. The method was thus applied to the transition from warm to snowball Earth found in PlaSim, a chaotic General Circulation Model (GCM) of intermediate complexity. Critical slowing down was found before the crisis, as seen from the slower decay of correlations at the approach of the criticality. While this phenomenon is known for stochastically forced nonchaotic systems, the underlying mechanism is more subtle in the case of deterministic chaotic systems like PlaSim. Physically, it is due to the excitation of the instability mechanism by spontaneous fluctuations along the attractor rather than by exogenous perturbations. A mathematical mechanism was also proposed based on the collision of the attractor with a repeller (Grebogi et al., 1983; Schneider et al., 2007). The main result was that this slowing down could be traced back to the approach of reduced ergodicity spectra to the imaginary axis.

The last application was concerned with the study of midlatitude blocking events in a hemispheric barotropic model of the troposphere with realistic forcing. It is found that these regimes are associated with the ergodicity spectrum responsible for a slow decay of correlations. This allowed to extract them as almost-invariant sets connected by preferred transition paths. These paths were shown to constitute a source of predictability allowing to design an early-warning indicator of transition from the zonal to the blocked regime with relatively good skills.

Several questions raised in the body of this dissertation remain to be discussed. A crucial topic is whether the real-world climate can in fact undergo abrupt or at least nonlinear changes in response to forcing.Indeed, if such events were to happen during the 21st century due to increased greenhouse gas concentrations, they could have a major impact on our societies. In particular, the current efforts to calculate the "climate sensitivity" (Knutti and Hegerl, 2008; Roe, 2009; Collins et al., 2013) may be of little help if nonlinear contributions are important (Rugenstein et al., 2015; Paynter and Frölicher, 2015) or if the climate response to forcing depends on the background climatic state (von der Heydt et al., 2014; Köhler et al., 2015; Knutti and Rugenstein, 2015). A dynamical systems perspective to these issues has been given by Zaliapin and Ghil (2010), with examples taken from low-dimensional systems (see also Zaliapin and Ghil, 2011). In this sense, the study of the ergodicity spectrum of a GCM in chapter 4 can be seen as a extension of their work in the dir-

ection of high-dimensional chaotic systems. Unfortunately, state-of-the-art climate models may not be able to simulate such abrupt changes (Valdes, 2011; Drijfhout et al., 2013). This is related to the question of structural stability of climate models considered by McWilliams (2007). It is sometimes argued that critical phenomena exhibited by some low-dimensional or intermediate complexity models may not exist in the real-world climate. For example, missing physical processes such as meridional eddy heat transport may balance instability mechanisms like the ice-albedo feedback. It has actually been shown in Dawson et al. (2012) and Drijfhout et al. (2013) that the opposite can occur. For instance, small-scale atmospheric processes may be important for such critical behavior. As a consequence, it is crucial to understand whether critical phenomena, such as the Meridional Overturning Circulation (MOC) collapse (Dijkstra, 2005, Chap. 6), persist as climate models become more realistic. We have seen in this work that the methodology of reduced transfer operators is very well suited to study critical phenomena. Future work will thus focus on the application of this framework to the investigation of the possibility of abrupt or nonlinear climate changes.

Secondly, this work has focused on the steady-state response of climate to forcing. However, our societies are primarily impacted by transient climate changes occurring during the century. Indeed, the rate at which greenhouse gas concentration increases, due to anthropogenic emissions is rather fast compared to the internal relaxation time of the climate system to a statistical steady state. These relaxation times are associated with the leading ergodicity eigenvalues of the climate system and may be as large as thousands of years or more due to ocean dynamics. Thus, it is important to go further than the study of the steady-state response of climate to forcing and to consider its transient behavior as well. Ruelle's response theory provides an interesting framework for the study of such transient phenomena. Its practical implementation for the linear response of selected observables has been shown to be feasible by Lucarini and Sarno (2011) and has been applied to a GCM of intermediate complexity in Ragone et al. (2015). On the other hand, the methodology of reduced transfer operators presented in chapter 2 is not directly applicable to transient problems, since one long transient time series is not sufficient to sample the time-dependent invariant measure. Moreover, in the transient case, it is not clear how to relate the commonly used sample correlation function (see e.g Boulton et al., 2014) to transfer operators. The main difficulty comes from the fact that transfer operators of nonautonomous systems do not constitute a one-parameter semigroup. This is a major hindrance to giving firm theoretical grounds to early-warning indicators based on the correlation function (or spectrum) such as the lag-1 autocorrelation in the transient case. More work is thus needed in this direction.

In this work, we have looked at the changes in the reduced ergodicity spectrum at the approach of the criticality. However, we have not considered how fast these changes occur and thus how far from an instability the system is. According to the perturbation theory of Kato (1995) (see also Gouëzel and Liverani, 2006; Baladi, 2008),

the sensitivity of the ergodicity spectrum to perturbations will depend on the size of the perturbation with respect to the norm of the resolvent of the transfer operators. In the special case of normal operators, the spectrum smoothly responds to the size of the perturbation (Trefethen and Embree, 2005, Chap. 2) and the spectral gap directly gives a measure of the distance to criticality. This the case for for Hamiltonian systems for which the semigroup of transfer operators is unitary. However, in the general case of nonnormal operators (which cannot be diagonalizable on an orthonormal basis), the ergodicity spectrum may be more sensitive to perturbations. Thus, pathological situations may arise, in which the ergodicity spectrum approaches the imaginary axis faster than expected for the normal case. The robustness to perturbation of the ergodicity spectrum depends on the microscopic dynamics of the system and has been studied in analytical terms by Gouëzel and Liverani (2006), Butterley and Liverani (2007) and coworkers for the hyperbolic case. Such considerations are directly related to the applicability of Ruelle's response theory (Ruelle, 1997, 1999; Baladi, 2008; Ruelle, 2009), for which the behavior of the leading ergodicity eigenvalues is important. It is thus important to understand how sensitive is the ergodicity spectrum of the climate system to perturbations, in order to know how close to a catastrophe the system is.

Lastly, the applicability of the method of reduced transfer operators is limited by the length of the time series available to estimate transition probabilities. Long control runs of coupled state-of-the-art GCMs are available in the context of the CMIP5 experiment (Taylor et al., 2012). Thus, it should be possible to directly carry the analysis ENSO dynamics of chapter 3 to such models, in order to understand better the important factors triggering El Niño events. This should also be the case regarding the study of meta-stable regimes of chapter 5. On the other hand, the short length of the available observational record could be partially overcome by the regression of an Empirical Model Reduction (EMR, Kondrashov et al., 2015) to data. Such a reduction allows to build an empirical model which is able to capture unavoidable memory effects due to the projection of a system without time-scale separation (Chorin et al., 2002; Kondrashov et al., 2015). Long time series are then easily obtained from simulations of the EMR which could be used to calculate reduced transfer operators on higher-dimensional spaces than currently accessible. Conversely, comparing the ergodicity spectrum of stochastic model reductions to original models used as test-beds could provide a more detailed diagnostic than comparison of correlation functions alone.

Finally, as discussed in chapter 3, the study of the reduced ergodicity spectrum provides a promising framework for the study of stochastic bifurcations, together with stochastic parametrizing manifolds of Chekroun et al. (2015c). With the growing number of applications of the theory of random dynamical systems to climate (Dijkstra, 2013), there is good hope that ergodic theory can lead to many interesting results in the field.

A

ROBUSTNESS OF THE REDUCED ERGODICITY EIGENVALUES ESTIMATES OF CHAPTER 4

In this section, we test the robustness of the eigenvalues of the reduced transition matrices represented figure 4.6 to the sampling length, the grid size and the lag. For convenience, all the tests are presented for the NH SIC only. However, the corresponding tests done for the Eq MST and (NH SIC, Eq MST) do not challenge the conclusions taken in this study. Unless specified, all the parameters used in the following to estimate the transition matrices, such as the length of the times series, the grid, or the lag, are taken the same as for the ones used section 4.3.3 to produce figure 4.6.

A.1 ROBUSTNESS TO THE SAMPLING LENGTH

To test the robustness of the approximated spectra to the length of the time series used to estimate the transition probabilities, one could calculate confidence intervals from a version of the non-parametric bootstrap (see Efron (1980) and Mudelsee (2010)), adapted to the estimation of transition matrices (see Craig and Sendi, 2002) as was done in Chekroun et al. (2014) (see also chapter 5). Instead, we simply look at the changes in the real part of the leading eigenvalues of the transition matrices when only the first half (4850 years) or quarter (2425 years) of the time series is used. The thus obtained real parts of the leading eigenvalues of transition matrices calculated for the NH SIC, with a lag of 1 year and on a grid of 50 boxes, are represented figure A.1. Furthermore, the inverse of the real part of the second eigenvalue is catalogued in the third and fourth column of table A.1.

It is sufficient for this analysis to see, by comparing figure 4.6 to figure A.1 and from table A.1, that using time series of NH SIC twice or even four times as short as the original one to estimate the transition probabilities results in errors of less than 10% in the inverse of the real part of the eigenvalues. This shows the convergence of the estimates with the length of the time series, and that the qualitative picture, of the approach of the eigenvalues to the imaginary axis as the attractor crisis is neared, is not affected by the sampling length.

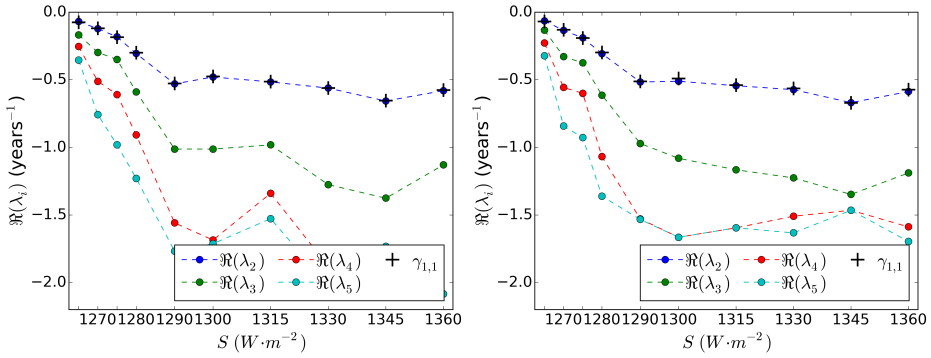

Figure A.1: Real part of the four leading secondary eigenvalues for the NH SIC, versus the solar constant, using only (a) half and (b) a quarter of the time series used to produce the corresponding figure 4.6.

A.2 ROBUSTNESS TO THE GRID SIZE

The robustness of our results to the size of the grid is now addressed. Figure A.2(a) to (c) represents the real part of the leading eigenvalues of transition matrices estimated on a grid of 25, 75 or a 100 boxes, respectively, instead of the original grid of 50 boxes used to produce figure 4.6. Figure A.2(a-c) and figure 4.6 are qualitatively similar, with the approach to 0 of the real part of the leading eigenvalues as the solar constant is decreased. The inverse of the real part of the second eigenvalue is also given in the fifth to the seventh column of table A.1 from which one can see that increasing the resolution results in differences in the inverse of the real part of the second eigenvalue of less than 5%. This suggests that the grid of 50 boxes used for the NH SIC is sufficiently thin to obtain good estimates of, at least, the second eigenvalue, allowing one to conclude that the outcome of this study is not challenged by the coarse resolution of the grid used to estimate the transition matrices.

A.3 ROBUSTNESS TO THE LAG

All the transition matrices in section 4.3.3 were calculated for a lag of 1 year, in order to have access to time scales as short as possible. However, due to the fact that the transition matrices are calculated on a reduced space, $\{P_\tau^h\}_{\tau \geq 0}$ does not constitute a semigroup, so that the SMT does not apply and the eigenvalues $\{\hat{\lambda}_i^h(\tau)\}_{1 \leq i \leq l}$ depend on the lag for which the transition matrix has been estimated. To verify that the conclusions of the analysis presented section 4.3.3 are not questioned by a different

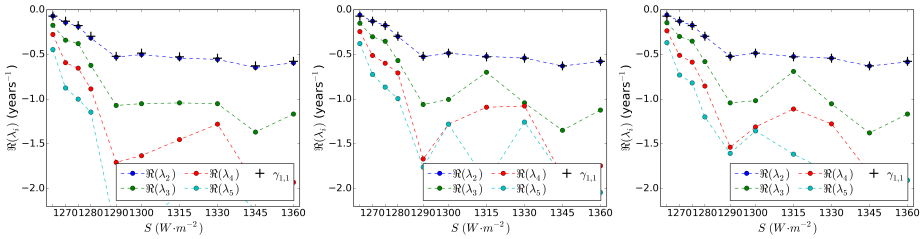

(a) (b) (c)

Figure A.2: Real part of the four leading secondary eigenvalues for the NH SIC, versus the solar constant, using a grid of (a) 25 boxes, (b) 75 boxes and (c) a 100 boxes, compared to the 50 boxes grid used to produce figure 4.6.

choice of the lag, we represent, in figure A.3(a) and (b), the real part of the leading secondary eigenvalues, calculated, as for figure 4.6, for the NH SIC and on a grid of 50 boxes but for a longer lag of 3 and 5 years, respectively. Again, the inverse of the real part of the first secondary eigenvalue thus obtained is catalogued in table A.1.

It is obvious from figure A.3, that eigenvalues far away from the imaginary axis are not well estimated for long lags as they are cornered to some cut-off value. This effect is expected, since the lag used to estimate the transition matrices gives a lower bound to the time scale associated with the eigenvalues that the reduced transition matrix presented in chapter 2 can resolve. However, even when a lag of 5 years is taken, the approach of the second eigenvalue to the imaginary axis as the control parameter is decreased towards its critical value can still be observed figure A.3(b), since the real part of this eigenvalue corresponds to a time scale larger than 5 years for $S < 1280(W m^{-2})$.

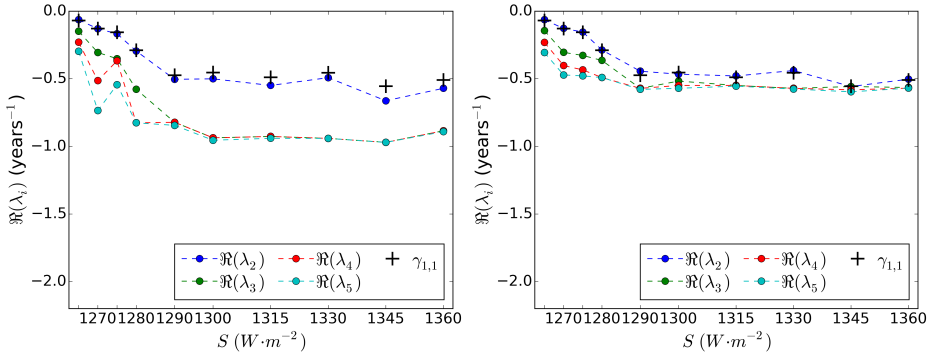

(a) (b)

Figure A.3: Real part of the four leading secondary eigenvalues for the NH SIC, versus the solar constant, using a lag of (a) 3 years and (b) 5 years, compared to the lag of 1 year used to produce figure 4.6.

Table A.1: Inverse of the real part of the second eigenvalue (in years) of transition matrices estimated for the NH SIC using different parameters, for different values of the solar constant. For the second column, the whole time series was used as well as a grid of 50 boxes and a 1 year lag, as for figure 4.6. For the third and the fourth columns, only half or a quarter (Fig. A.1.a and b, respectively) of the time series was used, respectively. For the fifth to the seventh column, a grid of 25 boxes, 75 boxes and a 100 boxes (Fig. A.2.a to c, respectively) was used. Finally, for the last two columns, a lag of 3 and 5 (Fig. A.3.a to b, respectively) years was used.

$S(Wm^{-2})$	Fig. 4.6	1/2 len.	1/4 len.	25 b.	75 b.	100 b.	3 yr	5 yr
1265	16.36	14.48	15.63	14.12	16.69	16.95	15.84	15.95
1270	7.65	8.22	7.45	7.02	7.77	7.81	7.70	7.85
1275	5.69	5.49	5.29	5.33	5.73	5.77	6.02	6.52
1280	3.31	3.28	3.26	3.16	3.34	3.36	3.40	3.49
1290	1.90	1.89	1.94	1.89	1.90	1.92	1.99	2.25
1300	2.04	2.09	1.96	1.99	2.06	2.06	2.00	2.15
1315	1.89	1.94	1.84	1.85	1.92	1.91	1.82	2.09
1330	1.83	1.78	1.75	1.80	1.85	1.84	2.04	2.28
1345	1.59	1.52	1.50	1.55	1.59	1.59	1.51	1.80
1360	1.72	1.72	1.70	1.68	1.73	1.71	1.75	1.99

B

ROBUSTNESS OF THE REDUCED ERGODICITY EIGENVALUES ESTIMATES OF CHAPTER 5

B.1 BOOTSTRAP TEST OF THE REDUCED ERGODICITY EIGENVALUES AND REGIMES

This appendix is concerned with the limited length of the record used to estimate the transition matrices $\{\hat{P}_\tau^{\mathscr{R}}\}$ defined in chapter 2. This statistical inference problem can result in errors, notably in the rates and the regimes calculated from $\{\hat{P}_\tau^{\mathscr{R}}\}$ in section 5.3.1 and 5.3.3 respectively, and requires an estimation of confidence intervals.

Following Chekroun et al. (2014), we use a version of the non-parametric bootstrap (Efron, 1980; Mudelsee, 2010), adapted to the estimation of transition matrices as done in (Craig and Sendi, 2002). It starts from the matrix T_τ counting the transitions of $\{y_t\}$ from one grid box to another, before the normalization has been applied to get the transition probabilities. From T_τ, N_s surrogate count matrices $\{T^*_{\tau,s}\}_{1\leq s\leq N_s}$ are generated. This is done, for each row i, by taking with replacement n_i target grid boxes among the n_i transitions starting from grid-box B_i of T_τ. This accounts for drawing n_i times from a Multinomial distribution with vector of probabilities $\{(\hat{P}_\tau^{\mathscr{R}})_{il}\}_{1\leq l\leq m}$. From these N_s surrogate count matrices, the transition matrices $\{\hat{P}^{\mathscr{R}*}_{\tau,s}\}_{1\leq s\leq N_s}$ are then calculated by normalizing their rows. These matrices can then be used to estimate the sampling error of any functions of the transition matrix $\hat{P}_\tau^{\mathscr{R}*}$.

A thousand surrogate matrices $\{\hat{P}^{\mathscr{R}*}_{\tau,s}\}_{1\leq s\leq N_s}$ are used to compute 99% confidence intervals for the rates represented in figure 5.4. For each lag τ, the leading rates have been calculated for every surrogate transition matrix in $\{\hat{P}^{\mathscr{R}*}_{\tau,s}\}_{1\leq s\leq N_s}$. For each rate $r_k(\tau)$ one gets a distribution of surrogate rates $\{(r_k(\tau))^*_s\}_{1\leq s\leq N_s}$. After sorting these distributions, the $(0.005 * N_s)^{th}$ and the $(0.995 * N_s)^{th}$ values are taken to give the lower bound and the upper bound, respectively, of the confidence interval for rate $r_k(\tau)$.

In this study, we added a bias correction to the intervals because the described construction of the surrogate matrices introduces a bias towards lower values for rates, in particular for the secondary rates. We give an example to explain this bias. Assume that only two transitions start from a box B_i, with targets B_k and B_l. In the surrogate, the probability to pick two different transitions (B_k and B_l) will be of $1/2$,

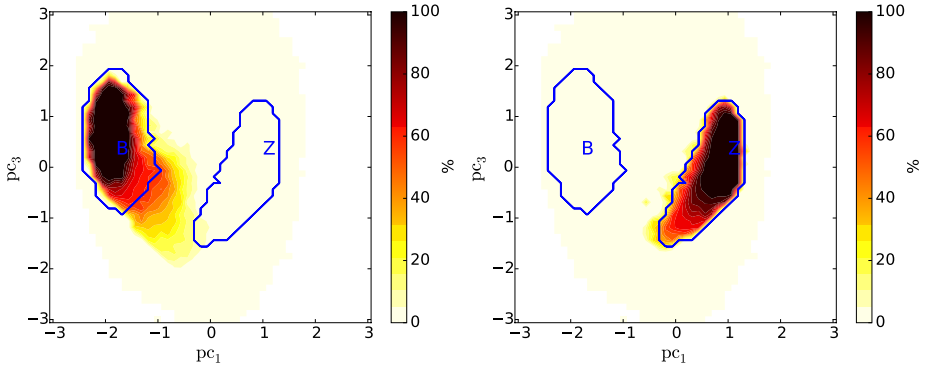

Figure B.1: The value at each grid box represents the fraction of surrogate regimes for which the grid box belongs to (a) the blocked regime or (b) the zonal regime out of a 100 surrogates. The surrogate regimes were detected by applying the algorithm of section 5.3.3 to the bootstrap surrogate transition matrices.

while the probability to pick two of the same transitions (twice B_k or twice B_l) will also be of $1/2$. Thus, a bias is introduced towards a weaker mixing resulting in lower values of the rates (in particular to the secondary ones more sensitive to such details). This bias was removed by centering the mean of the surrogate rates $\{(r_k(\tau))^*_s\}_{1\leq s\leq N_s}$ to the the value of the original rate $r_k(\tau)$ being tested.

The surrogate transition matrices $\{\hat{P}^{\mathcal{R}*}_{\tau,s}\}_{1\leq s\leq N_s}$ can also be used to test the robustness of the regimes to the sampling by running, for each $\hat{P}^{\mathcal{R}*}_{\tau,s}$, the regime detection algorithm described in section 5.3.3. The membership of a grid box to a regime can be given by a membership matrix $M_{i\beta}$ such that $M_{i\beta} = 1$ if grid box B_i belongs to regime E_β, and is zero otherwise. Confidence intervals are not well suited for statistics taking logical values. Instead, we compute, for each grid-box B_i, the fraction of surrogates for which B_i belongs to regime E_β. These fractions are plotted in figure B.1a,b for the blocked and the zonal regime, respectively, using $N_s = 100$ surrogates.

We can see that the core of the regimes are very robust to the sampling, as indicated by the amount of grid boxes in each regime for which a fraction close to a 100% of the boxes of the surrogates have been attributed to the same regime. However, boxes along the path of the transition from the zonal to the blocking regimes are less robust to the sampling. Such exit-region and entering-region for the zonal and the blocked regime, respectively, are indeed harder to attribute to a regime, since they correspond to regions where the invariance is weak. A possibility would be to add a simulated annealing step in the almost-invariant sets detection algorithm as has been used, for example, in Rosvall and Bergstrom (2008).

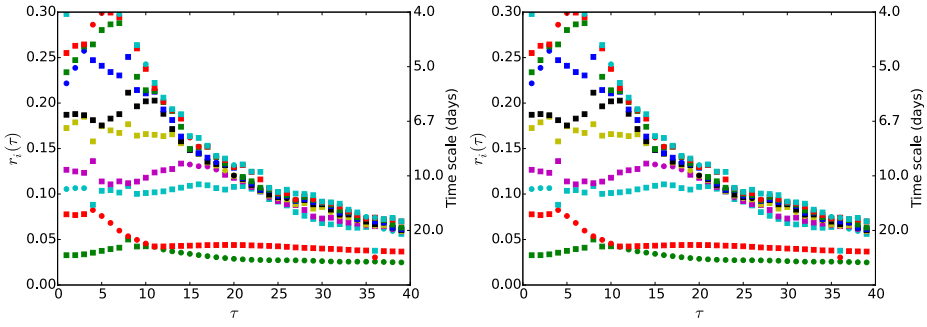

Figure B.2: Rates $r_k(\tau)$ as in figure 5.4 but calculated from estimates of transition matrices on a (a) 10×10 grid and (b) 100×100 grid.

B.2 ROBUSTNESS OF THE REDUCED ERGODICITY EIGENVALUES AND REGIMES TO THE GRID RESOLUTION

The robustness of the rates and the regimes to the grid resolution for which the transition matrices are estimated is tested next. Figure B.2a, b represent rates calculated from transition matrices estimated on a grid of 10×10 and 100×100 boxes respectively, to be compared with figure 5.4 of section 5.3.1. We can see that at least the 3 leading rates in green, red and cyan are not much affected by the grid resolution so that the analysis of section 5.3.1 remains valid under changes of the grid in this range. This robustness to the grid of the leading rates is in agreement with the fact that they represent slow large-scale motions less likely to be affected by small perturbations of the transition matrices.

Figure B.3a,b represent regimes detected from transition matrices estimated on a grid of 20×20 and 200×200 boxes respectively, to be compared with figure 5.6 of section 5.3.3. It can be seen that in both cases the regimes are very much alike to the one plotted figure 5.6 for the grid of 50×50 boxes. The quality of the regimes deteriorates for grids coarser than 20×20 (not represented here) but remains relatively good for resolutions as refined as 200×200 (Fig. B.3.b). This robustness of the regimes to very refined resolutions can be explained by the aggregative nature of the almost-invariant sets detection algorithm. Indeed, one expects the estimates of the transition probabilities between grid boxes to deteriorate as the grid becomes thinner and as the number of samples by grid box decreases. However, because the algorithm iteratively agglomerates grid boxes into clusters, the transition probabilit-

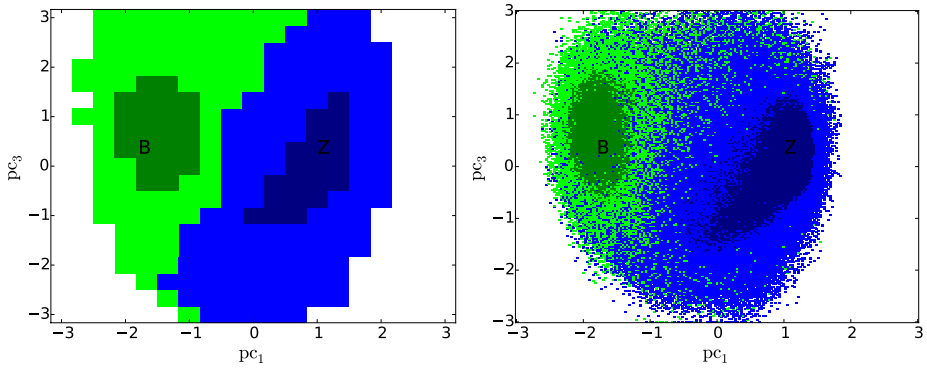

(a) (b)

Figure B.3: Almost-invariant sets and their regimes as for figure 5.6 but for a grid of (a) 20×20 and (b) 200×200.

ies between these coarser and coarser clusters become less and less sensitive to the sampling as the number of samples by clusters increases with their size.

B.3 ROBUSTNESS OF THE REGIMES TO THE TIME LAG

In addition to the robustness test of the regimes to the grid resolution, we next test their robustness to the choice of the time lag of the transition matrix from which they are detected. Regimes detected for lags τ of 7 and 50 days are plotted in figure B.4a,b, respectively, to be compared to figure 5.6 of section 5.3.3. In this range, we can see that the quality of the regimes is robust to the lag.

For lags shorter than 7 days, however, the algorithm is not able to distinguish the transition path between the zonal and the blocked regime from the regimes themselves (not shown here). Such result is in agreement with the fact that for lags smaller than 7 days, the complex pair of rates represented by green squares in figure 5.4, more likely to be associated with the transition, is dominant over the real eigenvalue represented by red circles and likely to be associated with the meta-stability of the regimes. Thus the motions associated with the transition appear to be dominant over the meta-stability of the regimes for such short lags.

The deterioration of the regimes for lags larger that 50 days is to be expected due to the fact that, as seen section 5.3.1, the leading rates of figure 5.4, associated with meta-stability, have time-scales not larger than 40 days, so that for longer lags, the motions associated with the meta-stable regimes are likely to decorrelate and cannot be detected by the algorithm.

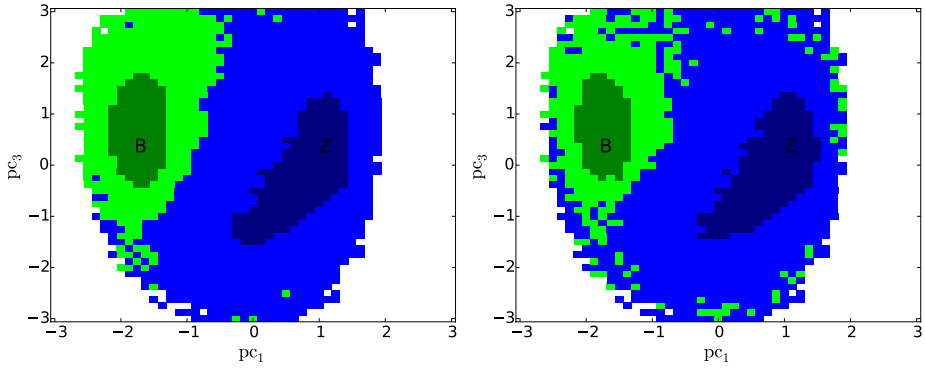

(a) (b)

Figure B.4: Almost-invariant sets and their regimes as for figure 5.6 but for a lag of (a) 7 days and (b) 50 days.

B.4 TEST OF THE SEMIGROUP PROPERTY

In this appendix, we justify that the distances plotted in figure 5.5a in section 5.3.1, between densities transferred by a power of 2 of $\hat{P}_8^{\mathscr{R}}$ and densities transferred by $\hat{P}_{2\times 8}^{\mathscr{R}}$, are mostly explained by memory effects rather than by the Galerkin approximation or by the sampling.

To do so, we first represent the same distances but calculated from transition matrices estimated from time series of only 250,000 realizations and as much as 1,000,000 realizations (Fig. B.5.a and b respectively), compared to the 500,000 realizations from which the distances represented figure 5.5 have been calculated. We can see that neither plots seem to be affected by the short or long length of the time-series. One has to go to record lengths shorter than 200,000 realizations to start to see a difference in the distances (not shown here). Thus, the distances represented in figure 5.5 are not likely to be due to the limited length of the time-series from which the transition probabilities have been calculated.

Secondly, to test the effect of the Galerkin approximation on the distances, we have again reproduced figure 5.5, using 500,000 realizations, but with a grid of 20×20 and 100×100 (Fig. B.6.a and b respectively). While for the 20×20 grid, the distances get larger, indicating that this increase is due to the Galerking approximation, the distances for the 100×100 grid resolution (Fig. B.6.b) are very much alike the one for the 50×50 resolution (Fig. 5.5). Note that this is also true when a record length of 1,000,000 realizations (not shown here), so that the similarities between the plots

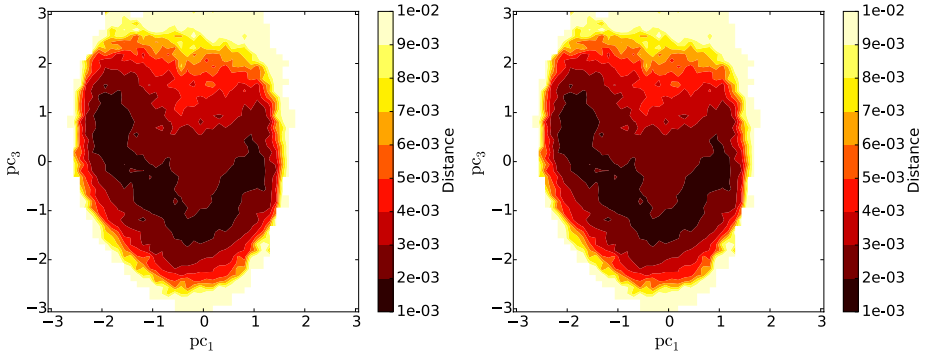

(a) (b)

Figure B.5: As for figure 5.5, the value at each grid-point represents the distance, for an initial density of 1 at this grid-point, between the density f_{8k}^{pow} transferred by the k^{th} poser of $\hat{P}_8$ and a density f_{8k}^{long} transferred by $\hat{P}^{\mathscr{R}}_{k\times 8}$ for $k = 2$. However, the transition matrices have been estimated from a time series of (a) 250,000 days and (b) 1,000,000 days, compared to the 500,000 of figure 5.5.

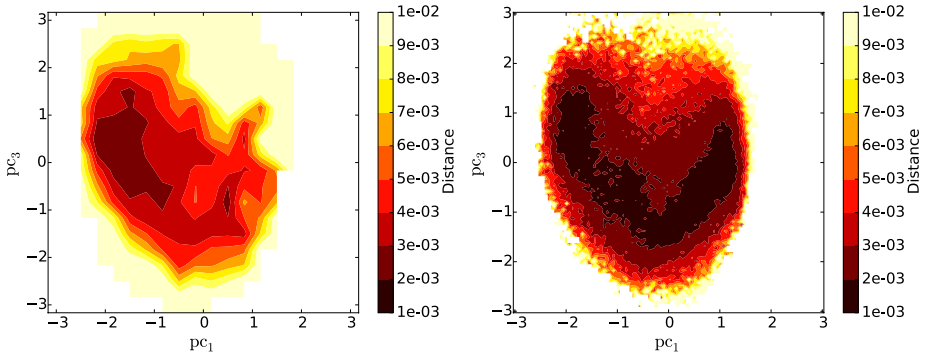

(a) (b)

Figure B.6: As for figure 5.5, the value at each grid-point represents the distance, for an initial density of 1 at this grid-point, between the density f_{8k}^{pow} transferred by the k^{th} poser of $\hat{P}_8$ and a density f_{8k}^{long} transferred by $\hat{P}^{\mathscr{R}}_{k\times 8}$ for $k = 2$. However, the transition matrices have been estimated from on a grid of (a) 20×20 and (b) 100×100 boxes, compared to the 50×50 boxes of figure 5.5.

is not likely to be due to a compensating effect between the grid resolution and the number of samples per grid point.

We can thus conclude that the distances represented in figure 5.5 for $\hat{P}_8^{\mathscr{R}2}$ and $\hat{P}_{2\times 8}^{\mathscr{R}}$ are mostly due to memory effects introduced by the only partial observation of the barotropic model.

BIBLIOGRAPHY

R. V. Abramov and A. J. Majda. Blended response algorithms for linear fluctuation-dissipation for complex nonlinear dynamical systems. *Nonlinearity*, 20:2793–2821, 2007.

V. S. Afraimovich, S. V. Gonchenko, L. M. Lerman, A. L. Shilnikov, and D. V. Turaev. Scientific heritage of L.P. Shilnikov. *Regular and Chaotic Dynamics*, 19:435–460, 2014.

A. A. Andronov and L. Pontryagin. Systemes grossiers. *Dokl. Akad. Nauk. SSSR*, 14:247–250, 1937.

A. A. Andronov, E. Leontovich, I. Gordon, and A. Maier. *Theory of Bifurcations of Dynamic Systems on a Plane*. Israel Program for Scientific Translations, Jerusalem, 1971.

D. V. Anosov. Roughness of geodesic flows on compact Riemannian manifolds of negative curvature. *Soviet Mathematics-Doklady*, 3:1068–70, 1962.

W. Arendt, C. J. K. Batty, M. Hieber, and F. Neubrander. *Vector-valued laplace transforms and cauchy problems*. Springer, Basel, birkhäuser edition, 2011.

L. Arnold. *Random Dynamical Systems*. Springer, Berlin, 2003.

V. I. Arnold. Proof of a theorem of A. N. Kolmogorov on the preservation of conditionally periodic motions under a small perturbation of the Hamiltonian. *Russ. Math. Surv.*, 18:9–36, 1963.

V. I. Arnold. *Catastrophe theory*. Springer-Verlag, Berlin, 1986.

V. I. Arnold and A. Avez. *Problemes Ergodiques de la Mecanique Classique*. Gauthier-Villars, Paris, 1967.

V. Baladi. *Positive Transfer Operators and Decay of Correlations*. World Scientific, Singapore, 2000.

V. Baladi. Linear response despite critical points. *Nonlinearity*, 21:T81–T90, 2008.

V. Baladi and C. Liverani. Exponential Decay of Correlations for Piecewise Cone Hyperbolic Contact Flows. *Communications in Mathematical Physics*, 314:689–773, 2012.

V. Baladi and M. Tsujii. Anisotropic Hoelder and Sobolev spaces for hyperbolic diffeomorphisms. *Ann. Inst. Fourier*, 57:127–154, 2007.

D. Barriopedro, R. García-Herrera, A. R. Lupo, and E. Hernández. A climatology of Northern Hemisphere blocking. *Journal of Climate*, 19:1042–1063, 2006.

D. S. Battisti and A. C. Hirst. Interannual Variability in a Tropical Atmosphere-Ocean Model: Influence of the Basic State, Ocean Geometry and Nonlinearity. *Journal of the Atmospheric Sciences*, 46:1687–1712, 1989.

I. Bendixson. Sur les courbes définies par des équations differentielles. *Journal de Mathématiques*, 24: 1–88, 1899.

J. Berner. Linking Nonlinearity and Non-Gaussianity of Planetary Wave Behavior by the Fokker-Planck Equation. *Journal of the atmospheric sciences*, 62:2098–2117, 2005.

K. Bhattacharya, M. Ghil, and I. L. Vulis. Internal variability of an energy-balance model with delayed albedo effects. *Journal of Atmospheric Sciences*, 39:1747–1773, 1982.

P. Billingsley. *Statistical Inference for Markov process*. University of Chicago Press, Chicago, 1961.

G. D. Birkhoff. Dynamical Systems. *NewYork, Amer. Math. Soc., Colloq. Publ.*, page 295, 1927.

G. D. Birkhoff. Proof of the Ergodic Theorem. *Proceedings of the National Academy of Sciences of the United States of America*, 17:656–660, 1931.

A. Bittracher, P. Koltai, and O. Junge. Pseudogenerators of Spatial Transfer Operators. *SIAM Journal Applied Dynamical Systems*, 14:1478–1517, 2015.

M. Blank, G. Keller, and C. Liverani. Ruelle-Perron-Frobenius spectrum for Anosov maps. *Nonlinearity*, 15: 1905, 2002.

T. Bódai, V. Lucarini, F. Lunkeit, and R. Boschi. Global instability in a Sellers-type model. *preprint arXiv:1402.3269v1*, 2013.

A. A. Bolibruch, Osipov Y. S., and Y. G. Sinai. *Mathematical events of the twentieth century*. Springer-Verlag, Berlin, 2005.

L. Boltzmann. *Wissenschaftliche Abhandlungen I. Band (1865-1874)*. Barth, Leipzig, 1909.

R. Boschi, V. Lucarini, and S. Pascale. Bistability of the climate around the habitable zone: A thermodynamic investigation. *Icarus*, 226:1724–1742, 2013.

C. A. Boulton, L. C. Allison, and T. M. Lenton. Early warning signals of Atlantic Meridional Overturning Circulation collapse in a fully coupled climate model. *Nature Communications*, 5:5752, 2014.

R. Bowen and D. Ruelle. The ergodic theory of Axiom A flows. *Inventiones Mathematicae*, 29:181–202, 1975.

G. Branstator and J. Berner. Linear and Nonlinear Signatures in the Planetary Wave Dynamics of an AGCM : Phase space tendencies. *Journal of the atmospheric sciences*, 62:1792, 2005.

G. Branstator and J. D. Opsteegh. Free solutions of the barotropic vorticity equation. *Journal of the atmospheric sciences*, 46:1799, 1989.

M. I. Budyko. The effect of solar radiation variations on the climate of the Earth. *Tellus*, 21:611 – 619, 1969.

O. Butterley. A note on operator semigroups associated to chaotic flows. *Ergodic Theory and Dynamical Systems*, pages 1–13, 2015.

O. Butterley and C. Liverani. Smooth Anosov flows: correlation spectra and stability. *Journal of Modern Dynamics*, 1:301–322, 2007.

B. Cessac and J. A. Sepulchre. Linear response, susceptibility and resonances in chaotic toy models. *Physica D: Nonlinear Phenomena*, 225:13–28, 2007.

J. G. Charney and J. G. DeVore. Multiple Flow Equilibria in the Atmosphere and Blocking. *Journal of the atmospheric sciences*, 36:1205, 1979.

J. G. Charney, R. FJortoft, and J. von Neumann. Numerical Integration of the Barotropic Vorticity Equation. *Tellus A*, 2:238–254, 1950.

J. G. Charney, M. Halem, and R. Jastrow. Use of Incomplete Historical Data to Infer the Present State of the Atmosphere. *Journal of the Atmospheric Sciences*, 26:1160–1163, 1969.

M. D. Chekroun, E. Simonnet, and M. Ghil. Stochastic climate dynamics: Random attractors and time-dependent invariant measures. *Physica D: Nonlinear Phenomena*, 240:1685–1700, 2011.

M. D. Chekroun, J. D. Neelin, D. Kondrashov, J. C. McWilliams, and M. Ghil. Rough parameter dependence in climate models and the role of Ruelle-Pollicott resonances. *Proceedings of the National Academy of Sciences of the United States of America*, 111:1684–1690, 2014.

M. D. Chekroun, M. Ghil, H. Liu, and S. Wang. Low-dimensional galerkin approximations of nonlinear delay differential equations. *Discrete and Continuous Dynamical Systems*, pages 1–43, 2015a.

M. D. Chekroun, H. Liu, and S. Wang. *Approximation of Stochastic Invariant Manifolds*. Springer, International, 2015b.

M. D. Chekroun, S. Wang, and H. Liu. *Stochastic parameterizing manifolds and non-Markovian reduced equations*. Springer, International, 2015c.

B. Chirikov. Resonance processes in magnetic traps. *J. Nucl. Energy, Part C: Plasma Physics*, 1:253–260, 1960.

A. Chojnowska-Michalik. Representation theorem for general stochastic delay equations. *Bull. Acad. Pol. Sci., Ser. Sci. Math. Astron. Phys.*, 26:635–642, 1978.

A. Chojnowska-Michalik and B. Goldys. Existence, uniqueness and invariant measures for stochastic semilinear equations on Hilbert spaces. *Probability theory and related fields*, 102:331– 356, 1995.

A. Chojnowska-Michalik and B. Goldys. Nonsymmetric Ornstein-Uhlenbeck semigroup as second quantized operator. *J. Math. Kyoto Univ.*, 36:481–498, 1996.

A. J. Chorin and O. H. Hald. *Stochastic tools in mathematics and science*. Springer, New York, 2009.

A. J. Chorin, O. H. Hald, and R. Kupferman. Optimal prediction with memory. *Physica D: Nonlinear Phenomena*, 166:239–257, 2002.

B. Christiansen. Atmospheric Circulation Regimes: Can Cluster Analysis Provide the Number? *Journal of Climate*, 20:2229, 2007.

A. Clauset, M. Newman, and C. Moore. Finding community structure in very large networks. *Physical Review E*, 70:066111, 2004.

M. Colangeli and V. Lucarini. Elements of a unified framework for response formulae. *Journal of Statistical Mechanics: Theory and Experiment*, 2014:P01002, 2014.

P. Collet and J.-P. Eckmann. *Concepts and results in chaotic dynamics*. Springer, Berlin, 2006.

M. Collins, R. Knutti, J. Arblaster, J.-L. Dufresne, T. Fichefet, P. Friedlingstein, X. Gao, W. J. Gutowski, T. Johns, G. Krinner, M. Shongwe, C. Tebaldi, A. J. Weaver, and M. Wehner. Long-term Climate Change: Projections, Commitments and Irreversibility. In *Climate Change 2013: The Physical Science Basis. Contribution of Working Group I to the Fifth Assessment Report of the Intergovernmental Panel on Climate Change*, pages 1029–1136. Cambridge University Press, Cambridge, United Kingdom and New York, NY, USA, 2013. ISBN 9781107415324.

T. M. Cover and J. A. Thomas. Entropy, Relative Entropy and Mutual Information. In *Elements of Information Theory*, chapter 2, pages 13–55. John Wiley & Sons, New Jersey, 1991. ISBN 0471062596.

B. a. Craig and P. P. Sendi. Estimation of the transition matrix of a discrete-time Markov chain. *Health economics*, 11:33–42, 2002.

D. Crommelin. Regime transitions and heteroclinic connections in a barotropic atmosphere. *Journal of the atmospheric sciences*, 60:229–246, 2003.

D. Crommelin and E. Vanden-Eijnden. Diffusion Estimation from Multiscale Data by Operator Eigenpairs. *Multiscale Modeling & Simulation*, 9:1588–1623, 2011.

D. Crommelin, J. D. Opsteegh, and F. Verhulst. A Mechanism for Atmospheric Regime Behavior. *Journal of the atmospheric sciences*, 61:1406–1419, 2004.

R. Curtain and H. Zwart. *An Introduction to Infinite-Dimensional Linear Systems*, volume 21. Springer, New York, texts in a edition, 1995.

G. Da Prato and J. Zabczyk. *Stochastic equations in infinite dimensions*, volume 44. Cambridge University Press, Cambridge, encycloped edition, 1992.

G. Da Prato and J. Zabczyk. *Ergodicity for Infinite Dimensional Systems*. Cambridge University Press, Cambridge, 1996.

G. Da Prato, A. Debussche, and B. Goldys. Some properties of invariant measures of non symmetric dissipative stochastic systems. *Probability Theory and Related Fields*, 123:355–380, 2002.

E. Darve, J. Solomon, and A. Kia. Computing generalized Langevin equations and generalized Fokker-Planck equations. *Proceedings of the National Academy of Sciences of the United States of America*, 106: 10884–9, 2009.

A. Dawson, T. N. Palmer, and S. Corti. Simulating regime structures in weather and climate prediction models. *Geophysical Research Letters*, 39:L21805, 2012.

A. Dawson, T. N. Palmer, and S. Corti. Simulating weather regimes: impact of model resolution and stochastic parameterization. *Climate Dynamics*, 2014.

H. Dekker and N. G. van Kampen. Eigenvalues of a diffusion process with a critical point, 1979.

M. Dellnitz and O. Junge. Almost invariant sets in Chua's circuit. *International Journal of Bifurcation and Chaos*, 7:2475–2485, 1997.

M. Dellnitz and O. Junge. On the Approximation of Complicated Dynamical Behavior. *SIAM Journal on Numerical Analysis*, 36:491–515, 1999.

M. Dellnitz, G. Froyland, C. Horenkamp, K. Padberg-Gehle, and A. Sen Gupta. Seasonal variability of the subpolar gyres in the Southern Ocean: a numerical investigation based on transfer operators. *Nonlinear Processes in Geophysics*, 16:655–664, 2009.

M. Dellnitz, M. H.-v. Molo, and A. Ziessler. On the computation of attractors for delay differential equations. *arXiv*, pages 1–19, 2015.

T. DelSole. A fundamental limitation of Markov models. *Journal of the atmospheric sciences*, 57:2158–2168, 2000.

K. Deng, P. Mehta, and S. Meyn. Optimal Kullback-Leibler aggregation via spectral theory of Markov chains. *Automatic Control, IEEE*, 56:2793–2808, 2011.

P. Deuflhard, M. Dellnitz, O. Junge, and C. Schütte. Computation of Essential Molecular Dynamics by Subdivision Techniques. In P. Deuflhard, J. Hermans, B. Leimkuhler, A. E. Mark, S. Reich, and R. D. Skeel, editors, *Computational Molecular Dynamics: Challenges, Methods, Ideas*, pages 98–115. Springer, Berlin Heidelberg, 1999.

O. Diekmann, S. A. van Gils, S. M. V. Lunel, and H.-O. Walther. *Delay Equations: Functional, Complex, and Nonlinear Analysis*, volume 110. Springer, New York, applied ma edition, 1995.

H. a. Dijkstra. *Nonlinear Physical Oceanography*. Springer, Dordrecht, 2005.

H. A. Dijkstra. *Nonlinear Climate Dynamics*. Cambridge University Press, Cambridge, 2013.

H. a. Dijkstra and M. Ghil. Low-Frequency Variability of the Large-Scale Ocean Circulation: A Dynamical Systems Approach. *Reviews of Geophysics*, pages 1–38, 2005.

J. L. Doob. Stochastic Processes and Statistics. *Proceedings of the National Academy of Sciences of the United States of America*, 20:376–379, 1934.

S. S. Drijfhout, E. Gleeson, H. a. Dijkstra, and V. Livina. Spontaneous abrupt climate change due to an atmospheric blocking-sea-ice-ocean feedback in an unforced climate model simulation. *Proceedings of the National Academy of Sciences*, 110:19713–19718, 2013.

L. Dugard and E. Verriest, editors. *Stability and Control of Time-delay Systems*. Springer-Verlag, London, 1998.

V. P. Dymnikov and A. S. Gritsoun. Climate model attractors: Chaos, quasi-regularity and sensitivity to small perturbations of external forcing. *Nonlinear Processes in Geophysics*, 8:201–209, 2001.

V. P. Dymnikov, V. N. Lykosov, and E. M. Volodin. Problems of modeling climate and climate change. *Izvestiya, Atmospheric and Oceanic Physics*, 42:568–585, 2006.

J.-P. Eckmann and D. Ruelle. Ergodic theory of chaos and strange attractors. *Reviews of modern physics*, 57:617, 1985.

B. Efron. The Jacknife, the bootstrap, and other resampling plans. Stanford University, Stanford, 1980.

E. Eliasen, B. Machenhauer, and E. Rasmussen. On a numerical method for integration of the hydrodynamical equations with a spectral representation of the horizontal fields. Inst. of Theor. Met., Københavns University, Copenhagen, 1970.

K.-J. Engel and R. Nagel. *One-parameter semigroups for linear evolution equations*. Springer, New York, 2001.

E. S. Epstein. The rols of initial uncertainties in prediction, 1969.

D. M. Fargue. Reducibilité des systèmes héréditaires a des systèmes dynamiques. *C. R. Acad. Sci. Paris Ser. B.*, 277:471–473, 1973.

Q. Feng, J. P. Viebahn, and H. a. Dijkstra. Deep ocean early warning signals of an Atlantic MOC collapse. *Geophysical Research Letters*, 41:6008–6014, 2014.

D. R. Fereday, J. R. Knight, A. A. Scaife, C. K. Folland, and A. Philipp. Cluster Analysis of North Atlantic-European Circulation Types and Links with Tropical Pacific Sea Surface Temperatures. *Journal of Climate*, 21:3687–3703, 2008.

C. Foias, O. Manley, R. Rosa, and R. Temam. *Navier-Stokes Equations and Turbulence*. Cambridge University Press, Cambridge, 2001.

K. Fraedrich and F. Lunkeit. Diagnosing the entropy budget of a climate model. *Tellus, Series A: Dynamic Meteorology and Oceanography*, 60:921–931, 2008.

K. Fraedrich, E. Kirk, and F. Lunkeit. PUMA: Portable University Model of the Atmosphere. Deutsches Klimarechenzentrum, Hamburg, 1998.

K. Fraedrich, H. Jansen, E. Kirk, U. Luksch, and F. Lunkeit. The Planet Simulator: Towards a user friendly model. *Meteorologische Zeitschrift*, 14:299–304, 2005a.

K. Fraedrich, H. Jansen, E. Kirk, and F. Lunkeit. The planet simulator: Green planet and desert world. *Meteorologische Zeitschrift*, 14:305–314, 2005b.

C. L. Franzke, A. J. Majda, and E. Vanden-Eijnden. Low-order stochastic mode reduction for a realistic barotropic model climate. *Journal of the atmospheric sciences*, 62:1722–1745, 2005.

C. L. Franzke, D. Crommelin, A. Fischer, and A. J. Majda. A Hidden Markov Model Perspective on Regimes and Metastability in Atmospheric Flows. *Journal of Climate*, 21:1740–1757, 2008.

C. L. Franzke, T. J. O'Kane, J. Berner, P. D. Williams, and V. Lucarini. Stochastic Climate Theory and Modelling. *Wiley Interdisciplinary Reviews: Climate Change*, 6:63–78, 2015.

C. L. E. Franzke. Warming trends: Nonlinear climate change. *Nature Climate Change*, 4:423–424, 2014.

G. Froyland. Extracting dynamical behavior via Markov models. In A. I. Mees, editor, *Nonlinear dynamics and statistics*, chapter 12, pages 281–321. Birkhäuser Boston, Boston, 2001.

G. Froyland. On ulam approximation of the isolated spectrum and eigenfunctions of hyperbolic maps. *Discrete and Continuous Dynamical Systems*, 17:671–689, 2007.

G. Froyland and M. Dellnitz. Detecting and Locating Near-Optimal Almost-Invariant Sets and Cycles. *SIAM Journal on Scientific Computing*, 24:1839–1863, 2003.

G. Froyland and K. Padberg. Almost-invariant sets and invariant manifolds - Connecting probabilistic and geometric descriptions of coherent structures in flows. *Physica D: Nonlinear Phenomena*, 238:1507–1523, 2009.

G. Froyland and K. Padberg-gehle. *Ergodic Theory, Open Dynamics, and Coherent Structures*, volume 70 of *Springer Proceedings in Mathematics & Statistics*. Springer New York, New York, NY, 2014.

G. Froyland, K. Padberg, M. England, and A. Treguier. Detection of Coherent Oceanic Structures via Transfer Operators. *Physical Review Letters*, 98:224503, 2007.

G. Froyland, O. Junge, and P. Koltai. Estimating Long-Term Behavior of Flows Without Trajectory Integration: The Infinitesimal Generator Approach. *SIAM Journal on Numerical Analysis*, 51:223–247, 2013.

G. Froyland, G. Gottwald, and A. Hammerlindl. A computational method to extract macroscopic variables and their dynamics in multiscale systems. *SIAM J. Applied Dynamical Systems*, 13:1816–1846, 2014a.

G. Froyland, R. M. Stuart, and E. van Sebille. How well-connected is the surface of the global ocean? *Chaos: An Interdisciplinary Journal of Nonlinear Science*, 24:033126, 2014b.

G. Gallavotti. *Nonequilibrium and irreversibility*. Springer, Cham, 2014.

G. Gallavotti and E. G. D. Cohen. Dynamical ensembles in stationary states. *Journal of Statistical Physics*, 80:931–970, 1995.

G. Gallavotti and V. Lucarini. Equivalence of Non-equilibrium Ensembles and Representation of Friction in Turbulent Flows: The Lorenz 96 Model. *Journal of Statistical Physics*, 156:1027–1065, 2014.

G. Gallavotti and D. Ruelle. SRB states and nonequilibrium statistical mechanics close to equilibrium. *Communications in Mathematical Physics*, 190:279–285, 1997.

C. W. Gardiner. *Handbook of Stochastic Methods*. Springer, Berlin Heidelberg, 2009.

P. Gaspard. *Chaos, Scattering and Statistical Mechanics*. Cambridge University Press, Cambridge, 1998.

P. Gaspard and S. Tasaki. Liouvillian dynamics of the Hopf bifurcation. *Physical Review E*, 64:056232, 2001.

P. Gaspard, G. Nicolis, A. Provata, and S. Tasaki. Spectral signature of the Pitchfork bifurcation: Liouville equation approach. *Physical Review E*, 51:74–94, 1995.

M. Ghil. Climate stability for a Sellers-type model. *Journal of Atmospheric Sciences*, 33:3–20, 1976.

M. Ghil. Hilbert problems for the geosciences in the 21st century. *Nonlinear Processes in Geophysics*, 8: 211–211, 2001.

M. Ghil. Natural Climate Variability. *Encyclopedia of Global Environmental Change*, 1:544–549, 2002.

M. Ghil and A. Robertson. "Waves" vs. "particles" in the atmosphere's phase space: A pathway to long-range forecasting? *Proceedings of the National Academy of Sciences of the United States of America*, 99: 2493–2500, 2002.

J. W. Gibbs. *Elementary Principles in Statistical Mechanics*. Scribner, New York, 1902.

D. Givon, R. Kupferman, and A. Stuart. Extracting macroscopic dynamics: model problems and algorithms. *Nonlinearity*, 17:R55–R127, 2004.

S. Gouëzel and C. Liverani. Banach spaces adapted to anosov systems. *Ergodic Theory and Dynamical Systems*, 26:189–217, 2006.

C. Grebogi, E. Ott, and J. a. Yorke. Crises, sudden changes in chaotic attractors, and transient chaos. *Physica D: Nonlinear Phenomena*, 7:181–200, 1983.

A. S. Gritsoun and G. Branstator. Climate Response Using a Three-Dimensional Operator Based on the Fluctuation-Dissipation Theorem. *Journal of the Atmospheric Sciences*, 64:2558–2575, 2007.

J. Guckenheimer and P. Holmes. *Nonlinear Oscillations, Dynamical Systems, and Bifurcation of Vector Fields*. Springer, New York, 1983.

M. Hairer and A. J. Majda. A simple framework to justify linear response theory. *Nonlinearity*, 23:909–922, 2010.

J. K. Hale and S. M. Verduyn Lunel. *Introduction to Functional Differential Equations*. Springer-Verlag, New York, 1993.

D. L. Hartmann. *Global Physical Climatology*. Academic Press, San Diego, 1994.

K. Hasselmann. Stochastic climate models Part I. Theory. *Tellus*, 28:473–485, 1976.

H. Held and T. Kleinen. Detection of climate system bifurcations by degenerate fingerprinting. *Geophysical Research Letters*, 31:1–4, 2004.

I. M. Held. The Gap between Simulation and Understanding in Climate Modeling. *Bulletin of the American Meteorological Society*, 86:1609–1614, 2005.

M. Henon and C. Heiles. The Applicability of the Third Integral of Motion: Some Numerical Experiments. *The Astronomical Journal*, 69:73–79, 1964.

J. M. Hollas. *Modern Spectroscopy*. Wiley, Chichester, 2004.

B. Hoskins. The potential for skill across the range of the seamless weather-climate prediction problem: a stimulus for our science. *Quarterly Journal of the Royal Meteorological Society*, 139:573–584, 2013.

J. Hurrel, M. Visbeck, and A. Pirani. WCRP Coupled Model Intercomparison Project - Phase 5. *CLIVAR Exchanges*, 16:1–52, 2011.

H. Itoh and M. Kimoto. Multiple attractors and chaotic itinerancy in a quasigeostrophic model with realistic topography: implications for weather regimes and low-frequency variability. *Journal of the atmospheric sciences*, 53:2217, 1996.

I. N. James. *Introduction to Circulating Atmospheres*. Cambridge University Press, Cambridge, 1994.

F.-F. Jin. An Equatorial Ocean Recharge Paradigm for ENSO . Part I : Conceptual Model Pacific from his analysis of the empirical relations of. *Journal of the Atmospheric Sciences*, 54:811–829, 1997a.

F.-F. Jin. An Equatorial Ocean Recharge Paradigm for ENSO. Part II: A Stripped-Down Coupled Model. *Journal of the Atmospheric Sciences*, 54:830–847, 1997b.

F.-F. Jin and J. D. Neelin. Modes of interannual tropical ocean-atmosphere interaction - a unified view. Part I: Numerical results. *Journal of the Atmospheric Sciences*, 50:3477–3503, 1993.

F.-F. Jin, S. T. Kim, and L. Bejarano. A coupled-stability index for ENSO. *Geophysical Research Letters*, 33: 1–4, 2006.

T. Jung, T. N. Palmer, and G. J. Shutts. Influence of a stochastic parameterization on the frequency of occurrence of North Pacific weather regimes in the ECMWF model. *Geophysical Research Letters*, 32: L23811, 2005.

M. Kac. On the notion of recurrence in discrete stochastic processes. *Bulletin of the American Mathematical Society*, 20:376–379, 1947.

O. Kallenberg. *Foundations of Modern Probability*. Springer-Verlag, New York, 2002.

E. Kalnay. *Atmospheric modeling, data assimilation, and predictability*, volume 54. Cambridge University Press, Cambridge, 2003.

K. Kaneko. Globally coupled circle maps. *Physica D: Nonlinear Phenomena*, 54:5, 1991.

T. Kato. *Perturbation Theory for Linear Operators*. Springer, Berlin, 1995.

A. Katok. Lyapunov exponents, entropy and periodic orbits for diffeomorphisms. *Institut des Hautes Etudes Scientifiques. Publications Mathématiques*, 51:137–173, 1980.

V. Kharin and F. Zwiers. On the ROC Score of Probability Forecasts. *Journal of Climate*, 16:4145–4150, 2003.

M. Kimoto and M. Ghil. Multiple Flow Regimes in the northern hemisphere winter. Part 1: Methodology and Hemispheric Regimes. *Journal of the atmospheric sciences*, 50:2625, 1993.

R. Knutti and G. C. Hegerl. The equilibrium sensitivity of the Earth's temperature to radiation changes. *Nature Geoscience*, 1:735–743, 2008.

R. Knutti and M. A. A. Rugenstein. Feedbacks, climate sensitivity and the limits of linear models. *Phil. Trans. R. Soc. A*, 373:20150146, 2015.

P. Köhler, B. de Boer, A. S. von der Heydt, L. B. Stap, and R. S. W. van de Wal. On the state-dependency of the equilibrium climate sensitivity during the last 5 million years. *Climate of the Past Discussions*, 11: 3019–3069, 2015.

A. N. Kolmogorov. On conservation of conditionally periodic motions for a small change in Hamilton's function. *Doklady Akademii Nauk SSSR*, 98:525–530, 1954.

A. N. Kolmogorov. New Metric Invariant of Transitive Dynamical Systems and Endomorphisms of Lebesgue Space. *Doklady of Russian Academy of Sciences*, 119:861–864, 1958.

P. Koltai. *Efficient approximation methods for the global long-term behavior of dynamical systems - Theory, algorithms and examples*. PhD thesis, Technische Universität at München, 2010.

D. Kondrashov, K. Ide, and M. Ghil. Weather regimes and preferred transition paths in a three-level quasigeostrophic model. *Journal of the atmospheric sciences*, 61:568–587, 2004.

D. Kondrashov, M. D. Chekroun, and M. Ghil. Data-driven non-markovian closure models. *Physica D*, 297: 33–55, 2015.

B. O. Koopman. Hamiltonian Systems and Transformations in Hilbert Space. *Proceedings of the National Academy of Sciences of the United States of America*, 17:315–318, 1931.

R. Kubo. The fluctuation-dissipation theorem. *Reports on Progress in Physics*, 29:255, 1966.

H. L. Kuo. On formations and intensification of tropical cyclone through latent heat release by cumulus convection.pdf. *Journal of the Atmospheric Science*, 22:40–63, 1965.

H. L. Kuo. Further Studies of the Parameterization of the Influence of Cumulus Convection on Large-Scale Flow. *Journal of the Atmospheric Sciences*, 31:1232–1240, 1974.

Y. A. Kuznetsov. *Elements of Applied Bifurcation Theory, Second Edition*. Springer-Verlag, New York, 1998.

A. a. Lacis and J. Hansen. A Parameterization for the Absorption of Solar Radiation in the Earth's Atmosphere. *Journal of the Atmospheric Sciences*, 31:118–133, 1974.

Y. Lan and I. Mezić. Linearization in the large of nonlinear systems and Koopman operator spectrum. *Physica D: Nonlinear Phenomena*, 242:42–53, 2013.

A. Lasota and M. C. Mackey. *Chaos, Fractals and Noise*. Springer, Berlin, 1994.

L. Laursen and E. Eliasen. On the effects of the damping mechanisms in an atmospheric general circulation model. *Tellus*, 41A:385–400, 1989.

M. Le Bellac, F. Mortessagne, and G. G. Batrouni. *Equilibrium and Non-Equilibrium Statistical Thermodynamics*. Cambridge University Press, 2004.

F. Ledrappier and L.-S. Young. The metric entropy of diffeomorphisms. I. Characterization of measures satisfying Pesin's entropy formula. *The Annals of Mathematics*, 122:509–539, 1985.

B. Legras and M. Ghil. Persistent anomalies, blocking and variations in atmospheric predictability. *Journal of the atmospheric sciences*, 42:433–471, 1985.

C. E. Leith. Theoretical Skill of Monte-Carlo Forecasts. *Monthly Weather Review*, 102:409–418, 1974.

C. E. Leith. Numerical Weather Prediction. *Reviews of Geophysics and Space Physics*, 13:681–684, 1975a.

C. E. Leith. Climate Response and Fluctuation Dissipation. *Journal of the Atmospheric Sciences*, 32:2022–2026, 1975b.

C. E. Leith. Objective Methods for Weather Prediction. *Annual Review of Fluid Mechanics*, 10:107–128, 1978.

C. E. Leith and R. H. Kraichnan. Predictability of Turbulent Flows. *Journal of Atmospheric Sciences*, 29: 1041–1058, 1972.

T. M. Lenton. Early warning of climate tipping points. *Nature Climate Change*, 1:201–209, 2011.

T. M. Lenton, H. Held, E. Kriegler, J. W. Hall, W. Lucht, S. Rahmstorf, and H. J. Schellnhuber. Tipping elements in the Earth's climate system. *Proceedings of the National Academy of Sciences of the United States of America*, 105:1786–93, 2008.

M. Leutbecher and T. N. Palmer. Ensemble forecasting. *Journal of Computational Physics*, 227:3515–3539, 2008.

K. Levenberg. A method for the solution of certain non-linear problems in least squares. *Quarterly Journal of Applied Mathmatics*, II:164–168, 1944.

R. Livi, S. Ruffo, and D. Shepelyansky. Kolmogorov Pathways from Integrability to Chaos and Beyond. *Lect. Notes Phys.*, 636:3–32, 2003.

E. N. Lorenz. Deterministic Nonperiodic Flow. *Journal of the atmospheric sciences*, 20:130, 1963.

E. N. Lorenz. *The nature and theory of the general circulation of the atmosphere*, volume 218. World Meteorological Organization, Geneva, 1967.

E. N. Lorenz. Three Approaches to Atmospheric Predictability. *Bulletin of the American Meteorological Society*, 50:345–351, 1969.

J. F. Louis. A parametric model of vertical eddy fluxes in the atmosphere. *Boundary-Layer Meteorology*, 17:187–202, 1979.

J. F. Louis, M. Tiedke, and M. Geleyn. A short history of the PBL parameterisation at ECMWF. In *Proceedings of the ECMWF Workshop on Planetary Boundary Layer Parameterization*, pages 59–80, Reading, 1981.

V. Lucarini. Response Operators for Markov Processes in a Finite State Space : Radius of Convergence and Link to the Response Theory for Axiom A Systems. *eprint arXiv:1506.07065*, pages 1–24, 2015.

V. Lucarini and T. Bódai. "...the edge state has been constructed also for a simplified climate model...". *Unpublished*, 2015.

V. Lucarini and S. Pascale. Entropy production and coarse graining of the climate fields in a general circulation model. *Climate Dynamics*, 43:981–1000, 2014.

V. Lucarini and S. Sarno. A statistical mechanical approach for the computation of the climatic response to general forcings. *Nonlinear Processes in Geophysics*, 18:7–28, 2011.

V. Lucarini, S. Calmanti, and V. Artale. Experimental mathematics: Dependence of the stability properties of a two-dimensional model of the Atlantic ocean circulation on the boundary conditions. *Russian Journal of Mathematical Physics*, 14:224–231, 2007.

V. Lucarini, K. Fraedrich, and F. Lunkeit. Thermodynamic analysis of snowball earth hysteresis experiment: Efficiency, entropy production and irreversibility. *Quarterly Journal of the Royal Meteorological Society*, 136:2–11, 2010.

V. Lucarini, S. Pascale, R. Boschi, E. Kirk, and N. Iro. Habitability and multistability in earth-like planets. *Astronomische Nachrichten*, 334:576–588, 2013.

V. Lucarini, R. Blender, C. Herbert, F. Ragone, S. Pascale, and J. Wouters. Mathematical and Physical Ideas for Climate Science. *Reviews of Geophysics*, 52:1 – 51, 2014.

A. M. Lyapunov. The general problem of motion stability. *Annals of Mathematics Studies*, 17, 1892.

A. J. Majda, I. Timofeyev, and E. Vanden-Eijnden. Models for stochastic climate prediction. *Proceedings of the National Academy of Sciences*, 96:14687–14691, 1999.

A. J. Majda, I. Timofeyev, and E. Vanden-Eijnden. A mathematical framework for stochastic climate models. *Communications on Pure and Applied Mathematics*, 54:891–974, 2001.

A. J. Majda, C. L. Franzke, A. Fischer, and D. Crommelin. Distinct metastable atmospheric regimes despite nearly Gaussian statistics: a paradigm model. *Proceedings of the National Academy of Sciences of the United States of America*, 103:8309, 2006.

J. C. Maxwell. V. Illustrations of the dynamical theory of gases. Part I. On the motions and collisions of perfectly elastic spheres. *Philosophical Magazine Series 4*, 19:19–32, 1860.

J. C. McWilliams. Irreducible imprecision in atmospheric and oceanic simulations. *Proceedings of the National Academy of Sciences of the United States of America*, 104:8709–8713, 2007.

G. Metafune. Lp-Spetrum of Ornstein-Uhlenbeck Operators. *Annali della Scuola Normale Superiore di Pisa*, 30:97–124, 2001.

G. Metafune, D. Pallara, and E. Priola. Spectrum of Ornstein-Uhlenbeck Operators in Lp Spaces with Respect to Invariant Measures. *Journal of Functional Analysis*, 196:40–60, 2002.

I. Mezić. Analysis of Fluid Flows via Spectral Properties of the Koopman Operator. *Annual Review of Fluid Mechanics*, 45:357–378, 2013.

K. C. Mo, M. Ghil, P. Physics, and L. Angeles. Cluster analysis of multiple planetary flow regimes. *Journal of Geophysical Research*, 93:10927–10952, 1988.

J. J. More, B. S. Garbow, and K. E. Hillstrom. User Guide for MINPACK-1. Argonne National Laboratory, Argonne, 1980.

J. Moser. On invariant curves of area-preserving mappings of an annulus. *Nachr. Akad. Wiss. Gottingen, Math.-Phys. Kl. II.*, 1:1–20, 1962.

M. Mudelsee. *Climate Time Series Analysis: Classical Statistical and Bootstrap Methods*. Springer, Dordrecht, 2010.

J. D. Neelin and H. a. Dijkstra. Ocean-Atmosphere Interaction and the Tropical Climatology Part I: The Dangers of Flux Correction. *Journal of climate*, 1995.

J. D. Neelin, D. S. Battisti, A. C. Hirst, F.-f. Jin, Y. Wakata, T. Yamagata, and S. E. Zebiak. ENSO Theory. *Journal of Geophysical Research*, 103:14261–14290, 1998.

S. A. Orszag. Transform Method for the Calculation of Vector-Coupled Sums: Application to the Spectral Form of the Vorticity Equation. *Journal of the Atmospheric Sciences*, 27:890–895, 1970.

V. I. Oseledets. A multiplicative ergodic theorem. Characteristic Ljapunov, exponents of dynamical systems. *Tr. Mosk. Mat. Obs.*, 19:179–210, 1968.

T. N. Palmer and P. D. Williams. *Stochastic Physics and Climate Modelling*. Cambridge University Press, Cambridge, 2009.

T. N. Palmer, G. Shutts, R. Hagedorn, F. Doblas-Reyes, T. Jung, and M. Leutbecher. Representing Model Uncertainty in Weather and Climate Prediction. *Annual Review of Earth and Planetary Sciences*, 33: 163–193, 2005.

D. Paynter and T. L. Frölicher. Sensitivity of radiative forcing, ocean heat uptake, and climate feedback to changes in anthropogenic greenhouse gases and aerosols. *Journal of Geophysical Research: Atmospheres*, 120:1–18, 2015.

C. S. Peirce. The numerical measure of the success of predictions. *Science*, 4:453–454, 1884.

J. P. Peixoto and A. H. Oort. *Physics of Climate*. American Institute of Physics, New York, 1992.

C. Penland. Noise Out of Chaos and Why it Won't Go Away. *Bulletin of the American Meteorological Society*, 84:921–925, 2003.

O. Perron. Über Stabilität und Asymptotisches Verhalten der Integrale von Gewöhnlichen Differentialgleichungen und Differenzengleichungen. *J. Reine Angew. Math.*, 161:41–64, 1929.

Y. B. Pesin. Characteristic Lyapunov Exponents and Smooth Ergodic Theory. *Russian Mathematical Surveys*, 32:55–114, 1977.

R. Pierrehumbert, D. Abbot, A. Voigt, and D. Koll. Climate of the Neoproterozoic. *Annual Review of Earth and Planetary Sciences*, 39:417–460, 2011.

G. Plaut and R. Vautard. Spells of Low-Frequency Oscillations and Weather Regimes in the Northern Hemisphere. *Journal of the atmospheric sciences*, 51:210–236, 1994.

H. Poincaré. Sur L'Equilibre D'Une Masse Fluide Animee D'Un Mouvement De Rotation. *Acta Mathematica*, 7:259–380, 1885.

H. Poincaré. Memoire sur les courbes definies par une equation differentielle. *Journal de mathématiques pures et appliquées*, 7:375–422, 1881.

H. Poincaré. Sur le problème des trois corps et les équations de la dynamique. *Acta mathematica*, 13: 1–270, 1890.

H. Poincaré. *Les methodes nouvelles des mecaniques celestes: Tome I*. Gauthier-Villars et fils, Paris, 1892.

M. Pollicott. On the rate of mixing of Axiom A flows. *Inventiones Mathematicae*, 81:413–426, 1985.

C. J. Poulsen and R. L. Jacob. Factors that inhibit snowball Earth simulation. *Paleoceanography*, 19:1–11, 2004.

F. Ragone, V. Lucarini, and F. Lunkeit. A new framework for climate sensitivity and prediction. *Climate Dynamics*, pages 1–25, 2015.

A. Ramm. Variational Principles for Eigenvalues of Compact Nonselfadjoint Operators. *Journal of Mathematical Analysis and Applications*, 80:291–293, 1981.

A. Ramm. Variational principles for eigenvalues of compact nonselfadjoint operators II. *Journal of Mathematical Analysis and Applications*, 91:30–38, 1983.

J. Roads. Predictability in the extended range. *Journal of the atmospheric sciences*, 44:3495, 1987.

G. Roe. Feedbacks, Timescales, and Seeing Red. *Annual Review of Earth and Planetary Sciences*, 37:93–115, 2009.

E. Roeckner, K. Arpe, L. Bengtsson, S. Brinkop, L. Dümenil, M. Esch, E. Kirk, F. Lunkeit, M. Ponater, B. Rockel, R. Sausen, U. Schlese, S. Schubert, and M. Windelband. Simulation of present day climate with the ECHAM model: impact of model physics and resolution. Technical Report, 93. Max Planck Institut für Meteorologie, Hamburg, 1992.

L. Roques, M. D. Chekroun, M. Cristofol, S. Soubeyrand, and M. Ghil. Parameter estimation for energy balance models with memory. *Proceedings of the Royal Society A: Mathematical, Physical and Engineering Sciences*, 470:20140349–20140349, 2014.

M. Rosvall and C. T. Bergstrom. Maps of random walks on complex networks reveal community structure. *Proceedings of the National Academy of Sciences of the United States of America*, 105:1118, 2008.

M. S. Roulston and J. D. Neelin. The response of an ENSO Model to climate noise, weather noise and intraseasonal forcing. *Geophysical Research Letters*, 27:3723–3726, 2000.

C. W. Rowley, I. Mezić, S. Bagheri, P. Schlatter, and D. S. Henningson. Spectral analysis of nonlinear flows. *Journal of Fluid Mechanics*, 641:115, 2009.

D. Ruelle. Microscopic Fluctuations and Turbulence. *Physics Letters A*, 72:81–82, 1979.

D. Ruelle. Measures describing a turbulent flow. *Annals of the New York Academy of Sciences*, 357:1–9, 1980.

D. Ruelle. Resonances of Chaotic Dynamical Systems. *Physical review letters*, 56:405–407, 1986a.

D. Ruelle. Locating resonances for AxiomA dynamical systems. *Journal of statistical physics*, 44:281–292, 1986b.

D. Ruelle. *Chaotic Evolution and Strange Attractors*. Cambridge University Press, Cambridge, 1989a.

D. Ruelle. *Elements of Differentiable Dynamics and Bifurcation Theory*. Academic Press, San Diego, 1989b.

D. Ruelle. The thermodynamic formalism for expanding maps. *Communications In Mathematical Physics*, 125:239–262, 1989c.

D. Ruelle. Differentiation of SRB States. *Communications in Mathematical Physics*, 1887:227–241, 1997.

D. Ruelle. Smooth Dynamics and New Theoretical Ideas in Nonequilibrium Statistical Mechanics. *Journal of Statistical Physics*, 95:393–468, 1999.

D. Ruelle. A review of linear response theory for general differentiable dynamical systems. *Nonlinearity*, 22:855–870, 2009.

D. Ruelle and F. Takens. On the nature of turbulence. *Communications in mathematical physics*, 20:303–322, 1971.

M. Rugenstein, J. Sedlacek, and R. Knutti. Is the linear global radiative forcing-feedback framework still useful ? In *Geophysical Research Abstracts*, volume 17, page 11477, 2015.

M. Rychlik. Bounded variation and invariant measures. *Studia Mathematica*, 76:69–80, 1983.

B. Saltzman. *Dynamical paleoclimatology: generalized theory of global climate change*. Academic Press, San Diego, 2002.

T. Sasamori. The Radiative Cooling Calculation for Application to General Circulation Experiments. *Journal of Applied Meteorology*, 7:721–729, 1968.

B. Schalge, R. Blender, J. Wouters, K. Fraedrich, and F. Lunkeit. Evidence for a fluctuation theorem in an atmospheric circulation model. *Physical Review E*, 87:052113, 2013.

M. Scheffer, J. Bascompte, W. a. Brock, V. Brovkin, S. R. Carpenter, V. Dakos, H. Held, E. H. van Nes, M. Rietkerk, and G. Sugihara. Early-warning signals for critical transitions. *Nature*, 461:53, 2009.

T. M. Schneider, B. Eckhardt, and J. a. Yorke. Turbulence transition and the edge of chaos in pipe flow. *Physical Review Letters*, 99:1–4, 2007.

C. Schütte and Marco Sarich. Metastability and Markov State Models in Molecular Dynamics: Modeling, Analysis, Algorithmic Approaches, 2013.

C. Schütte, A. Fischer, W. Huisinga, and P. Deuflhard. A Direct Approach to Conformational Dynamics Based on Hybrid Monte Carlo. *Journal of Computational Physics*, 151:146–168, 1999.

J. R. Scott, J. Marotzke, and P. H. Stone. Interhemispheric Thermohaline Circulation in a Coupled Box Model. *Journal of Physical Oceanography*, 29:351, 1999.

W. D. Sellers. A Global Climatic Model Based on the Energy Balance of the Earth-Atmosphere System. *Journal of Applied Meteorology*, 8:392–400, 1968.

F. M. Selten. An efficient description of the Dynamics of Barotropic Flows. *Journal of the atmospheric sciences*, 52:915, 1995.

A. J. Semtner. A Model for the Thermodynamic Growth of Sea Ice in Numerical Investigations of Climate. *Journal of Physical Oceanography*, 6:379–389, 1976.

L. P. Shilnikov. A case of the existence of a countable number of periodic motions. *Soviet Mathematics-Doklady*, 6:163–166, 1965.

L. P. Shilnikov. Bifurcation theory and turbulence. In R. Sagdeev, editor, *Nonlinear and Turbulent Processes in Physics*, pages 1627–1635, 1984.

L. P. Shilnikov, G. Nicolis, and C. Nicolis. Bifurcation and Predictability Analysis of a Low-Order Atmospheric Circulation Model. *International Journal of Bifurcation and Chaos*, 05:1701–1711, 1995.

a. J. Simmons and a. Hollingsworth. Some aspects of the improvement in skill of numerical weather prediction. *Quarterly Journal of the Royal Meteorological Society*, 128:647–677, 2002.

Y. G. Sinai. On the Notion of Entropy of a Dynamical System. *Doklady of Russian Academy of Sciences*, 124: 250, 1959.

Y. G. Sinai. Gibbs Measures in Ergodic Theory. *Russian Mathematical Surveys*, 27:21–69, 1972.

A. Slingo and J. M. Slingo. Response of the National Center for Atmospheric Research community climate model to improvements in the representation of clouds. *Journal of Geophysical Research*, 96:15341, 1991.

S. Smale. Structurally Stable Systems are not Dense. *American Journal of Mathematics*, 88:491–496, 1966.

S. Smale. Differentiable dynamical systems. *Bulletin of the American Mathematical Society*, 73:747–818, 1967.

P. Smyth. Model selection for probabilistic clustering using cross-validated likelihood. *Statistics and Computing*, 3425:63–72, 1999.

P. Smyth, K. Ide, M. Ghil, C. Science, P. Physics, and L. Angeles. Multiple Regimes in Northern Hemisphere Height Fields via Mixture Model Clustering*. *Journal of the atmospheric sciences*, 56:3704–3723, 1999.

G. L. Stephens, G. W. Paltridge, and C. M. R. Platt. Radiation Profiles in Extended Water Clouds. III: Observations. *Journal of the Atmospheric Sciences*, 35:2133–2141, 1978.

G. L. Stephens, S. Ackerman, and E. A. Smith. A Shortwave Parameterization Revised to Improve Cloud Absorption. *Journal of the Atmospheric Sciences*, 41:687–690, 1984.

D. B. Stephenson. Use of the "odds ratio" for diagnosing forecast skill. *Weather and Forecasting*, 15: 221–232, 2000.

D. B. Stephenson, a. Hannachi, and a. O'Neill. On the existence of multiple climate regimes. *Quarterly Journal of the Royal Meteorological Society*, 130:583–605, 2004.

T. Stocker, D. Qin, G.-K. Plattner, M. Tignor, S. Allen, J. Boschung, A. Nauels, Y. Xia, V. Bex, and P. Midgley, editors. *IPCC, 2013: Climate Change 2013: The Physical Science Basis. Contribution of Working Group I to the Fifth Assessment Report of the Intergovernmental Panel on Climate Change*. Cambridge University Press, Cambridge, United Kingdom and New York, NY, USA, 2013.

M. H. Stone. Linear Transformations in Hilbert Space: III. Operational Methods and Group Theory. *Proceedings of the National Academy of Sciences of the United States of America*, 16:172–175, 1930.

S. H. Strogatz. *Nonlinear Dynamics and Chaos: With Applications to Physics, Biology, Chemistry, and Engineering*. Westview Press, Boulder, 1994.

M. J. Suarez and P. S. Schopf. A delayed action oscillator for ENSO. *Journal of Atmospheric Sciences*, 45: 3283–3287, 1988.

F. Takens. Detecting strange attractors in turbulence. *Dynamical Systems and Turbulence, Warwick 1980*, 898:366–381, 1981.

A. Tantet and H. a. Dijkstra. An interaction network perspective on the relation between patterns of sea surface temperature variability and global mean surface temperature. *Earth System Dynamics*, 5:1–14, 2014.

K. E. Taylor, R. J. Stouffer, and G. a. Meehl. An Overview of CMIP5 and the Experiment Design. *Bulletin of the American Meteorological Society*, 93:485–498, 2012.

J. E. Thornes and D. B. Stephenson. How to judge the quality and value of weather forecast products. *Meteorological Applications*, 8:307–314, 2001.

G. Tirabassi, J. P. Viebahn, V. Dakos, H. a. Dijkstra, C. Masoller, M. Rietkerk, and S. Dekker. Interaction network based early-warning indicators of vegetation transitions. *Ecological Complexity*, 19:148–157, 2014.

L. N. Trefethen and M. Embree. *Spectra and Pseudospectra: The Behavior of Nonnormal Matrices and Operators*. Princeton University Press, Princeton and Oxford, 2005.

E. Tziperman, L. Stone, M. A. Cane, and H. Jarosh. El nino chaos: overlapping of resonances between the seasonal cycle and the pacific ocean-atmosphere oscillator. *Science*, 264:72–74, 1994.

S. M. Ulam. *Problems in Modern Mathematics*. Wiley, New York, science edition, 1964.

P. Valdes. Built for stability. *Nature Geoscience*, 4:414–416, 2011.

G. K. Vallis. *Atmospheric and Oceanic Fluid Dynamics*. Cambridge University Press, Cambridge, 2006.

M. van der Mheen, H. a. Dijkstra, A. Gozolchiani, M. den Toom, Q. Feng, J. Kurths, and E. Hernandez-Garcia. Interaction network based early warning indicators for the Atlantic MOC collapse. *Geophysical Research Letters*, 40:2714–2719, 2013.

P. van der Vaart, H. a. Dijkstra, and F.-F. Jin. The Pacific Cold Tongue and the ENSO Mode : A Unified Theory within the Zebiak - Cane Model. *Journal of Atmospheric Sciences*, 57:967–988, 2000.

E. van Sebille, M. H. England, and G. Froyland. Origin, dynamics and evolution of ocean garbage patches from observed surface drifters. *Environmental Research Letters*, 7:044040, 2012.

J. P. Viebahn and H. a. Dijkstra. Critical Transition Analysis of the Deterministic Wind-Driven Ocean Circulation - A Flux-Based Network Approach. *International Journal of Bifurcation and Chaos*, 24: 1430007, 2014.

A. Voigt and J. Marotzke. The transition from the present-day climate to a modern Snowball Earth. *Climate Dynamics*, 35:887–905, 2010.

A. S. von der Heydt, H. a. Dijkstra, P. Köhler, and R. V. D. Wal. On the background state dependency of (palaeo) climate sensitivity. *Geophysical Research Letters*, 41:6484–6492, 2014.

J. von Neumann. Proof of the Quasi-Ergodic Hypothesis. *Proceedings of the National Academy of Sciences of the United States of America*, 18:70–82, 1932.

H. von Storch and F. Zwiers. *Stastistical Analysis in Climate Research*. Cambridge University Press, Cambridge, 1999.

T. T. Warner. *Numerical Weather and Climate Prediction*. Cambridge University Press, Cambridge, 2010.

E. R. Weeks, H. L. Swinney, and M. Ghil. Transitions Between Blocked and Zonal Flows in a Rotating Annulus with Topography. *Science*, 278:1598–1601, 1997.

R. T. Wetherald and S. Manabe. The Effects of Changing the Solar Constant on the Climate of a General Circulation Model. *Journal of Atmospheric Sciences*, 32:2044–2059, 1975.

P. D. Williams. Spontaneous generation and impact of inertia-gravity waves in a stratified, two-layer shear flow. *Geophysical Research Letters*, 30:2255, 2003.

P. D. Williams, T. W. N. Haine, and P. L. Read. Stochastic resonance in a nonlinear model of a rotating , stratified shear flow , with a simple stochastic inertia-gravity wave parameterization. *Nonlinear Processes in Geophysics*, 11:127, 2004.

P. D. Williams, T. W. N. Haine, and P. L. Read. On the generation mechanisms of short-scale unbalanced modes in rotating two-layer flows with vertical shear. *Journal of Fluid Mechanics*, 528:1, 2005.

P. D. Williams, T. W. N. Haine, and P. L. Read. Inertia-Gravity Waves Emitted from Balanced Flow: Observations, Properties, and Consequences. *Journal of the atmospheric sciences*, 65:3543, 2008.

P. D. Williams, M. J. P. Cullen, M. K. Davey, and J. M. Huthnance. Mathematics applied to the climate system: outstanding challenges and recent progress. *Philosophical transactions. Series A, Mathematical, physical, and engineering sciences*, 371:20120518, 2013.

A. Wörz-Busekros. Global Stability in Ecological Systems with Continuous Time Delay. *SIAM J. Appl. Math.*, 35:123–134, 1978.

J. Wouters and V. Lucarini. Disentangling multi-level systems: averaging, correlations and memory. *Journal of Statistical Mechanics: Theory and Experiment*, 2012:P03003, 2012.

J. Wouters and V. Lucarini. Multi-level Dynamical Systems: Connecting the Ruelle Response Theory and the Mori-Zwanzig Approach. *Journal of Statistical Physics*, 151:850–860, 2013.

K. Yosida. *Functional Analysis*. Springer-Verlag, Berlin Heidelberg New York, 1980.

L.-s. Young. Developments in Chaotic Dynamics. *Notices of the AMS*, 45:1318–1328, 1998.

L.-S. Young. What are SRB measures , and which dynamical systems have them? *Journal of Statistical Physics*, 108:733–754, 2002.

I. Zaliapin and M. Ghil. Another look at climate sensitivity. *Nonlinear Processes in Geophysics*, 17:113–122, 2010.

I. Zaliapin and M. Ghil. Reply to Roe and Baker's comment on "Another look at climate sensitivity" by Zaliapin and Ghil (2010). *Nonlinear Processes in Geophysics*, 18:129–131, 2011.

G. Zaslavsky and B. Chirikov. On the mechanism of one-dimensional Fermi acceleration. *Akad. Nauk USSR*, 159:306–309, 1964.

S. E. Zebiak and M. A. Cane. A model of El Nino-Southern Oscillation. *Monthly Weather Review*, 115: 2262–2278, 1987.

R. Zwanzig. *Nonequilibrium Statistical Mechanics*. Oxford University Press, Oxford, 2001.

LIST OF PUBLICATIONS

1. Tantet, A., M. D. Chekroun, J. D. Neelin, H. A. Dijkstra. Mixing Spectrum in Reduced Phase Space of Stochastic Evolution Equations. Part II: Application to Stochastic Bifurcation and El Niño, *arXiv*, submitted to *Physica D*, 2016.

2. Chekroun M. D., A. Tantet, J. D. Neelin, H. A. Dijkstra. Mixing Spectrum in Reduced Phase Space of Stochastic Evolution Equations. Part I: Theory, *arXiv*, submitted to *Physica D*, 2016.

3. Tantet, A., V. Lucarini, F. Lunkeit, H. A. Dijkstra. Crisis of the Chaotic Attractor of a Climate Model: A Transfer Operator Approach, *arXiv: 1507.02228*, submitted to *Nonlinearity*, 2015.

4. Ihshaish, H., A. Tantet, J. C. M. Dijkzeul, H. A. Dijkstra. Par@Graph - a parallel toolbox for the construction and analysis of large complex climate networks, *Geosci. Model Dev.*, 8:319-349, doi:10.5194/gmd-8-3321-2015, 2015.

5. Tantet, A., F. R. van der Burgt, H. A. Dijkstra. An early warning indicator for atmospheric blocking events using transfer operators, *Chaos*, 25:036406, doi:10.1063/1.4908174, 2015.

6. Tantet, H. A. Dijkstra. An interaction network perspective on the relation between patterns of sea surface temperature variability and global mean surface temperature, *Earth Syst. Dynam.*, 5:1-14, doi:10.5194/esd-5-1-2014, 2014.

For the most recent preprints, please visit:
`https://www.researchgate.net/profile/Alexis_Tantet`

ACKNOWLEDGMENTS

During these three years, the PhD has been at the center of a very reach experience. Not because of the involvement such a work demands, but rather for the scientific dedication, the experience abroad, and most importantly, the encounters that came with it.

First and foremost, I cannot thank enough my supervisor, Henk Dijkstra, for giving me the opportunity to engage in this remarkable experience. As a mentor, I could rely on his support, benefit from his ever useful guidance and yet enjoy the freedom of looking for my own way. I had the utmost pleasure to exchange passionately with the scientist and found inspiration in his insight and creativity. I could also appreciate the vibrant atmosphere that he created in the ocean group and his encouragements to interact with other researchers. At last, I would like to wholeheartedly thank him for his honesty and humor which made the adventure all the more pleasant.

These values I could also find in my dear collaborators and friends Mickaël Chekroun and Valerio Lucarini, both of them I had the chance to meet in the Alpine heights of Gran Paradiso. The topic of this thesis would probably not have been the same without these encounters, as well as my scientific instruction and progress. I risk to disappoint Valerio, not giving him the formal acknowledgment that he deserves, yet I would like to thank him warmly for receiving me as a friend from the start, sharing his insights and excitement on statistical mechanics and night dynamics. I am deeply thankful to Professor Chekroun for introducing me to the marvelous world of transfer operators and to share with me his studies on mathematics, among other topics. Most importantly, I am grateful for his patience and generosity and for welcoming me in his group of AOS in UCLA.

I believe it is not a hazard if, among this community, I had the chance to meet these other researchers to whom I am very thankful. First, Michael Ghil for his remarkable lectures and even more memorable sense of good life which I had the pleasure to discover around a cigar in the fresh Alpine night. In such good times, Dmitri Kondrashov is usually not too far and I really enjoyed our scientific and not so scientific exchanges. I would also like to thank Paul Williams for our ever enthusiastic exchanges at schools, workshops and conferences. Finally, I am very grateful to David Neelin, for our recent collaboration, his insights on climate physics and his benevolence.

This PhD would not have been the same if not for the exciting group of people that was gathered under the LINC project. I cannot thank enough Marcelo Barreiro for his warm and lively welcome in his group of Montevideo, Uruguay. I am in particular very grateful to his invaluable teachings on the circulation of the atmosphere. I would also

like to thank Manfred Mudelsee, for his patient and rigorous training on statistical methods for climate, which surely helps me in my research very much.

I consider myself very lucky that this project was also the ground of priceless friendships. With whom to start but my dear Hishamo. Colleague during the day, tango partner, deacon, confident or roommate at night, this sure is more intense with him. Many from the project will confirm. In particular, Johan Dijkzeul, whom I admire for his endurance with Dr. Ihshaish, but most importantly whom I would like to thank dearly for taking part in the gang and surprising us when we least expect it. Thanks to their stay and outing in the Netherlands, the complicated Enrico Ser Giacomi, the out of equilibrium Giulio Tirabassi, the spicy Victor Rodriguez, the chatty Juan Ignacio Deza and the lyrical Fernando Arizmendi could also corroborate. The latter, I am particularly thankful of, for hosting me in his cozy residence, in company of the playful Felipe, which made my stay in Uruguay all the more enjoyable. Finally, it was with great pleasure that I participated to the schools, workshops and conferences with Verónica Martín Gómez and her soft vocabulary, Miguel Bermejo, Veronika Stolbova, Dong Zhou, Yang Wang, Marc Segond and Ruggero Vasile as well as with professors and researchers Markus Abel, Vartkes Goetcherian, Avi Gozolchiani, Shlomo Havlin, Emilio Hernandez-Garcia, Jürgen Kurths and in particular Christina Masoller for making it happen.

As part of the project but also of the ocean group, I would like to thank Qingyi warmly for making my arrival at IMAU so easy and for bringing her cheerful touch to all these breaks, schools and workshops. To my colleagues from the ocean group, Fiona, Claudia, Michiel, Maria, Michael, Mariët, Eric, Inti, thank you for making it such a lively atmosphere. To Jan, many thanks for our animated discussions, for your acute critics and for showing us your latest west-coast moves. I am very grateful to Anna von der Heydt for her useful advice and calm discussions on turbulence. I am very grateful to all the researchers in the coastal, ice and atmospheric groups, to the staff and to the faculty of IMAU for making it such a pleasant atmosphere. I have learned to appreciate how precious and rare such an environment is and I sure will be missing it. In particular, let me thank kindly my dear officemates Carina and Michiel for their joyful discussions, for sharing their Dutch tips and for making the working day so enjoyable. Finally, I would like to thank Will de Ruijter heartily for sharing his passion and curiosity, for our enthusiastic discussions and for his wise optimism.

How can I thank enough my Tricolore pals and friends, Abdel, Dorota, Sudhanshu, Chen Wei and Simon? I've enjoyed each and every "tranquille" moments with this "chingada" team and wish for many more to come. I am sincerly grateful for meeting my dear friends Dewi, Lisa and Drazen, who introduced me to their community of friends from the beginning, to the market tradition and made my arrival in Utrecht so pleasant. To Dewi, for his kind presence during these years and whom I admire for his serenity. To Lisa, for all her warmth, radiance, and making us feel at home wherever we are. To Drazen, for showing me that I may be "sophisticated" but that the real cool lies in the second-hand stores.

This PhD also marks the accomplishment of a long cycle of study during which I grew up with the help of my family and my close friends. I would like to grasp this occasion to thank them dearly.

Let me start with Arnaud, my oldest friend. We have followed each other since secondary school and had the chance to share many things together. I am grateful that this friendship continues, together with our dear high school friends Antoine, Baudouin, Emmanuel, Paul, Stella, Thibaut and Tristan. Wherever we go, wherever we are, this friendship means a lot to me.

Preparation class was not a piece of cake, but the support of my dear friends Nicolas and Victor allows me to feel warmth when looking back at this period. I then had the chance to meet amazing people in Marseille during the engineering school. The list is too long, but I would like to express my deepest gratitude to my flatmates Axel and his scams, Aurélien and his perspicacity and delicateness Myriam and her endurance, Pitch and his communicative smile. Let me thank everyone from the "orange mechalist" for all these good moments which continue, as well as the "farigoule" for making the experience so different and loud. I would also like to thank Aurélien and Gabriel personally, their role in my life growing ever since the school.

I would like to finish with those who where there from the beginning. First my beloved cousins, Sophie and Alix and their parents Veronique and Olivier, for this time growing up in Noirmoutier and Chatou. My dear godmother Julie, Manu, Anne and Pierre-Etienne, for their presence all these years. My cousins Ludo and Victor and their mother Sylvie, for their ever loving attention, together with Soraya, Faouzi, and Marie-Helene. My grand mothers and my grand parents who could not follow me during this PhD, but definitely led me to it. I am sincerely grateful to Marceau, Nicolas, Laetitia and Patricia. It has not always been easy but you truly are part of my family.

And of course, who would I become if not for the support and encouragements of my dear, dear sisters, Claire and Clémentine, that I treasure. You lead the way and make it so much reacher. And to my parents for an education towards freedom and their unconditional love and protection.

To urr, for flying together to lands which have no name.

CURRICULUM VITAE

The author was born on July 19th, 1989 in Paris, France and grew up in the peaceful suburb of Chatou and Le Vésinet, where the impressionist painters would find inspiration along the Seine. There, he went through primary to high school, before to move to the Phocean city of Marseille, where he enrolled the engineering school Centrale. In front of the Mediterranean see, he could confirm his interest in fluid dynamics and climate and completed his diploma with a master thesis in physical oceanography at GEOMAR in Kiel, Germany. In 2012, he moved to the city of Buys Ballot, Utrecht, the Netherlands to start his PhD at the Institute for Marine and Atmospheric Research of Utrecht University under the supervision of Henk Dijkstra as part of the LINC Marie Curie initial training network. During these three years, he shifted his topic from network analysis to the ergodic theory of climate. The results of these investigations are summarized in this thesis.

This document was typeset using `classicthesis` developed by André Miede.